

General Disclaimer

One or more of the Following Statements may affect this Document

- This document has been reproduced from the best copy furnished by the organizational source. It is being released in the interest of making available as much information as possible.
- This document may contain data, which exceeds the sheet parameters. It was furnished in this condition by the organizational source and is the best copy available.
- This document may contain tone-on-tone or color graphs, charts and/or pictures, which have been reproduced in black and white.
- This document is paginated as submitted by the original source.
- Portions of this document are not fully legible due to the historical nature of some of the material. However, it is the best reproduction available from the original submission.

DEVELOPMENT OF A HIGH CAPACITY BUBBLE DOMAIN MEMORY ELEMENT AND RELATED EPITAXIAL GARNET MATERIALS FOR APPLICATION IN SPACECRAFT DATA RECORDERS

ITEM 2

The Optimization of Material-Device Parameters for Application in Bubble Domain Memory Elements for Spacecraft Data Recorders

By

P. J. Besser, et al

June 1976

(NASA-CR-144960) DEVELOPMENT OF A HIGH
CAPACITY BUBBLE DOMAIN MEMORY ELEMENT AND
RELATED EPITAXIAL GARNET MATERIALS FOR
APPLICATION IN SPACECRAFT DATA RECORDERS.

ITEM 2: THE (ROCKWELL INTERNATIONAL CORP.,
Prepared under Contract NAS 1-12981

N76-25340
HC \$7.50

UNCLAS
42144

G3/19

Rockwell International Corporation

Anaheim, California

For

Langley Research Center

National Aeronautics and Space Administration



1. Report No. NASA CR 144960		2. Government Accession No.		3. Recipient's Catalog No.	
4. Title and Subtitle Development of a High Capacity Bubble Domain Memory Element and Related Epitaxial Garnet Materials for Application in Spacecraft Data Recorders				5. Report Date June 1976	
				6. Performing Organization Code	
7. Author(s) P. J. Besser, et al				8. Performing Organization Report No. C74-192/501	
9. Performing Organization Name and Address Rockwell International Electronics Research Division 3370 Miraloma Ave Anaheim, California 92803				10. Work Unit No.	
				11. Contract or Grant No. NAS 1-12981	
12. Sponsoring Agency Name and Address Langley Research Center NASA Hampton, Virginia 23365				13. Type of Report and Period Covered Final 2/18/74 - 10/31/75	
				14. Sponsoring Agency Code	
15. Supplementary Notes Final Report - Item 2 The Optimization of Material - Device Parameters for Application in Bubble Domain Memory Elements for Spacecraft Data Recorders					
16. Abstract <p>This effort has been primarily a phenomena-oriented study of bubble domain materials and devices. One of the materials development goals was a materials system suitable for operation of 16 μm period bubble domain devices at 150 kHz over the temperature range -10°C to +60°C. Several material compositions and hard bubble suppression techniques were characterized and the most promising candidates were evaluated in device structures. The technique of pulsed laser stroboscopic microscopy was used to characterize bubble dynamic properties and device performance at 150 kHz. Techniques for large area LPE film growth were developed as a separate task.</p> <p>Device studies included detector optimization, passive replicator design and test and on-chip bridge evaluation. As a technology demonstration an 8 chip memory cell was designed, tested and delivered. The memory elements used in the cell were 10 kilobit serial registers designed on the basis of the information gained on earlier tasks of the program.</p>					
17. Key Words (Suggested by Author(s)) Bubble Domain Materials Hard Bubble Suppression Techniques Large Area Film Growth Detector Studies Memory Cell Design/Fabrication				18. Distribution Statement Unclassified - Unlimited	
19. Security Classif. (of this report) Unclassified		20. Security Classif. (of this page) Unclassified		22. Price*	
				21. No. of Pages 172	

FOREWORD

The work on Contract NAS1-12981 has been divided into two separate but concurrent efforts, Item 1 and Item 2. This report covers the work performed on Item 2 during the interval 18 February 1974 to 31 October 1975. The results of Item 1 will be reported separately.

The contents of this report represent the contributions of many individuals. Dr. P. J. Besser, Staff Scientist, Applied Magnetics Department was principal investigator on the program. Program responsibility was assigned to the Applied Magnetics Department, Mr. J. L. Archer, Manager. The bulk of the program effort was distributed between five groups: Magnetic Circuits, Mr. R. F. Bailey, Group Leader; Magnetic Devices, Dr. L. R. Tocci, Group Leader; Garnet Film Processing, Mr. R. G. Warren, Group Leader; and Magnetic Materials, Dr. D. M. Heinz, Group Leader. Other individuals who made major technical contributions to this program and/or report and their areas of effort are: Mr. R. G. Warren (Task 2), Dr. D. M. Heinz (Task 1), Dr. R. D. Henry (Task 3), Dr. M. T. Elliott (Tasks 1 and 3), Dr. T. Kobayashi (Tasks 4 and 5), Dr. P. K. George (Tasks 6, 7 and 8), Mr. R. G. Wolfshagen (Task 8), Mr. O. D. Bohning (Task 8), Mr. J. L. Williams (Tasks 7 and 8), Dr. L. R. Tocci (Task 8), Dr. T. T. Chen (Task 8), and Mr. J. P. Reekstin (Artwork and Mask Fabrication).

CONTENTS

	<u>Page</u>
FOREWORD	ii
1. SYNOPSIS	1
2. TASK 1; DESIGN OF IMPROVED BUBBLE COMPOSITION	4
2.1 Introduction	4
2.2 Trial Composition Containing Gadolinum	6
2.3 Comparison of Compositions from Item 1	12
2.4 Trial Composition Not Containing Gadolinum	12
2.5 Candidate Compositions	19
3. TASK 3; HARD BUBBLE SUPPRESSION TECHNIQUES	22
3.1 Introduction	22
3.2 Hard Bubble Suppression Techniques	22
3.3 Conclusions	29
4. TASK 2; LARGE AREA FILM GROWTH	30
4.1 Introduction	30
4.2 Substrate Processing	30
4.3 Garnet Film Growth	31
5. TASK 4. - DEVICE EVALUATION OF CANDIDATE MATERIALS AND HARD BUBBLE SUPPRESSION TECHNIQUES	36
5.1 Device Characterization	36
5.1.1 Bias Margin at Room Temperature	37
5.1.2 Temperature Dependence of Bias Margin	40
5.2 Summary and Conclusions	45
6. TASK 5 - EFFECTS OF HARD BUBBLE SUPPRESSION LAYERS AND CRYSTAL ORIENTATION ON MATERIAL AND DEVICE CHARACTERISTICS STUDIED USING A HIGH SPEED OPTICAL SAMPLING TECHNIQUE	46
6.1 High Speed Optical Sampling Technique	46
6.2 Effects of Hard Bubble Suppression Layers	49
6.2.1 Radial Velocity Measurements	49
6.2.2 Device Characterization	55
6.3 Effects of Crystal Orientation	56

CONTENTS (Cont)

	<u>Page</u>
6.3.1 Radial Velocity Measurements	57
6.3.2 Device Characterization	62
7. TASK 6 - MAGNETORESISTANCE DETECTOR STUDY	66
7.1 Stretcher Dynamics	66
7.1.1 90 Deg vs 110 Deg Chevrons and Stacking Properties of the Chevrons	66
7.1.2 Period and Mobility Dependence of Chevron Margins	67
7.1.3 Permalloy Interconnect Geometry and Margins	70
7.2 Detector Sensitivity	72
7.2.1 90 Deg vs 110 Deg Chevrons (Two Level Detector)	73
7.2.2 Period Dependence of the Output	73
7.2.3 90 vs 110 Deg Chevrons (One Level Detector)	76
7.2.4 Length, Geometry and Drive Field Dependence of the Detector Output	78
7.2.5 Spacing Dependence of the Detector Output	79
7.2.6 Thickness Dependence of Output For One-Level Detectors	81
7.3 Detector Noise Study	83
7.3.1 Introduction	83
7.3.2 Experimental Apparatus	84
7.3.3 Basic Magnetoresistance Variation	86
7.3.4 Detector Operation and Origin of the Large I_w Output at Low Drive Field	90
7.3.5 Geometrical and Drive Field Dependence of the Zero State Error Rate	94
7.3.6 Frequency Dependence of Zero State Noise	99
7.3.7 Zero and One State Noise For One- and Two-Level Detectors	99
7.4 Conclusions and Recommendations	99
8. TASK 7. PASSIVE REPLICATOR AND ON-CHIP BRIDGE DESIGN AND EVALUATION	105
8.1 Passive Replicator Design	105
8.2 Fabrication and Characterization of the Passive Replicator Test Patterns	105
8.3 On-Chip Bridge Design	107
8.4 Test Results for an On-Chip Bridge	114
8.5 Conclusions and Recommendations	117

ILLUSTRATIONS

Figure	Page
1. Velocity as a Function of Drive Field at -10°C for a $\text{Y}_{2.22}\text{Sm}_{0.15}\text{Gd}_{0.40}\text{Tm}_{0.23}\text{Ga}_{0.95}\text{Fe}_{4.05}\text{O}_{12}$ Film	7
2. Variation of Bubble Diameter With Bias Field for $\text{Y}_{2.22}\text{Sm}_{0.15}\text{Gd}_{0.40}\text{Tm}_{0.23}\text{Ga}_{0.95}\text{Fe}_{4.05}\text{O}_{12}$ Film	8
3. Bias Field Needed to Maintain Constant Bubble Diameter as a Function of Temperature for a $\text{Y}_{2.22}\text{Sm}_{0.15}\text{Gd}_{0.40}\text{Tm}_{0.23}\text{Ga}_{0.95}\text{Fe}_{4.05}\text{O}_{12}$ Film	8
4. Velocity as a Function of Drive Field at -10°C for a $\text{Y}_{2.43}\text{Sm}_{0.15}\text{Gd}_{0.20}\text{Tm}_{0.15}\text{La}_{0.07}\text{Ga}_{1.03}\text{Fe}_{3.97}\text{O}_{12}$ Film	10
5. Variation of Bubble Diameter with Bias Field for a $\text{Y}_{2.43}\text{Sm}_{0.15}\text{Gd}_{0.20}\text{Tm}_{0.15}\text{La}_{0.07}\text{Ga}_{1.03}\text{Fe}_{3.97}\text{O}_{12}$ Film	10
6. Bias Field Needed to Maintain Constant Bubble Diameter as a Function of Temperature for a $\text{Y}_{2.43}\text{Sm}_{0.15}\text{Gd}_{0.20}\text{Tm}_{0.15}\text{La}_{0.07}\text{Ga}_{1.03}\text{Fe}_{3.97}\text{O}_{12}$ Film	11
7. Temperature Dependence of Bubble Diameter at Runout and Collapse for $\text{Y}_{2.62}\text{Sm}_{0.38}\text{Ga}_{1.17}\text{Fe}_{3.87}\text{O}_{12}$ and $\text{Y}_{2.10}\text{Eu}_{0.60}\text{Tm}_{0.30}\text{Ga}_{1.15}\text{Fe}_{3.85}\text{O}_{12}$ Films	14
8. Bias Field Needed to Maintain Constant Bubble Diameter as a Function of Temperature for a $\text{Y}_{2.10}\text{Eu}_{0.60}\text{Tm}_{0.30}\text{Ga}_{1.15}\text{Fe}_{3.85}\text{O}_{12}$ Film	15
9. Bias Field Needed to Maintain Constant Bubble Diameter as a Function of Temperature for a $\text{Y}_{2.62}\text{Sm}_{0.38}\text{Ga}_{1.17}\text{Fe}_{3.83}\text{O}_{12}$ Film ..	15
10. Velocity as a Function of Drive Field at -10°C for a $\text{Y}_{2.69}\text{Sm}_{0.20}\text{La}_{0.11}\text{Ga}_{1.13}\text{Fe}_{3.87}\text{O}_{12}$ Film	16
11. Variation of Bubble Diameter with Bias Field for a $\text{Y}_{2.69}\text{Sm}_{0.20}\text{La}_{0.11}\text{Ga}_{1.13}\text{Fe}_{3.87}\text{O}_{12}$ Film	17
12. Bias Field Needed to Maintain Constant Bubble Diameter as a Function of Temperature for a $\text{Y}_{2.69}\text{Sm}_{0.20}\text{La}_{0.11}\text{Ga}_{1.13}\text{Fe}_{3.87}\text{O}_{12}$ Film	18
13. Velocity as a Function of Drive Field for a $\text{Y}_{2.14}\text{Eu}_{0.56}\text{Tm}_{0.30}\text{Ga}_{1.1}\text{Fe}_{3.9}\text{O}_{12}$ Film with a 200A Permalloy Suppression Layer	23
14. Velocity as a Function of Drive Field for a $\text{Y}_{1.57}\text{Eu}_{0.78}\text{Tm}_{0.65}\text{Ga}_{1.05}\text{Fe}_{3.95}\text{O}_{12}$ with a 200A Permalloy Suppression Layer	23
15. Stripwidth Variation in $\text{Y}_{2.62}\text{Sm}_{0.38}\text{Ga}_{1.17}\text{Fe}_{3.83}\text{O}_{12}$ With Capping Film Thickness	26
16. A. Portion of a Defect Map of a Unsuppressed Bubble Film B. Defect Map of Same Region of Film with Suppression Layer on top	27

CONTENTS (Cont)

	<u>Page</u>
9. TASK 8 - MEMORY CELL FABRICATION	119
9.1 Memory Element Design and Characterization	119
9.1.1 10^4 Bit Chip Architecture	119
9.1.2 Design Evaluation	124
9.1.3 Testing of Devices for the Memory Cell	130
9.2 Memory Cell Package	135
9.2.1 Mechanical Design	135
9.2.2 Field Coil Electrical Tests	138
9.2.3 Field Coil Distribution Variations	138
9.2.4 Bias Shunt, Tilt, and Z-Bias Modulator Characteristics	140
9.2.5 Z-Bias Field Gradients and Variances	144
9.2.6 Bias Structure Proximity Effects	144
9.2.7 Memory Cell Temperature Measurements	144
9.2.8 Test Fixtures and Connector Cabling Identification	153
9.3 Memory Cell Characterization	160
9.3.1 Cell Testing	160
9.3.2 Test Results	160
REFERENCES	170

ILLUSTRATIONS (Cont)

Figure		Page
17.	Velocity as a Function of Drive Field for $\text{Y}_{2.46}\text{Gd}_{0.15}\text{Sm}_{0.15}\text{Tm}_{0.15}\text{La}_{0.09}\text{Ga}_{1.05}\text{Fe}_{3.95}\text{O}_{12}$	28
18.	Six LPE Growth Stations with Laminar Flow Benches	32
19.	Platinum Substrate Holder for LPE Film Growth	32
20.	1.0, 1.5 and 2.0 in. Diameter GGG Substrates and Bubble Domain Garnet Films	33
21.	Bias Margin as Function of Drive Field at Room Temperature for YEu Ion-Implanted Sample	38
22.	Bias Margin as Function of Drive Field at Room Temperature for YEu Bottom-Capped Sample	38
23.	Bias Margin as Function of Drive Field at Room Temperature for YEu Top-Capped Sample	39
24.	Bias Margin as Function of Drive Field at Room Temperature for YSmLa Ion-Implanted Sample	39
25.	Bias Margin as Function of Drive Field at Room Temperature for YSmLa Bottom-Capped Sample	40
26.	Bias Margin as Function of Temperature for YEu Ion-Implanted Sample	42
27.	Pias Margin as Function of Temperature at $H_R = 50$ Oe for YEu Bottom-Capped Sample	43
28.	Bias Margin as Function of Temperature at $H_R = 50$ Oe for YEu Top-Capped Sample	43
29.	Bias Margin as Function of Temperature at $H_R = 50$ Oe for YSmLa Ion-Implanted Sample	44
30.	Bias Margin as Function of Temperature at $H_R = 50$ Oe for YSmLa Bottom-Capped Sample	44
31.	Block Diagram of the Optical Sampling System as it is Used for Free Bubble Measurements	47
32.	Block Diagram of the Optical Sampling System as it is Used for Device Studies	47
33.	Schematic of Special Device Preparation	48
34.	Bubble Radius as a Function of Time-Typical of Low Drive Cases	50
35.	Bubble Radius as a Function of Time-Typical of Intermediate Drive Cases	50
36.	Bubble Radius as a Function of Time-Typical of High Drive Cases ...	51
37.	Radial Wall Velocity vs Pulse Field for Sample 4-25-21 (Ion-implanted)	52
38.	Radial Wall Velocity vs Pulse Field for Sample D4 (Bottom-capped)	52
39.	Radial Wall Velocity vs Pulse Field for Sample D6 (Top-capped)	53
40.	Radial Wall Velocity vs Pulse Field for Sample T17 (Triple-layered)	53
41.	Radial Wall Velocity vs Pulse Field for Sample T10 (Triple-layered)	54
42.	Bubble Collapse Data for Sample T10 (Triple-layered)	54

ILLUSTRATIONS (Cont)

Figure		Page
43.	Relationship Between the [111] Axis, Surface Normal, and Crystallographic Axes	57
44.	Domain Dimensions as a Function of Time for $H_p = 10$ Oe	58
45.	Domain Dimensions as a Function of Time for $H_p = 30$ Oe	59
46.	Domain Dimensions as a Function of Time for $H_p = 50$ Oe	59
47.	Radial Velocity of Bubble Wall as a Function of Pulse Field in Two Principal Directions	60
48.	Orientation of the In-Plane Easy Axis with Respect to the Tilt Plane, [112] Axis, and Devices	60
49.	Slonczewski Critical Velocity as a Function of In-plane Anisotropy . . .	61
50.	Chevron Step Stretcher Used in Device Study	63
51.	Domain Length as a Function of Time in the Chevron Step Stretcher for the Tilted Sample	64
52.	Domain Length as a Function of Time in the Chevron Step Stretcher for the Supposedly Untilted Sample	65
53.	Stacking Dependence of the 100 kHz Margin for 90 Deg and 110 Deg Chevrons	67
54.	Overlap of Chevron and T-Bar Margins as a Function of Frequency . . .	68
55.	Chevron Period Dependence of Margins for $Y_{1.7}Eu_{0.65}Ga_{1.06}Fe_{3.94}O_{12}$ (Wall Mobility ≈ 400 cm/s/Oe)	69
56.	Chevron Period Dependence of Margins for $Y_{1.92}Sm_{0.1}Ca_{0.98}Ge_{0.98}Fe_{4.02}O_{12}$ (Wall Mobility ≈ 1500 cm/s/Oe)	70
57.	Detector Interconnection Test Patterns	71
58.	Magnetoresistance Results for Two-level 90 Deg Chevron Detector	74
59.	Magnetoresistance Results for Two-level 110 Deg Chevron Detector	75
60.	Peak-to-Peak Magnetoresistance Variation for Two-level 110 Deg Detector vs Chevron Period	77
61.	Relative Output for Two-level 110 Deg Detector vs Chevron Period . . .	77
62.	Sensitivity Measurements for One- and Two-Level 28 μ m Period Detectors	78
63.	Sensitivity Measurements for One Level 16 μ m Period Detectors	81
64.	Drive Field Dependence of the Magnetoresistance for a Thin 28 μ m Period One-Level Set-in Shorted Detector	82
65.	Photograph of Experimental Test Station Used for Making Detector Error Rate Studies	84
66.	Block Diagram of Test Equipment Circuitry Used for Error Rate Studies	85
67.	Peak-to-Peak Magnetoresistive Output for Two-level 28 μ m Period Detector	86
68.	Magnetoresistive Output for One-level 28 μ m Period Detector	88
69.	Ordered Domain Structure Observed by Ferrofluid Decoration	88

ILLUSTRATIONS (Cont)

Figure		Page
70.	Magnetoresistance Variation for Two-level Detector Illustrating Amplitude and Phase Shift Modes of Operation	91
71.	Magnetoresistance Variation of One-level Detector Illustrating Amplitude Shift Mode	93
72.	Typical Error Rate Characteristics for Gaussian Noise (Calculated). . .	95
73.	Zero State Noise vs Number of Chevrons in Detector; (a) as Determined by Error Rate Measurements; (b) as Determined by Spectrum Analyzer	96
74.	Zero State Noise vs Drive Field for Fixed Stretch; (a) as Determined by Error Rate Measurements; (b) as Determined by Spectrum Analyzer	97
75.	Error Rate vs Bridge Scheme, Current and Detection Mode	98
76.	Zero State Spectrum Analyzer Results for 50 and 200 kHz Detector Operation	100
77.	Frequency Dependence of Noise as Determined by Error Rate Measurements	101
78.	Zero and One State Noise for One- and Two-Level Detectors as Determined by Error Rate Measurements	101
79.	Test Mask Replicator Patterns	106
80.	150 kHz Replicator Test Results for Large Spacing	108
81.	150 kHz Replicator Test Results for Small Spacing	111
82.	On-chip Bridge Test Mask Arrangement	115
83.	Output Test Results for On-Chip Bridge	116
84.	Comparison of Zero and One State Error Rates for On-and-Off Chip Bridge Completion	118
85.	Chip Organizations	120
86.	Nominal Pulse Phasing and Pulsewidth for the 10K Bit Chip	123
87.	10K Bit Chip	123
88.	Overall Operating Margin of the 10 Kbit Chip at 25°C	125
89.	Operating Margins of Several Components of the 10 Kbit Chip	125
90.	Operating Margin of the 10 Kbit Chip at 60°C	126
91.	Operating Margin of the 10 Kbit Chip at -10°C	126
92.	Start/Stop Operating Margins of Several Components of the 10K Bit Chip at -10°C	128
93.	The Upper Margin Edge for Start/Stop vs the d-c In-Plane Field for the Bent H Corner With a Diagonal Bar	129
94.	The Upper Margin Edge for Start/Stop vs the In-Plane d-c Field for the 90 Deg T-Bar Corner with a Diagonal Bar	129
95.	Die Test Data	133
96.	Composite Data on Eight Devices for Memory Cell	134
97.	Machined Ceramic Substrate	135
98.	Flexible Circuitry	136
99.	Exploded View of Memory Cell	137
100.	Assembled Cell	138
101.	Memory Cell Parts	139
102.	Magnetic Bias Assembly (Left) and Drive Coil Assembly (Right)	139
103.	Memory Cell Showing Magnets	140

ILLUSTRATIONS (Cont)

<u>Figure</u>		<u>Page</u>
104.	Coil Impedance and Q	141
105.	Coil Sensitivity (Outside Magnetic Structure)	143
106.	Coil Sensitivity (Assembled Configuration)	143
107.	Bias Shunt, Winding, and Tilt Characteristics	145
108.	Bias Assembly Field Gradients (Both Shunts at Max Position)	146
109.	Bias Assembly Field Gradients (Both Shunts at Zero Position)	147
110.	Bias Assembly Field Gradients (One Shunt Max, One Shunt Min)	148
111.	Cell-Cell Bias Interaction (3 Cells Stacked)	149
112.	Cell-Cell Bias Interaction (Aiding and Opposing)	149
113.	Cell-Cell Bias Interaction (3 Cells Adjacent)	150
114.	Cell-Cell Bias Interaction (2 Cells Adjacent)	150
115.	Cell-Cell Bias Interaction Uniformity (X Direction)	151
116.	Cell-Cell Bias Interaction Uniformity (Y Direction)	151
117.	Temperature Gradient at 3 Amp (Chips Switched)	152
118.	Temperature Gradient at 3 Amp (Chips On)	152
119.	Temperature Gradient at 3.35A (Chips Switched)	153
120.	Characterization Test Fixture	155
121.	Exerciser Sense Chann. 1	157
122.	Flexible Cable Winding Diagram	158
123.	Connector Pin Identification	159
124.	Module Detector Outputs	166
125.	Ping-Pong Detection	167
126.	Cell Waveforms	168
127.	Timing Relationships	169

TABLES

Table		Page
1.	Domain and Material Parameters of Trial Composition $\text{Y}_{2.0}\text{Sm}_{0.2}\text{Gd}_{0.4}\text{Tm}_{0.4}\text{Ga}_{0.95}\text{Fe}_{4.05}\text{O}_{12}$	6
2.	Domain and Material Parameters of Trial Composition $\text{Y}_{2.22}\text{Sm}_{0.15}\text{Gd}_{0.40}\text{Tm}_{0.23}\text{Ga}_{0.95}\text{Fe}_{4.05}\text{O}_{12}$	7
3.	Domain and Material Parameters of Trial Composition $\text{Y}_{2.43}\text{Sm}_{0.15}\text{Gd}_{0.20}\text{Tm}_{0.15}\text{La}_{0.07}\text{Ga}_{1.03}\text{Fe}_{3.97}\text{O}_{12}$	9
4.	Domain and Material Parameters of Trial Composition $\text{Y}_{2.46}\text{Sm}_{0.15}\text{Gd}_{0.15}\text{Tm}_{0.15}\text{La}_{0.09}\text{Ga}_{1.05}\text{Fe}_{3.95}\text{O}_{12}$	12
5.	Domain and Material Parameters of Three Compositions at -10, 25, and 60°C	13
6.	Domain and Material Parameters of Trial Composition $\text{Y}_{2.69}\text{Sm}_{0.20}\text{La}_{0.11}\text{Ga}_{1.13}\text{Fe}_{3.87}\text{O}_{12}$ (Original Melt)	16
7.	Domain and Material Parameters of Trial Composition $\text{Y}_{2.69}\text{Sm}_{0.20}\text{La}_{0.11}\text{Ga}_{1.13}\text{Fe}_{3.87}\text{O}_{12}$ Film (Modified Melt)	18
8.	Domain and Material Parameters of Trial Composition $\text{Y}_{2.5}\text{Eu}_{0.5}\text{Ga}_{1.07}\text{Fe}_{3.93}\text{O}_{12}$	19
9.	Static Domain and Material Parameters of Candidate Composition $\text{Y}_{2.5}\text{Eu}_{0.5}\text{Ga}_{1.07}\text{Fe}_{3.93}\text{O}_{12}$	20
10.	Wall Mobility Values Over the Temperature Range for Candidate Composition $\text{Y}_{2.5}\text{Eu}_{0.5}\text{Ga}_{1.07}\text{Fe}_{3.93}\text{O}_{12}$	20
11.	Static Domain and Material Parameters of Candidate Composition $\text{Y}_{2.69}\text{Sm}_{0.20}\text{La}_{0.11}\text{Ga}_{1.13}\text{Fe}_{3.87}\text{O}_{12}$	20
12.	Wall Mobility Values Over the Temperature Range for Candidate Composition $\text{Y}_{2.69}\text{Sm}_{0.20}\text{La}_{0.11}\text{Ga}_{1.13}\text{Fe}_{3.87}\text{O}_{12}$	20
13.	Initial Mobility Values for $\text{Y}_{2.69}\text{Sm}_{0.20}\text{La}_{0.11}\text{Ga}_{1.13}\text{Fe}_{3.87}\text{O}_{12}$	21
14.	Summary of Garnet Processing Yield For 1.5 in. Diameter Substrates	34
15.	Summary of Garnet Processing Yield for 1 in. Diameter Substrates	35
16.	Summary of Film Growth and Characterization Yield	35
17.	Material Parameters for Candidate Materials	37
18.	Bias Margins and Minimum Drive Fields at Room Temperature	41
19.	Samples Used for Radial Wall Velocity Measurements	49
20.	Material Parameters for Untilted and Tilted Samples	57
21.	Geometry Dependence of Margins (28 μm Period)	71
22.	Summarized Results (90 vs 110 deg)	78
23.	28 μ Period Detectors	80
24.	Wafer Fabrication	107
25.	Material and Device Parameters	124
26.	Die Level Test Procedures	132
27.	Tuned Resonant Electrical Data	142
28.	Setup Notes	161
29.	Composite Margin Tests - I Room Temperature	162
30.	Composite Margin Tests - II Variable Temperature	163
31.	Composite Parameter Matching Requirements	164

DEVELOPMENT OF A HIGH CAPACITY BUBBLE DOMAIN MEMORY ELEMENT AND RELATED EPITAXIAL GARNET MATERIALS FOR APPLICATION IN SPACECRAFT DATA RECORDERS

ITEM 2

The Optimization of Material-Device Parameters for Application in Bubble Domain Memory Elements for Spacecraft Data Recorders

By

P. J. Besser, et al

1. SYNOPSIS

The objectives of this item of the contract are: (1) to develop and optimize a liquid phase epitaxial garnet material for application in spacecraft data recorders, and (2) to evaluate techniques to obtain high level, low noise detector outputs for bubble memory elements and to provide optimizing criteria for the material/device interface characteristics. To meet these objectives, work under this item has been divided into eight parts. Task 1 is concerned with the design and evaluation of a material system which will provide the necessary bubble material properties. Task 2 is concerned with the growth and yield of useful bubble material films greater than 1.25 in. in diameter. Task 3 is concerned with hard bubble suppression techniques which will permit device operation at the data rate and over the temperature range desired for the spacecraft data recorders. Task 4 is concerned with device evaluation of the material produced under Task 1 and the hard bubble suppression techniques. Task 5 is an evaluation of the effects of hard bubble suppression layers and crystal orientation on device performance using pulsed laser stroboscopic microscopy (PLSM). Task 6 is concerned with detector optimization and Task 7 with improved passive replicator designs. Task 8 is the fabrication of an operating bubble domain memory cell.

The details of the approach to each task and the results obtained are described in the body of the report. Because of the close interrelationship of Tasks 1 and 3 they are presented sequentially in Sections 2 and 3.

The primary goal of the Task 1 work was to develop a material capable of operating in 16 μ m period devices at data rates of 150 kHz over the temperature range of -10°C to +60°C. An additional objective was to obtain a temperature coefficient of less than 0.25 percent 1/C° for the characteristic length parameter of the material. Several trial compositions were evaluated in the course of the program. Two candidate compositions were selected for device evaluation, $Y_{2.69}Sm_{0.20}La_{0.11}Ga_{1.13}Fe_{3.87}O_{12}$ and $Y_{2.5}Eu_{0.5}Ga_{1.07}Fe_{3.93}O_{12}$. Germanium-substituted garnets were excluded from consideration to avoid overlap with Air Force Contract F33615-75-C-5010.

Task 3 was directed toward selection and evaluation of a hard bubble suppression technique which would permit reliable circuit operation at 150 kHz from -10°C to $+60^{\circ}\text{C}$. Two candidate techniques were chosen to be evaluated with the material candidates in the device testing of Task 4. These are ion implantation and a multi-layer garnet technique which produces a 90 deg domain wall at the interface between the bubble layer and the suppressing layer. The latter approach is referred to as the Type III layer technique in most literature references and throughout this report. In the course of the Task 3 work it was discovered that the Type III technique also had the potential of suppressing dynamic conversion, which, although not a problem for the data rate goals of this program, is a potential barrier to the achievement of device operation at megahertz data rates.

The development effort of Task 2 established confidence that garnet wafers as large as 1.5 in. in diameter and as thin as 0.012 in. can be produced with the same high quality as that demonstrated in the previously standard 1.0 in. diameter, 0.020 in. thick wafers. This verification and the development of large area films is essential to meeting the eventual cost goals of Item 1.

The device evaluation of the candidate materials and hard bubble suppression techniques has been the subject of Task 4. The test vehicle for this evaluation was intended to be the partially populated 10^5 bit ($\sim 10^4$ bits capacity), $16\mu\text{m}$ period device to be developed under Task 4 of Item 1. Difficulties in the fabrication of working masks of this device delayed its development to the point where it was no longer useful to the program. Consequently the work on the partially populated device was discontinued and the Task 4 evaluation was performed with the detector test pattern used in Task 6. All combinations of materials and hard bubble suppression techniques operated satisfactorily at 150 kHz over the temperature range of -10°C to $+60^{\circ}\text{C}$. It was concluded that the selection of the final material and hard bubble suppression technique for the spacecraft data recorder program should therefore be based on other considerations such as ease of fabrication, reproducibility of properties and maximum mobility requirements for domain stripout.

On Task 5, a recently developed high speed optical sampling technique was used to investigate dynamic effects in materials and devices. The bubble expansion and contraction measurements showed a domain wall velocity saturation which was essentially independent of composition and hard bubble suppression technique. The device studies determined the relation of domain stretching velocity in chevron expanders to an in-plane anisotropy resulting from a misorientation of the $\langle 111 \rangle$ axis from the normal to the film plane.

The detector optimization studies of Task 6 can be separated into the categories of stretcher dynamics (margins), detector output and detector noise. The dependence of chevron margins on chevron angle, stack length, period, mobility and geometry was determined. Detector output was characterized as a function of its dependence on period, stretch length, permalloy-to-garnet spacing, drive field and permalloy thickness. Zero and one state noise measurements were performed on one and two level detectors. These studies have greatly increased the insight into the operation of bubble domain detectors and have resulted in guidelines for optimizing detector output.

Part of the Task 6 requirement was the design and test of an on-chip bridge. The information on the drive field dependence of the detector noise indicated that the preferred configuration for an all-permalloy bridge was one with the completion arms oriented 90 deg from the active arms.

A total of 30 different passive replicator configurations were designed and tested under Task 7. Several of the new designs are promising in terms of their operation at high bias and the insensitivity of their characteristics to garnet-to-permalloy spacing.

The Task 8 effort consisted of (1) memory element design and fabrication, (2) memory cell package design and fabrication, and (3) chip-package integration and cell test. The 10^4 bit chip design selected allowed the evaluation of two potential final chip configurations for Item 1: (1) dual passive replicators with off-track annihilators to alternate detection between two halves of a split guard rail detector, and (2) a single passive replicator feeding a guardrail detector. The package design is derived from the commercial Rockwell POS/8 configuration. The package has been extensively characterized for its stand-alone properties and for package interaction effects.

2. TASK1; DESIGN OF IMPROVED BUBBLE COMPOSITION

2.1 Introduction

The objective of this task has been the design of an improved bubble material which will have the necessary properties for application in spacecraft data recorders. The material requirements for this program specify the development of a bubble composition which provides the following:

- (1) A temperature coefficient of the characteristic length $\frac{1}{\ell} \frac{\partial \ell}{\partial t} = \ell_T$ which is less than -0.25 percent/ $^{\circ}\text{C}$ over the temperature range of -10°C to $+60^{\circ}\text{C}$.
- (2) A domain mobility sufficient to provide a data rate of 1.5×10^5 bits per second in a continuous mode over the temperature range.
- (3) Four micron diameter bubbles.
- (4) Stable device operation which calls for an estimated room temperature quality factor $q \geq 4$.

The influence these requirements have on the choice of other material properties and the rationale used in selecting materials to meet these requirements will now be considered.

- (1) In selecting materials to meet the ℓ_T requirement, the general direction taken was to utilize materials with high Neel temperatures, T_N , and low compensation temperatures, T_{comp} . For high T_N materials, the temperature coefficients of wall energy

$$\sigma_{W_T} = \frac{1}{\sigma_W} \frac{\partial \sigma_W}{\partial T}$$

and magnetization

$$M_T = \frac{1}{M} \frac{\partial M}{\partial T}$$

should be small over the temperature range. Since $\ell_T = \sigma_{W_T} - 2M_T$, for high T_N materials, ℓ_T should be small also.

The magnetization of a garnet composition must be adjusted to the proper level to obtain desirable bubble parameters. This adjustment may be carried out by substitution of magnetic rare earth ions on dodecahedral lattice sites or of diamagnetic ions on tetrahedral or octahedral iron sites.

Bubble garnets with high T_N values can be obtained by minimizing the amount of substitution for iron. This can be achieved either by employing a rare earth ion with a large moment antiparallel to the major iron sublattice and/or by more efficient diamagnetic substitution on the tetrahedral lattice sites. The former was implemented by the incorporation of gadolinium onto the dodecahedral sites. However, so small a concentration had to be used (so as not to produce a high T_{comp} which would cause M_T to be positive in the temperature range of interest) that this idea was eventually discarded. Greater tetrahedral site preference by diamagnetic ions results in a smaller total substitution for iron and a higher T_N . This may be realized by the use of germanium instead of gallium to decrease the magnetization. With the reduction in the ℓ_T values of the final candidate compositions, the change from gallium to germanium was not required.

- (2) From the required data rate and bubble diameter, a minimum wall mobility, μ_W , of 120 cm/sec-Oe may be calculated for an average drive field of 4 Oe which is typically obtained from device propagation structures. If the fall-off of μ_W at low temperatures and the peak velocity required in some device structures are taken into account, a μ_W of about 480 cm/sec-Oe at room temperature is probably necessary to meet the data rate requirements.
- (3) From bubble stability considerations it is desirable to have the operating bubble diameter, d , approximately equal to eight times the characteristic length. For $d = 4 \mu m$, this leads to $\ell \approx 0.5 \mu m$. Assuming a wall energy σ_W , of ~ 0.2 ergs/cm² and using $\sigma_W = 4\pi M^2 \ell$ yields a magnetization, $4\pi M$, of 225 gauss. In characterizing bubble films it is more appropriate to specify a demagnetized domain width, W (rather than the bubble diameter, d , which is a function of applied field and more difficult to measure accurately). The stripwidth to be used with a 16 μm period device is about 3.5 μm .
- (4) Since $q = K_u/2\pi M^2$, where K_u is the uniaxial anisotropy, q is very sensitive to M . Inasmuch as the magnetization of 4 μm bubble material is greater than that of 6 μm bubble material, a larger K_u value is required to produce the desired q . However, higher T_N materials have small K_u and M_T values so that from $q_T = K_{uT} - 2M_T$, the q_T should be lower than for 6 μm bubble materials. The indications are that a room temperature value of $q \geq 4$ is needed to assure reliable device operation with 4 μm bubbles at elevated temperatures.

2.2 Trial Compositions Containing Gadolinium

The first trial composition for the program was $Y_{2.0}Sm_{0.2}Gd_{0.4}Tm_{0.4}Ga_{0.95}Fe_{4.05}O_{12}$. It was selected on the basis of the stable device operation exhibited by $Y_{2.62}Sm_{0.38}Ga_{1.17}Fe_{3.83}O_{12}$. Modifications were made, (a) to increase the wall mobility, μ_W , by decreasing the samarium content and, (b) to raise T_N by incorporating gadolinium, thereby reducing the amount of gallium required to obtain the desired magnetization. The thulium was included for lattice matching to the gadolinium gallium garnet (GGG) substrate and also to contribute to the growth induced anisotropy. The melt composition was designed to place the film in slight tension due to film-substrate lattice mismatch and to contain the minimum amount of gallium consistent with the desired magnetization. Room temperature characterization of a film from this first melt is presented in Table 1. Dynamic measurements were made on an ion-implanted film.

TABLE 1. - DOMAIN AND MATERIAL PARAMETERS OF TRIAL COMPOSITION
 $Y_{2.0}Sm_{0.2}Gd_{0.4}Tm_{0.4}Ga_{0.95}Fe_{4.05}O_{12}$

h (thickness) $3.1 \mu m$	ℓ (characteristic length) $0.58 \mu m$
w (stripwidth) $4.5 \mu m$	ℓ_T (-10 to $+60^\circ C$) $-1.3\%/C^\circ$
H_{col} (collapse field) 88.0 Oe	H_a (anisotropy field) 1390 Oe
$4\pi M$ (magnetization) 225 gauss	q (quality factor) 6.2
σ_W (wall energy) 0.24 ergs/cm ²	μ_W (wall mobility) 370 cm/sec-Oe
Δa (lattice mismatch) 0.002\AA	H_c (coercivity) 0.6 Oe
T_N (Neel temperature) $153.5^\circ C$	

Although many of the measured properties are close to those projected for this composition, the ℓ_T value was too large and the μ_W value less than desired. A compositional change was made in an attempt to reduce ℓ_T and raise μ_W (at the expense of σ_W) by reducing the samarium content. The second melt composition thus became $Y_{2.22}Sm_{0.15}Gd_{0.40}Tm_{0.23}Ga_{0.95}Fe_{4.05}O_{12}$. Characterization of an ion-implanted film from this second melt yielded the static properties at room temperature and dynamic properties at $-10^\circ C$ presented in Table 2. The reduction in samarium content was obviously only partially successful in meeting the material goals. The ℓ_T value was reduced about a third but was still much too large. In addition, σ_W and H_a were reduced more than expected. On the other hand, the $-10^\circ C$ dynamic properties, Figure 1, were becoming very attractive for the μ_W value exceeds the requirements for this program. Also the H_c value was appreciably reduced. The sharp turnover, attributable to dynamic conversion (Ref 1), is seen not to occur until $\Delta H \geq 7$ Oe and $v \geq 1300$ cm/sec. Additional data on the variation in the bubble diameter with applied field are shown in Figure 2. A plot of the bias field required to keep the bubble diameter constant with temperature, Figure 3, revealed that the only range in bubble diameter stable over the entire temperature interval was $4.75 \pm 0.2 \mu m$. (Even so, the biasing magnet would have to be capable of tracking non-monotonically with temperature.)

TABLE 2. - DOMAIN AND MATERIAL PARAMETERS OF TRIAL COMPOSITION

$\text{Y}_{2.22}\text{Sm}_{0.15}\text{Gd}_{0.40}\text{Tm}_{0.23}\text{Ga}_{0.95}\text{Fe}_{4.05}\text{O}_{12}$

h (thickness) $3.4 \mu\text{m}$

w (stripwidth) $4.3 \mu\text{m}$

H_{col} (collapse field) 83.6 Oe

$4\pi M$ (magnetization) 195 gauss

σ_W (wall energy) 0.16 ergs/cm^2

Δa (lattice mismatch) 0.0015\AA

T_N (Neel temperature) 148.5°C

ℓ (characteristic length) $0.53 \mu\text{m}$

ℓ_T (-10 to $+60^\circ \text{C}$) $-0.86\%/^\circ \text{C}$

H_a (anisotropy field) 770 Oe

q (quality factor) 3.9

μ_W (wall mobility, -10°C)
 800 cm/sec-Oe

H_c (coercivity, -10°C), 0.1 Oe

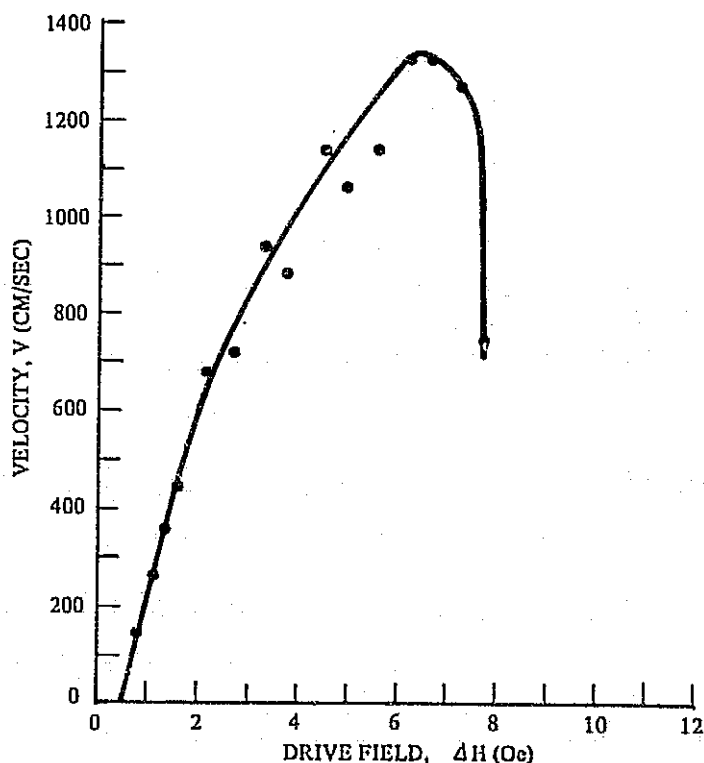


Figure 1. Velocity as a Function of Drive Field at -10°C for a $\text{Y}_{2.22}\text{Sm}_{0.15}\text{Gd}_{0.40}\text{Tm}_{0.23}\text{Ga}_{0.95}\text{Fe}_{4.05}\text{O}_{12}$ Film

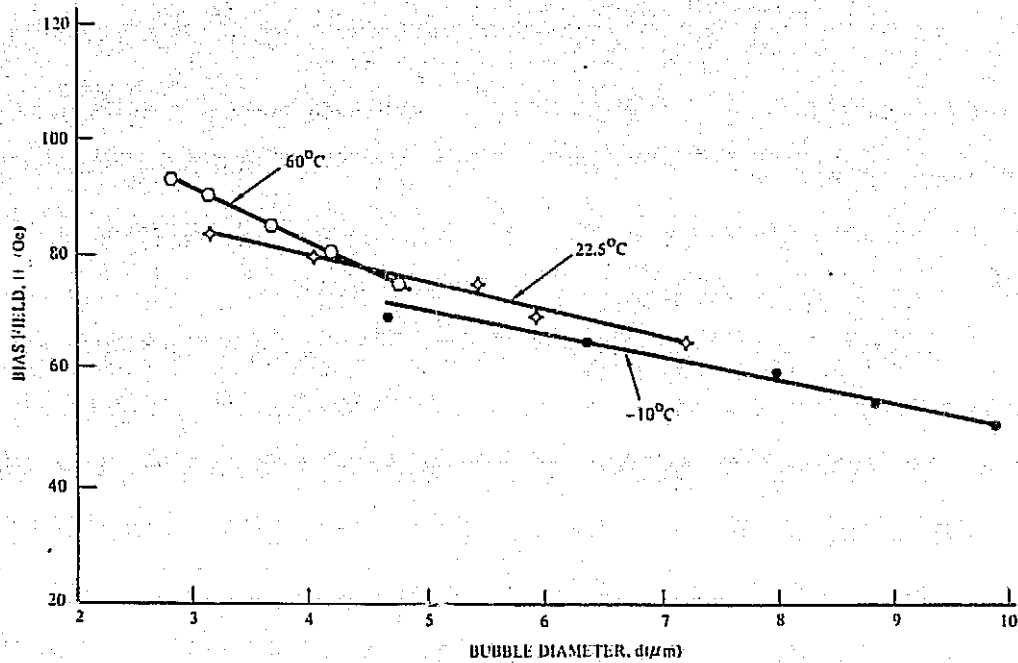


Figure 2. Variation of Bubble Diameter With Bias Field for $\text{Y}_{2.22}\text{Sm}_{0.15}\text{Gd}_{0.40}\text{Tm}_{0.23}\text{Ga}_{0.95}\text{Fe}_{4.05}\text{O}_{12}$ Film

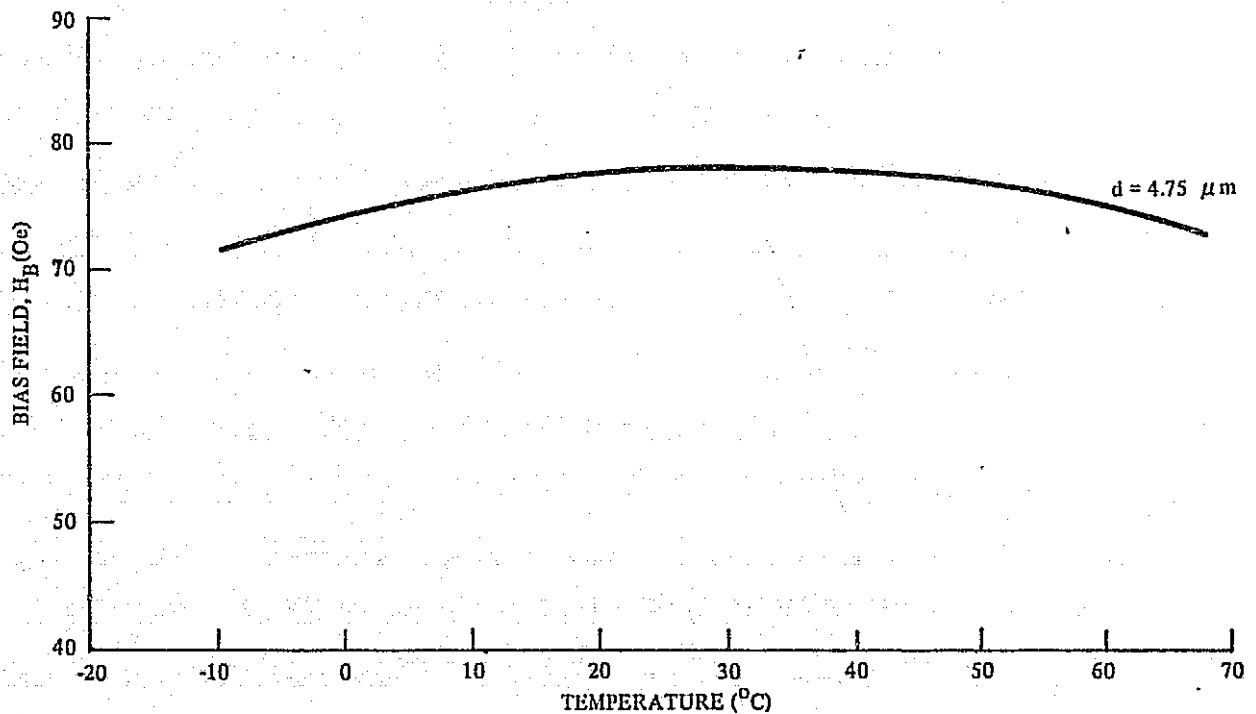


Figure 3. Bias Field Needed to Maintain Constant Bubble Diameter as a Function of Temperature for a $\text{Y}_{2.22}\text{Sm}_{0.15}\text{Gd}_{0.40}\text{Tm}_{0.23}\text{Ga}_{0.95}\text{Fe}_{4.05}\text{O}_{12}$ Film

It was concluded at that time that the values of ℓ_T might be reduced further by lowering the gadolinium content of the films. The nominal composition for the next melt was $\text{Y}_{2.43}\text{Sm}_{0.15}\text{Gd}_{0.20}\text{Tm}_{0.15}\text{La}_{0.07}\text{Ga}_{1.03}\text{Fe}_{3.97}\text{O}_{12}$. Due to the reduction in gadolinium, it became necessary to increase the gallium content of the film to adjust the magnetization, and to add a large ion, lanthanum, for lattice constant matching with the GGG substrate. The samarium content was left unchanged since the previous dynamic properties were satisfactory. Room temperature static characterization and -10°C dynamic characterization of an ion-implanted film of this composition yielded the properties presented in Table 3.

TABLE 3.— DOMAIN AND MATERIAL PARAMETERS OF TRIAL COMPOSITION
 $\text{Y}_{2.43}\text{Sm}_{0.15}\text{Gd}_{0.20}\text{Tm}_{0.15}\text{La}_{0.07}\text{Ga}_{1.03}\text{Fe}_{3.97}\text{O}_{12}$

h (thickness) $5.0\ \mu\text{m}$	ℓ (characteristic length) $0.44\ \mu\text{m}$
w (stripwidth) $4.28\ \mu\text{m}$	ℓ_T (-10 to $+60^\circ\text{C}$) $-0.45\%/^\circ\text{C}$
H_{col} (collapse field) $123.6\ \text{Oe}$	H_a (anisotropy field) $860\ \text{Oe}$
$4\pi M$ (magnetization) $223\ \text{gauss}$	q (quality factor) 3.9
σ_W (wall energy) $0.17\ \text{ergs/cm}^2$	H_c (coercivity, -10°C) $0.13\ \text{Oe}$
Δa (lattice mismatch) -0.0004\AA	μ_W (wall mobility, -10°C) $820\ \text{cm/sec-Oe}$
T_N (Neel temperature) 139°C	V_p (critical velocity, -10°C) $800\ \text{cm/sec}$

These static properties were close to the anticipated values for this composition. The dynamic characteristics at -10°C are shown in Figure 4. The critical velocity (V_p) value is that for the onset of dynamic conversion (Ref 1). For $150\ \text{kHz}$ operation with a $4\ \mu\text{m}$ diameter bubble the average bubble velocity is $240\ \text{cm/sec}$. Thus, having a critical velocity in the vicinity of $1000\ \text{cm/sec}$ should ensure that device operation is not approaching the dynamic conversion region of the material. In addition, the temperature dependence of the characteristic length was half the value of the previous composition and scaled well with the change in the gadolinium content. Also the quality factor q at $+60^\circ\text{C}$ was 3.2 . Figure 5 shows the variation of the diameter of bubbles with applied field at different temperatures. The bias field changes with temperature (Figure 6) needed to keep the bubble diameter constant requires a biasing magnet temperature coefficient of $-0.09\ \text{percent}/^\circ\text{C}$ which represented a significant increase in the stability range. Also this coefficient can be obtained with existing commercial permanent magnet materials.

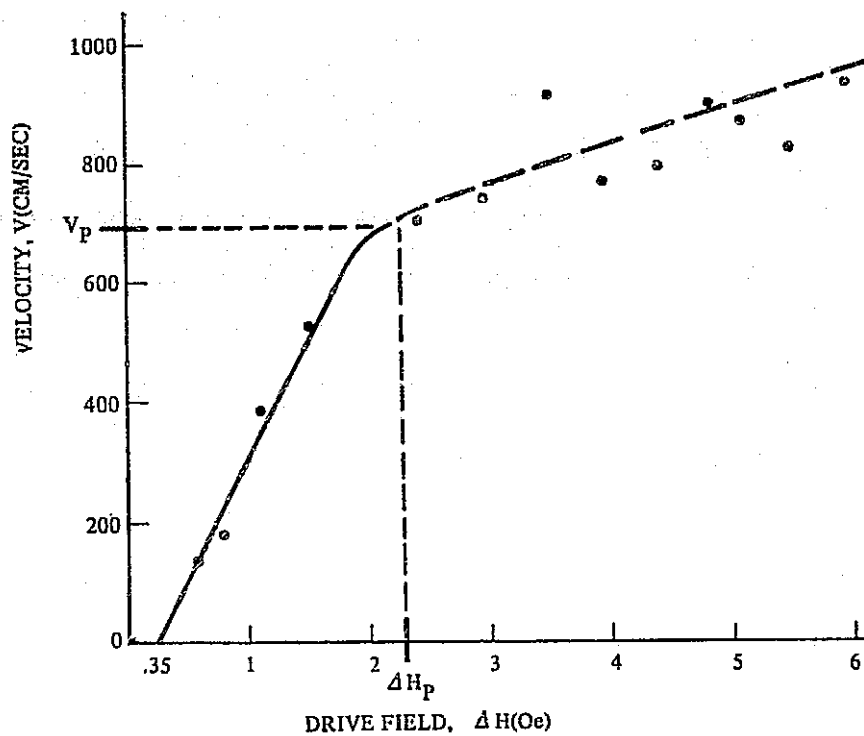


Figure 4. Velocity as a Function of Drive Field at -10°C for a $\text{Y}_{2.43}\text{Sm}_{0.15}\text{Gd}_{0.20}\text{Tm}_{0.15}\text{La}_{0.07}\text{Ga}_{1.03}\text{Fe}_{3.97}\text{O}_{12}$ Film

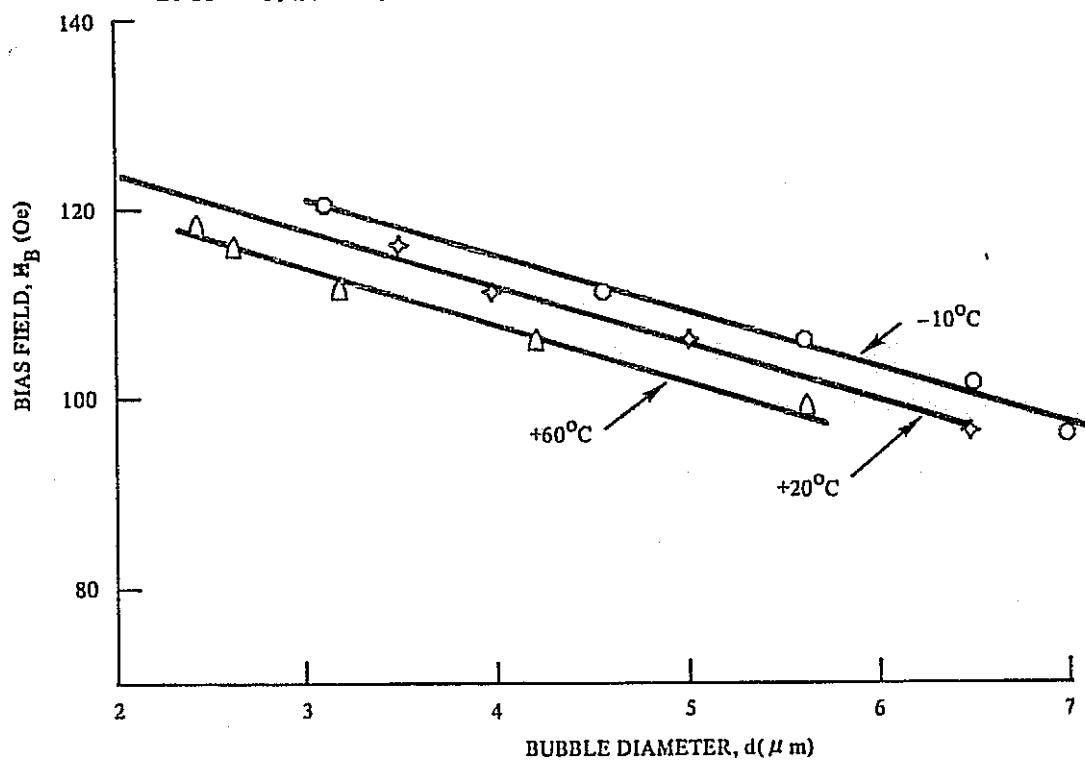


Figure 5. Variation of Bubble Diameter with Bias Field for a $\text{Y}_{2.43}\text{Sm}_{0.15}\text{Gd}_{0.20}\text{Tm}_{0.15}\text{La}_{0.07}\text{Ga}_{1.03}\text{Fe}_{3.97}\text{O}_{12}$ Film

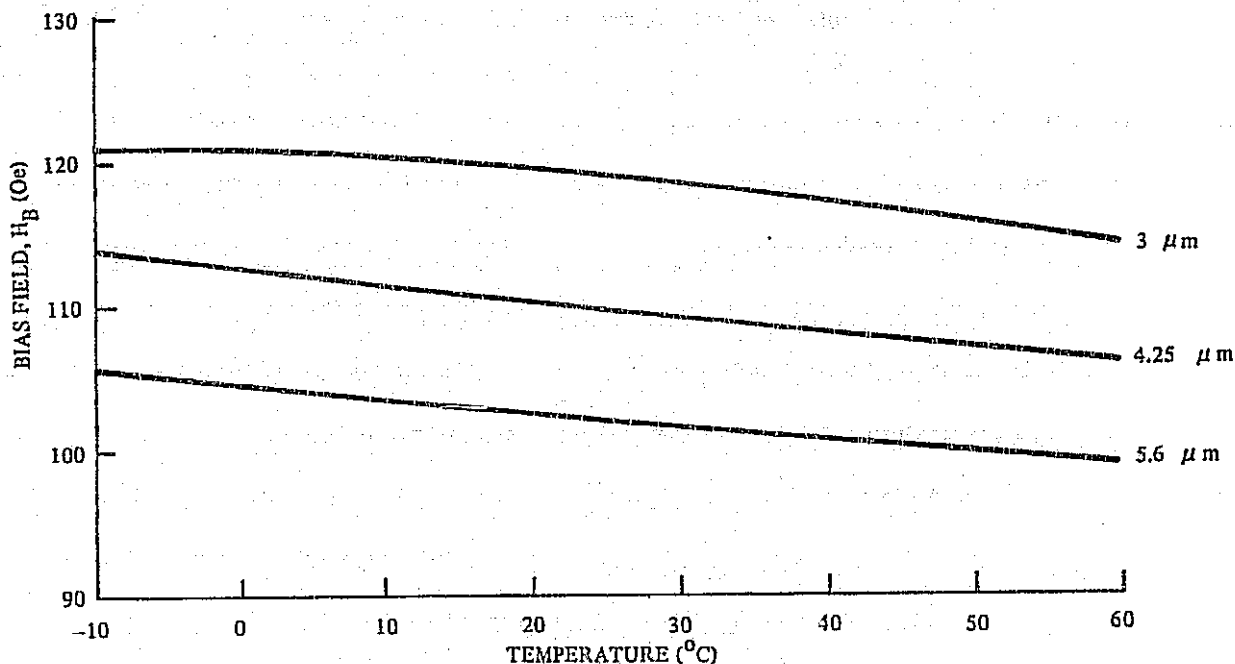
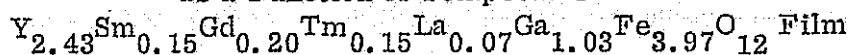
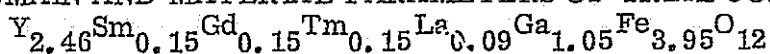


Figure 6. Bias Field Needed to Maintain Constant Bubble Diameter as a Function of Temperature for a



A fourth variation of the original composition was then prepared. The nominal composition was $\text{Y}_{2.46}\text{Sm}_{0.15}\text{Gd}_{0.15}\text{Tm}_{0.15}\text{La}_{0.09}\text{Ga}_{1.05}\text{Fe}_{3.95}\text{O}_{12}$. Again the gadolinium content was lowered in an attempt to further reduce ℓ_T . As a consequence, the gallium content was slightly altered to adjust for the magnetization change, and the yttrium and lanthanum contents were altered to obtain the desired film-substrate lattice parameter mismatch. The samarium content was again left unchanged. Room temperature static characterization and -10°C dynamic characterization of an ion-implanted film of this composition yielded the properties shown in Table 4. The decrease of 6°C in T_N from the previous composition was accounted for by the additional substitution of gallium needed to offset the slight reduction in gadolinium. The temperature coefficient of the characteristic length was reduced very little by this reduction in gadolinium. Of particular note was the fact that the mobility had decreased in this composition. In addition, the quality factor, q , was measured at $+60^\circ\text{C}$ to be 2.7. The sharper decrease in q from room temperature to $+60^\circ\text{C}$ exhibited by this composition (1.7 compared to 0.7 with the previous composition) and the lower wall mobility indicated that further reduction in the gadolinium content was unwarranted.

TABLE 4. - DOMAIN AND MATERIAL PARAMETERS OF TRIAL COMPOSITION



h (thickness) $4.7\ \mu\text{m}$	ℓ (characteristic length) $0.47\ \mu\text{m}$
w (stripwidth) $4.4\ \mu\text{m}$	ℓ_T (-10 to $+60^\circ\text{C}$) $-0.41\%/^\circ\text{C}$
H_{col} (collapse field) $107.0\ \text{Oe}$	H_a (anisotropy field) $890\ \text{Oe}$
$4\pi M$ (magnetization) $203\ \text{gauss}$	q (quality factor) 4.4
σ_W (wall energy) $0.16\ \text{ergs/cm}^2$	H_c (coercivity, -10°C) $0.27\ \text{Oe}$
Δa (lattice mismatch) -0.001\AA	μ_W (wall mobility, -10°C) $740\ \text{cm/sec-Oe}$
T_N (Neel temperature) 133°C	V_p (critical velocity, -10°C) $950\ \text{cm/sec}$

2.3 Comparison of Compositions from Item 1

In order to relate the properties of the gadolinium-containing compositions to the parameters exhibited by the compositions utilized under Item 1, material characterization was performed on the two Item 1 compositions and the last trial composition at -10 , 25 , and 60°C . These results are presented in Table 5. It can be seen that all of these gallium-substituted garnets have ℓ_T values slightly in excess of the objective of $-0.25\ \text{percent}/^\circ\text{C}$. Data on the temperature variation of the bubble stability range and the bias field needed to maintain a constant bubble diameter are also shown in Figures 7 through 9. The stability range data shows that operation at a constant midrange diameter is possible over the entire temperature interval without danger of close approach to collapse or run-out at the extremes of -10°C and $+60^\circ\text{C}$. For both Item 1 materials, the temperature coefficient of the bias field needed to maintain a constant diameter (H_T) over this range is $\sim 0.25\ \text{percent}/^\circ\text{C}$. This value of H_T can be realized with commercially available permanent magnet materials. Therefore, stable device operation can be achieved over the -10 to $+60^\circ\text{C}$ temperature range with these materials even though their ℓ_T values are in the range of -0.3 to $-0.4\ \text{percent}/^\circ\text{C}$. Considerations of such data led to the conclusion that the ℓ_T goal of $-0.25\ \text{percent}/^\circ\text{C}$ was more stringent than required, and a ℓ_T of $-0.4\ \text{percent}/^\circ\text{C}$ would be sufficient. Dynamic characterization was carried out on ion-implanted films.

2.4 Trial Composition Not Containing Gadolinium

Another gallium-substituted garnet, related to the samarium composition of Item 1, was the next trial composition. The new formulation contained less samarium than the Item 1 composition, but contained no gadolinium. The absence of the large gadolinium ion required that another large ion (e.g., lanthanum) be incorporated for lattice matching with the GGG substrate. The nominal composition based on melt formulation and growth conditions was $\text{Y}_{2.69}\text{Sm}_{0.20}\text{La}_{0.11}\text{Ga}_{1.13}\text{Fe}_{3.87}\text{O}_{12}$. Room temperature static characterization and -10°C dynamic characterization of an ion-implanted film of this composition yielded the properties shown in Table 6.

TABLE 5. -DOMAIN AND MATERIAL PARAMETERS OF THREE COMPOSITIONS
AT -10, 25, AND 60° C

Item 1 Sm Composition: $Y_{2.62}Sm_{0.38}Ga_{1.17}Fe_{3.83}O_{12}$ ($h = 4.6 \mu m$)							
Temp(°C)	$H_{col}(Oe)$	$H_{BS}(Oe)$	$W(\mu m)$	$4\pi M(gauss)$	$\sigma_w(ergs/cm^2)$	$\ell(\mu m)$	$\mu_w(cm/sec-Oe)$
10	119.5	93.0	4.9	247	0.28	0.57	180
25	114.7	93.0	4.5	225	0.20	0.50	200
60	105.2	85.4	4.3	201	0.15	0.47	300
Item 1 Eu Composition: $Y_{2.10}Eu_{0.60}Tm_{0.30}Ga_{1.15}Fe_{3.85}O_{12}$ ($h = 5.0 \mu m$)							
-10	135.9	106.0	5.0	270	0.34	0.56	220
25	130.0	104.0	4.7	248	0.25	0.51	600
60	117.8	93.3	4.5	220	0.18	0.48	1100
Item 2 Composition: $Y_{2.46}Sm_{0.15}Gd_{0.15}Tm_{0.15}La_{0.09}Ga_{1.05}Fe_{3.95}O_{12}$ ($h = 5.0 \mu m$)							
-10	87.7	69.3	6.2	201	0.24	0.76	320
25	90.8	74.0	5.3	188	0.17	0.61	440
60	87.5	73.9	4.6	166	0.11	0.49	650
The average values of ℓ_T and H_T , and bubble diameter variation over this temperature range are:							
Composition	$\ell_T(°C^0)$	$H_T(°C^0)$	$d(\mu m)$				
Item 1 Sm	0.3	0.29	3.75 ± 0.75				
Item 1 Eu	0.35	0.22	5.0 ± 1.0				
Item 2	0.41	0.10	4.5 ± 0.8				

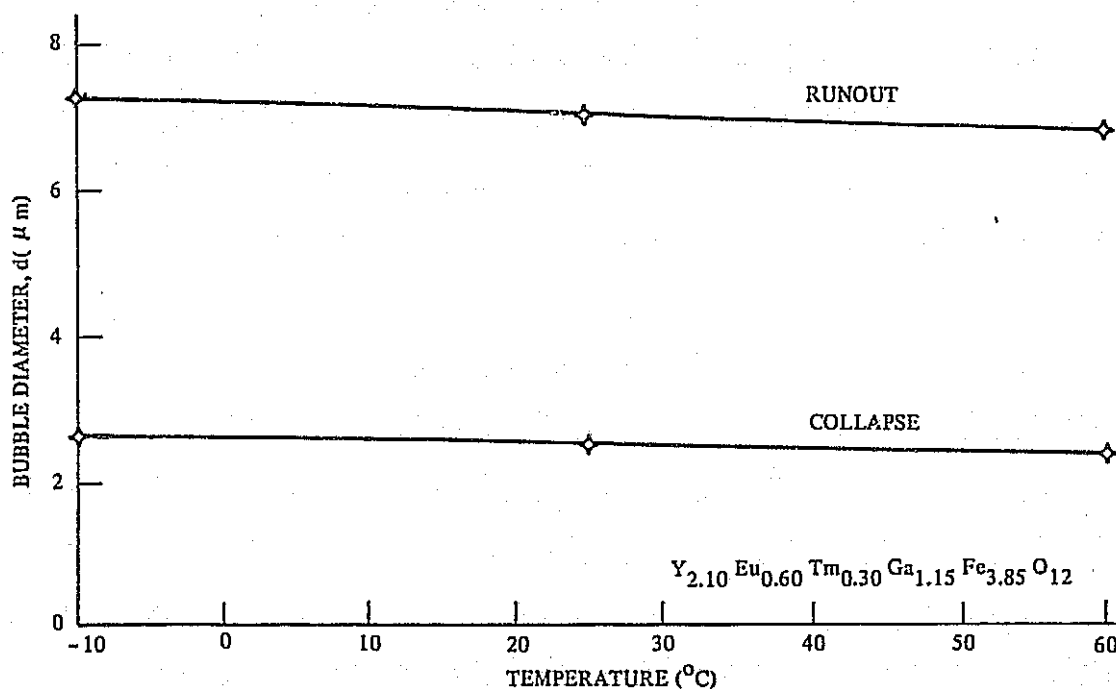
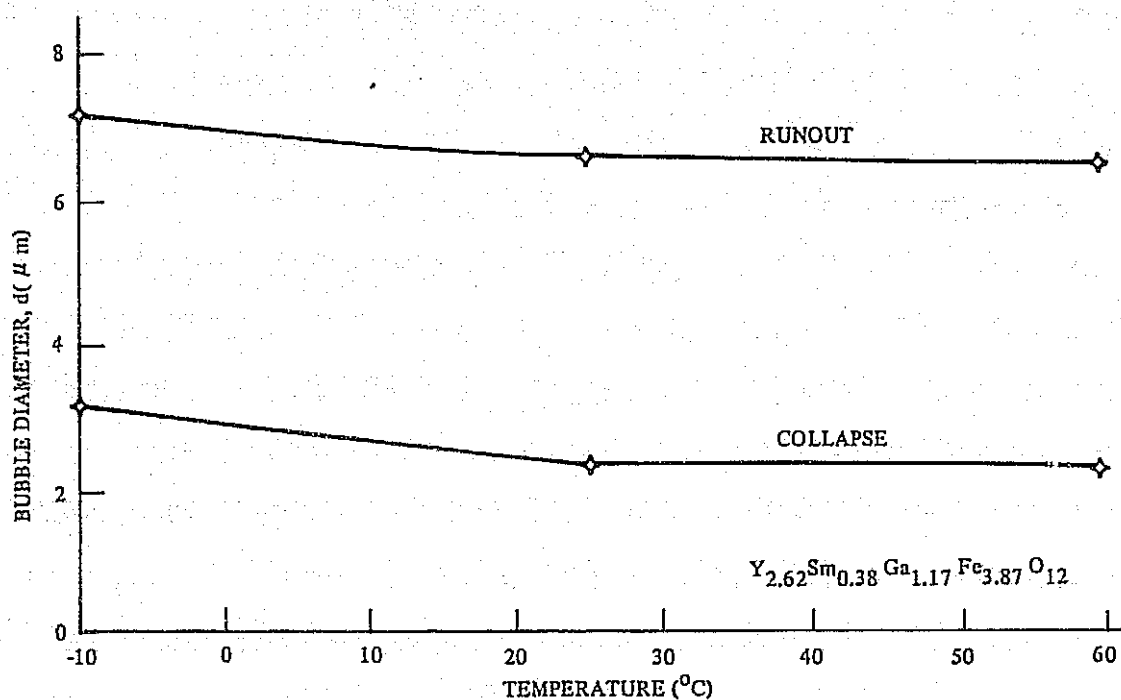


Figure 7. Temperature Dependence of Bubble Diameter at Runout and Collapse for Y_{2.62}Sm_{0.38}Ga_{1.17}Fe_{3.87}O₁₂ and Y_{2.10}Eu_{0.60}Tm_{0.30}Ga_{1.15}Fe_{3.85}O₁₂ Films

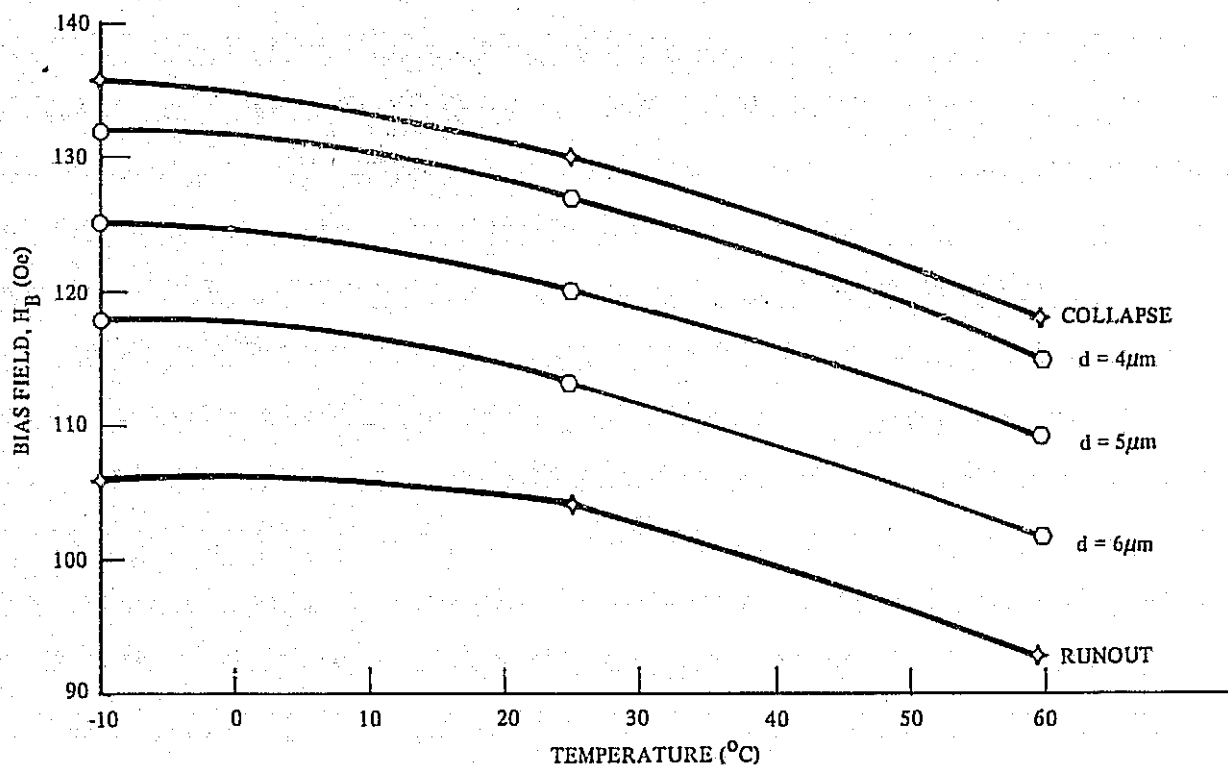


Figure 8. Bias Field Needed to Maintain Constant Bubble Diameter as a Function of Temperature for a $\text{Y}_{2.10}\text{Eu}_{0.60}\text{Tm}_{0.30}\text{Ga}_{1.15}\text{Fe}_{3.85}\text{O}_{12}$ Film

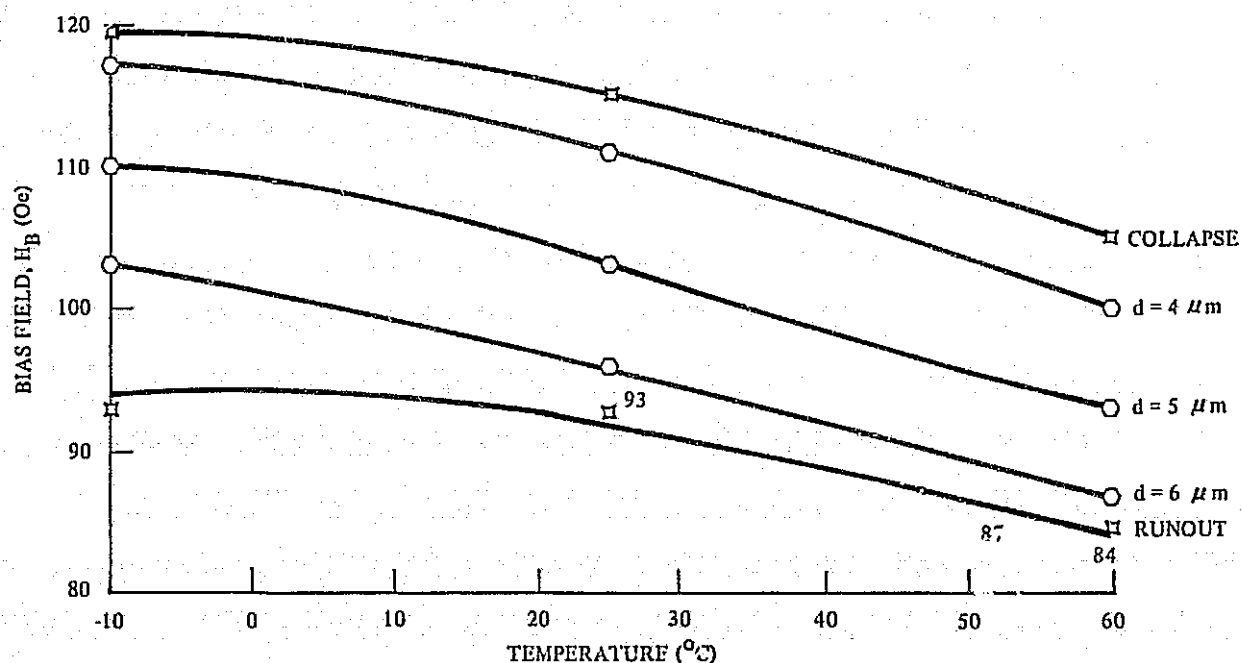


Figure 9. Bias Field Needed to Maintain Constant Bubble Diameter as a Function of Temperature for a $\text{Y}_{2.62}\text{Sm}_{0.38}\text{Ga}_{1.17}\text{Fe}_{3.83}\text{O}_{12}$ Film

TABLE 6. - DOMAIN AND MATERIAL PARAMETERS OF TRIAL COMPOSITION
 $\text{Y}_{2.69}\text{Sm}_{0.20}\text{La}_{0.11}\text{Ga}_{1.13}\text{Fe}_{3.87}\text{O}_{12}$
 (Original Melt)

h (thickness) 4.4 μm	ℓ (characteristic length) 0.41 μm
w (stripwidth) 3.9 μm	ℓ_T (-10 to +60° C) -0.44%/C°
H_{col} (collapse field) 108.5 Oe	H_a (anisotropy field) 820 Oe
$4\pi M$ (magnetization) 200 gauss	q (quality factor) 4.1
σ_w (wall energy) 0.13 ergs/cm ²	μ_w (wall mobility, -10° C) 480 cm/sec-Oe
Δa (lattice mismatch) 0.002Å	H_c (coercivity, -10° C) 0.4 Oe
T_N (Neel temperature) 122.5° C	V_p (critical velocity, -10° C) 2130 cm/sec at 10.1 Oe

These static properties were close to the anticipated values for this composition but the $4\pi M$ and T_N values suggest that the gallium content is too high. The increase in coercivity and decrease in mobility (Figure 10) of this composition over the gadolinium-containing samples, suggested that more samarium was present in this film than was

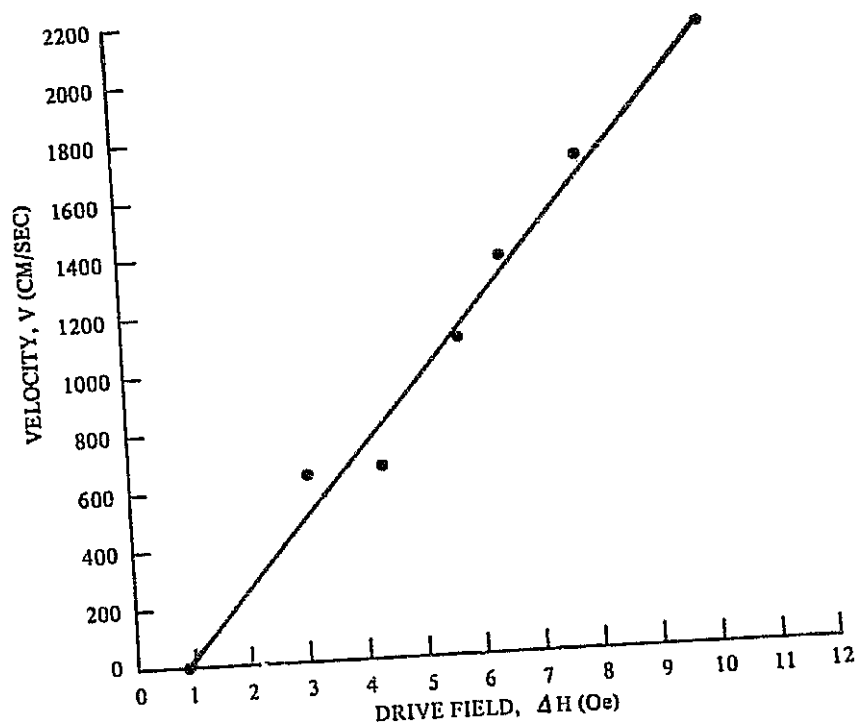


Figure 10. Velocity as a function of Drive Field at -10° C for a
 $\text{Y}_{2.69}\text{Sm}_{0.20}\text{La}_{0.11}\text{Ga}_{1.13}\text{Fe}_{3.87}\text{O}_{12}$ Film

intended from the melt formulation and growth conditions. That would also account for the small observed lattice mismatch even though the gallium content was slightly high. Figures 11 and 12 show the bubble diameter variation with temperature and the bias field coefficient needed to keep the bubble diameter constant over this range of temperatures ($H_T \approx -0.18$ percent/ $^{\circ}\text{C}$).

In order to reduce the samarium content of films from this melt, a 10 percent addition of both yttrium and lanthanum was made to the melt. Room temperature static characterization and -10°C dynamic characterization of an ion-implanted film then revealed the properties presented in Table 7. These properties are quite attractive for meeting program goals so that this trial composition was made a candidate for Task 4.

Since the damping of wall motion due to europium is only about one-sixth that of samarium, the control of the concentration of europium in a film need not be so critical in preparing a large number of films with matched properties. Consequently, a europium composition, $\text{Y}_{2.5}\text{Eu}_{0.5}\text{Ga}_{1.07}\text{Fe}_{3.93}\text{O}_{12}$, was prepared. It exhibited the room temperature properties presented in Table 8. Dynamic characterization was carried out on an ion-implanted film. In addition to the very good l_T , the values of q and μ_w were very desirable. Also the lattice matching to the substrate was achieved without the addition of another large ion so that this composition contained only four cations. The properties of this trial composition are also quite attractive so that it too was made a candidate for Task 4.

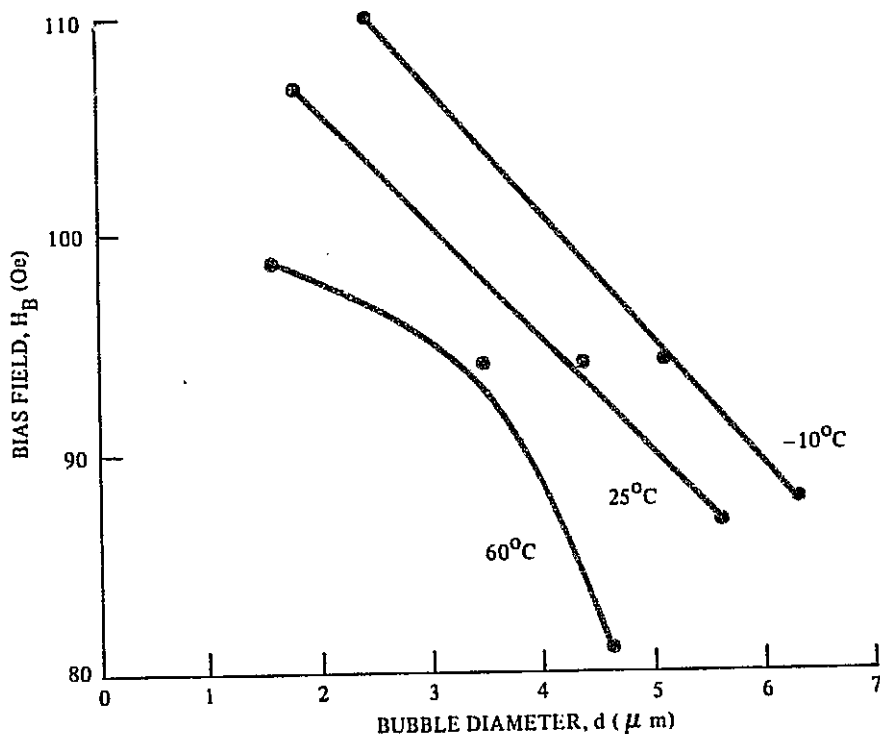


Figure 11. Variation of Bubble Diameter with Bias Field for a $\text{Y}_{2.69}\text{Sm}_{0.20}\text{La}_{0.11}\text{Ga}_{1.13}\text{Fe}_{3.87}\text{O}_{12}$ Film

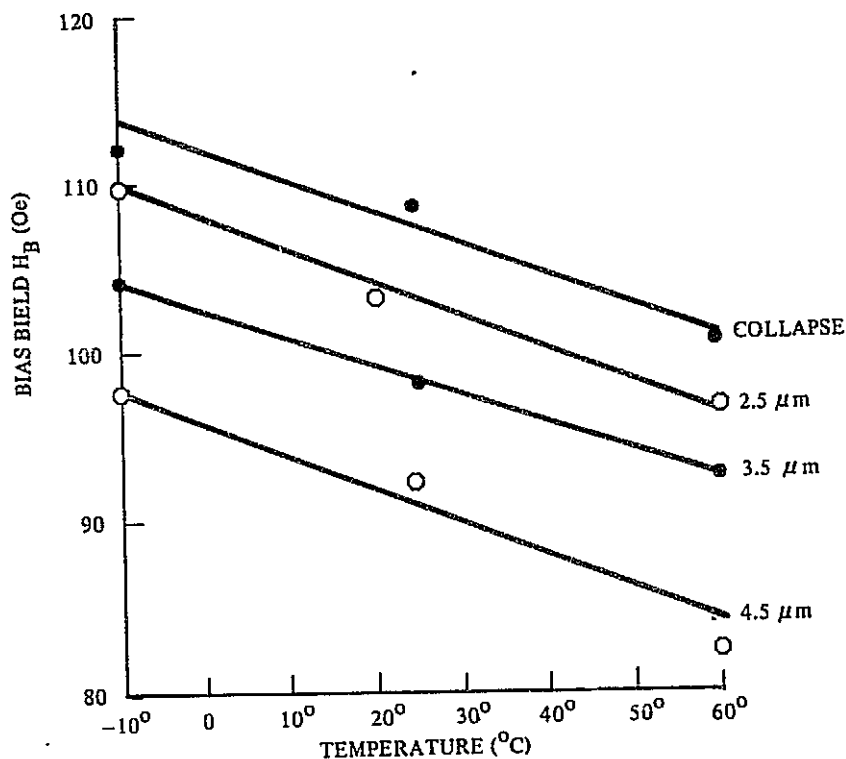


Figure 12. Bias Field Needed to Maintain Constant Bubble Diameter as a Function of Temperature for a $\text{Y}_{2.69}\text{Sm}_{0.20}\text{La}_{0.11}\text{Ga}_{1.13}\text{Fe}_{3.87}\text{O}_{12}$ Film

TABLE 7. - DOMAIN AND MATERIAL PARAMETERS OF TRIAL COMPOSITION $\text{Y}_{2.69}\text{Sm}_{0.20}\text{La}_{0.11}\text{Ga}_{1.13}\text{Fe}_{3.87}\text{O}_{12}$
(Melt Modified with Increased Yttrium and Lanthanum)

h (thickness) 4.8 μm	l (characteristic length) 0.42 μm
w (stripwidth) 4.1 μm	l_T (-10 to +60°C) -0.36%/C°
H_{col} (collapse field) 113.2 Oe	H_a (anisotropy field) 820 Oe
$4\pi M$ (magnetization) 204 gauss	q (quality factor) 4.0
σ_w (wall energy) 0.14 ergs/cm ²	μ_w (wall mobility) 1040 cm/sec-Oe
T_N (Neel temperature) 122.0° C	H_c (coercivity) 0.2 Oe

TABLE 8. - DOMAIN AND MATERIAL PARAMETERS OF TRIAL COMPOSITION
 $\text{Y}_{2.5}\text{Eu}_{0.5}\text{Ga}_{1.07}\text{Fe}_{3.93}\text{O}_{12}$

h (thickness) 4.0 μm	ℓ (characteristic length) 0.45 μm
w (stripwidth) 4.0 μm	ℓ_T (-10 to +60° C) -0.28%/C°
H_{col} (collapse field) 113 Oe	H_a (anisotropy field) 1077 Oe
$4\pi M$ (magnetization) 223 gauss	q (quality factor) 4.8
σ_w (wall energy) 0.18 ergs/cm ²	μ_w (wall mobility) 2270 cm/sec-Oe
Δa (lattice mismatch) 0.0047Å	H_c (coercivity) 0.2 Oe
T_N (Neel temperature) 130.8° C	

2.5 Candidate Compositions

A review of all the trial compositions suggested that the program goals were best met by the $\text{Y}_{2.5}\text{Eu}_{0.5}\text{Ga}_{1.07}\text{Fe}_{3.93}\text{O}_{12}$ and the $\text{Y}_{2.69}\text{Sm}_{0.20}\text{La}_{0.11}\text{Ga}_{1.13}\text{Fe}_{3.87}\text{O}_{12}$ compositions. Six films of each of these compositions were grown to be evaluated under Task 4 of Item 2. Of the six films, two were ion-implanted to suppress hard bubbles, two were double layer structures with a suppression layer grown below the bubble film, and two were double layer structures with a suppression layer grown on top of the bubble film. Funding did not permit the preparation and evaluation of triple layer films for Task 4. The stripwidths of the layered films were adjusted by annealing in an oxygen atmosphere to coincide with the stripwidths of the implanted films. Before being processed for device testing, all the films were fully characterized. Characterization data are presented in Tables 9 through 12.

The ℓ_T values shown in Tables 9 and 11 indicate that not only can as-grown films exhibit stripwidths which are relatively insensitive to temperature changes over a wide range of temperatures, but also capping these films further improves this stability. In fact, the use of a triple layer structure instead of the double layer allows these values to be even lower. For the $\text{Y}_{2.69}\text{Sm}_{0.20}\text{La}_{0.11}\text{Ga}_{1.13}\text{Fe}_{3.87}\text{O}_{12}$ triple layer structure, ℓ_T data of less than 0.08 percent/C° has consistently been measured. Perhaps the effect of the capping layer on the stripwidth (see Task 3) compensates for the change in the bubble film stripwidth with temperature. This potential advantage must be weighed against the additional processing complexity involved in growth of a third layer.

TABLE 9. - STATIC DOMAIN AND MATERIAL PARAMETERS OF
CANDIDATE COMPOSITION $Y_{2.5}Eu_{0.5}Ga_{1.07}Fe_{3.93}O_{12}$

	W(μ m)	h(μ m)	H _{col} (Oe)	σ_w (ergs/cm ²)	4 π M (gauss)	l(μ m)	l _T (%C ⁰)
Implant 1	4.1	3.4	95.6	0.18	212	0.49	0.39
Implant 2	3.9	3.7	107.0	0.17	220	0.45	--
Top Cap 1	4.1	3.2	107.7	0.25	250	0.51	0.24
Top Cap 2	4.1	3.3	109.3	0.25	249	0.51	--
Bottom Cap 1	4.1	3.7	111.5	0.22	237	0.49	0.34
Bottom Cap 2	3.9	3.9	109.3	0.19	237	0.45	--

TABLE 10. - WALL MOBILITY VALUES OVER THE TEMPERATURE RANGE
FOR CANDIDATE COMPOSITION $Y_{2.5}Eu_{0.5}Ga_{1.07}Fe_{3.93}O_{12}$

Temperature	-10°C	+25°C	+60°C
Implant No. 1	610 cm/sec-Oe	1000 cm/sec-Oe	1430 cm/sec-Oe
Top Cap No.	1400	1700	3250
Bottom Cap No. 1	1380	1470	1890

TABLE 11. - STATIC DOMAIN AND MATERIAL PARAMETERS OF CANDIDATE
COMPOSITION $Y_{2.69}Sm_{0.20}La_{0.11}Ga_{1.13}Fe_{3.87}O_{12}$

	W(μ m)	h(μ m)	H _{col} (Oe)	σ_w (ergs/cm ²)	4 π M (gauss)	l(μ m)	l _T (%C ⁰)
Implant 1	3.6	3.1	102.9	0.18	227	0.43	--
Implant 2	3.7	3.3	109.8	0.19	233	0.43	0.16
Top Cap 1	4.0	3.3	119.0	0.27	267	0.49	--
Top Cap 2	4.0	3.3	118.3	0.27	265	0.49	0.14
Bottom Cap 1	3.9	3.3	120.6	0.26	266	0.47	--
Bottom Cap 2	4.1	3.8	121.0	0.24	251	0.48	0.13

TABLE 12. - WALL MOBILITY VALUES OVER THE TEMPERATURE RANGE
FOR CANDIDATE COMPOSITION $Y_{2.69}Sm_{0.20}La_{0.11}Ga_{1.13}Fe_{3.87}O_{12}$

Temperature	-10°C	+25°C	+60°C
Implant No. 2	750 cm/sec-Oe	800 cm/sec-Oe	800 cm/sec-Oe
Bottom Cap No. 2	850	--	750
Top Cap No. 2	1400	1000	750

Also of note is the strange temperature dependence of the mobility of $\text{Y}_{2.69}\text{Sm}_{0.20}\text{La}_{0.11}\text{Ga}_{1.13}\text{Fe}_{3.87}\text{O}_{12}$. The $+60^\circ\text{C}$ values are seen to be, Table 12, lower than the values at -10°C , for both the bottom and top capped films. These mobility values were measured in the drive field region between ~ 3 and ~ 8 Oe. The measurements were made within this range because of the correspondence to realistic drive fields used in device operation. The initial mobility data listed in Table 13 does not show this anomalous temperature dependence. The difference between the initial mobility values and those obtained at 3 to 8 Oe drive is probably due to the occurrence of nonlinear velocity-field effects at the higher drive fields.

TABLE 13. — INITIAL MOBILITY VALUES FOR
 $\text{Y}_{2.69}\text{Sm}_{0.20}\text{La}_{0.11}\text{Ga}_{1.13}\text{Fe}_{3.87}\text{O}_{12}$

Film	$\mu_w (-10^\circ\text{C})$ cm/sec-Oe	$\mu_w (+60^\circ\text{C})$ cm/sec-Oe
Bottom Cap No. 2	1000	1500
Top Cap No. 2	1400	1500

Although both of these compositions meet every material requirement initially set, the only evaluation of these films that is really meaningful is their performance in device circuits. Consequently these 12 films (six of each composition) were forwarded for device fabrication. The results of this testing is reported in Section 5.

3. TASK 3; HARD BUBBLE SUPPRESSION TECHNIQUES

3.1 Introduction

A determination of the collapse fields for bubbles in films of garnet compositions shows the existence of a range of values. The low collapse field value is associated with normal bubbles while the higher collapse field values are attributed to hard bubbles. A well-known property of hard bubbles is their tendency to propagate at velocities much below the values exhibited by normal bubbles. Characteristics of this nature make the suppression of hard bubbles mandatory in order to obtain reliable device operation at frequencies corresponding to 1.5×10^5 bps in a continuous mode over the temperature range of -10 to $+60^\circ\text{C}$.

At the start of this program, five hard bubble suppression techniques had been utilized. Four of those methods involve the deposition of an additional (suppression) layer (Refs 2, 3, 4) while the fifth involves ion-implantation into the upper region of the bubble film (Ref 5). Three of the four multi-layer techniques use garnets for the second layer while the remaining one consists of a thin permalloy layer on the bubble garnet (Ref 2). All of these techniques have been shown to suppress hard bubble generation at room temperature. However, problems with certain of the methods are evident from device data and variable temperature considerations. One of the 180 deg domain cap techniques (Ref 3) is of dubious value because of spurious bubble nucleation problems while the other 180 deg domain cap technique (Ref 3) suffers from a very limited temperature range of operation. Serious problems with the other techniques were not immediately obvious at the start of this program. Consequently, the techniques of hard bubble suppression that were investigated included ion-implantation, the Rockwell Type III 90 deg cap, and the use of a permalloy layer. All of these techniques were studied not only in terms of their effectiveness in suppressing hard bubbles but also in terms of their temperature range of applicability. In the course of this work evidence was obtained which indicates that some of the techniques offer greater resistance to dynamic conversion than others.

3.2 Hard Bubble Suppression Techniques

Permalloy layer. - A hard bubble suppression technique which utilizes a thin permalloy layer has been reported by Lin and Keefe (Ref 2). This technique presumably works in the same manner as the Type III layer reported by Henry, et al (Ref 4), but could represent a considerable cost savings compared to either layering with another garnet composition or ion-implanting the bubble film. Prior to the initiation of this program, workers in this laboratory made a cursory examination of the effect of a 200Å permalloy layer on the dynamic properties of

$\text{Y}_{2.14}\text{Eu}_{0.56}\text{Tm}_{0.30}\text{Ga}_{1.1}\text{Fe}_{3.9}\text{O}_{12}$. The bubble velocity data was taken using the Vella-Coleiro method (Ref 6) without the bias field correcting ramp. The data (Figure 13) showed that although the wall mobility appears to be unaffected by the permalloy layer, the threshold field for initiation of bubble motion has increased from 0.4 to 3.0 Oe. This experiment was repeated on this program using a film of $\text{Y}_{1.57}\text{Eu}_{0.78}\text{Tm}_{0.65}\text{Ga}_{1.05}\text{Fe}_{3.95}\text{O}_{12}$. The results of this study (Figure 14).

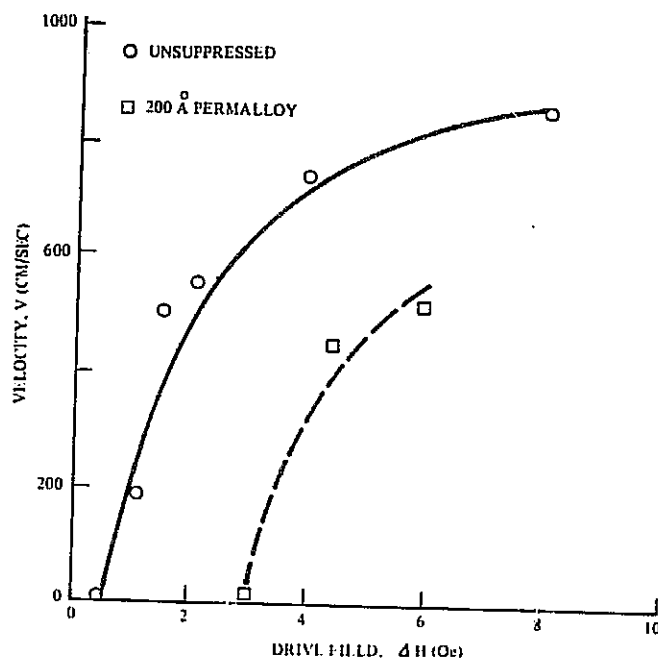


Figure 13. Velocity as a Function of Drive Field for a $\text{Y}_{2.14}\text{Eu}_{0.56}\text{Tm}_{0.30}\text{Ga}_{1.1}\text{Fe}_{3.9}\text{O}_{12}$ Film with a 200Å Permalloy Suppression Layer

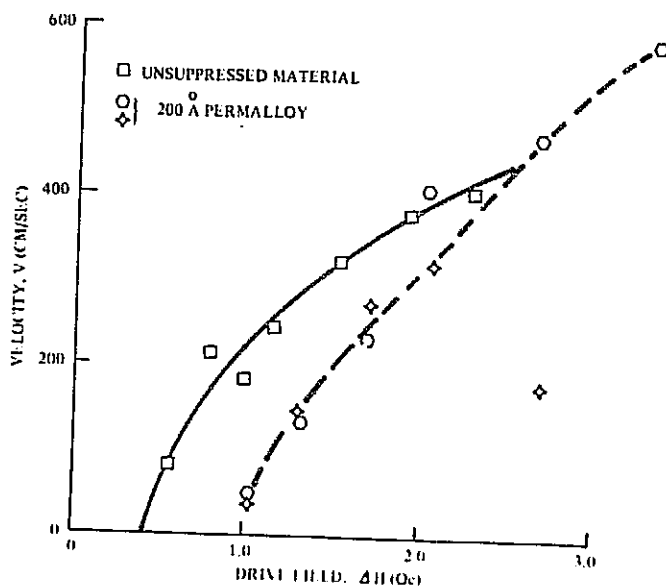


Figure 14. Velocity as a Function of Drive Field for a $\text{Y}_{1.57}\text{Eu}_{0.78}\text{Tm}_{0.65}\text{Ga}_{1.05}\text{Fe}_{3.95}\text{O}_{12}$ Film with a 200Å Permalloy Suppression Layer

confirm that the threshold field has been significantly increased, in this case from 0.5 to 1.0 Oe, by the addition of the 200Å permalloy layer. Although bubble behavior was essentially isotropic in the garnet, gross inhomogeneities appear to have been introduced into the film by the addition of the permalloy layer. Regions could be found where bubbles translated in one direction with low drive fields but required nearly twice as great threshold fields for motion in the opposite direction. The total significance of this increase in threshold field can only be understood when one remembers that dynamic conversion (Ref 1) can limit the useful velocity of a bubble. The critical velocity, V_p , is related to the maximum useful drive field, H_p , by

$$V_p = \frac{\mu_w}{2} (H_p - H_t)$$

where μ_w is the wall mobility and H_t is the threshold field. If H_t is increased by layering with permalloy while V_p , μ_w and H_p (all garnet film properties) remain constant, in an extreme case it is possible to obtain a situation where $H_t > H_p$. As a result, a bubble can only move in the dynamically converted state. Even if this extreme is not reached, it is still undesirable to cut down the operation region of the drive field ($H_p > H > H_t$). To ascertain if this increase is a function of permalloy film thickness, the 200Å film was removed from the garnet film and a 100Å film of permalloy was deposited. Unfortunately, the 100Å layer did not suppress hard bubbles. From these preliminary experiments, the conclusion was drawn that for applications in which the threshold drive field is important, the permalloy hard bubble suppression technique should not be employed until the cause of the high coercivity variation is identified and eliminated.

Ion-implantation. - At the present time, ion-implantation is the standard technique for hard bubble suppression. We have shown that suppression by ion-implantation is temperature dependent. It may disappear at low temperature if the dosage is too small (Ref 4) or at high temperature if the implant depth is too shallow (unpublished data of P. J. Besser). However, under proper conditions ion implantation effectively suppresses hard bubbles over the temperature range of interest. In addition to verifying that ion-implantation did indeed result in hard bubble suppression over the temperature range of interest for the compositions studied under Items 1 and 2, ion-implantation was investigated with the purpose of determining the dependence of suppression on the orientation between the ion beam and the crystallographic axes of the film. The technique was also investigated to determine the uniformity achieved in the dynamic properties over the surface of the films.

In an attempt to determine if channeling is occurring during ion-implantation for hard bubble suppression, the following experiment was performed. Eight (111) samples cut from the same film were oriented 0, 15, 30, 45, 75, 90, 105, and 120 deg from an arbitrary direction in the plane. These samples were then implanted with neon ions at 2×10^{14} ions/cm² (80 KeV), five degrees from normal. The bubble collapse field was then measured for each of the samples. For significant channeling, one might expect the collapse field to vary with the degree of channeling and hence the orientation angle. Within experimental uncertainties, it was found that all the films exhibited the same collapse field after implantation; hence it appears that channeling during implantation does not occur.

While conducting these investigations, it was discovered that the LPE garnet films under study were covered by a thin red film. This red film is believed to be formed from a closed-volume LPE growth when the wafer is removed from the melt, and as such, might be characteristic of this type of growth process. The composition of this film has tentatively been identified as a high lead-content garnet and consequently it is difficult to remove. Evidence has been obtained that this red post-growth film is responsible for some of the problems in the dynamic response of bubble domains to drive fields. A local coercivity variation has been observed in ion-implanted films. It is hypothesized that ion-implantation into and/or through the extraneous film results in local inhomogeneities which are reflected in the coercivity variations. In addition, the pink film might be responsible for the coercivity variations found with permalloy layering. Growth of films without this post-growth layer might then allow the permalloy suppression technique to be used.

The following conclusions can be drawn from these experiments and the characterized results on the candidate compositions presented in Para 2.5. Ion-implantation is a practical method for hard bubble suppression over the temperature range of interest (-10°C to $+60^{\circ}\text{C}$). The currently occurring local coercivity variations are not important for data rates in the range of 1.5×10^5 bps. However, if a device is to be operated at velocities approaching the material critical fields, then either these local coercivity variations will have to be removed, or another method must be found to suppress hard bubbles.

Type III layers. - The Rockwell Type III hard bubble suppression layer was first described by Henry, et al (Ref 4). The method consists of producing a 90 deg capping layer by growing a $\text{Y}_{2.65}\text{Gd}_{0.35}\text{Fe}_5\text{O}_{12}$ (YGdIG) film on the GGG substrate followed by the overgrowth of the bubble film, or by growing a thin layer of YGdIG over the bubble domain film. The growth-induced anisotropy in this composition is small and the easy axis is in or nearly in the plane of the film. In addition, the suppressing layer is grown in compression on GGG (or the bubble domain film). Since the magnetostriction constant of YGdIG is negative, the stress-induced anisotropy and the demagnetizing field of the film also tend to force the magnetization into the film plane, producing the 90 deg capping layer.

The initial study of the Type III layer addressed the static changes introduced by the additional layer. For this work, a YGdIG cap was used with the gallium-substituted film $\text{Y}_{2.62}\text{Sm}_{0.38}\text{Ga}_{1.17}\text{Fe}_{3.83}\text{O}_{12}$. Data taken on the variation of the static bubble parameters as a function of the suppression layer thickness revealed that both the collapse field and the demagnetized domain stripwidth increased with the layer thickness (Figure 15). For a layer $0.5 \mu\text{m}$ thick, there was a 50 percent increase in the stripwidth and a corresponding increase in the bubble stripout and collapse diameters. The stripwidth is a linear function of the layer thickness. Static characterization is unable to determine the optimum thickness of the YGdIG to use for hard bubble suppression. One must wait for detailed device propagation studies to determine this dimension. However, with a capping film layer as thin as $0.09 \mu\text{m}$, there is suppression. Films $0.2 \mu\text{m}$ or greater in thickness suppress hard bubbles, but planar domain walls form within this layer which attract bubbles. Thus, the Type III suppression layer should be less than $0.2 \mu\text{m}$ in thickness. These capped films were tested for hard bubble suppression at -10°C , and $+60^{\circ}\text{C}$, as well as room temperature. In all cases, the YGdIG layer suppressed the formation of hard bubbles.

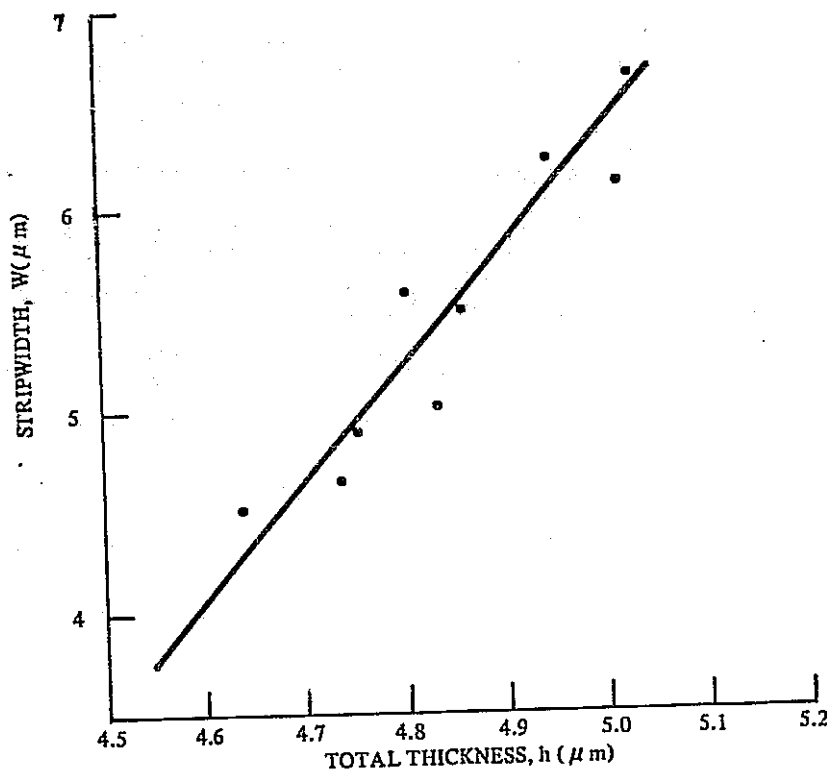
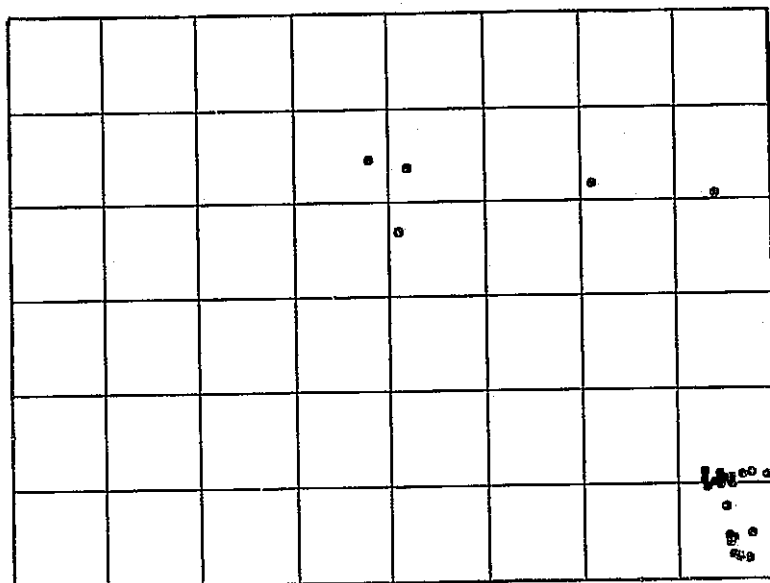


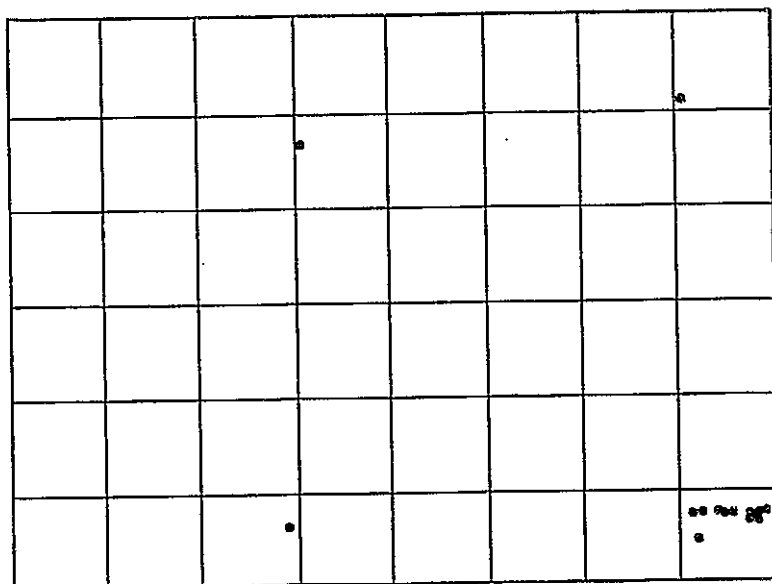
Figure 15. Stripwidth Variation in $\text{Y}_{2.62}\text{Sm}_{0.38}\text{Ga}_{1.17}\text{Fe}_{3.83}\text{O}_{12}$
With Capping Film Thickness

An experiment was performed to determine the bubble properties of annealed triple layer films. A triple layer gallium-substituted film of composition $\text{Y}_{2.46}\text{Sm}_{0.15}\text{Gd}_{0.15}\text{Tm}_{0.15}\text{La}_{0.09}\text{Ga}_{1.05}\text{Fe}_{3.95}\text{O}_{12}$ was broken into a number of sections. These sections were annealed at various temperatures. The results indicate that annealing a triple layer film is no different than an oxygen anneal of an as-grown bubble film. At temperatures above the equilibrium temperature, the stripwidth decreases and the magnetization increases. The effect was shown to be reversible.

A check was made to determine whether the extra suppression layer introduced additional defects which might reduce the possible device yield. This experiment was performed by mapping the bubble film defects which visibly pinned an ac excited domain pattern. A portion of such a standard defect map is shown in Figure 16-A. A Type III suppression layer was then grown on top of the bubble film, and the mapping process repeated. As evident in Figure 16-B, the addition of the suppression layer has introduced no extra defects and in fact seems to have removed some. A slight reduction in defect densities has been the trend observed during the course of this Type III layer investigation. Of course, the "defects" removed were not dislocations but most likely only surface contamination removed in the extra cleaning process before the top cap was grown. In any event, the capping procedure introduces no additional defects.



A.



B.

Figure 16. A. Portion of a Defect Map of a Unsuppressed Bubble Film
 B. Defect Map of Same Region of Film with Suppression Layer on Top

The remaining effort on this study was devoted to a comparison of the dynamic properties of bubbles in films which have a Type III hard bubble suppression layer and those which have been ion-implanted. Three variations of the Type III suppression technique were studied, viz: (1) a suppression layer between the bubble film and the substrate, (2) a suppression layer above the bubble film, and (3) a suppression layer above and below the bubble film (triple layer). In the two double layer samples, as well as in the ion-implanted films, the velocity versus drive field characteristic of bubble domains shows a pronounced nonlinearity or saturation effect which has been attributed to "dynamic conversion" by other investigators. The saturation effect in gallium-substituted garnets typically has its onset at a velocity of $\sim 2,000$ cm/sec. This is approximately the value of the theoretical critical velocity. No such saturation is observed in the triple layer films at velocities up to $\sim 5,000$ cm/sec (Figure 17) on a film of composition $\text{Y}_{2.46}\text{Sm}_{0.15}\text{Gd}_{0.15}\text{Tm}_{0.15}\text{La}_{0.09}\text{Ga}_{1.05}\text{Fe}_{3.95}\text{O}_{12}$. Consequently the preliminary conclusion is that this triple layer hard bubble suppression technique may also be effective in suppressing velocity saturation. * This would be extremely significant since such saturation or "conversion" has been one of the major obstacles to high frequency bubble domain device operation. It should be mentioned that further studies of the dynamic conversion suppression using double layers were carried out on company funds. These studies gave a preliminary indication that the double layer structure can have the same suppression effect as the triple layer provided the bias field is applied with the correct choice of polarity. The use of the incorrect polarity did not seem to prevent dynamic conversion. The type of wall structure which must be present (on the capped films) to allow this dependence on bias field polarity is not yet understood and is still being investigated.

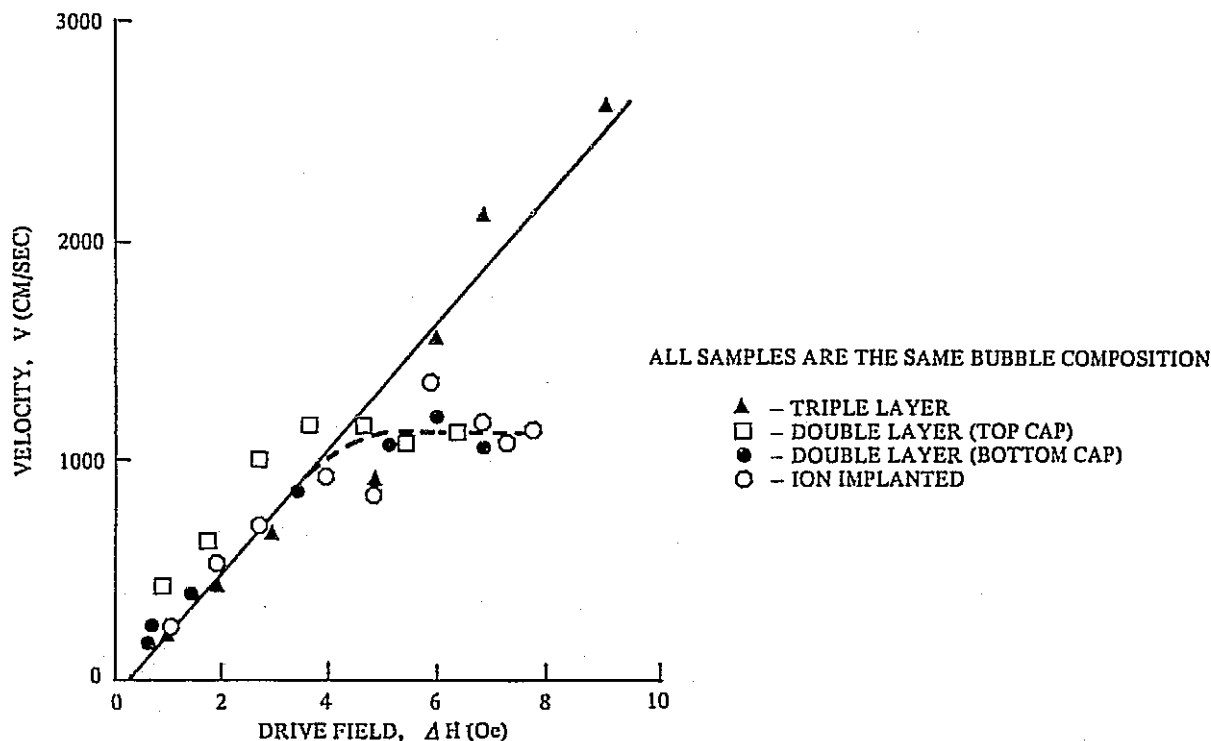


Figure 17. Velocity as a Function of Drive Field for $\text{Y}_{2.46}\text{Gd}_{0.15}\text{Sm}_{0.15}\text{Tm}_{0.15}\text{La}_{0.09}\text{Ga}_{1.05}\text{Fe}_{3.95}\text{O}_{12}$ (Ion-implanted, Top Suppression Layered, Bottom Suppression Layered, and Triple Layered Films)

* See note added in proof, page 55.

3.3 Conclusions

The studies conducted under this task have shown that the Type III multilayer suppression technique is sufficiently promising so that it should be included, along with ion-implantation, in the device evaluation of Task 4. Samples of the candidate compositions were prepared both with Type III suppression layers and with ion-implantation as the suppression technique. These films were statically and dynamically characterized (data included under Para 2.5). The device data on these samples is reported in Section 5.

4. TASK 2; LARGE AREA FILM GROWTH

4.1 Introduction

The objective of this task was to develop techniques for the LPE growth of films on substrates greater than 1.25 in. in diameter. As a result of our cost/yield analysis for large capacity elements, 1.5 in. diameter wafers were selected for this work. In addition, it was decided to evaluate the feasibility of changing the substrate thickness from the standard 0.020 in. to 0.012 in. since this would further reduce the garnet material contribution to the cost of the memory element. As a control sample, a group of 1 in. diameter, 0.020 in. and 0.010 in. thick GGG substrates were processed along with the 1.5 in. diameter material. The results reported here were obtained in the interval 18 Feb 1974 to 18 May 1974 and are representative of the processing techniques used at that time.

4.2 Substrate Processing

Thirty two 1.5 in. diameter, 0.029 in. thick, GGG slices, were purchased in as-cut form and were committed to the substrate processing procedure. The 32 slices were separated into two groups of 16 each, since this is the maximum capacity of our double face lapping equipment for this diameter substrate. The first group was lapped with 9 μ m Al₂O₃ abrasive, down to a thickness of 0.023 in. This is to remove wafer sawing damage and to provide flat parallel surfaces for the subsequent polishing procedure. The second set of 16 was lapped down to 0.017 in. thick. To obtain 0.010 in. to 0.012 in. finished wafers by the standard process, the starting slices would be 0.020 in. thick to result in a material cost savings of approximately 30 percent.

Twelve wafers of each thickness were wax mounted on two 9 in. diameter polishing plates, which are used on our 24 in. Speedfam polishing machines. Twelve 1.5 in. diameter substrates are the maximum capacity of these plates for the mounting configuration we use. The initial polishing pressure was 6.4 psi, which is the pressure normally used for processing 1 in. diameter substrates. Under this pressure, excessive polishing plate temperatures occurred in both the 9 in. diameter top plate holding the substrates and the 24 in. plate which holds the polishing cloth. Excessive temperatures can result in mounting wax softening and loss of samples. Subsequent polishing of the 1.5 in. diameter material was done at a loading pressure of 2.3 psi. The polishing media for the final polishing was Syton* HT. The wafers were polished to a thickness 0.020 in. on the first plate and 0.012 in. on the second plate. Both sides of each wafer were polished with the material removal being equal on both sides. The second polished surface was designated the "epi" surface on which the device quality film was to be grown. Table 14 shows the processing steps and gives yields and causes for processing losses.

Twenty 1 in. diameter x 0.017 in. thick GGG substrates were cut from a boule for the thin 1 in. diameter substrates. These were lapped to a thickness of 0.0145 in. and were processed in the same manner as the 1.5 in. diameter material to a final thickness of 0.010 in. In all cases the final hour of polishing was done at a substrate loading of 0.82 psi. For the 1 in. material 20 substrates were processed since this is the capacity of each polishing plate for that diameter.

GGG wafers for the 1 in. diameter x 0.020 in. thick portion of the effort were obtained from our standard inventory of substrate material.

A summary of the process yields for the 1 in. wafers is shown in Table 15.

*A product of the Monsanto Corporation.

The yield losses at the lapping process step are shown in Table 14 and 15 to be caused by a malfunctioning pneumatic lift. The top plate of the double faced planetary action lapping machine is raised and lowered by a pneumatic cylinder. The compressibility of the air in the cylinder plus the less than perfect guide rail mechanical action of the plate caused a sporadic lowering action. This caused substrate breakage by impacting the high point of the wafer when the plate was lowered. An oil reservoir has been installed on this equipment and this has eliminated the problem.

The polishing loss indicated as "Syton flow restriction," in Table 14 was caused by a plugged orifice of a flow control needle valve in the Syton gravity feed system. This caused heating of the polishing plate (ran too dry) and thus softened the wax used to hold the substrate. Greater care in flushing the delivery system between runs, valve replacement to a configuration less likely to plug and filtering of the Syton were all actions taken to avoid this as a further problem.

A phosphoric acid (H_3PO_4) etch was used as a post polish evaluation step. The polished substrates were immersed in a bath of H_3PO_4 , held at 180°C , for 30 sec. This etch in conjunction with a microscopic inspection of the substrate surface at 110X using Nomarski attachment illumination was used as the quality control of the polished surface. Thermal shock problems were encountered primarily with the larger diameter-thinner wafers during the etching process. The addition of a preheater section just above the H_3PO_4 bath eliminated the problem. The preheater allowed both the larger thin wafer and the wafer holder to slowly attain the bath temperature prior to immersion.

4.3 Garnet Film Growth

Films of $(\text{YEuTm})_3(\text{GaFe})_5\text{O}_{12}$ were grown on the polished substrates discussed in the previous sections. The films were divided into two groups having nominal strip domain widths, w , of $4.5\text{ }\mu\text{m}$ (for $16\text{ }\mu\text{m}$ period devices) and $6.5\text{ }\mu\text{m}$ (for $24\text{ }\mu\text{m}$ period devices). The latter group provided a control sample since that was the domain width which has been in standard use in our laboratory at that time. All of the films were grown from the same melt by making a slight Ga addition to obtain the films with a w of $6.5\text{ }\mu\text{m}$ after the films with w of $4.5\text{ }\mu\text{m}$ had been grown. This film composition was selected for the large area LPE development because it was one of the two candidate materials for the initial Item 1 work.

The melt flux system was the commonly used 50:1 $\text{PbO}:\text{B}_2\text{O}_3$ weight ratio with a $\text{Fe}_2\text{O}_3/\text{RE}_2\text{O}_3$ molar ratio of 20 where RE_2O_3 is the sum of the rare earth and yttrium oxides. A melt solute concentration of 9 mole percent was used. The melt volume was approximately 650 ml and it was contained in a one liter platinum crucible. Figure 18 is a photograph of six LPE stations in our laboratory. Each pair of furnaces have their own laminar flow station to provide a clean loading and unload area. Also shown are the raising and lowering mechanisms which also provide rotational motion during growth and post deposition spin. Figure 19 shows a platinum substrate holder used for single or double film growth. This holder is used in the horizontal position with axial rotation and rotation reversal. Figure 20 shows 1 in., 1.5 in and 2 in. diameter substrates and grown films. Using this equipment and methods, 45 growth runs were made. All of the runs were done at the same growth temperature of 918°C , which was 15°C below the melt supersaturation temperature. Film growth rates of $\approx 0.5\text{ }\mu\text{m}/\text{min}$ resulted from the above conditions. All films were grown in the horizontal position with an axial rotation rate of 140 rpm and with the direction of the rotation reversed after each one revolution.

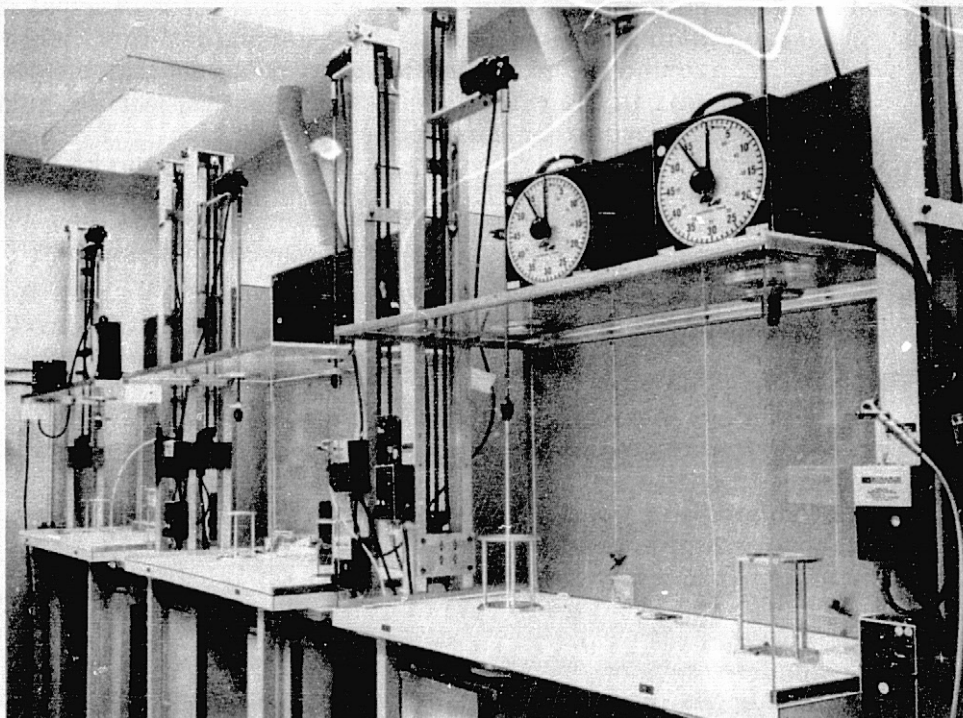


Figure 18. Six LPE Growth Stations with Laminar Flow Benches

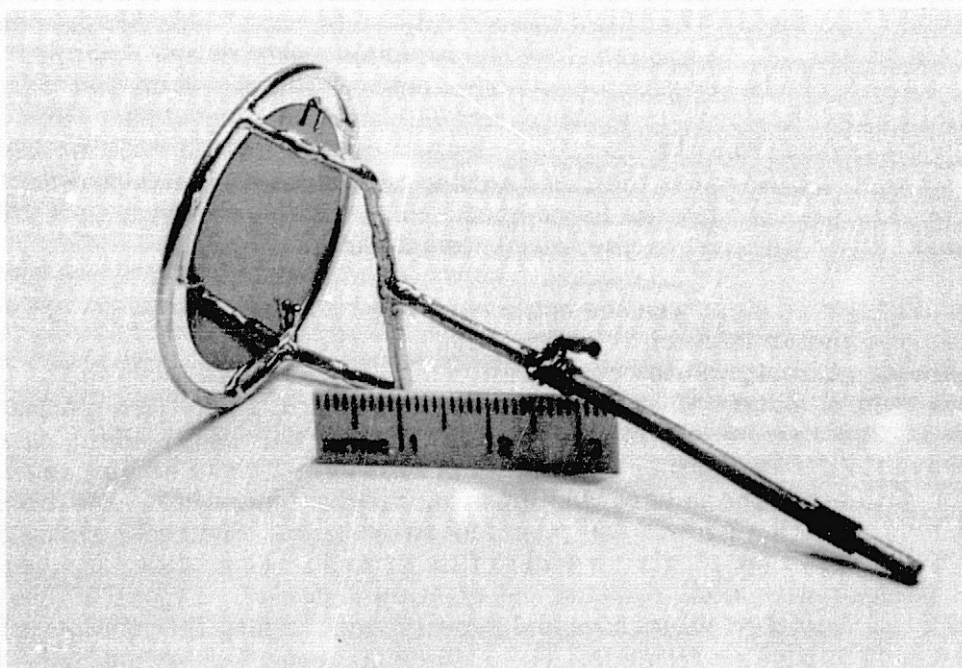


Figure 19. Platinum Substrate Holder for LPE Film Growth

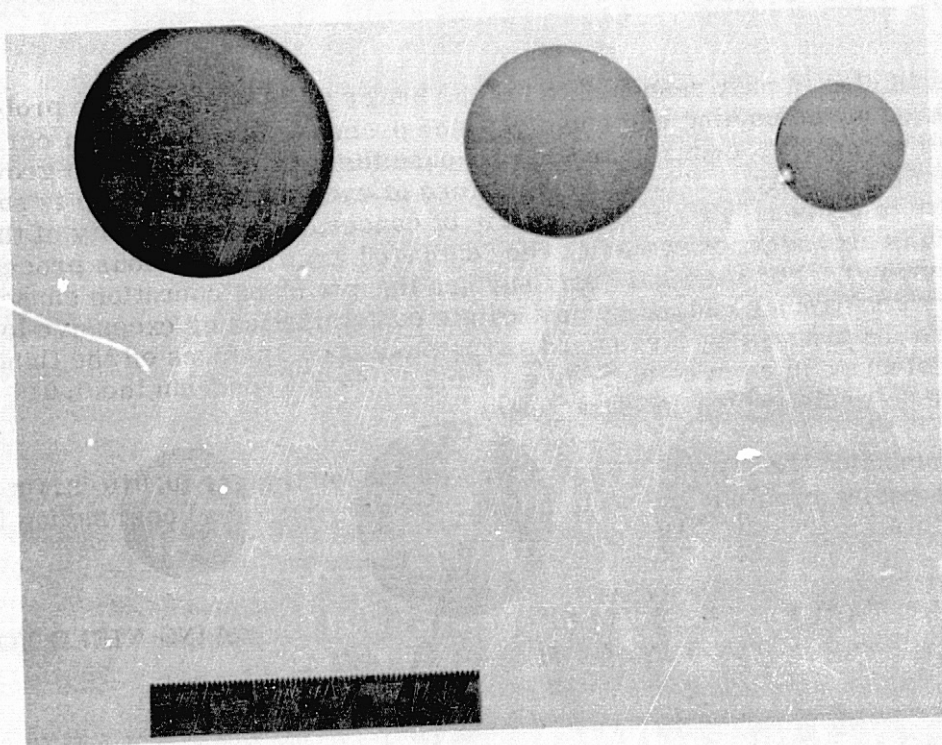


Figure 20. 1.0, 1.5 and 2.0 in. Diameter GGG Substrates and Bubble Domain Garnet Films

Twelve of the growth runs were made with two films grown per run by placing two substrates back to back in the holder. Earlier work with this configuration here and elsewhere (Ref 7) suggested that no problems would be encountered using 1 in. dia substrates with a thickness on the order of 0.020 in., however, this work was our first experience with the larger (1.5 in.) diameter and thin (0.012 in.) material. The technique of separating the substrates after growth with a razor blade, (required because of the melt flux which gets between two substrates) worked very well with the larger diameter thinner material. There was no breakage or film loss caused by the separation technique. No film processing losses were attributable to the thinner substrates. Because of the thermal shock problem encountered during the H_3PO_4 etch, the insertion and withdrawal rates of these thinner wafers in the LPE furnace were decreased. A short handling learning curve for the processing personnel appeared to be the single most important aspect of the thin samples.

Tables 14 and 15 include film processing yield data as well as cumulative yields for all process steps. Table 16 presents film growth-characterization yields and gives causes of the losses. The 1 in. - 0.020 in. samples have the better overall yield but no lapping-polishing losses are included since the substrates were from the finished substrate inventory. The highest loss cause of the 1 in.-0.010 in. samples was film defect density and not handling. The defects are both substrate and film growth related and do not adversely reflect on the thinner material. This is also true for the thin 1.5 in. samples. The larger starting sample size for the 1 in. dia

material is also in part responsible for the better yield values. The problems encountered at the lapping and chemical etch process steps have been corrected. Improved process procedures should decrease the largest single film growth reject cause, defect density. The inherent nature of each processing step is such that only the ability to process without breakage is of concern. Defect density of the finished substrate is dependent of removing the "damage" from the previous process step (e.g., lapping). For the final "epi" surface the polishing operation cannot result in added surface damage caused by particulate contamination or excessive loading. Therefore the processing steps used can produce good surfaces on the thinner wafers and the defect yield as seen in Tables 14 and 15 do not condemn the 0.010 in. substrate as would appear by first glance.

Processing the larger 1.5 in. diameter and/or thinner (0.010 in.) material is not a processing problem and will, in fact, provide increased cost saving for bubble device films.

TABLE 14. -SUMMARY OF GARNET PROCESSING YIELD FOR
1.5 IN. DIAMETER SUBSTRATES

Process Step	Finished Wafer Thickness					
	0.020 in.			0.012 in.		
	Started	Out	% Yield	Started	Out	% Yield
Lapping	16	14(1)	87.5	16	13(2)	81.2
Polishing	12	11(3)	91.7	12	12	100.0
Chemical Etch	11	11	100.0	12	10(4)	83.3
Film Growth-Characterization	11	7(5)	63.6	10	6(6)	60.0
(Cumulative Yield)			51%			40.6 %

Notes:

1. Malfunction pneumatic lift on lapping machine
2. Malfunction pneumatic lift on lapping machine
3. Syton flow restriction-heating-1 substrate came off of polishing plate
4. Thermal shock H_3PO_4 etch.
5. See Table 16.
6. See Table 16.

TABLE 15. -SUMMARY OF GARNET PROCESSING YIELD FOR
1 IN. DIAMETER SUBSTRATES

Process Step	Finished Wafer Thickness					
	0.020 in.			0.010 in.		
	Started	Out	% Yield	Started	Out	% Yield
Lapping				20	19 ⁽¹⁾	95
Polishing		20		19	19	100
Chemical Etching	20	19 ⁽²⁾	95.0	19	19	100
Film Growth and Characterization	19	16 ⁽³⁾	84.2	19	14 ⁽⁴⁾	74
(Cumulative Yield)			80.0%			70.0%

Notes:

1. Malfunctioning pneumatic lift on lapping machine.
2. Thermal shock H_3PO_4 etch.
3. See Table 16.
4. See Table 16.

TABLE 16. -SUMMARY OF FILM GROWTH AND CHARACTERIZATION YIELD
(45 GROWTH RUNS WITH 57 SUBSTRATES)
(34 - 1 IN, 23 - 1.5 IN.)

Cause of Loss	Number Lost Related to Substrate Size and Thickness			
	1 In. Dia		1.5 In. Dia	
	0.020 in.	0.010 in.	0.020 in.	0.012 in.
Handling	0	1	1	1
High Defect Density ($>10/cm^2$)	3	4	1	3
Post Growth Cleaning ⁽¹⁾	0	0	1	0
Lost ⁽²⁾	0	0	1	0

- (1) Post deposition cleaning involves a scrubbing operation - at this step contamination caused scratching of this sample.
- (2) Film misplaced - not found.

5. TASK 4. - DEVICE EVALUATION OF CANDIDATE MATERIALS AND HARD BUBBLE SUPPRESSION TECHNIQUES

The objective of this task is to evaluate candidate materials and hard bubble suppression techniques in terms of device operation at 150 kHz in a continuous mode over the temperature range of -10°C to $+60^{\circ}\text{C}$. YEuGa and YSmLaGa iron garnets have been chosen for candidate materials and ion-implantation and double-layering have been chosen for hard bubble suppression techniques. The samples chosen are listed in Table 17 along with their material parameters.

Notice that the demagnetized domain stripwidth, W_s , lies in the range of 3.6 to $4.1\text{ }\mu\text{m}$ for these samples. The mid-range operating bubble diameter is nominally equal to W_s . Material/device parameter studies have shown that the desirable ratio of stripwidth to device period is ~ 0.20 , which, for a $16\text{ }\mu\text{m}$ period, corresponds to $W_s = 3.2\text{ }\mu\text{m}$. However, in order to effectively utilize this value of W_s in a $16\text{ }\mu\text{m}$ period device requires that the gaps between the permalloy elements be $\sim 0.80\text{ }\mu\text{m}$. At the time these film samples were grown the standard artwork/mask fabrication and device processing procedures were such that the $16\text{ }\mu\text{m}$ period device gaps were $\sim 1.3\text{ }\mu\text{m}$. Having this large gap with a W_s of $3.2\text{ }\mu\text{m}$ would result in very poor device margins. Consequently a compromise was reached by increasing the target value of W_s to $4.0\text{ }\mu\text{m}$. By the time the devices were actually completed the artwork/mask/processing effort on Item 1 had progressed to the point that gaps of $\sim 1.0\text{ }\mu\text{m}$ were obtained in the samples of this task. At this time it was not possible to attempt to reduce W_s by annealing because of the effect on program funding and schedules. As a consequence some of the device data obtained reflects the use of a less than optimum ratio of stripwidth to period.

It was originally planned to use the partially populated 10^4 bit device for this task. But since a good mask of the 10^4 bit device was not made available in time, Task 4 was carried out using the $16\text{ }\mu\text{m}$ period test pattern mask. This mask is described in detail in Section 7. These samples were also used in Task 5. Since the high speed optical sampling technique used in Task 5 requires a special sample preparation, the processing of these samples will be discussed in Section 6. However, one remark has to be made. That is, the top-capped sample from candidate material II (Wafer No. 4-27-7) was totally damaged during the process and no replacement was made.

5.1 Device Characterization

The conventional margin measuring technique was used. A die was mounted on a printed circuit test board and put into a bias field and rotating field coil structure. Temperature was controlled by controlling the flow rate of liquid nitrogen cooled air blown into the coil structure and monitored by a Si diode mounted close to the sample on the board. The accuracy of temperature control was somewhat better than $\pm 1^{\circ}\text{C}$.

The 90 deg chevron detector test loop (defined as pattern 10 in Section 7) was chosen somewhat arbitrarily since there was very little difference in the operating margin between different test loops. The margin was measured by monitoring detector output. The operating frequency was 150 kHz.

TABLE 17. MATERIAL PARAMETERS FOR CANDIDATE MATERIALS

Candidate Material I ($\text{Y}_{2.5}\text{Eu}_{0.5}\text{Ga}_{1.07}\text{Fe}_{3.93}\text{O}_{12}$)								
Wafer No.	Suppression Technique	H_0 (Oe)	H_2 (Oe)	σ_w (erg/cm ²)	$4\pi M_s$ (G)	W_s (μm)	h (μm)	ℓ (μm)
4-25-21	Ion-Implanted	95.6	72.5	0.175	212	4.06	3.4	0.489
4-25-22	Bottom-Capped	109.3	85.2	0.192	231	3.86	3.4	0.452
4-25-30	Top-Capped	107.7	84.5	0.254	250	4.14	3.2	0.452
Candidate Material II ($\text{Y}_{2.69}\text{Sm}_{0.2}\text{La}_{0.11}\text{Ga}_{1.13}\text{Fe}_{3.87}\text{O}_{12}$)								
Wafer No.	Suppression Technique	H_0 (Oe)	H_2 (Oe)	σ_w (erg/cm ²)	$4\pi M_s$ (G)	W_s (μm)	h (μm)	ℓ (μm)
4-27-2	Ion-Implanted	109.8	87.0	0.186	232	3.68	3.3	0.432
4-27-3	Bottom-Capped	120.6	94.0	0.263	265	3.93	3.3	0.468
4-27-7	Top-Capped	119.0	100.4	0.274	266	4.00	3.3	0.483
H_0	=	bubble collapse field						
H_2	=	bubble stripout field						
σ_w	=	domain wall energy						
$4\pi M_s$	=	magnetization						
W_s	=	demagnetized domain strip width						
h	=	film thickness						
ℓ	=	characteristic length						

5.1.1 Bias Margin at Room Temperature. - A die representing each candidate material and each hard bubble suppression technique was first characterized at room temperature (25°C). If a die did not show a satisfactory margin, it was replaced by another die until a reasonable margin was obtained.

Typical results are shown in Figures 21 to 25. In the figures the solid circles (•) represent the lower margin and the open circles (o) and crosses (x) represent the upper margin of the consecutive bit and alternate bit patterns, respectively. At first glance, the margin diagrams look very different from one another. It should be pointed out, however, that the variation of the margin diagram among dice from the same wafer can be as great. Therefore, every feature should not be considered as representing differences between materials or hard bubble suppression techniques. In fact, most of the features seem to be attributable to differences in material parameters

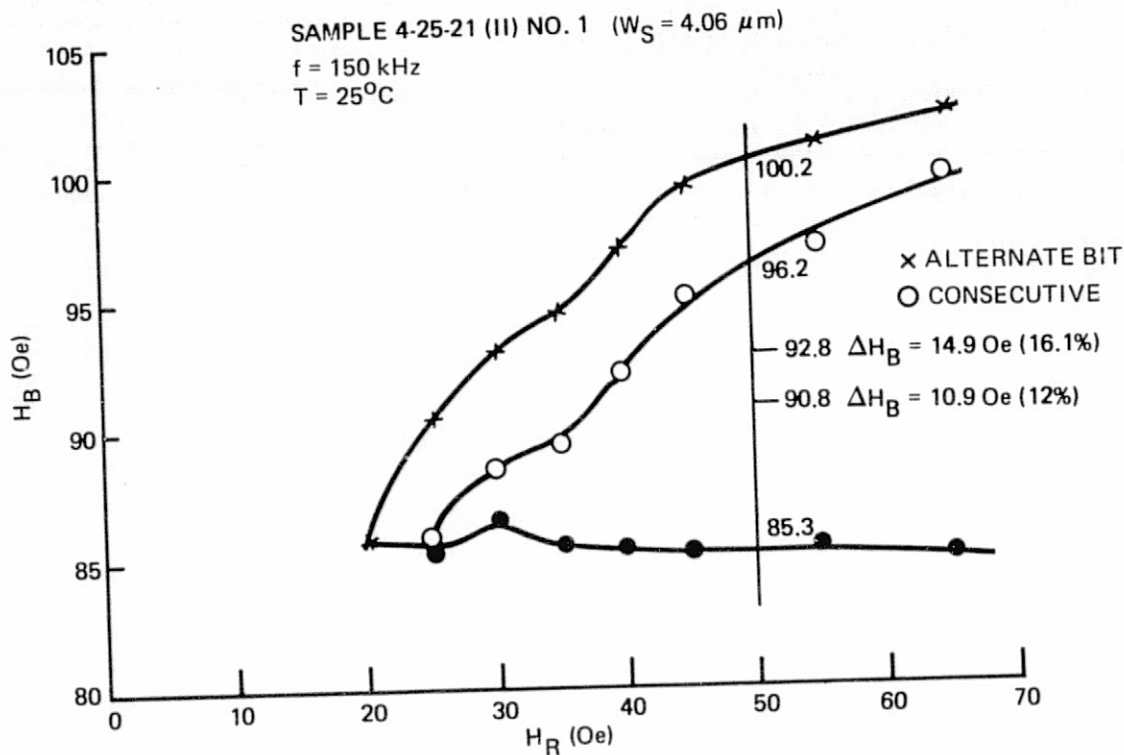


Figure 21. Bias Margin as Function of Drive Field at Room Temperature for YEu Ion-Implanted Sample

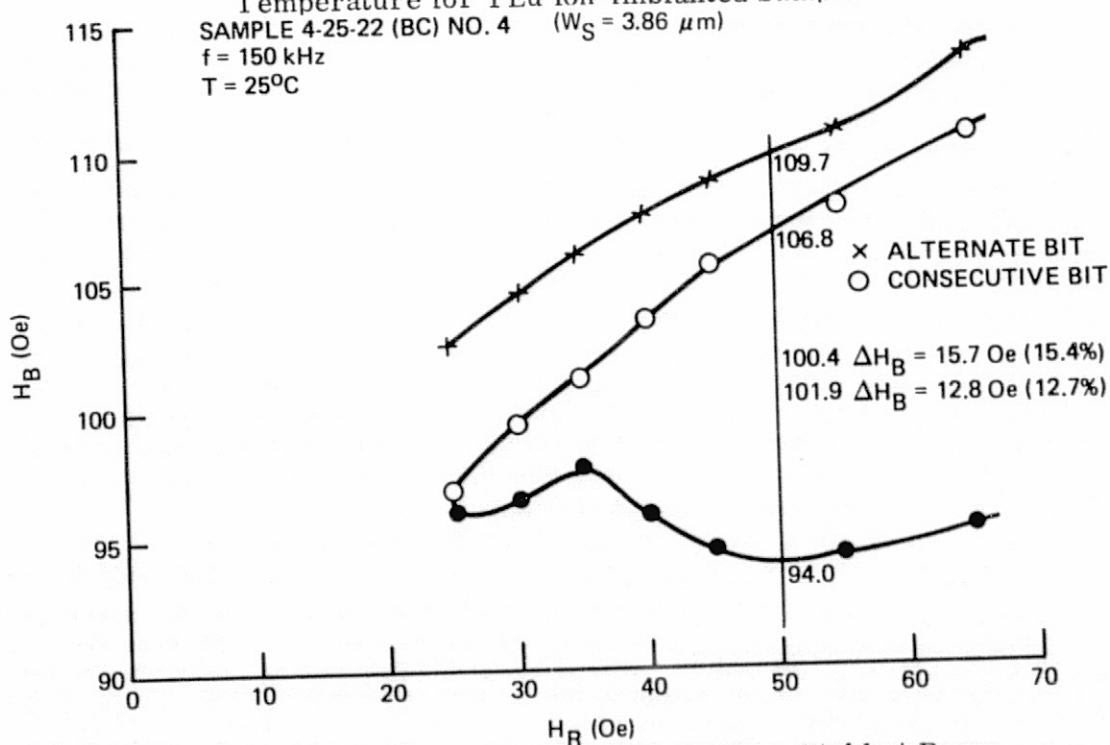


Figure 22. Bias Margin as Function of Drive Field at Room Temperature for YEu Bottom-Capped Sample

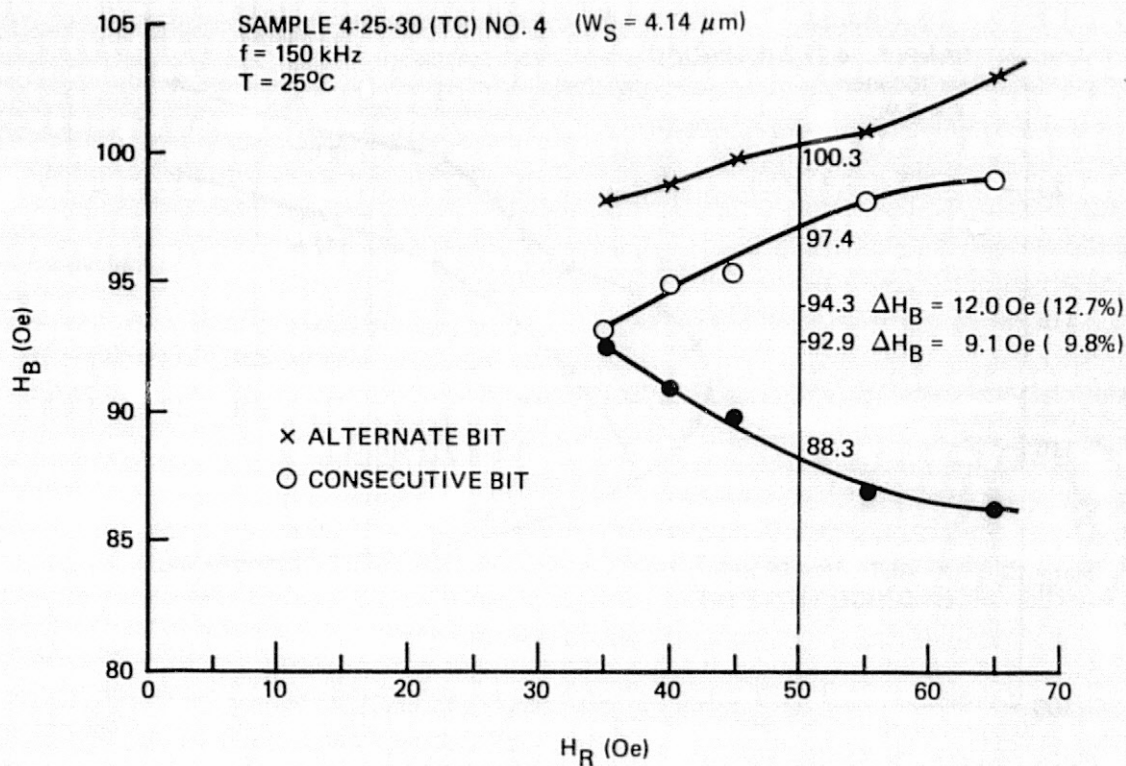


Figure 23. Bias Margin as Function of Drive Field at Room Temperature for YEu Top-Capped Sample

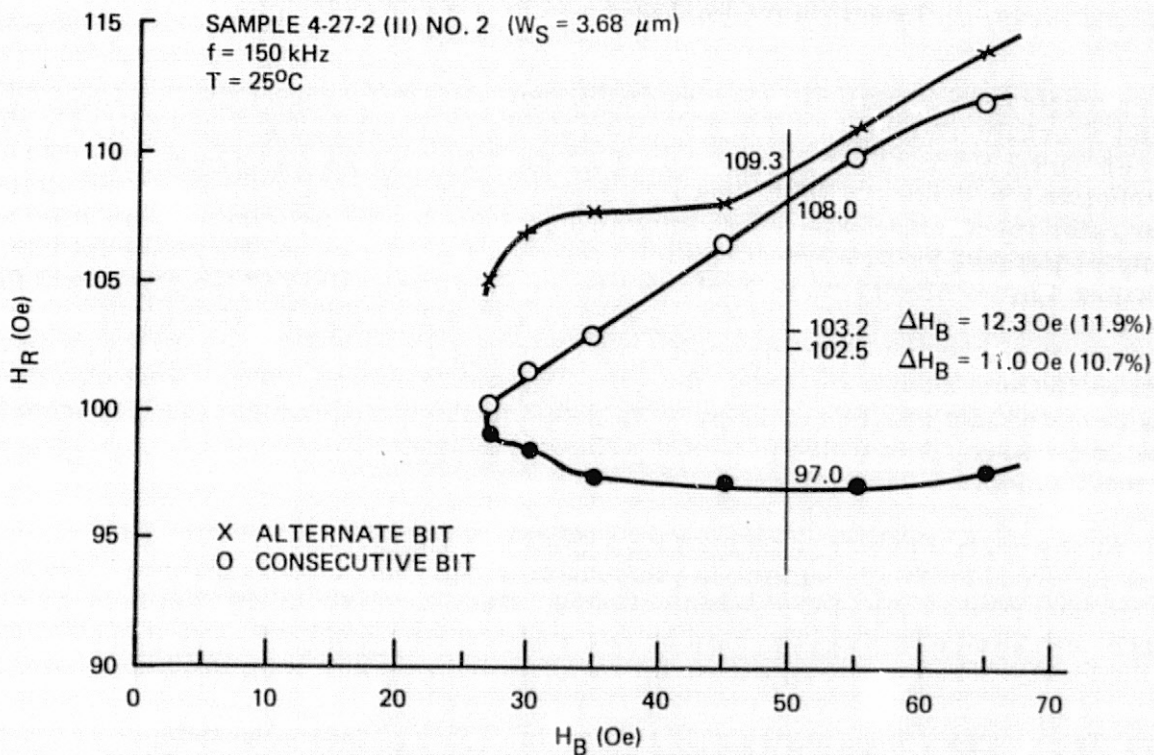


Figure 24. Bias Margin as Function of Drive Field at Room Temperature for YSmLa Ion-Implanted Sample

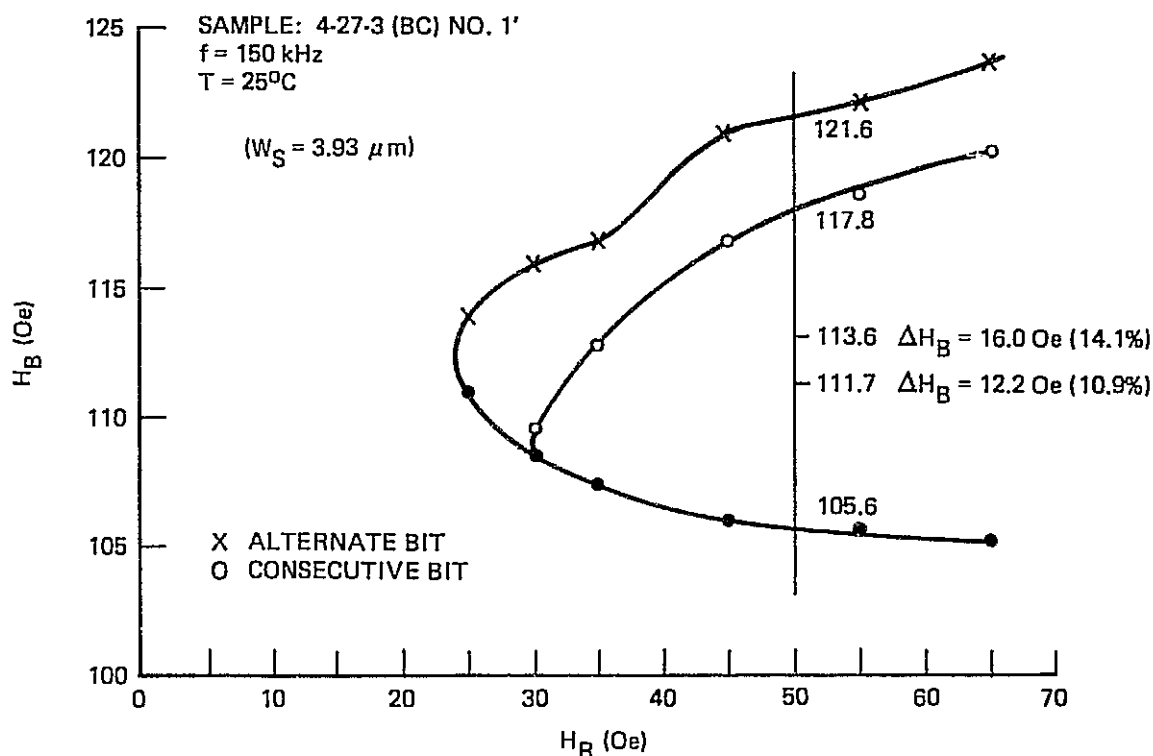


Figure 25. Bias Margin as Function of Drive Field at Room Temperature for YSmLa Bottom-Capped Sample

and/or fabrication conditions. For example, the large differences between consecutive bit and alternate bit margins at higher drive field can be attributed to oversized bubbles. For comparison purpose, the consecutive bit and alternate bit margins at $H_R = 50 \text{ Oe}$ are tabulated in Table 18. Note that the difference between consecutive bit and alternate bit margins (percentage-wise) is roughly proportional to the stripwidth. The difference is only ~1 percent for $3.68 \text{ } \mu\text{m}$ stripwidth whereas it is ≥ 3 percent for the stripwidth exceeding $4 \text{ } \mu\text{m}$. Also given in Table 18 are the minimum values of the drive field for consecutive bit propagation, which may also be correlated with the stripwidth. Returning to the figures, we notice that when the bias margin extends into lower drive fields ($\leq 35 \text{ Oe}$), it tends to shrink abruptly (Figures 21, 22, and 24). Visual observations revealed that this is caused by strip domains stretching out into the loop from the detector feedthrough to which part of the chevron guard rail is shorted as a consequence of a mask defect.

In any case, the bias margin at $H_R = 50 \text{ Oe}$ is ≥ 10 percent and this can be increased considerably by optimizing the bubble size. Further, spontaneous nucleation was not observed in any of the samples tested. Thus it is fair to say that both materials (YEuGa and YSmLaGa) and both hard bubble suppression techniques (ion-implantation and double-layering) are adequate as far as room temperature margin is concerned.

5.1.2 Temperature Dependence of Bias Margin. - Temperature dependence of the bias margin for each sample at a fixed drive field of 50 Oe is shown in Figures 26 to 30. For one sample (4-25-2), it is shown for $H_R = 40 \text{ Oe}$ as well for comparison (see Figure 26(a) and (b)). It is seen that each sample shows the general profile of bias

TABLE 18. BIAS MARGINS AND MINIMUM DRIVE FIELDS AT ROOM TEMPERATURE

Sample	Composition	Surface Treatment	Domain Stripwidth	H_R^+ min Consec Bits	ΔH_B at $H_R = 50$ Oe	
					Consec Bits	Alternate Bits
4-27-2	YSmLaGa	Ion-implanted	3.68 μ m	27 Oe	11.0 Oe (10.7%)	12.3 Oe (11.9%)
4-27-3	YSmLaGa	Bottom-capped	3.93 μ m	30 Oe	12.2 Oe (10.9%)	16 Oe (14.1%)
4-25-21	YEuGa	Ion-implanted	4.06 μ m	30 Oe	10.9 Oe (12.0%)	14.9 Oe (16.1%)
4-25-22	YEuGa	Bottom-capped	3.86 μ m	25 Oe	12.8 Oe (12.7%)	15.7 Oe (15.4%)
4-25-30	YEuGa	Top-capped	4.14 μ m	35 Oe	9.1 Oe (9.8%)	12.0 Oe (12.7%)

+ Minimum value of the drive field

* Bias field margin

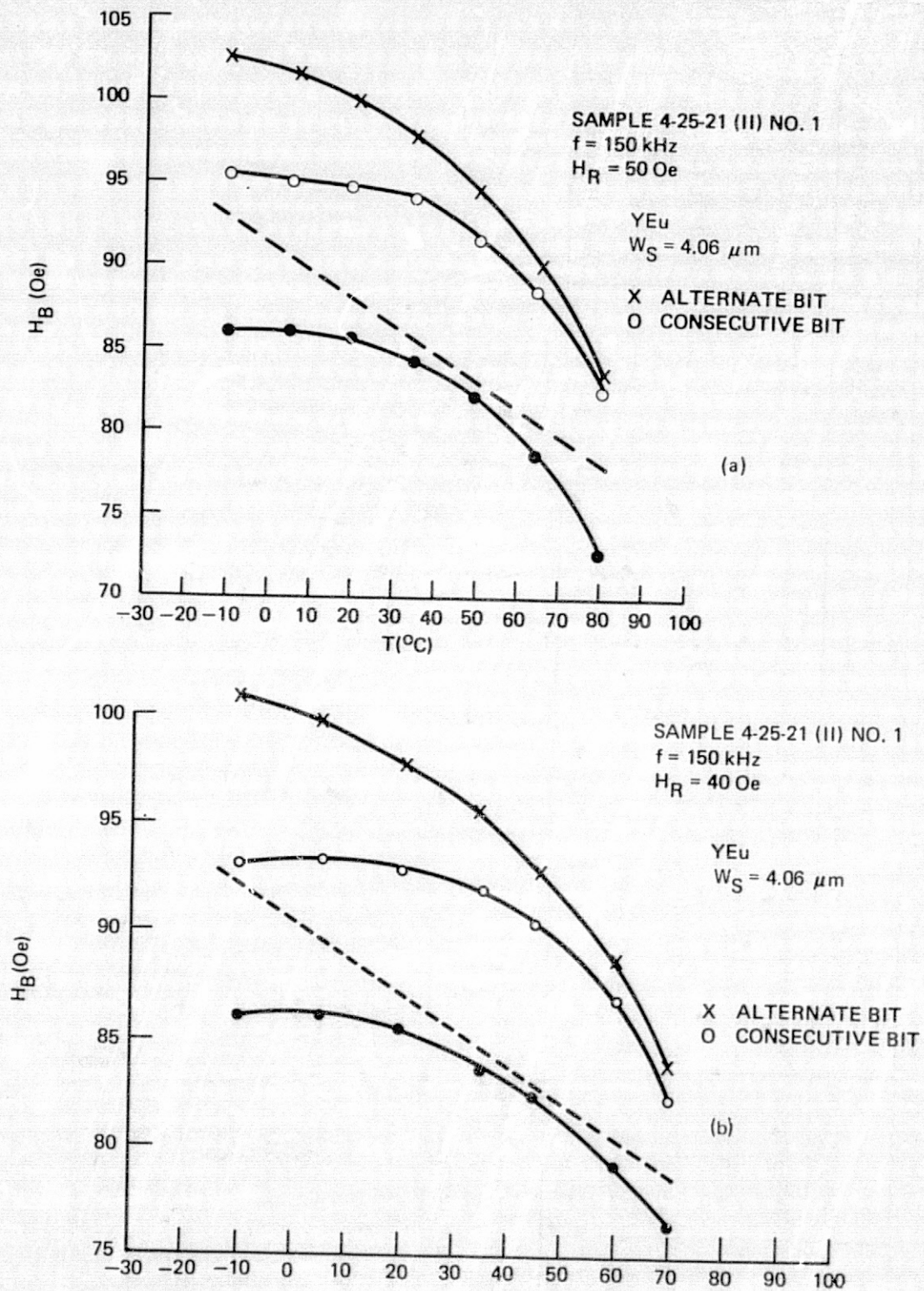


Figure 26. Bias Margin as Function of Temperature for YEu Ion-Implanted Sample

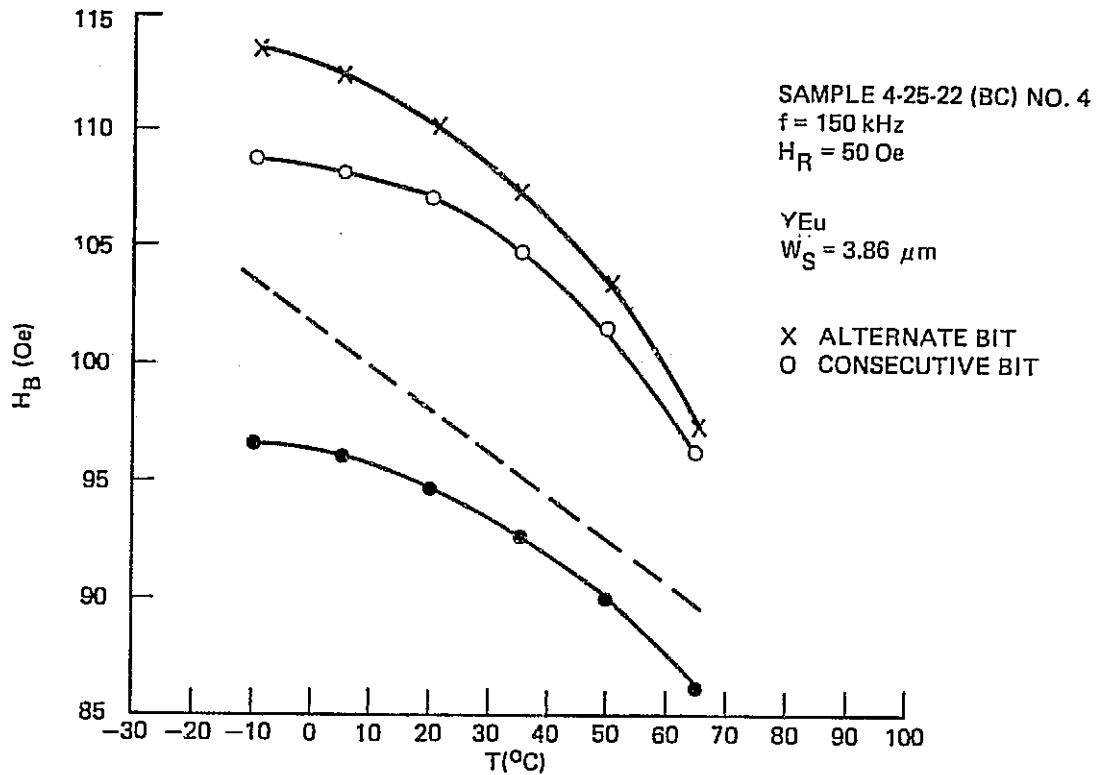


Figure 27. Bias Margin as Function of Temperature at $H_R = 50 \text{ Oe}$ for YEu Bottom-Capped Sample

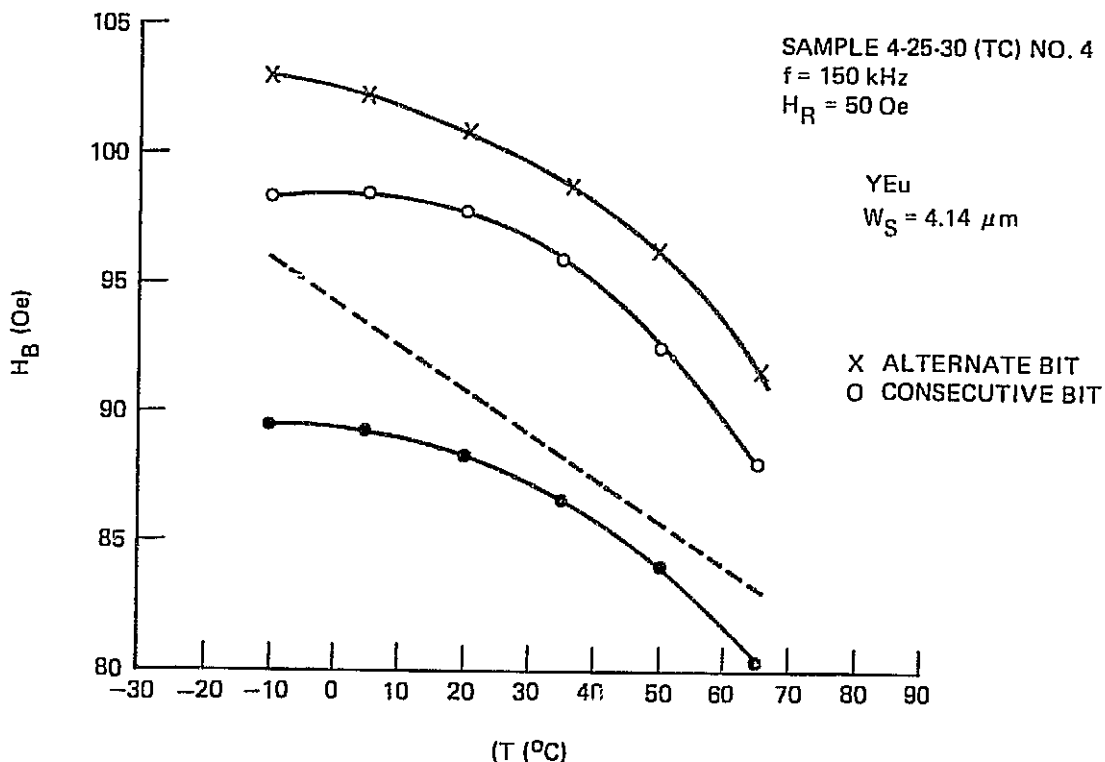


Figure 28. Bias Margin as Function of Temperature at $H_R = 50 \text{ Oe}$ for YEu Top-Capped Sample

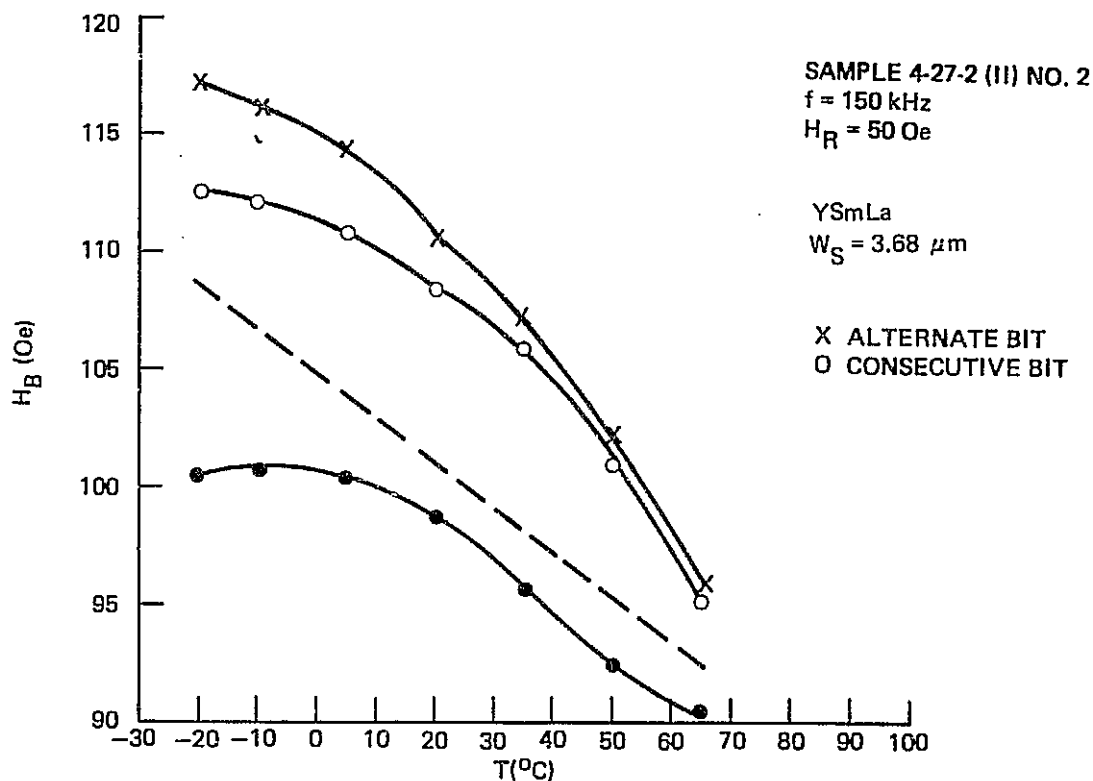


Figure 29. Bias Margin as Function of Temperature at $H_R = 50 \text{ Oe}$ for YSmLa Ion-Implanted Sample

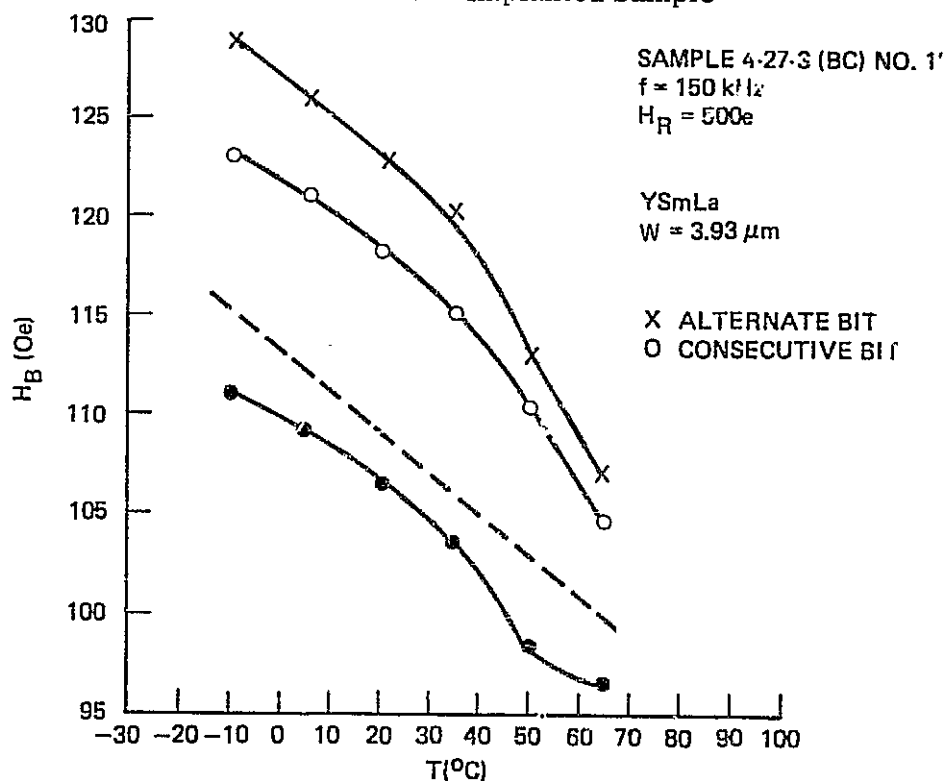


Figure 30. Bias Margin as Function of Temperature at $H_R = 50 \text{ Oe}$ for YSmLa Bottom-Capped Sample

margin as a function of temperature characteristic of YEu and YSm compositions. It more or less matches the temperature profile of Ba ferrite permanent magnets in the required temperature range as can be seen from the dashed curve which is drawn in each figure assuming a temperature coefficient of $-0.19\%/^{\circ}\text{C}$.

The effect of oversized bubbles manifests itself even more markedly in the temperature dependence of the bias margin. Let us look at the cases where the stripwidth is greater than $4\text{ }\mu\text{m}$. In Figures 26(a) and 28 we see that the consecutive bit margin shows a maximum at around room temperature while the alternate bit margin monotonically increases with decreasing temperature, the effect of oversizing is enhanced at lower temperatures, resulting in shrinkage of consecutive bit margins. This is further evidenced by the temperature dependence curve plotted in Figure 26(b) for a lower drive field at which the effect of bubble-bubble interactions is expected to be greater.

In summary what the temperature dependences of the bias margins have revealed is that there is little difference between the materials and the surface treatments. The temperature profile of Ba ferrite permanent magnets matches the temperature dependence of the bias margins fairly well and as seen from Figures 26 and 28, the matching will be much better if bubble size is optimized to increase consecutive bit margins at lower temperatures. Spontaneous bubble nucleation was not a problem at any temperature.

5.2 Summary and Conclusion

Two candidate materials, YEuGa and YSmLaGa iron garnets and two hard bubble suppression techniques, ion-implantation and double-layering were evaluated in terms of device operation at 150 kHz in a continuous mode over the temperature range of -10°C to 60°C . Although each sample representing each material or surface treatment exhibited somewhat different features in the bias margin diagram, most of these features can be attributed to differences in material parameters, especially the stripwidth. The temperature dependence of the bias margin showed that it matches that of the Ba ferrite magnetization adequately.

Thus it is concluded that both materials and both hard bubble suppression techniques are adequate for use in flight recorder application. The selection of the final material and hard bubble suppression technique for the recorder program should therefore be based on other considerations such as ease of fabrication and reproducibility of properties.

6. TASK 5 - EFFECTS OF HARD BUBBLE SUPPRESSION LAYERS AND CRYSTAL ORIENTATION ON MATERIAL AND DEVICE CHARACTERISTICS STUDIED USING A HIGH SPEED OPTICAL SAMPLING TECHNIQUE

It has been reported in Section 4 that various hard bubble suppression techniques (ion-implantation, multilayering, etc) have different effects on the dynamic properties of bubbles. Most notable is the absence of velocity saturation in triple-layered films. The misorientation of the [111] axis of the substrate relative to its surface normal is also known to have appreciable effects on the dynamic properties⁸. It is the objective of this task to study the effects of hard bubble suppression layers and crystal orientation on material and device dynamic properties.

Much of the fundamental static and/or quasi-static characterization of materials and devices is done using an optical microscope. It is only natural to turn to optical methods also when the dynamic character of bubbles is investigated. The high speed optical sampling microscope system⁹ developed by Humphrey and co-workers at the California Institute of Technology has the capability of optically sampling a dynamic event with a 10 nsec single exposure photograph and is well suited for studying the dynamic behavior of bubbles. This system was made available to us and used throughout this task.

6.1 High Speed Optical Sampling Technique

The optical sampling microscope system⁹ used here, which was developed by Humphrey and co-workers at the California Institute of Technology, is capable of making a series of single exposure photographs at known sample times with a 10 nsec exposure time. It thus allows a detailed analysis of the dynamic behavior of bubbles during their high speed motion. The system as it is used for free bubble measurements and for device studies is shown in Figures 31 and 32, respectively.

Figure 31 shows a block diagram of the optical sampling system as it is used for free bubble measurements. It consists of the laser illuminated optical microscope, 16 mm movie camera, sampling oscilloscope and pulse generators. An observation is initiated by a timing pulse originating from the movie camera (indicating that the shutter is open) or by an external clock at the same frequency (not shown) if a photographic record is not desired. This timing pulse triggers the pulse generator and the sampling oscilloscope horizontal sweep external trigger as indicated. The sweep unit then triggers the laser light source after adding a delay appropriate to the position in the sweep. A portion of the light from the laser shines on a fast photodiode (PIN diode) giving a pulse that triggers the vertical sample gate coincident with the light pulse. The time of the light flash can then be adjusted in relation to the applied field pulses in any desired way by using the delay internal to the pulse generator and observing the field pulse on the sampling oscilloscope. The time relationship between the laser pulse and the magnetic field pulse is therefore adjusted avoiding all ambiguities due to instrumented delays, etc. Time sweeps of events can be taken by using the horizontal sweep generator of the oscilloscope and movie camera with each frame representing a single exposure of the transient domain shape at that time. Although the results look like motion pictures, they are not; they are photographs taken at 16 Hz of a repetitious event taken at various delays.

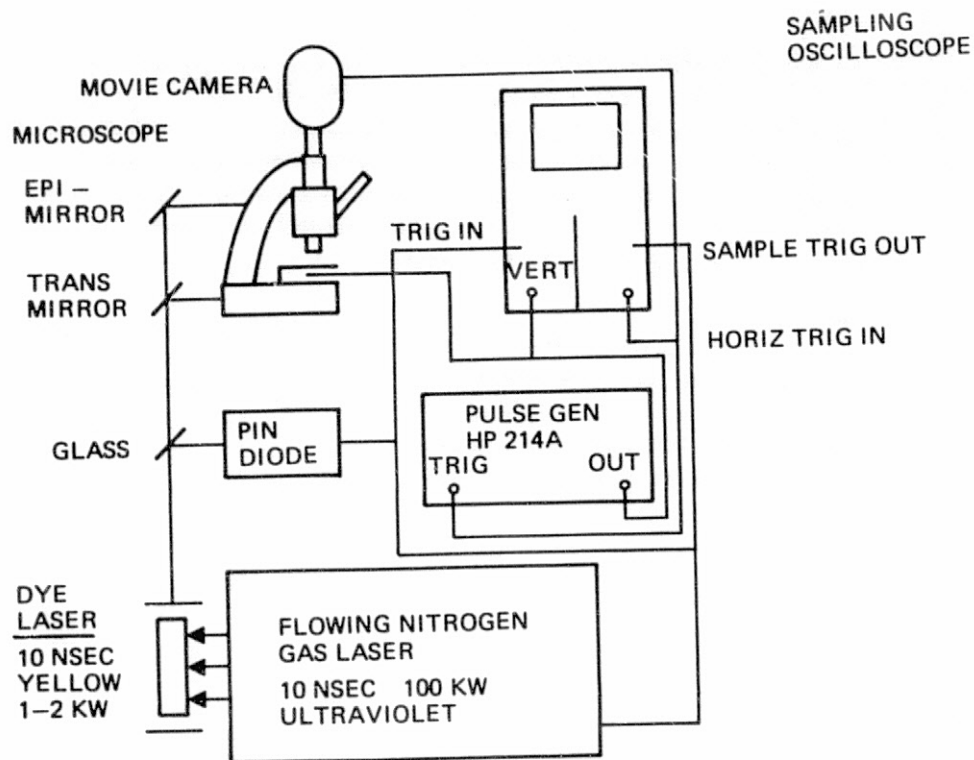


Figure 31. Block Diagram of the Optical Sampling System as it is Used for free bubble measurements

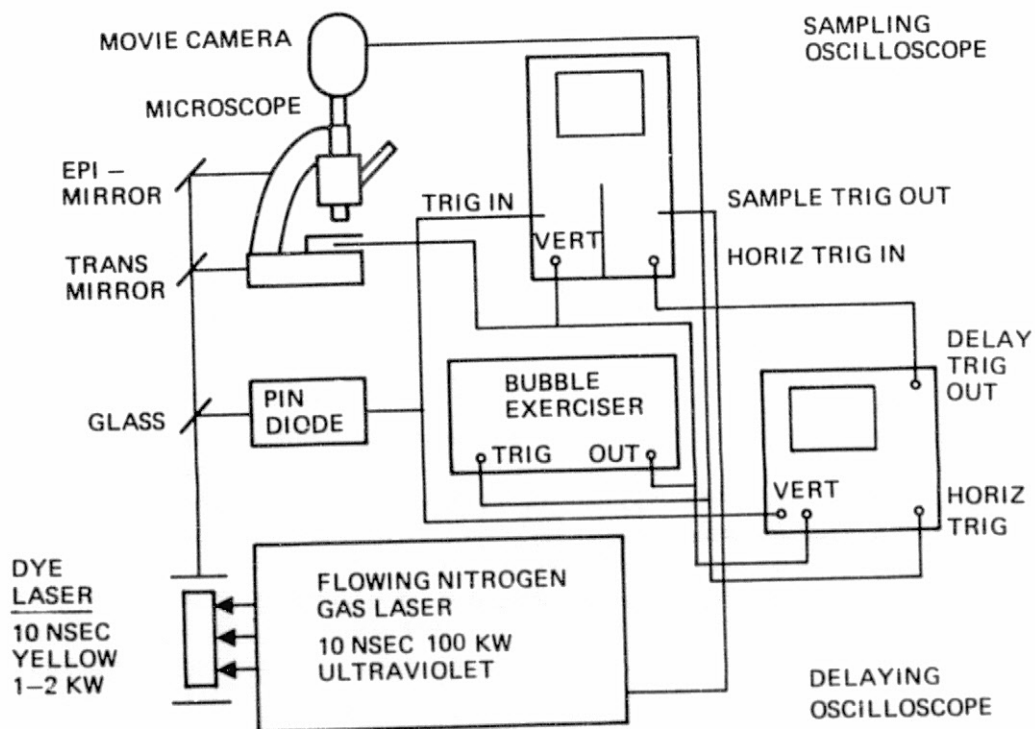


Figure 32. Block Diagram of the Optical Sampling System as it is Used for Device Studies

Device investigations require a slightly modified electronic arrangement. A block diagram with this change can be seen in Figure 32. The general timing pulse originating from the camera triggers the bubble exerciser which generates a burst of rotating fields. This timing pulse also triggers the auxilliary delay sweep oscilloscope on which the burst pattern is displayed. The delay sweep trigger is used to choose the desired clock cycle of the rotating fields and the time sweep through the cycle is provided by the sampling oscilloscope.

Special sample preparation is required to minimize the extreme interference pattern obtained when coherent light illuminates the symmetric repetitious structures typical of devices. Figure 33 is a schematic representation of device configurations that can be satisfactorily observed with coherent illumination. Epi-illumination is used for observing the bubble domains through the substrate. It is necessary to remove the epitaxial layer from the back side of the substrate to reduce light absorption and improve the contrast of the bubble image. The most satisfactory sample, illustrated on the left of Figure 33 has 150 to 200 Å layer of metallic reflector (e.g., chromium) labeled mirror A, directly on the surface of the garnet film. The usual SiO₂ spacer and the permalloy overlay is placed over the mirror. The coherent light reflects from the mirror and does not diffract; yet the device pattern can be seen through the mirror. In other words, the metallic reflector acts as a half-silvered mirror. Somewhat less satisfactory but still usable and more readily available is a modification, Mirror B, in which the reflector is placed over the permalloy structure as indicated on the right of Figure 33. Mirror A is especially effective for small devices whose circuit period is less than 20 μm . Mirror A was used for the devices

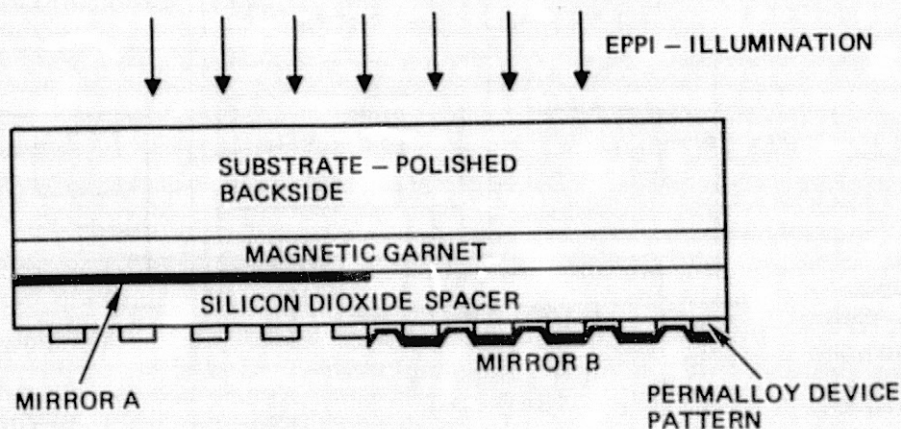


Figure 33. Schematic of Special Device Preparation

(16 μ m period detector test loops, see the previous section) for the study of the effects of hard suppression layers, while Mirror B was used for the devices (28 μ m period quad circuits) prepared for the study of the effects of crystal misorientation.

6.2 Effects of Hard Bubble Suppression Layers

It has been reported in Section 4 that various hard bubble suppression techniques have different effects on the dynamic properties of bubbles. For example, permalloy coating increases dynamic coercivity considerably. Ion-implantation causes local coercivity variations while top-capping does not. Most notable of all, however, is the elimination of velocity saturation by triple-layering. The objective of this subtask is to study the effects of multi-layering on material and device dynamic properties.

6.2.1 Radial Velocity Measurements. - The bubble expansion technique¹⁰ which was introduced along with the optical sampling technique⁹ provides a new method for measuring the radial wall velocity of bubble domains¹¹. This technique is very useful for determining saturation velocities. Thus, the bubble expansion technique was used to evaluate multilayered samples. The samples including an ion-implanted one selected for evaluation are listed in Table 19.

In the bubble expansion experiment, uniform expanding pulse fields were provided by a small pancake coil driven by an HP 214A pulse generator. The rise time of the field was 7 nsec. A field of sparsely distributed bubbles is photographed at various known times after the application of an expanding field pulse. The diameter is then measured from the photograph and the radius plotted as a function of the time at which the photograph was taken.

TABLE 19. SAMPLES USED FOR RADIAL WALL VELOCITY MEASUREMENTS

Sample Number	Composition	Hard Bubble Suppression Technique
4-25-21	YEuGa	Ion-Implanted
4-25-22 (D4)	YEuGa	Bottom-Capped
4-25-30 (D6)	YEuGa	Top-Capped
T17	YEuGa	Triple-Layered
T10	YSmGa	Triple-Layered

Figures 34 through 36 are representative of the results taken at three characteristic drive fields. Figure 34 is for the low drive region where a 12 Oe pulse is applied for 0.3 μ sec. It can be seen that the bubble expands to the new equilibrium size appropriate for the applied field (bias plus pulse field) before the end of the pulse. Figure 36 shows a bubble expanding in a 60 Oe pulse field. Exceptionally linear plots such as this one are characteristic of all the data at high pulse field amplitudes. Figure 35 is characteristic of some intermediate drive where an initial linear portion is observed followed by the exponential-like character of the lower drive region. A bubble does not remain round when expanded for a prolonged length of time at high drive fields¹⁰. Therefore, all measurements made here are limited to the time before this shape distortion occurs.

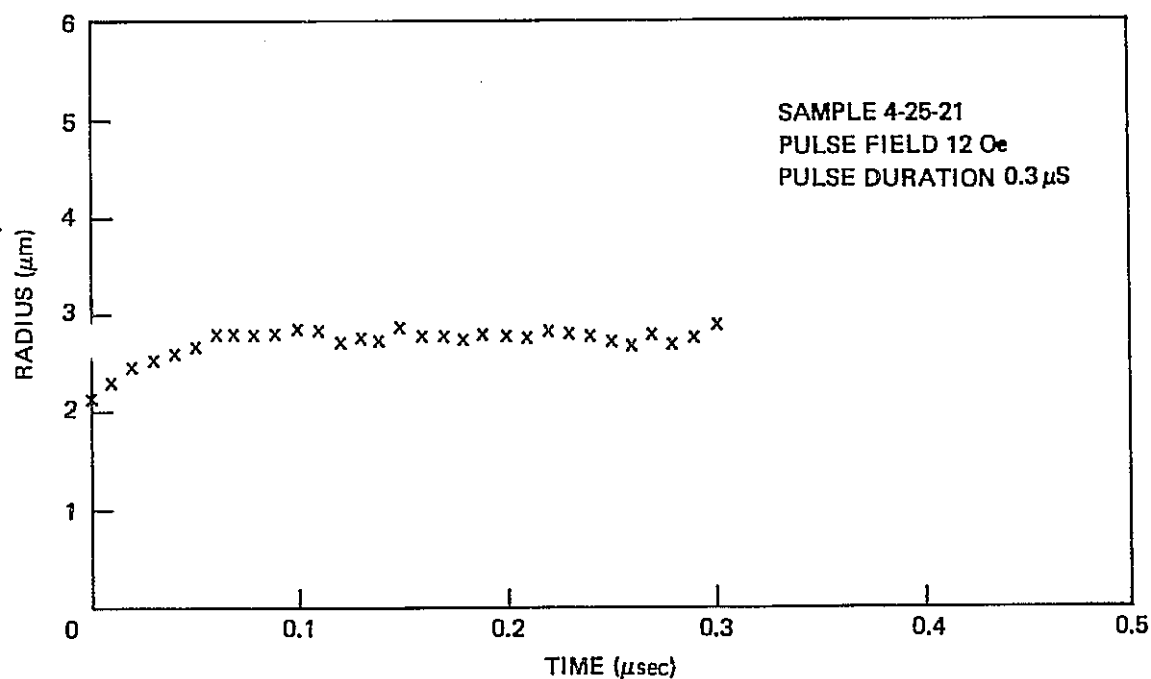


Figure 34. Bubble Radius as a Function of Time Typical of Low Drive Cases

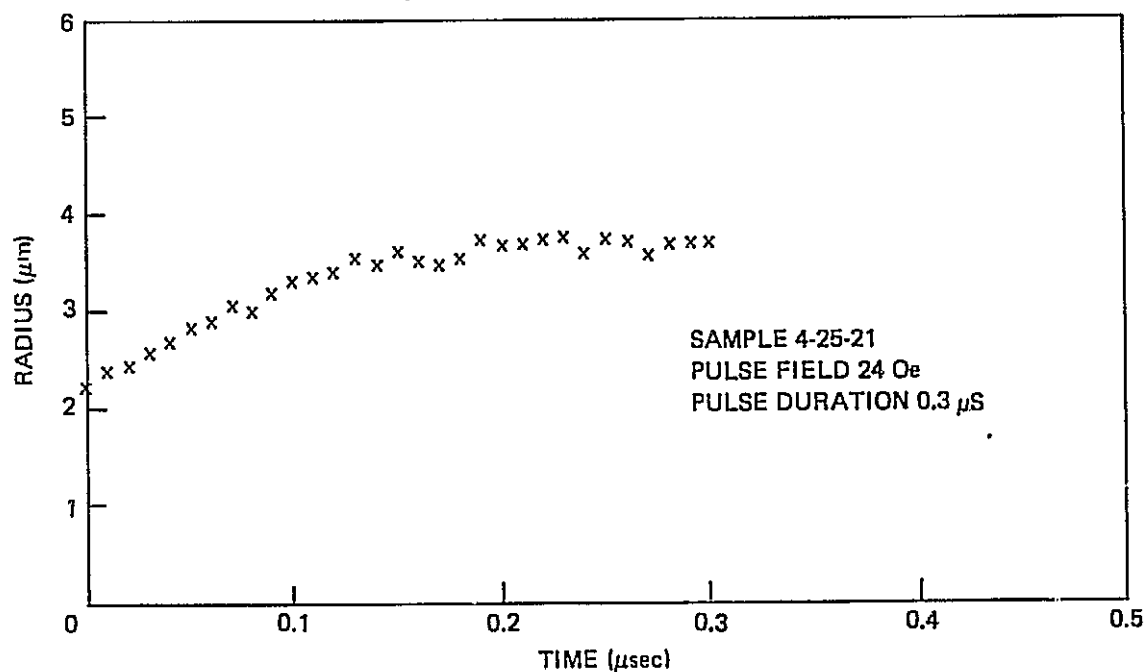


Figure 35. Bubble Radius as a Function of Time Typical of Intermediate Drive Cases

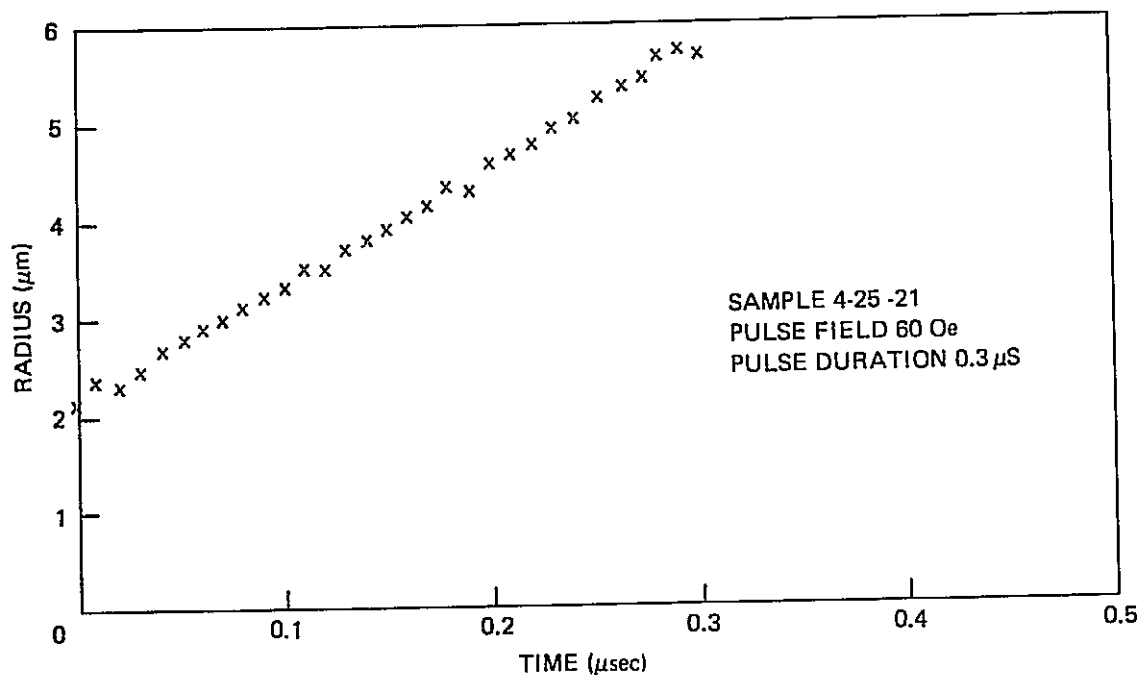


Figure 36. Bubble Radius as a Function of Time Typical of High Drive Cases

Radial velocity is the slope of the radius vs time plot. Figure 37 shows the observed radial velocity as a function of applied pulse field for Sample 4-25-21 (ion-implanted). Each bar indicates the range of two independent measurements (two bubbles). For fields ≥ 40 Oe, where the data is linear as in Figure 36, a least square straight line fit was made to the data and the calculated slope of this fit was used to represent the velocity. For pulse fields ≤ 40 Oe, data similar to Figures 34 and 35 was obtained where the linear portion of the radial velocity curve was limited. Thus, the accuracy of the calculated velocity becomes poor for pulse fields ≤ 15 Oe. In any case, the velocity is seen to saturate at 1000 ~1500 cm/sec.

Figures 38 through 41 show the results for the multilayered samples. It can be seen that all samples unambiguously exhibit velocity saturation. Samples D4, D6, and T17 which have the same composition as the ion-implanted sample and similar material parameters show more or less the same velocity profile as the ion-implanted sample. It should be noted that within the experimental error no appreciable differences have been observed for the reversal of the bias field for the double-layered samples (D4 and D6).

Bubble collapse measurements were made on Sample T10 to compare the two techniques and the results are shown in Figure 42. The number plotted indicates the number of bubbles that collapsed at the same time in the field of view for a given pulse field amplitude. The velocity was calculated using the collapse time τ and the initial and collapse diameters measured from the photographs. It can be seen that the saturation velocity agrees with that obtained from the bubble expansion technique fairly well.

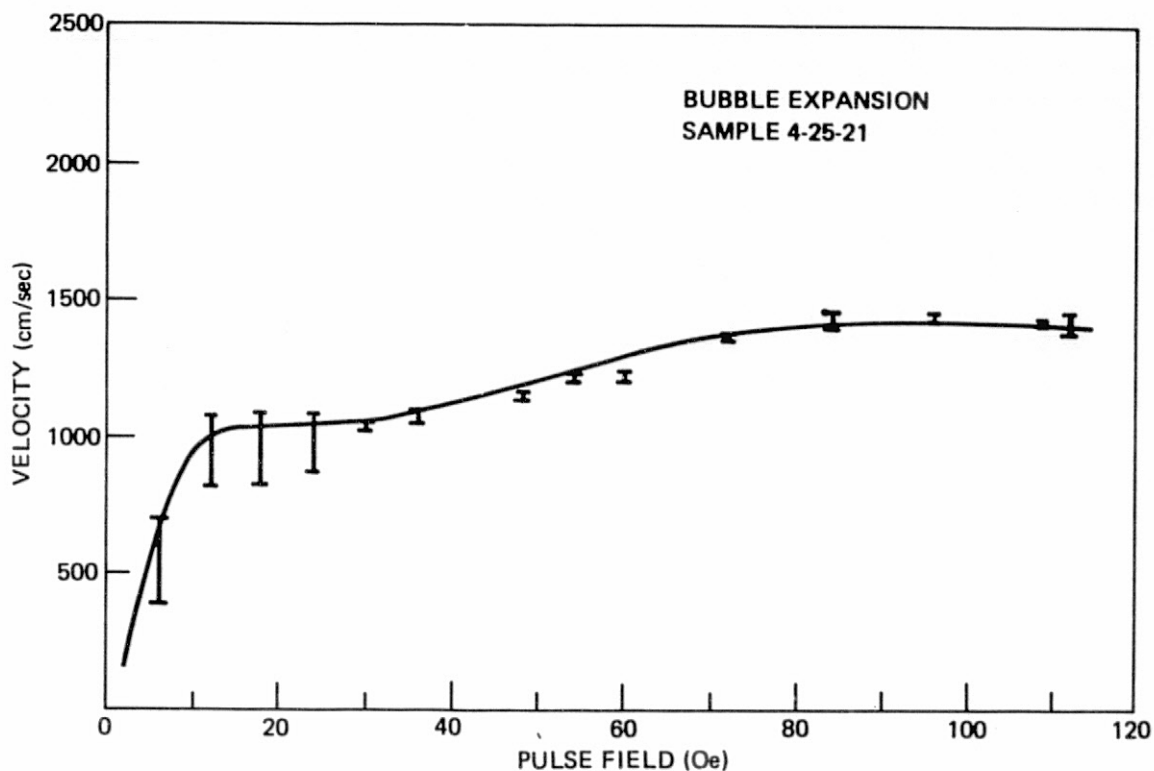


Figure 37. Radial Wall Velocity vs Pulse Field for Sample 4-25-21 (Ion-implanted)

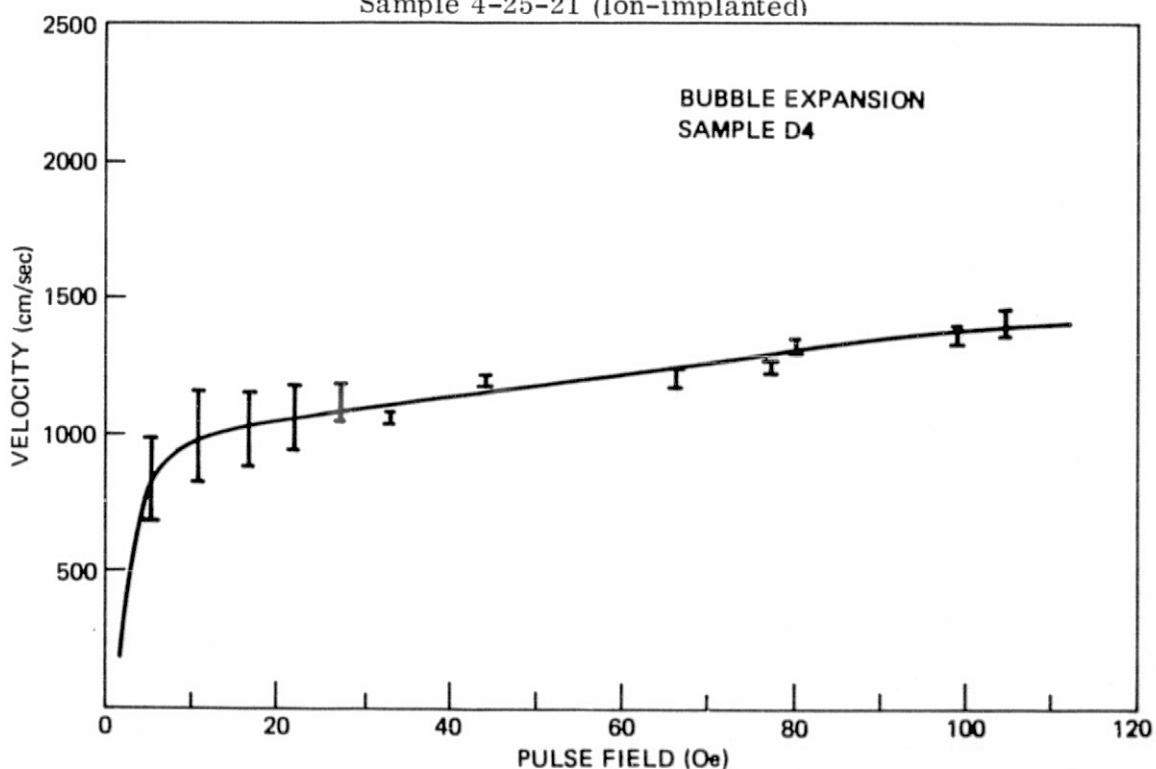


Figure 38. Radial Wall Velocity vs Pulse Field for Sample D4 (Bottom-capped)

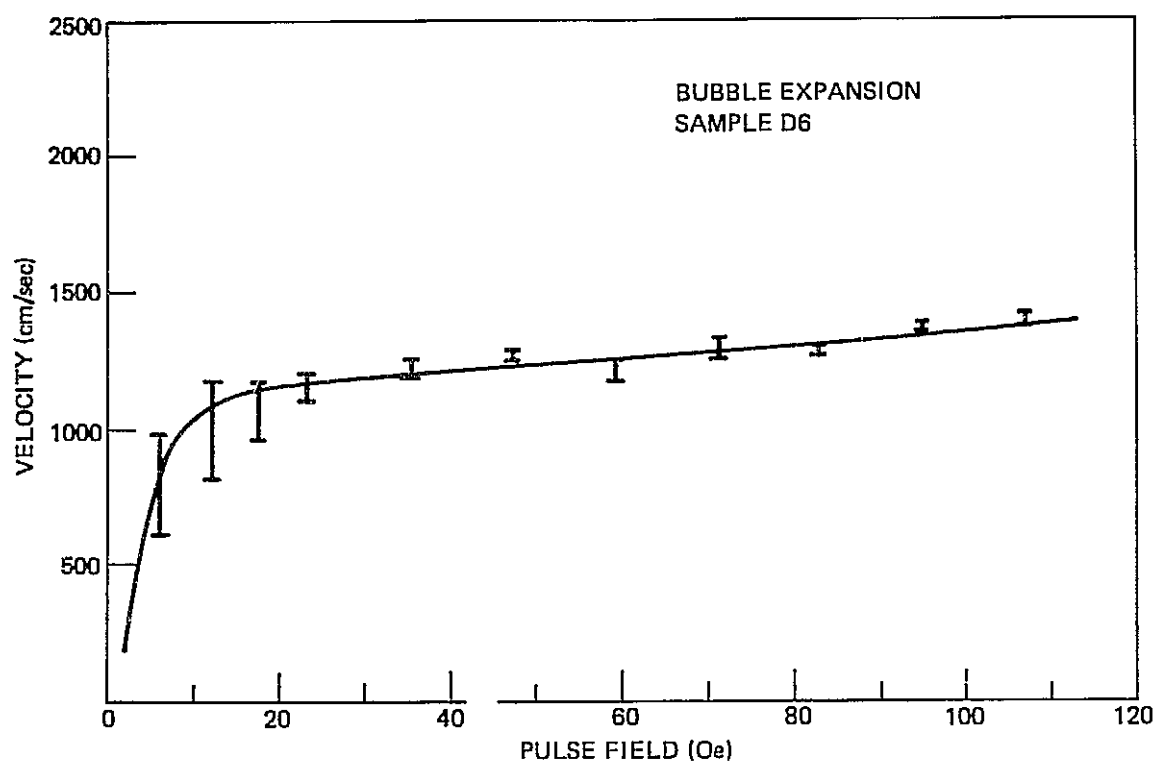


Figure 39. Radial Wall Velocity vs Pulse Field for Sample D6 (Top-capped)

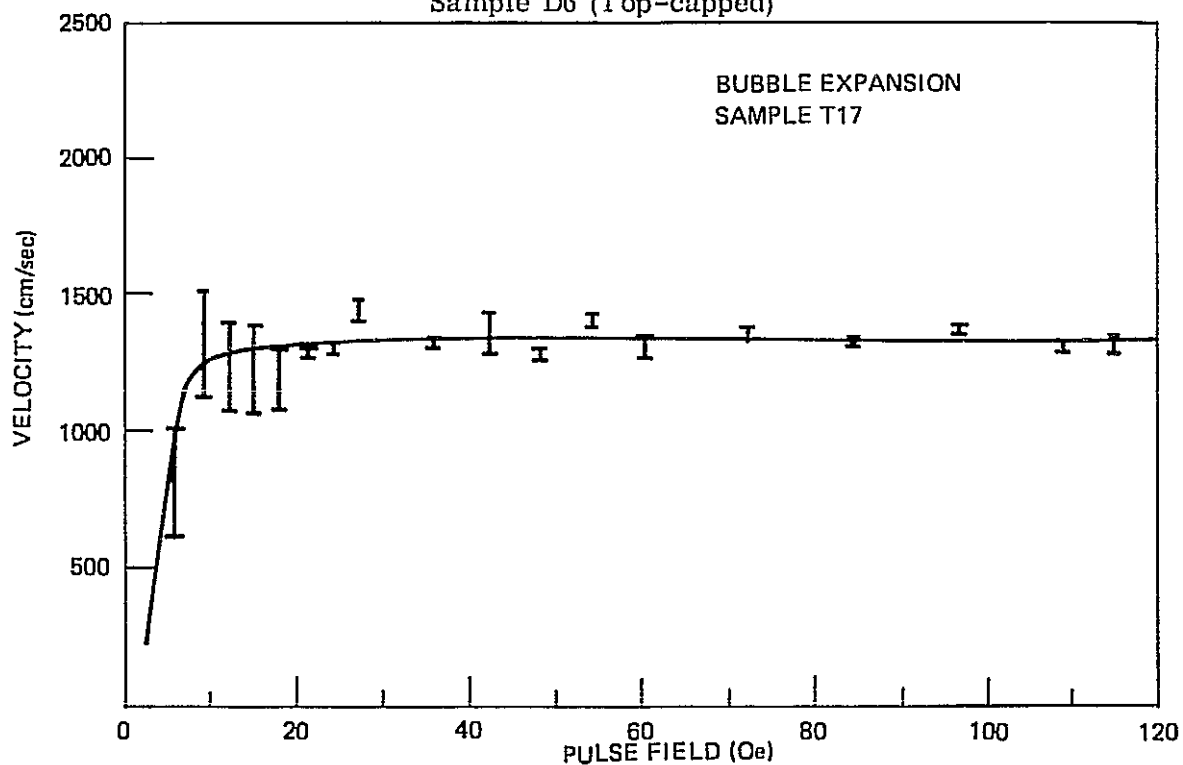


Figure 40. Radial Wall Velocity vs Pulse Field for Sample T17 (Triple-layered)

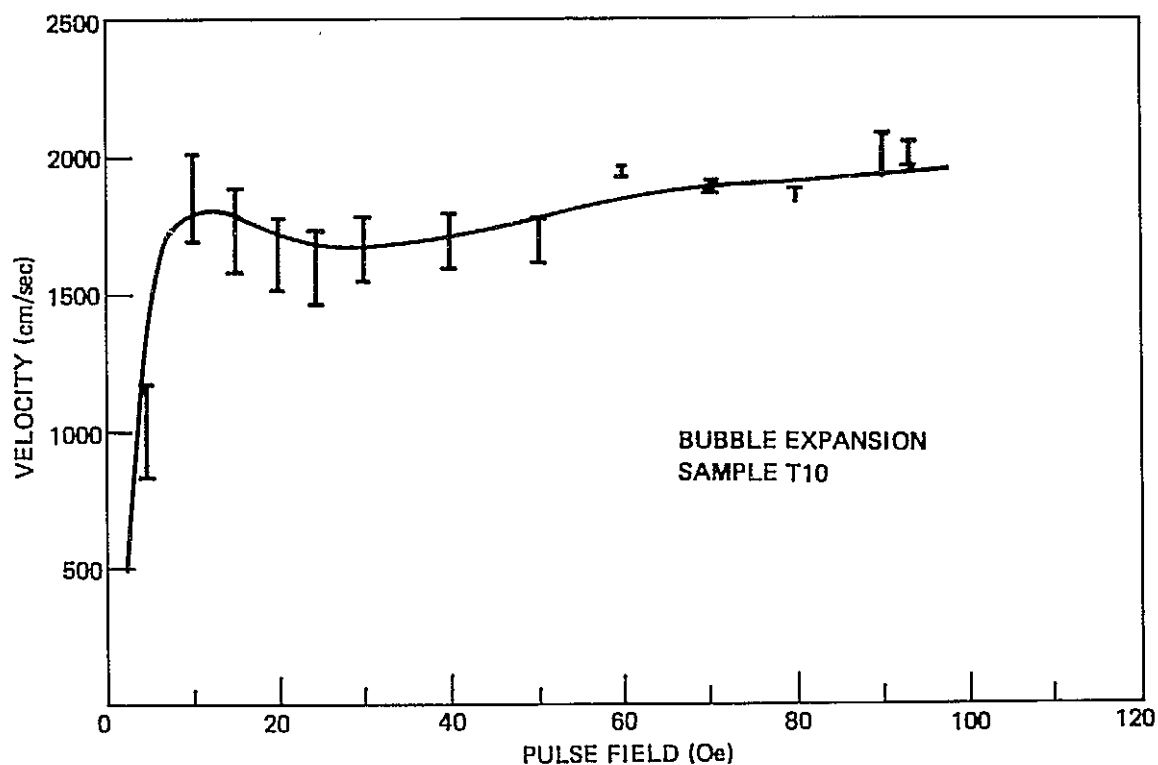


Figure 41. Radial Wall Velocity vs Pulse Field for Sample T10 (Triple-layered)

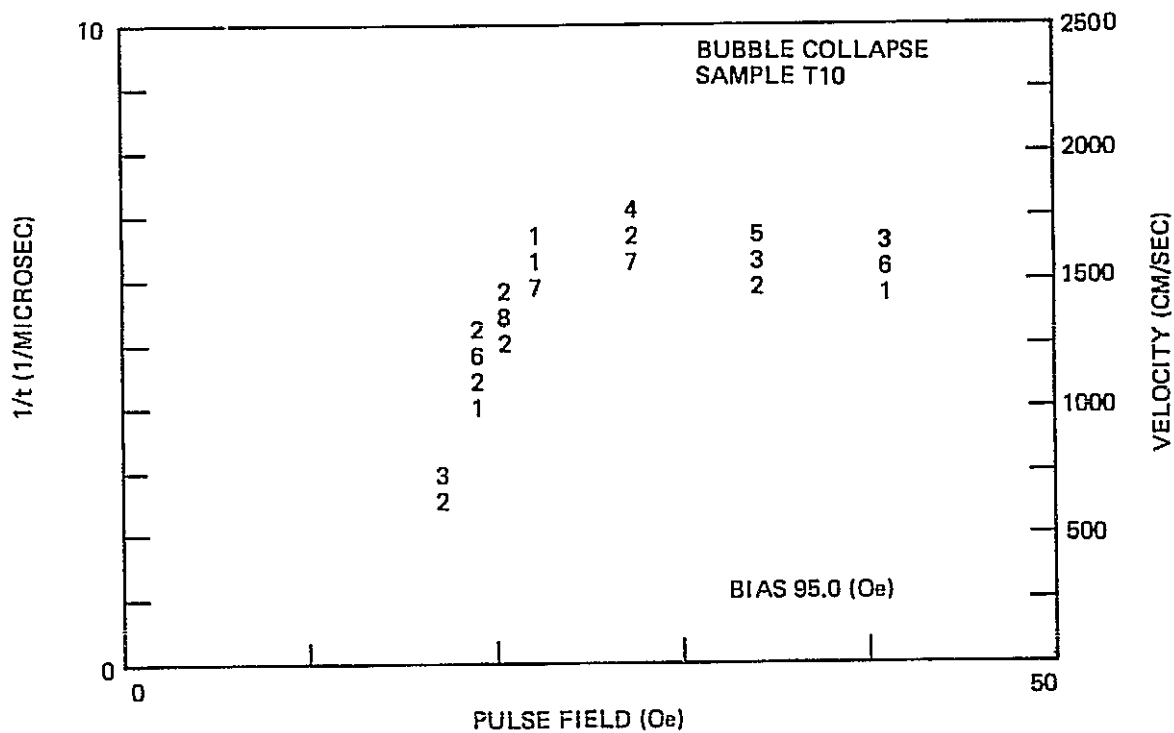


Figure 42. Bubble Collapse Data for Sample T10 (Triple-layered)

It is thus concluded that all the samples investigated exhibit velocity saturation in the bubble expansion measurement regardless of the surface treatments. This seems to contradict earlier observation (Figure 17) that the triple-layered sample did not show velocity saturation in bubble transport measurements. There are several possible explanations for the contradiction. First, the bubble transport measurements were made at low drive fields ($\Delta H \geq 10$ Oe), while the bubble expansion technique does not provide sufficient accuracy in this drive field range. It is thus possible that triple-layering does eliminate the Slonczewski breakdown¹² which is believed to be responsible for velocity saturation and dynamic conversion¹ and that the velocity saturation observed in the bubble expansion measurements is due to an entirely different mechanism such as the Walker breakdown¹³ which is calculated to take place at higher drive fields than the Slonczewski breakdown for the samples under consideration. A second possible explanation is related to the ballistic overshoot reported recently by Malozemoff and DeLuca¹⁴ on their transport measurements. Using high speed laser photography (similar to the technique used here) to measure bubble position as a direct function of time, they observed a large displacement after the gradient pulse turned off, with a relaxation time of several microseconds. The true velocity calculated from the distance the bubble traveled "during the pulse" exhibited a sharp saturation. Although the overshoot effect has not been examined for triple-layered films, it is conceivable that ballistic overshoots in these films are such that the bubble velocity calculated from the "final position" looks as if it were linear with drive field. * It thus seems important to undertake bubble transport measurements in triple-layered films using a high speed optical sampling technique to resolve these questions.

6.2.2 Device Characterization. - As was mentioned in Section 4, $16\mu\text{m}$ period detector test loops were fabricated on the ion-implanted and double-layered samples listed in Table 19 for Tasks 4 and 5. It was concluded from the data of the previous section that no appreciable differences due to the surface treatments were observed in the operating margin measurements. It became apparent that this was also the case in the device characterization study using the optical sampling microscope. The optical sampling microscope did, however, reveal some useful information on the dynamic behavior of bubble propagation in actual devices. That is, the bubble motion is very nonuniform, resulting in a large amount of variation in the domain wall velocity. Typically, the maximum velocity is as high as four times the average value for the T-bar structure and the ratio is nearly five for the chevron structure¹⁵.

* Triple layer samples have since been shown to exhibit large ballistic overshoot. The authors wish to thank A. P. Malozemoff and L. C. Deluca of the IBM Research Labs for supplying this information.

In summary, the optical sampling technique did not reveal any distinction in device performance between the different hard bubble suppression techniques. However, it provided basic knowledge of the dynamic behavior of bubble propagation in actual devices.

6.3 Effects of Crystal Orientation

It has been reported in the literature^{16, 17, 18} that a relatively small misorientation of the [111] axis relative to the substrate normal causes a considerably larger misorientation (~3 times) of the magnetic easy axis of the epitaxially grown magnetic garnet film. If a misoriented film was used for a field access bubble device, the rotating "in-plane" field would have an ac field component along the direction of the magnetic easy axis. Such an ac component would modulate the bias field and presumably result in device operating margin degradation. The effect of substrate misorientation on device operating margins was examined by Tocci, et al¹⁹ for a sample having a tilt angle (of the [111] axis) of 1.4 deg. Although the magnetic easy axis tilt was found to be as much as 4.75 deg, it did not have an adverse effect on the operating margins.

It was also found that substrate misorientation induces an in-plane anisotropy¹⁶. The induced in-plane anisotropy was in turn held responsible for a domain wall velocity anisotropy observed in a misoriented film⁸. The velocity anisotropy may have important implications in bubble devices, in particular, at high frequencies since it is the lower velocity that determines a limiting frequency. It may also be an important consideration even at moderate frequencies since the chevron stretcher detector commonly used in the devices may have considerably different domain stretch rates depending upon the orientation of the stretch direction relative to the velocity anisotropy axis.

It is the objective of this subtask to investigate the effects of substrate misorientation on material and device characteristics with the emphasis on the determination of an in-plane anisotropy and its effect on domain stretch at the detector.

Two samples have been chosen for this subtask which had been characterized by Tocci et al¹⁹ in their margin measurements. One sample has a tilt angle of 1.4 deg and the other 0 deg determined by x-ray Laue photography. The accuracy of the x-ray measurement is estimated to be ± 0.2 deg for the larger tilt and ± 0.4 deg for the smaller tilt. Both samples have nominal composition $\text{Y}_{2.62}\text{Sm}_{0.38}\text{Ga}_{1.15}\text{Fe}_{3.85}\text{O}_{12}$. The material parameters for these samples are

given in Table 20. The relationships between the surface normal and crystallographic axes are illustrated for the tilted sample in Figure 43 where θ_c is the tilt angle of the [111] axis from the surface normal and ϕ_c is the azimuthal angle of the tilt plane measured from the projected [112] direction in the sample plane.

TABLE 20. MATERIAL PARAMETERS FOR UNTILTED AND TILTED SAMPLES

Sample No.	θ_c (deg)	W (μm)	σ_w (erg/cm ²)	H ₀ (Oe)	4 π M (G)	h (μm)	λ (μm)
2-18-55	0	6.0	0.163	87.4	174	5.93	0.674
2-18-53	1.4	5.66	0.154	93.0	177	6.06	0.614

6.3.1 Radial Velocity Measurements. - The radial wall velocity of an expanding bubble in a misoriented sample was found to be anisotropic⁸. The portion of the wall moving perpendicular to the in-plane easy axis expands at a higher velocity than that moving parallel to it. Thus the bubble expansion technique is well suited for characterizing a misoriented sample since it can determine the velocity anisotropy and in-plane easy axis simultaneously. We have therefore used this technique to characterize our tilted sample.

In the bubble expansion experiment, as we have described in Para 6.2.1, a uniform pulse field is applied to expand a bubble and photographs are taken at various known times after the onset of the field pulse. Because of the in-plane anisotropy in the tilted sample, the shape of the original static bubble is elliptical with its major (minor) axis along the in-plane easy (hard) axis²⁰. However, the velocity anisotropy is such that the portion of the wall parallel to the in-plane easy axis expands at a higher velocity than does the portion perpendicular to it. Thus, the original minor axis of the elliptical bubble expands more rapidly than the major axis and soon overtakes it.

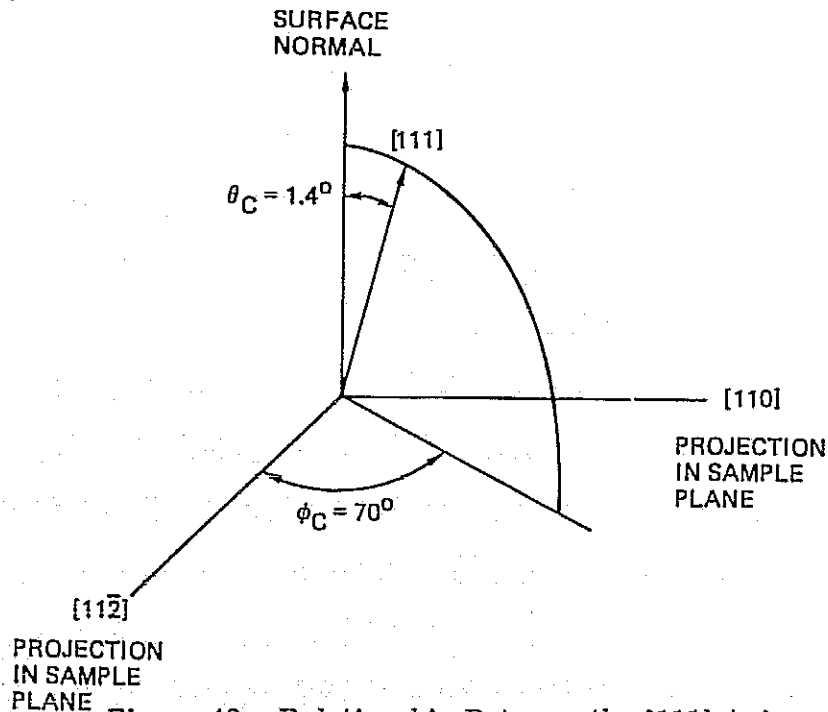


Figure 43. Relationship Between the [111] Axis, Surface Normal, and Crystallographic Axes

Figures 44 through 46 show the major and minor axes of the expanding bubble as a function of time after the onset of a $1\mu\text{sec}$ pulse for three characteristic pulse amplitudes. It can be seen from the figures that the original minor axis quickly overtakes the major axis as mentioned above. For low drive fields the bubble expands to new equilibrium size and therefore the major and minor axes interchange again in response to the static stability requirement (Figure 44). At high drive fields the velocities along both directions are constant with time resulting in linear plots such as those of Figure 46. This of course, implies velocity saturation. For intermediate drives initial linear portions are followed by nonlinear curves as seen from Figure 45.

The velocities along both directions were calculated from the initial slopes of the dimension plots and are plotted vs pulse field in Figure 47. It is seen that the velocity is quite anisotropic. The saturation velocity along the original major axis (in-plane easy axis) is 1200 cm/sec and that along the original minor axis (in-plane hard axis) is 2500 cm/sec. The ratio of the latter to the former is about 2:1.

The in-plane easy axis was found to lie at -40° from the $[11\bar{2}]$ direction defined in Figure 43. The axis relationships are illustrated in Figure 48 along with the orientation of the chevron stretchers of the quad circuits used in the device characterization. According to theory¹⁶, the in-plane easy axis lies at the angle ϕ_p that satisfies the relation

$$\phi_p = -\frac{1}{2} \phi_c \quad (1)$$

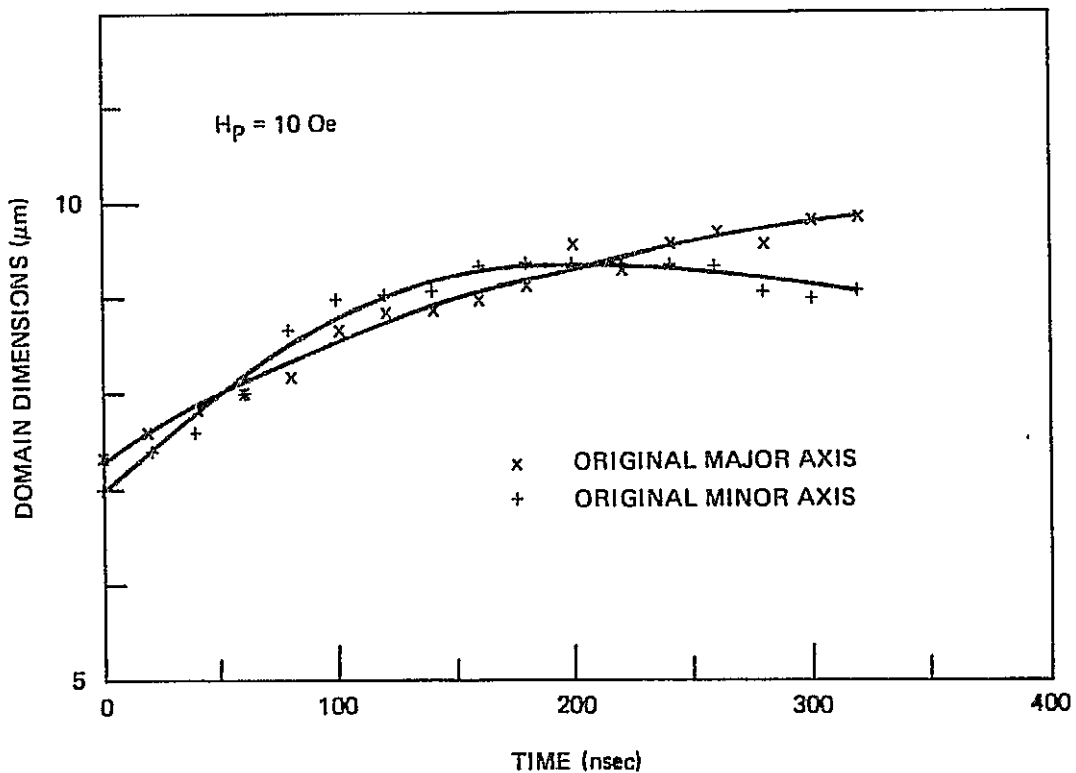


Figure 44. Domain Dimensions as a Function of Time for $H_p = 10 \text{ Oe}$

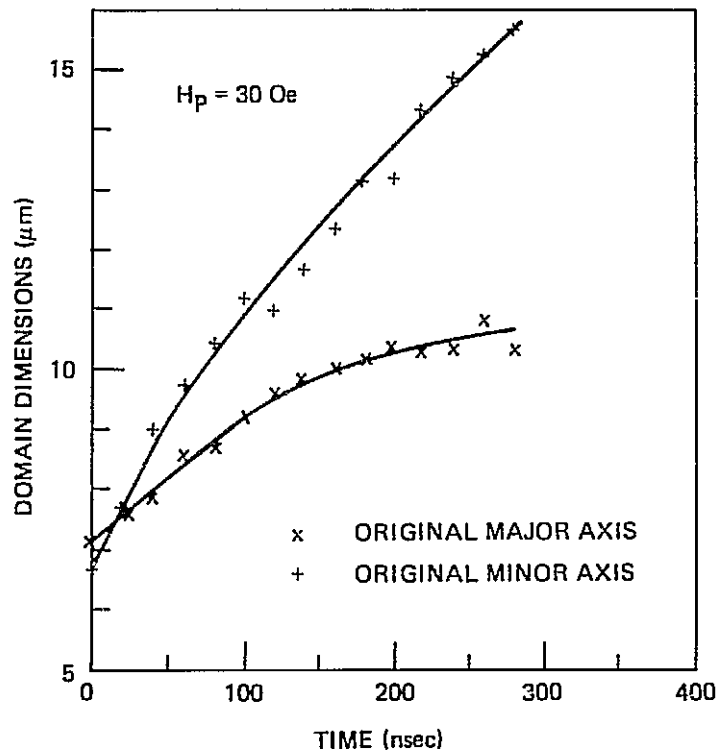


Figure 45. Domain Dimensions as a Function of Time for $H_p = 30 \text{ Oe}$

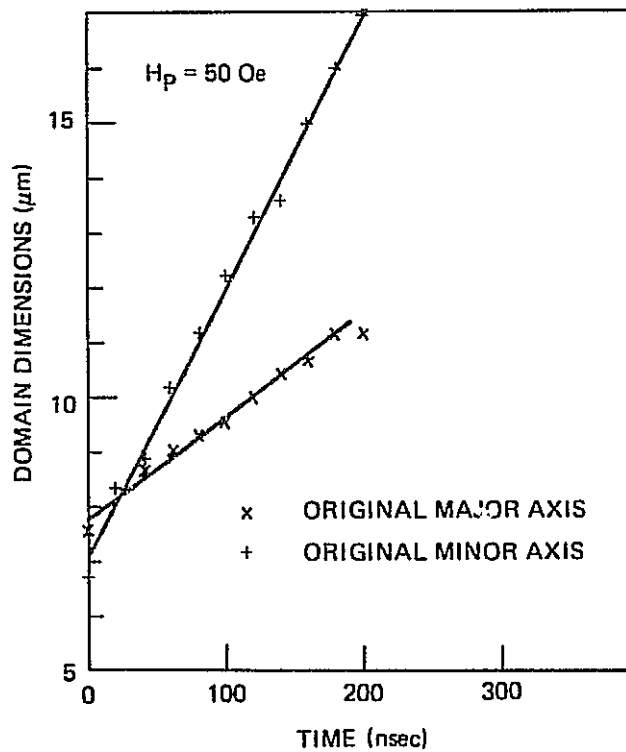


Figure 46. Domain Dimensions as a Function of Time for $H_p = 50 \text{ Oe}$

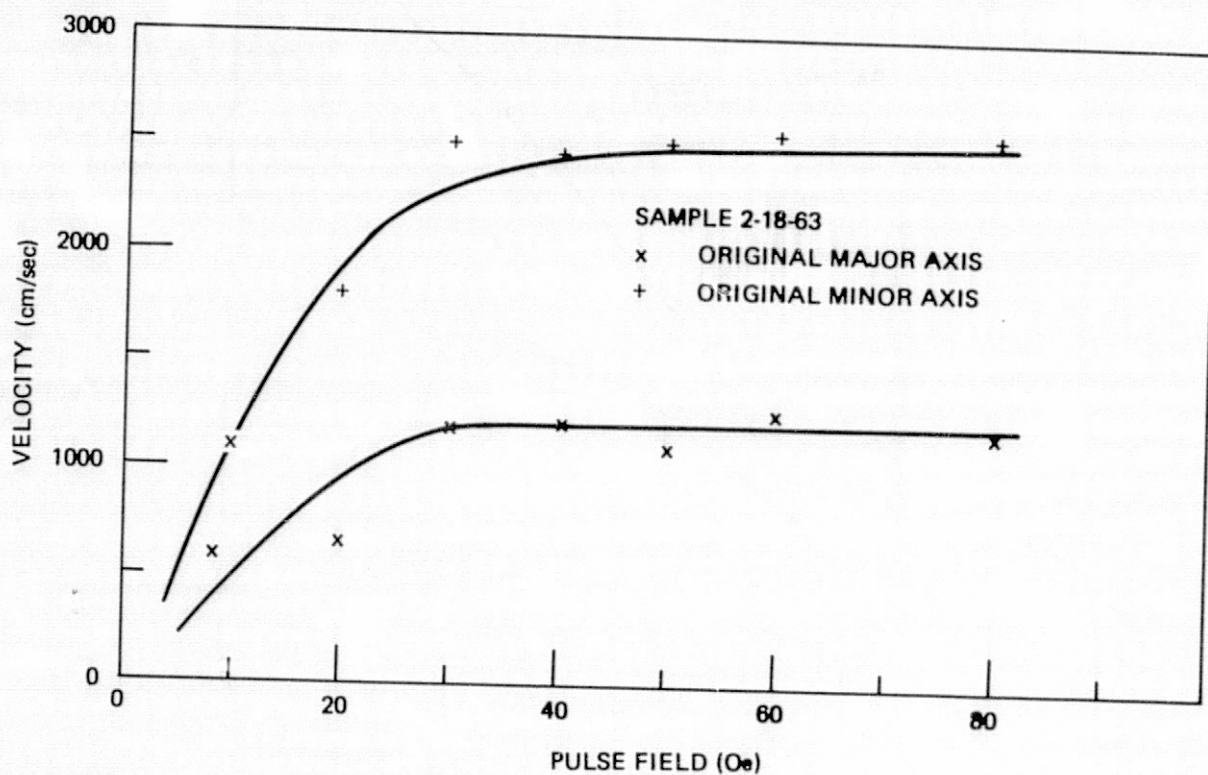


Figure 47. Radial Velocity of Bubble Wall as a Function of Pulse Field in Two Principal Directions

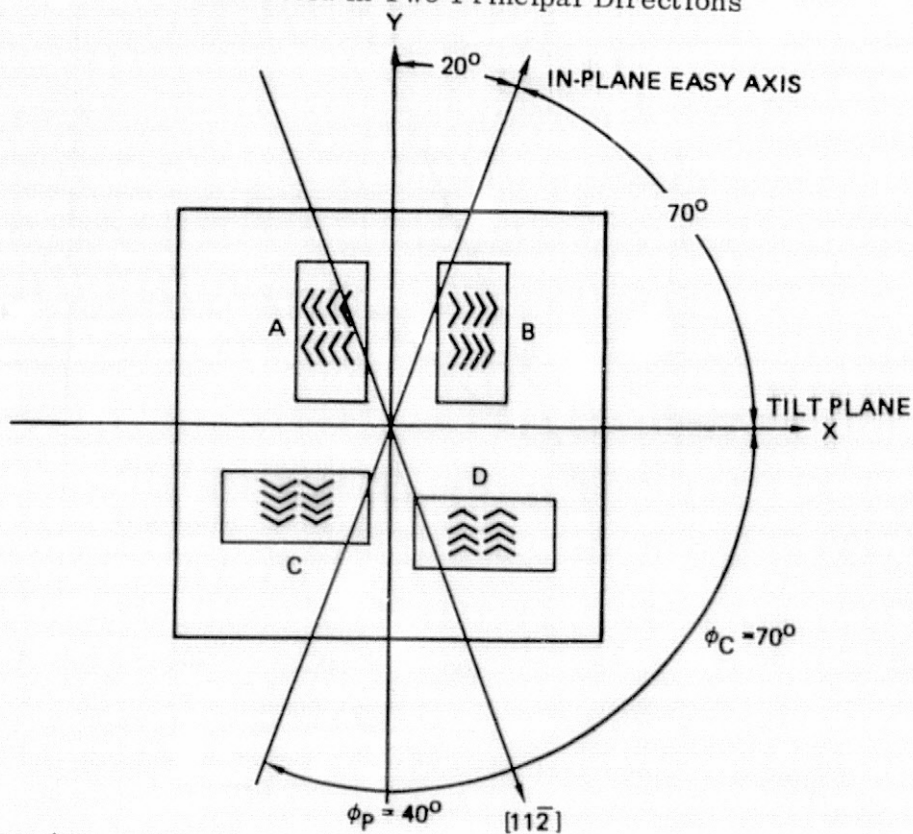


Figure 48. Orientation of the In-plane Easy Axis with Respect to the Tilt Plane, $[11\bar{2}]$ Axis, and Devices

The angle ϕ_c for the present sample was measured to be 70 deg. Thus, the theoretical value for ϕ_p is -35 deg in good agreement with the value -40 deg determined from the velocity anisotropy.

The above theory¹⁶ also predicts the in-plane anisotropy energy as

$$K_p = \frac{2\sqrt{2}}{3} (A - \frac{1}{2} B_2) \sin^2 \theta_c \quad (2)$$

where θ_c is the tilt angle of the [111] axis in radians and A and B_2 are growth anisotropy parameters. For YSmGa garnet films A and B_2 are roughly 4×10^4 ergs/cm³ and -3×10^4 ergs/cm³, respectively²¹; so K_p should be roughly 1250 ergs/cm³. On the other hand, Schlömann²² has recently given a theoretical consideration to the effect of in-plane anisotropy on the Slonczewski critical velocity¹², V_p . The result is shown in Figure 49, where the ordinate axis (V_p) is normalized with respect to the critical velocity with no in-plane anisotropy (V_{p0}) and $V_{p\perp}$ and $V_{p\parallel}$ imply the critical velocities in the direction perpendicular and parallel to the in-plane easy axis, respectively. For our sample $K_p/2\pi M_s^2 \sim 1$ and the theory predicts $V_{p\perp}/V_{p\parallel} \sim 2$ which agrees with the observed saturation velocity ratio. V_{p0} for our sample is calculated for the straight wall* to be ~1600 cm/sec assuming $\omega = 1.76$ rad/sec Oe, $A = 2 \times 10^{-7}$ erg/cm, and $K_u = 7400$ erg/cm³. The saturation velocity, V_0 , is then ~500 cm/sec on the basis of the Slonczewski formula¹² ($V_0 = 0.3 V_p$) or ~900 cm/sec on the basis of the Hagedorn formula ($V_0 = 0.55 V_p$). Thus the Hagedorn formula combined with Schlömann's theory provides the anisotropic saturation velocities in reasonable agreement with the observed ones.

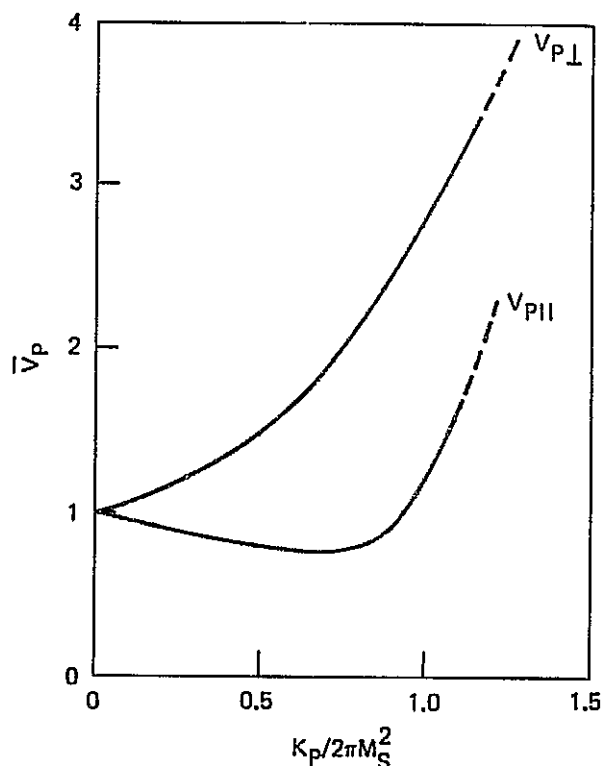


Figure 49. Slonczewski Critical Velocity as a Function of In-plane Anisotropy (After Schlömann²²)

* It is not clear how to take into account the curvature of an expanding bubble.

Since the saturation velocities in both directions are known, the saturation velocity in an arbitrary direction, $V_{s\alpha}$, can be given by

$$V_{s\alpha} = V_{s\parallel} + (V_{s\perp} - V_{s\parallel}) \sin^2 \alpha \quad (3)$$

where α is the angle between the direction of wall motion and the in-plane easy axis and $V_{s\parallel}$ and $V_{s\perp}$ are the saturation velocities in the direction parallel and perpendicular to the in-plane easy axis. In the present sample $V_{s\parallel} = 1200$ cm/sec and $V_{s\perp} = 2500$ cm/sec.

6.3.2 Device Characterization. - In the previous section we have shown that the domain wall velocity in the tilted sample is quite anisotropic. It is therefore expected that the domain stretch rate in the chevron stretcher will be quite different depending upon the orientation of the stretch direction relative to the in-plane easy axis. Although the effective drive field for domain stretch is not known, it is estimated to be sufficiently high to drive the wall to its saturation velocity. Let α be the angle between the domain stretch direction and the in-plane easy axis. Then from Eq (3) the domain stretch velocity for our sample is expected to be

$$V_{s\alpha} = 1200 + 1300 \sin^2 \alpha \quad (\text{cm/sec}) \quad (4)$$

Our sample has quad circuits A, B, C, and D as illustrated in Figure 48. The angle α is 70 deg for circuits A and B and 20 deg for C and D. Thus, the stretch velocities for circuits A, B and circuits C, D are estimated to be

$$V_{s70} \sim 2350 \text{ cm/sec (A, B)} \quad (5)$$

$$V_{s20} \sim 1350 \text{ cm/sec (C, D)}$$

Domain stretch velocities were measured for the quad circuits using the optical sampling microscope. Measurements were made at the chevron step stretcher sketched in Figure 50. At time $t = 0$ the rotating field is in the $+x$ direction as shown in Figure 50. The length of the strip domain (along y direction) was measured as a function of time at an operating frequency of 150 kHz. A typical result is shown in Figure 51. At $t \sim 2 \mu\text{sec}$ (108 deg) the domain reaches the stretcher and starts to expand. Expansion is more or less linear in time until t exceeds $4 \mu\text{sec}$ (216 deg). For $t \geq 4.5 \mu\text{sec}$ (245 deg) the domain starts to leave the left-hand side of the stretcher and the stretch velocity decreases. Bit patterns (consecutive or alternate) make little difference in the stretch rate presumably due to the short stretch.

It can be seen from Figure 51 that there is indeed a difference in the stretch velocity but the difference is not as large as expected from Eq (5). It should also be noted that both stretch velocities, 3250 cm/sec and 2450 cm/sec, are considerably higher than the saturation velocities given in Eq (5). Similar observations were experienced in the measurements of the velocity of bubble propagation in field access devices¹⁵; i.e., the bubble velocity can reach a value considerably higher than the theoretically predicted critical velocity or experimentally observed saturation velocity for free bubbles. We believe that this discrepancy is attributed to the presence of in-plane fields (rotating field plus permalloy stray field) in devices. It appears that the effect of in-plane fields is to increase the saturation velocity by ~ 1000 cm/sec in the present case.

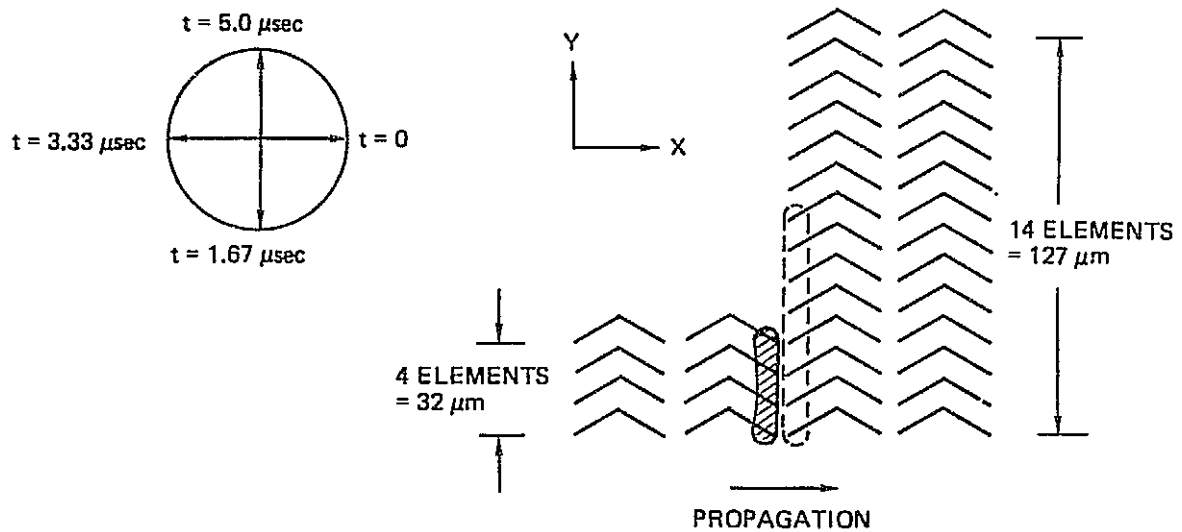


Figure 50. Chevron Step Stretcher Used in Device Study

Similar measurements were made on the untilted sample and a typical result is shown in Figure 52. It is immediately made apparent that there is also a considerable difference in the stretch velocity between the two orthogonal stretchers. An in-plane anisotropy is therefore suspected. Indeed, bubble expansion measurements showed a non-negligible velocity anisotropy. The saturation velocities along the two principal axes are 1350 cm/sec and 1900 cm/sec. It is seen from Figure 49 that $K_p/2\pi M_s^2 \sim 0.3$ would give rise to a velocity anisotropy of this order. $K_p/2\pi M_s^2 \sim 0.3$ in turn corresponds to a tilt angle of only ~ 0.4 deg. Since the accuracy of the x-ray measurement for a nearly 0 deg tilt is ± 0.4 deg, it is conceivable that the supposedly untilted sample does actually have a tilt of ~ 0.4 deg.

The in-plane easy axis was found to lie at 30 deg from the y axis defined in Figure 48. This means $\alpha = 60$ deg for circuits A and B and $\alpha = 30$ deg for C and D. Thus, we have

$$\begin{aligned} V_{s60} &\sim 1800 \text{ cm/sec (A, B)} \\ V_{s30} &\sim 1500 \text{ cm/sec (C, D).} \end{aligned} \tag{6}$$

Again the observed stretch velocities are much higher than these values. An increase of 800 ~ 900 cm/sec presumably due to in-plane fields in the circuit would bring these values close to the observed stretch velocities.

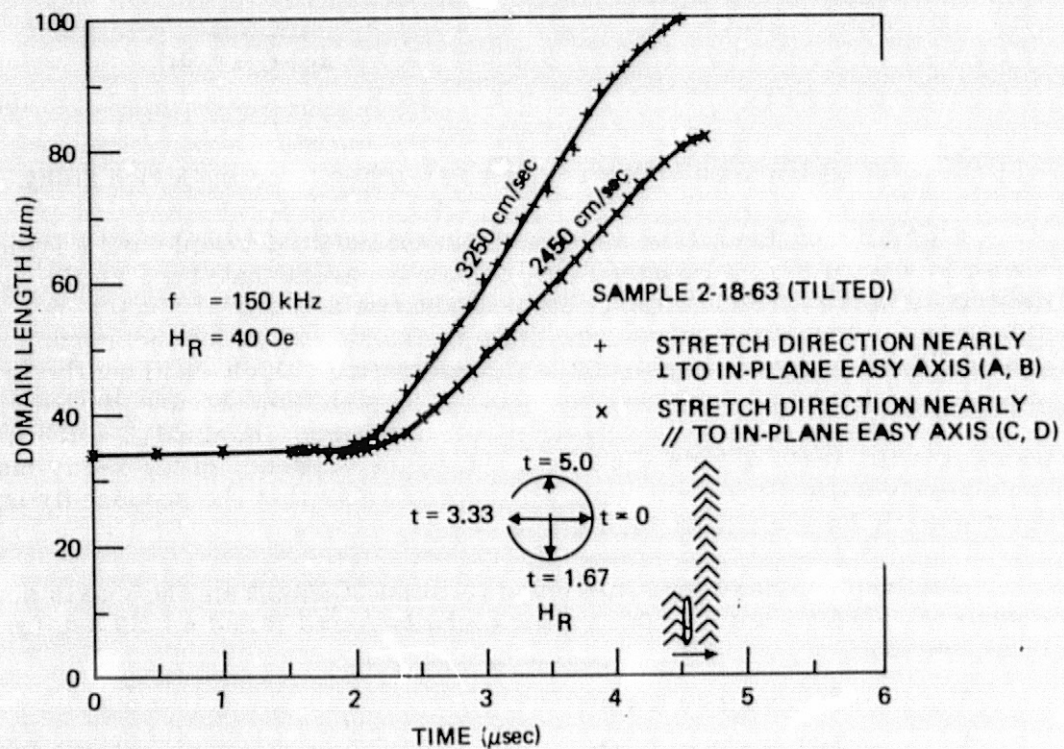


Figure 51. Domain Length as a Function of Time in the Chevron Step Stretcher for the Tilted Sample

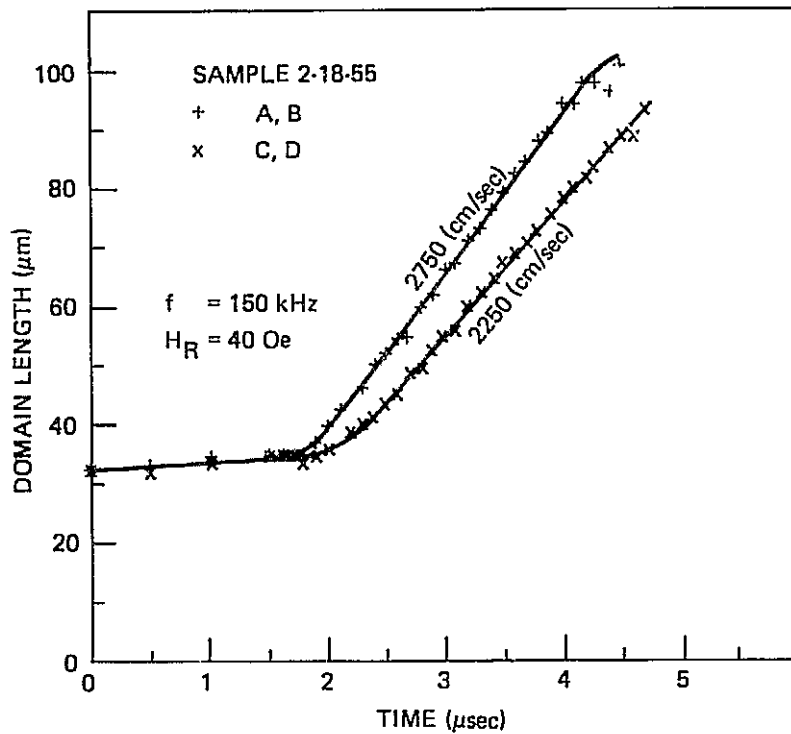


Figure 52. Domain Length as a Function of Time in the Chevron Step Stretcher for the Supposedly Untilted Sample

In summary, the substrate misorientation produced a considerable domain "stretch anisotropy" but this anisotropy is not as large as the saturation velocity anisotropy of a free bubble wall. This is probably attributable to in-plane fields present in the device. The effect of in-plane fields seems to be such that they increase saturation velocities in all directions thus diluting the anisotropy. Since the results obtained here are based on the limited number of samples, the intentional tilting of the [111] axis is not recommended until more data are accumulated and the effect of in-plane fields on domain wall motion is fully understood.

7. TASK 6 - MAGNETORESISTANCE DETECTOR STUDY

The two main goals of the detector study were to ensure that a system error rate of 10^{-8} could be met and that the output would be on the order of 5 mv over the -10°C to 60°C temperature range. As it turns out the latter requirement is the most restrictive of the two, hence considerable effort was spent investigating detector sensitivity as function of geometry and this work is reported in Section 7.2. Because the stretcher design plays an important role in determining whether consecutive or alternate bits can be propagated the problem of stretcher dynamics is considered in Section 7.1. There it is shown that by increasing the period the bit-bit interaction can be significantly reduced allowing consecutive bit operation over the entire operating margin. Finally in Section 7.3 the magnetoresistance and noise properties of the one and two-level chevron stretcher detectors are considered yielding further insight into the operation of the detectors and indicating how the detection electronics can be improved to reduce error rates.

The detector magnetoresistance study was fundamentally aimed at establishing how the permalloy geometry affected the detection process. No attempt has been made to determine what effect permalloy processing or garnet material parameters have on the sensitivity. Our feeling is that the material parameters are largely constrained by other device requirements and that aside from the magnetization most other parameters are relatively unimportant. Since the magnetization is related to the minimum drive field it is generally agreed that it should be chosen to be as small as possible consistent with other constraints. Hence studying the effect of garnet material parameters on the detection process does not appear to be fruitful. On the other hand, previous experience has clearly indicated that permalloy processing is very important from the standpoint of sensitivity and reproducibility. Also the effect of second order permalloy parameters such as in-plane anisotropy remain largely unknown. For this reason we regard the processing area as a candidate for future work. No attempt was made in this study to explore the effect of processing other than examining several runs made under supposedly similar conditions.

7.1 Stretcher Dynamics

Involved in any chevron stretcher design are considerations such as period, linewidth, angle, etc in connection with the basic chevron element itself. It has been the custom to integrate many of the input-output functions into a five chevron-track which either contains an in-line detector or a replicator connected to a guard-rail detector⁽²³⁾. 110 deg chevrons are almost universally employed in this track and also in the detector area itself. Because these elements play a role in determining the overall operating margin it is important to know which chevron designs are optimum and also compatible with the storage loop elements. For this reason a study was undertaken to determine how to optimize the basic chevrons. Also considered was the effect on margins of adding permalloy interconnections to the stretcher to form a one-level detector.

7.1.1 90 Deg vs 110 deg chevrons and stacking properties of the chevrons. The first experiments performed were designed to determine whether a 90 deg angle

chevron propagated better than one with a 110 deg angle. At the same time the dependence of the margin with stacking was determined. The results are summarized in Figure 53 and show almost no difference in margin with angle for 3 or more chevrons in the stack. The results did show, however, that as the number of chevrons in a stack is increased the locations in bias of the lower margin decreases about 2 to 3 Oe in going from 1 to 5 chevrons. Figure 54 shows that for a three chevron stack the margin overlap between chevron and T-bar elements is nearly optimum. Hence decreasing the number of stacked chevron elements does not appear advantageous. Increasing the number from three to five will make little difference in the margin overlap. According to our measurements the largest shift in location of the lower margin occurs in going from one to three chevrons.

7.1.2 Period and mobility dependence of chevron margins. - The optimum period for a chevron track is determined by a compromise between bit-bit interactions at the low end and mobility limitations at the high end. In order to resolve this problem consecutive and alternate bit margins were taken electronically on a series of gold interconnected detectors (two level) for which the period was varied from 24 to 40 microns. Forward-reverse propagation through the detector in a region of 12 chevrons was used to obtain the data at 100 kHz shown in Figure 55. The detection limit is defined as the point at which any bit in a series of five fails to elongate while transversing the detector. The effect may clearly be seen electronically as a "hole" in the output pattern produced by the detector. Figure 55 shows that for a given drive field as the period is increased a point is reached where the mobility is no longer great enough to maintain propagation with a wide margin. It also shows that the bit-bit interaction

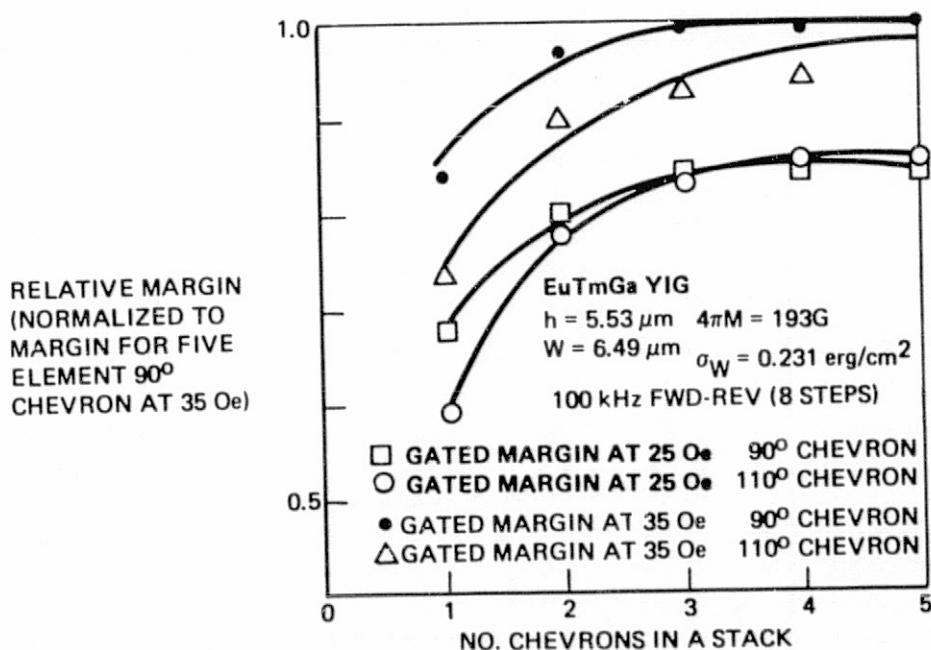


Figure 53. Stacking Dependence of the 100 kHz Margin for 90 Deg and 110 Deg Chevrons

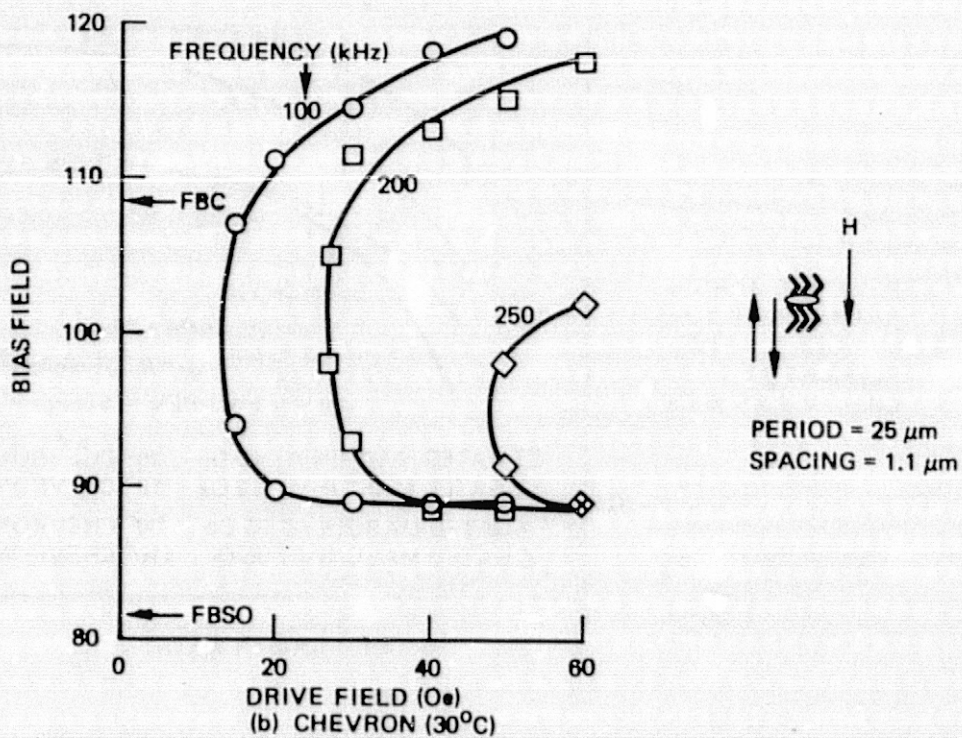
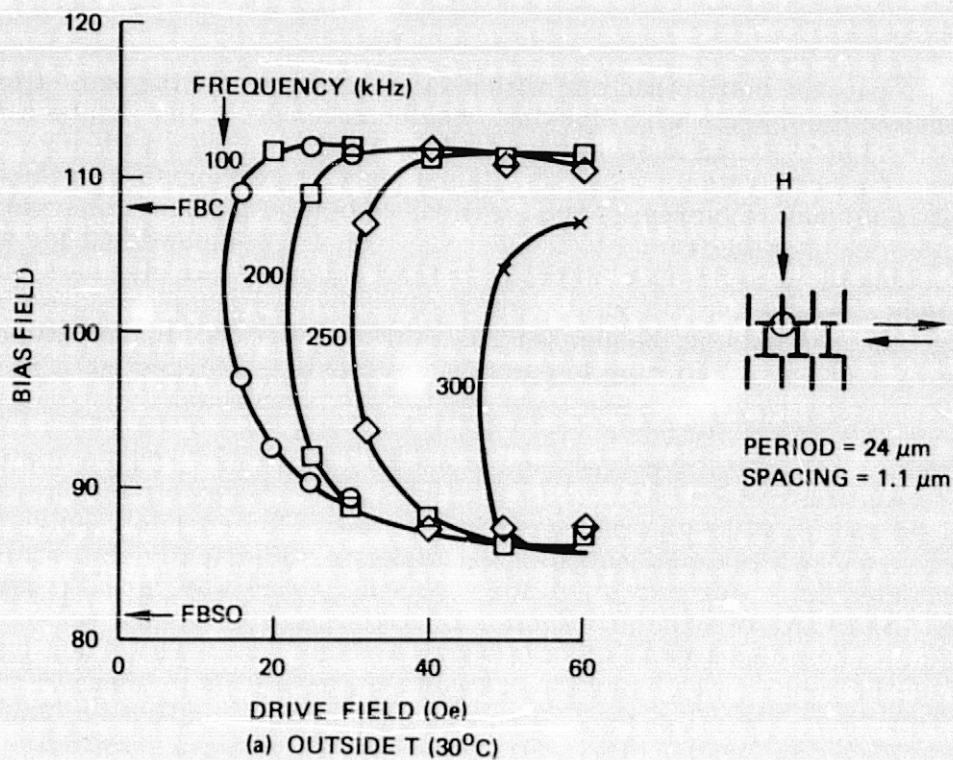


Figure 54. Overlap of Chevron and T-Bar Margins as a Function of Frequency

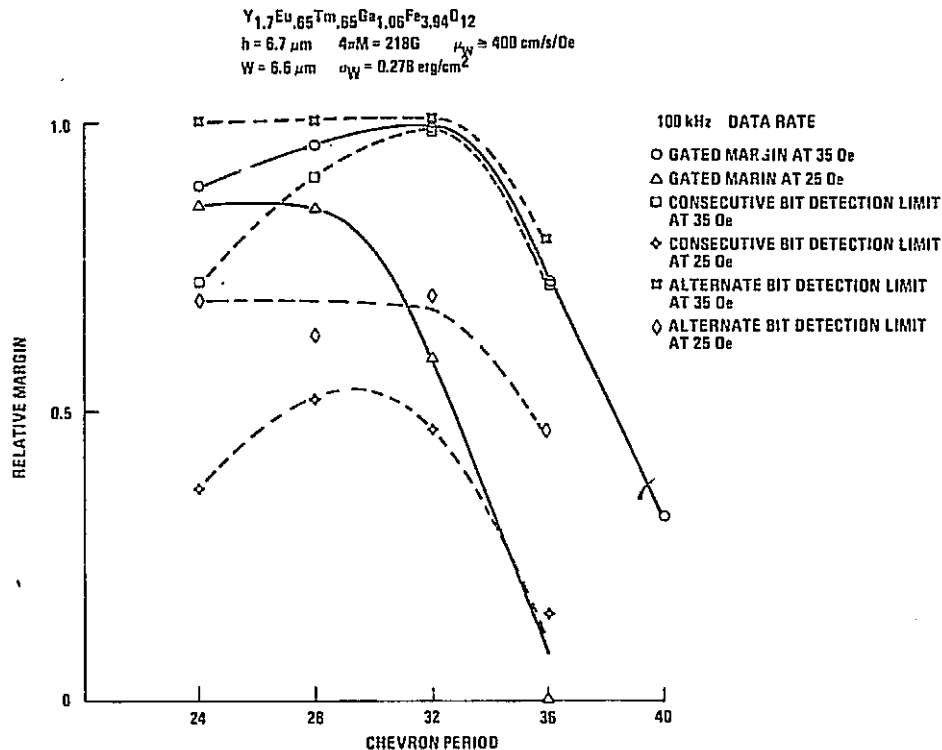


Figure 55. Chevron Period Dependence of Margins for
 $Y_{1.7}Eu_{0.65}Tm_{0.65}Ga_{1.06}Fe_{3.94}O_{12}$ (Wall Mobility $\approx 400 \text{ cm/s/Oe}$)

becomes important at shorter periods. This is reflected in the consecutive bit detection limits which lie below the corresponding alternate bit margins for short periods. If detection is to be achieved over the whole operating margin for consecutive bits at 35 Oe drive field the period should be about 32 microns for this sample. If only alternate bit detection is desired over what normally would be the consecutive bit operating range then a period anywhere between 24 and 32 microns would be satisfactory. At 25 Oe drive field the mobility limit sets in at about a 28 micron period. At this field value because the bubble field is a significant fraction of the drive field it tends to dominate in this regime with the result that both consecutive and alternate bit detection limits fall below the margin limit.

Clearly these results are mobility dependent and therefore to obtain some feeling for this aspect the previous measurements were repeated in connection with a much higher mobility sample. The results, which are summarized in Figure 56, confirm more or less what is expected. At 35 Oe drive field the consecutive bit margin and detection limit coincide. At 25 Oe bit-bit interactions cause the detection limit to fall slightly below the margin limit. Because the mobility is so much higher here the maximum operating period can be 40 microns with no margin narrowing. At higher frequencies this clearly will not be the case and therefore in designing the detector one should choose the shortest possible period consistent with the operating frequency and consecutive bit detection (if so desired). Figures 55 and 56 allow one to make reasonable estimates of optimum period designs. Figures 55 and 56 indicate that the maximum allowable velocities in the two samples considered differ by about a factor of 1.25 even though the mobilities differ by more than a factor of 3. Since the peak

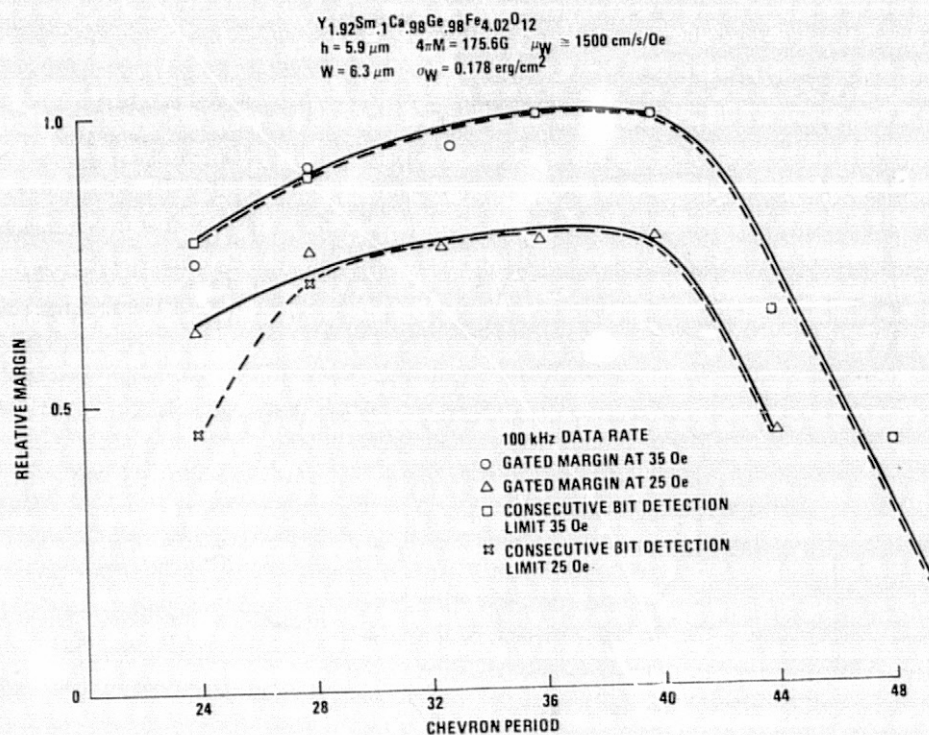


Figure 56. Chevron Period Dependence of Margins for $Y_{1.92}Sm_{0.1}Ca_{0.98}Ge_{0.98}Fe_{4.02}O_{12}$ (Wall Mobility $\approx 1500 \text{ cm/s/Oe}$)

velocity in a chevron pattern is about a factor of 5 greater than the average velocity, if the critical velocity for a material is known an estimate of the maximum allowable period for a given operating frequency can be made. Such information on the critical velocity is just now becoming available for various materials. The measurements presented in Figures 55 and 56 are based upon chevrons for which the gap and separation were equal to $1.8 \mu m$ which was one-half the linewidth.

7.1.3 Permalloy interconnect geometry and margins. - It is possible that the permalloy interconnection scheme used in a one-level detector will affect its output and also its margins. In Section 7.2 the former aspect is considered and here we present margin data on closed propagation loops each containing a different one-level detector geometry. The layouts of the loops were made all the same so that if differences were found it could be attributed to the effect of the detector geometry. The test pattern is shown in Figure 57 and was also used in the study presented in Section 7.2 on detector sensitivity. Several different geometries were chosen based upon existing designs or variations which were likely to improve the output (end shorted) or the propagation margin (fine interconnection, horizontal). The half end shorted version was selected based upon past experience in connection with a two-level version which could be used to generate an output limited to 180° of field rotation (useful for multiplexing). The data taken on these patterns are summarized in Table 21 and is the result of making measurements on two different samples from the same wafer. For comparison purposes, results for a two-level detector are also included. The effect of adding the permalloy appears to be reflected by an increase in the minimum drive field of the one-level patterns. We expect the minimum drive to be around 15 Oe at

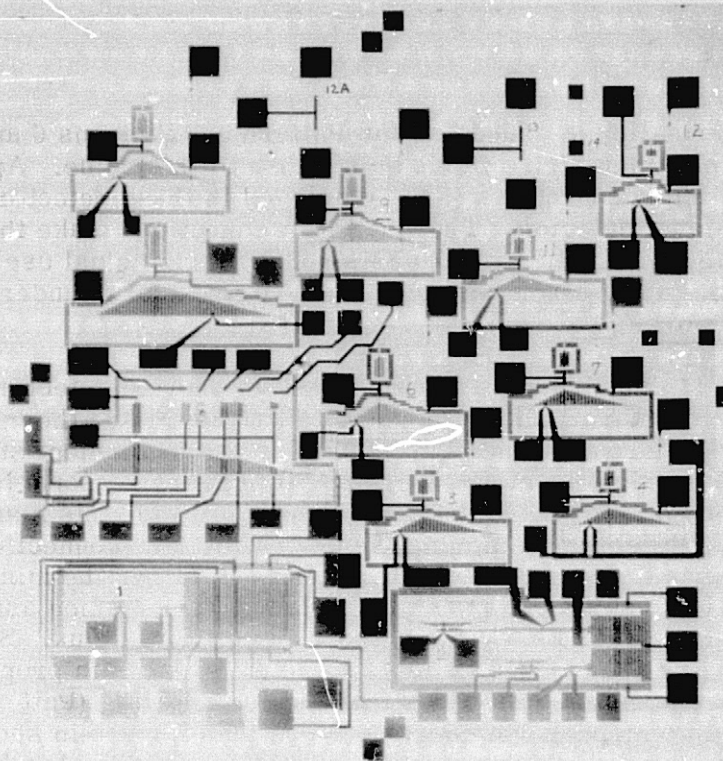


Figure 57. Detector Interconnection Test Patterns

TABLE 21. GEOMETRY DEPENDENCE OF MARGINS (28 μ m PERIOD) GAP = 1.5 μ m,
NORMAL SEPARATION = 1.8 μ m (WIDE SEPARATION = 3.6 μ m),
ANGLE = 110° (UNLESS SPECIFIED)

GEOMETRY	PATTERN	DESCRIPTION	150 kHz MIN DRIVE FIELD	150 kHz MARGIN AT 40 Oe
	5	Two Level (Conductor Shorted at Chevron Ends)	15 Oe	15 Oe
	11	One Level 18 Element Set-in Shorted	20 Oe	14.5–15.5 Oe
	8	One Level 36 Element Set-in Shorted	20 Oe	17 Oe
	3	One Level 18 Element End Short	20 Oe	16–17 Oe
	9	One Level 18 Element End Short Wide Separation	20 Oe	12.5–13.5 Oe
	6	One Level 18 Element Horizontal Wide Separation	15 Oe	13 Oe
	12	One Level 9 Element Set-in Shorted	19 Oe	15.5 Oe
	10	One Level 18 Element End Short 90° Chevron	17 Oe	16.5 Oe
	4	One Level 18 Element End Short Fine Interconnect	15 Oe	16.5 Oe
	7	One Level 18 Element Half End Shorted	16 Oe	16 Oe

150 kHz when no permalloy is added, as for Pattern 5. Patterns 6 and 4 not unexpectedly have minimum drive fields quite close to this value. Apparently this is because of the fine interconnections ($\leq 1\mu$) employed in these detectors rendering them similar to the two-level detector. The fine interconnections make them extremely difficult to fabricate consistently and for this reason their actual use in a device design is not contemplated. They have, however, been very useful in understanding how the one-level detector works.

Patterns 12, 11, and 8 form a series of set-in shorted detectors of increasing length. The minimum drive fields for them is about 20 Oe and the margins about 15.5 Oe. The slight increase in margin in going to the 36 element stretcher (Pattern 8) is probably not significant and therefore it appears reasonable to conclude that stretcher length does not affect the margins significantly for this many chevrons in a stack. The slight modification of moving the permalloy interconnections out to the chevron ends (Pattern 3) seems to have little effect on either the minimum drive field or margins. This is somewhat unexpected in view of the common assumption that at the ends the permalloy tends to act like a short circuit to the flux. Stroboscopic microscopy, however, does indeed indicate some differences in propagation behavior due to interconnect placement. One finds that for end shorting (Pattern 3) the strip is distorted in a wavelike manner considerably more than for set-in shorting (Patterns 8, 11, 12). The phase-lag in both cases is comparable so that the low bias failure modes are probably not much different. At high bias the strip contracts to a bubble and the transition from the chevron end to its center is probably the limiting step. In this case the end shorting (Pattern 3) would appear more desirable because the shorts are farther away from the bubble when they form competing poles for the field orientation along the detector. Hence the similarity of the end and set-in shorted results is really quite reasonable.

Patterns 6 and 9 are different from all the others in that the vertical separation between chevrons is one linewidth ($3.6\mu\text{m}$). Clearly this has a detrimental effect on the margins. It is believed that for this case that the larger separation between chevrons causes the bubble to collapse prematurely as it passes from one chevron to another during propagation at high bias. The effect is analogous to simply having large gaps in a T-bar circuit. The result is that the upper portion of the margin is lost as is found experimentally here.

The margin results for Pattern 10 indicate that the 90 deg chevron works as well as the 110 deg chevron when end shorted (Pattern 3) which offers a cross-check on the data taken in Para 7.1.1. The slightly lower drive field found for this case seems to be a real effect. Stroboscopic measurements indicate the wave-like distortion of the strip is more severe for the 90 deg chevron (Pattern 10) than for the 110 deg chevron (Patterns 8, 11, 12). This is not reflected in the margin data of Table 21, however.

The overall impression left by these results is that as long as the chevron-to-chevron separation is on the order of the gaps the interconnection scheme has little effect on the continuous propagation margins. This presumes that stripout near the ends of the chevron stack is prevented by zig-zagging out to the desired configuration from the stack ends as was done here. Hence the choice of interconnection scheme depends more on output sensitivity than margin considerations.

7.2 Detector Sensitivity

In order to establish which of the one and two-level detectors considered in connection with the stretcher dynamics study had the highest output sensitivity several different experiments were performed in which chevron period, permalloy thickness, and permalloy to garnet spacing were varied. The interconnection geometry was also varied. The results indicate that from the output standpoint the two-level detector is superior to the one level. The reason for this is explained in some detail in Para 7.3.3. The two-level detector, however, has the disadvantage that it requires several processing steps and a critical alignment. The critical alignment makes the use of this detector impractical for bubble circuits of 24 μm period or smaller from the process yield standpoint. On the other hand one expects to find some similarities between the one and two-level detectors and therefore optimization of the two-level detector should yield some information useful to one-level detector design. For this reason experiments were performed initially on the two-level detectors.

7.2.1 90 Deg vs 110 Deg Chevrons - Two-Level Detector. The results of Section 7.1.1 revealed that the 90 deg chevron has as good a margin as the 110 deg chevron. Accordingly measurements were made on the output at 30 and 40 Oe drive field for these detectors. Because the results for the 90 deg and 110 deg detectors turned out to be so similar further measurements were made to determine the basic drive field dependence of the magnetoresistance. It was expected that the flatter 110 deg chevron should magnetize more rapidly with drive field (along the propagation direction). In fact the reverse was true. The results are shown in Figures 58 and 59 along with waveform insets showing the measured outputs at 30 and 40 Oe drive field. The location in drive field of the low to high magnetoresistance transition differs by only 3 Oe for the two cases and hence not much difference in output behavior is expected since the form of the two curves is similar. This conclusion is further enhanced by the all bubble magnetoresistance curves showing about the same drive field shift from the no bubble state.

It has been pointed out that the output of the two-level detector shows a pronounced after-effect particularly at low drive fields⁽²⁴⁾. A comparison of this effect for the 90 and 110 deg chevron at a drive field of 24 Oe also appears in Figures 58 and 59. The motivation for making both no bubble and all bubble measurements is discussed in Section 4.3.4 in detail. The fact that these measurements were made at different bias fields is unimportant as we are looking for differences between the results for the 90 deg and 110 deg detectors. These results do seem to indicate that the 110 deg chevron suffers more from the after-effect. At higher drive fields (30 to 40 Oe), however, the after-effect becomes small and slight differences in signal waveform become more important. From the output standpoint it appears that there is very little difference between detectors based upon 90 and 110 deg chevrons. This is confirmed in Para 7.2.3 for the one-level version.

7.2.2 Period dependence of the output. - While the drive field at which the transition from the low to high magnetoresistance state occurs shows little sensitivity to chevron angle it does show sensitivity to period or equivalently to the demagnetizing factor along the propagation direction. Figure 60 shows a series of magnetoresistance curves for two-level detectors with varying period. As is discussed in Para 7.3.4 (noise study) and is also suggested by Figures 58 and 59 the low drive field output of a two-level detector may be regarded as the difference in voltage between a curve such as

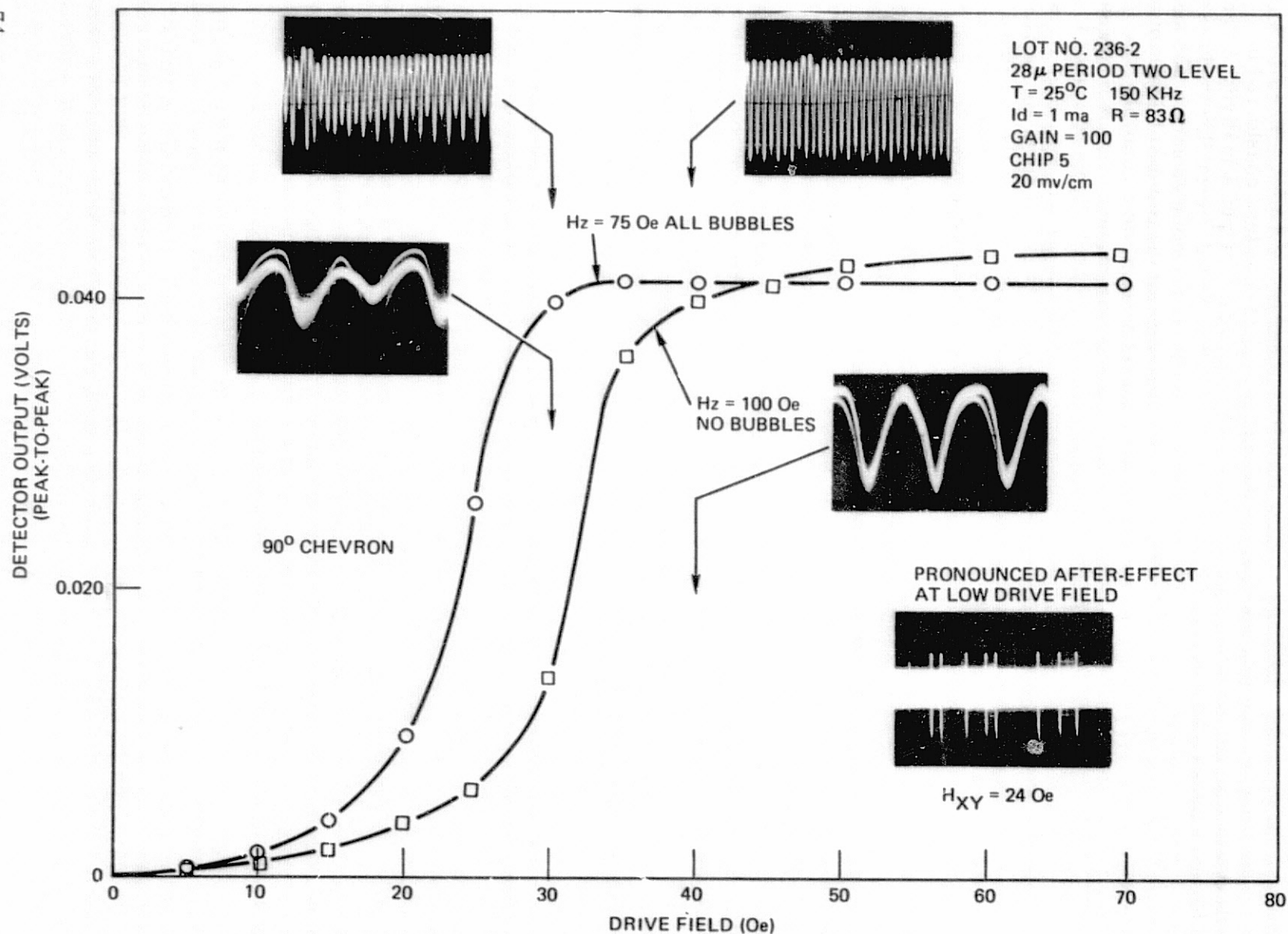


Figure 58. Magnetoresistance Results for Two-level 90 Deg Chevron Detector

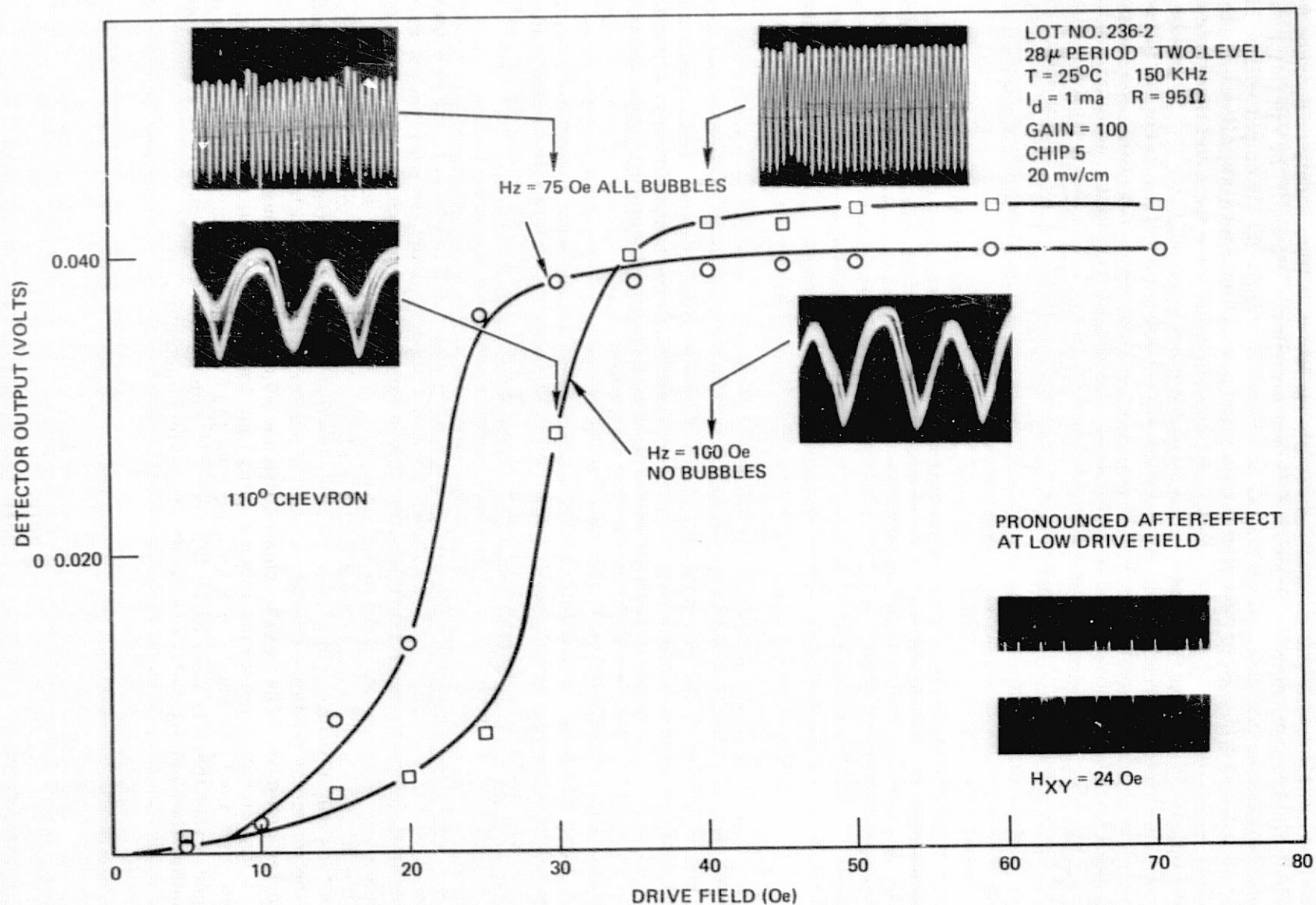


Figure 59. Magnetoresistance Results for Two-level 110 Deg Chevron Detector

is shown in Figure 60 and one shifted about 8 Oe lower in field. This is because the bubble field is equivalent to about an 8 Oe uniform field. Hence if the operating drive field happens to fall in the steep region of a curve in Figure 60 the output will be high. Conversely varying the period (and possibly the permalloy thickness) allows one to adjust where the transition lies relative to the operating drive field and therefore enables one to control the output. Figure 61 supplies proof that this can indeed be done. Shown in a plot of the detector output for 25 and 35 Oe drive fields versus period. Referring back to Figure 60 confirms just what is found experimentally. As the period is increased the transition moves to the left becoming at first more optimum for the detector output and then less optimum as it passes to the left of the operating drive field. The output apparently does not go down at the larger periods because the net detector resistance is still increasing linearly with period. The output at 35 Oe for any given period is higher than that at 25 Oe because the drive field is higher and therefore lies closer to the transition.

The results of Figure 61 shows that the effective demagnetizing factor controlling the location of the transition as well as its steepness vary almost linearly with period. This is what one would expect based upon an ellipsoidal model for a chevron. For an ellipsoid or a thin bar it is known that the dependence of the demagnetizing factor is t/L where t is the thickness and L the length. A similar dependence is expected for the chevron where the period becomes analogous to the bar length. The permalloy cannot be made too thin, however, or else it will be saturated by the drive field possibly resulting in a reduced margin and higher minimum drive fields. If a low transition drive field is required the combination of period (subject to mobility limitations) and thickness can be used to avoid this situation. Hence, it is fairly clear how one should go about optimizing the two-level detector. There is some question as to whether the active and dummy detectors will be properly matched in the transition region due to slight differences in demagnetizing factor associated with processing. Also the control of the drive field becomes more important when operating near or at the transition. This problem can be avoided, however, by operating at a drive field slightly below the transition allowing the bubble to switch the detector into the higher magnetoresistance state only in the active detector. Operation in this way may allow one to eliminate a permalloy dummy in favor of a resistor which further reduces the noise produced by the detectors as is discussed in Para 7.3.5 (noise study).

7.2.3 90 vs 110 Deg Chevrons - One Level Detector. - In Para 7.2.4 it is shown that at 36 Oe drive field 90 and 110 deg chevrons produce about the same output in a one-level detector. To further confirm this a series of output measurements were made on 18 element 90 and 110 deg detectors. The results are summarized in Table 22 and show that at normal drive fields the 90 and 110 deg set-in shorted detector has less output probably due to its lower resistance. Measurements were also made of the magnetoresistance characteristics of Pattern 11 and a 36 element set-in shorted detector. The results showed that the 90 deg chevron magnetizes in the $\phi = 0$ deg direction somewhat more rapidly than its 110 deg counterpart which was also confirmed previously in connection with the two-level measurements. Hence it appears that there is very little difference in output between 90 and 110 deg chevrons whether they are part of a two-level or one-level detector.

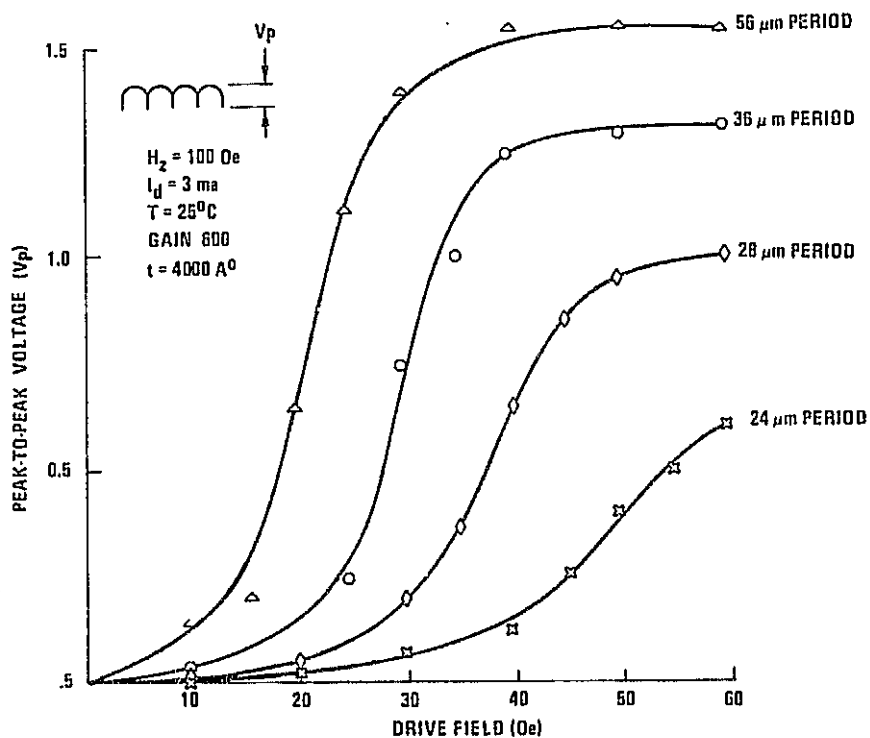


Figure 60. Peak-to-Peak Magnetoresistance Variation for Two-level 110 Deg Detector vs Chevron Period

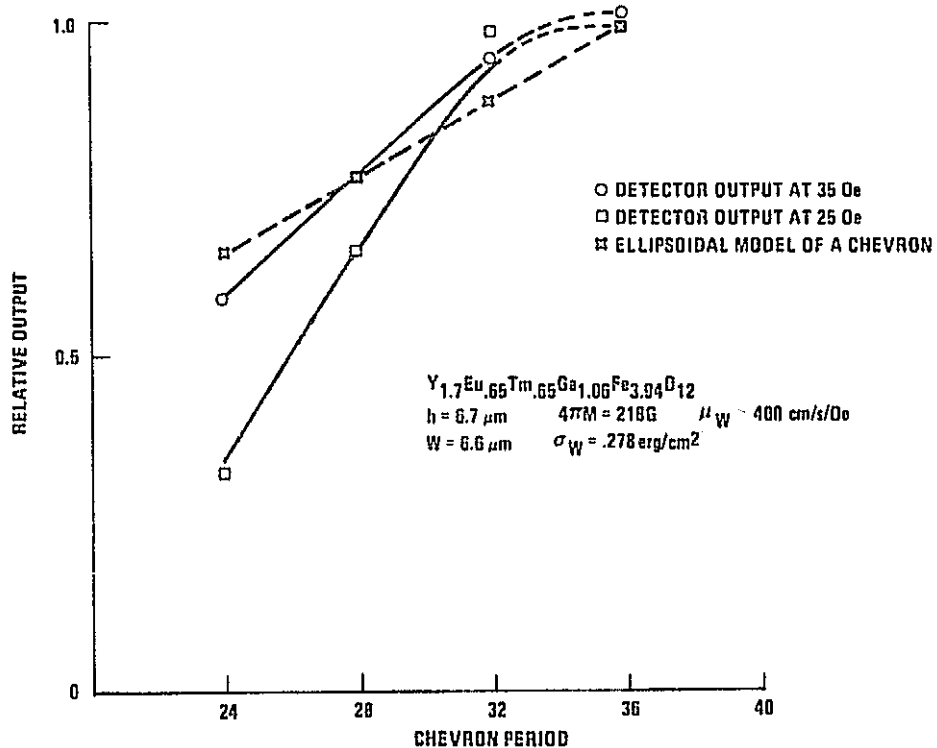


Figure 61. Relative Output for Two-level 110 Deg Detector vs Chevron Period

TABLE 22. SUMMARIZED RESULTS (90 VS 110 DEG)

Pattern	Description	Output* @ $H_{xy} =$		
		25 Oe	37.5 Oe	50 Oe
10	18 element 90 deg chevron end shorted	120 $\mu\text{v/ma}$	125 $\mu\text{v/ma}$	93 $\mu\text{v/ma}$
3	18 element 110 deg chevron end shorted	86 $\mu\text{v/ma}$	125 $\mu\text{v/ma}$	93 $\mu\text{v/ma}$
11	18 element 110 deg chevron set-in shorted	80 $\mu\text{v/ma}$	86 $\mu\text{v/ma}$	73 $\mu\text{v/ma}$

*Hypothetically clamped and strobed for maximum 0 to 1 output

7.2.4 Length, geometry and drive field dependence of the detector output. -

Figure 62 summarizes the results of making detector sensitivity measurements on all of the one- and two-level $28\mu\text{m}$ period test patterns of Figure 57. The results are based upon maximum 0 to 1 detection window for an unclamped signal. The measurements made on detectors of varying length indicate clearly a linear dependence of the output on chevrons in the stack (N). This taken together with the noise results of Para 7.3 (noise study) implies a \sqrt{N} dependence of the signal to noise ratio. Figure 62

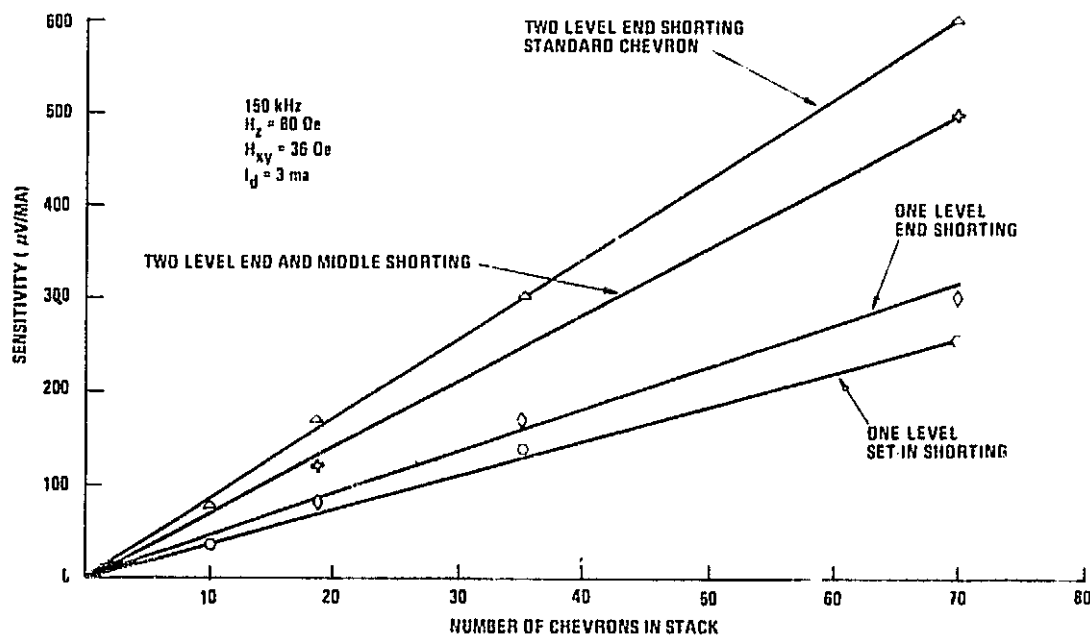


Figure 62. Sensitivity Measurements for One- and Two-Level $28\mu\text{m}$ Period Detectors

also shows the output superiority of the two-level detector over its one-level counter-part. It is interesting to note that if the gold shorts on the output side of a two-level detector are moved to the chevron center the amplitude of the output remains relatively unchanged. The form of the output, however, is altered making bi-phase detection possible by multiplexing together two such detectors-oriented 180° out of phase. Of the one-level detectors the end shorted configuration gives the highest output followed closely by the set-in shorted version. All of the other detector outputs fall near or below these results. This suggests that on the whole the shorting configuration produces no fundamental changes in the operation of the one-level detector.

These results were taken at a drive field of 36 Oe and for the one-level detectors are characteristic of a fairly wide range of drive fields about that point. This is illustrated in Table 23 where the outputs for 25, 37.5 and 50 Oe are tabulated. While there is certainly some variation with drive field for the one-level detectors the value at 36 Oe is on the whole characteristic of the particular pattern tested. For the two-level detectors the variation with drive field is considerably more pronounced. The reason for this is discussed in detail in Para 7.3.4 (noise study) and occurs due to a change in the way the detector works at higher drive fields. At high drive fields the detector output results from a phase shift (of the magnetization) mode of operation rather than an amplitude shift mode. For a one-level detector the amplitude shift mode extends to higher drive fields. Whereas the magnetoresistance amplitude for a two-level detector saturates at about 40 Oe for $\phi = 0$ (direction of propagation) this does not occur in a one-level detector until about 60 Oe. Hence at 50 Oe the one-level detector is still operating in an amplitude shift mode whereas the two-level is not, thus resulting in the difference in drive field behavior. As for the two-level detector, the point at which the one-level detector saturates is controlled by the demagnetizing factor of the chevron and can be varied by changing the period or permalloy thickness.

Finally in Figure 63 are shown the results of making output sensitivity measurements on the one-level test patterns of Figure 57 for a 16μ period mask. Comparing Figures 62 and 63 shows a considerable reduction in output in going from a 28.8 to a 16μ period. It is likely that this is caused by the increased relative thickness of the 16μ patterns which were fabricated on 3200 \AA permalloy. Exact scaling would yield a thickness of 2200 \AA which means that the resistance is about a factor of 1.5 lower than it should be. This is just about the same factor difference in output obtained in our measurements. The reason for increasing the relative thickness was motivated by the higher drive fields required to produce propagation in the 16μ device. Minimum drive field considerations indicate a factor of 1.25 is involved in going from a 28μ to a 16μ period pattern ($4\pi M_{28} = 200$, $2\pi M_{16} = 250$). Hence the optimum design thickness should be about $2200 \times 1.25 = 2800 \text{ \AA}$ which is somewhat less than used here. For this thickness we would expect the outputs of Figure 63 to increase by about 14 percent.

7.2.5 Spacing dependence of the detector output. - Before output sensitivity measurements were made on the 16μ period detectors it was necessary to establish the correct permalloy to garnet spacing. This was done by taking 150 kHz continuous margins on four different spacing samples cut from one wafer. The same circuit Pattern (11) was fabricated on each. The results indicated that in the range of spacings from 3500 to 7000 \AA the minimum drive fields were substantially unchanged as were the margins. The maximum 0 to 1 sensitivity in this range was about $50\mu\text{V}/\text{ma}$ and varied little over the drive field range of 40 to 50 Oe corresponding to normal operation for a 16μ period device. When the spacing was increased to 1μ

TABLE 23. 28 μ m PERIOD DETECTORS

Pattern	Description	25 Oe	Output* @ $H_{xy} =$	
			37.5 Oe	50 Oe
5	18 element two-level 120 deg chevron	200 μ v/ma	230 μ v/ma	110 μ v/ma
5	18 element two-level 90 deg chevron	210 μ v/ma	190 μ v/ma	150 μ v/ma
5	18 element two-level 120 deg chevron (wide separation)	210 μ v/ma	230 μ v/ma	100 μ v/ma
5	36 element two-level 120 deg chevron	-	430 μ v/ma	200 μ v/ma
5	18 element two-level 120 deg chevron half- shorted	86 μ v/ma	140 μ v/ma	80 μ v/ma
11	18 element 110 deg chevron set-in shorted	80 μ v/ma	86 μ v/ma	73 μ v/ma
3	18 element 110 deg chevron end shorted	86 μ v/ma	125 μ v/ma	93 μ v/ma
10	18 element 90 deg end shorted	120 μ v/ma	125 μ v/ma	93 μ v/ma
8	36 element 110 deg set-in shorted	150 μ v/ma	170 μ v/ma	180 μ v/ma
6	18 element horizontal wide separation	66 μ v/ma	53 μ v/ma	40 μ v/ma
9	18 element 110 deg chevron end shorted wide separation	80 μ v/ma	100 μ v/ma	80 μ v/ma
12	9 element 110 deg chevron set-in shorted	40 μ v/ma	53 μ v/ma	40 μ v/ma
4	18 element 110 deg chevron end shorted fine interconnection	-	66 μ v/ma	66 μ v/ma
7	18 element half end shorted	53 μ v/ma	66 μ v/ma	53 μ v/ma

*Hypothetically clamped and strobed for maximum 0 to 1 output

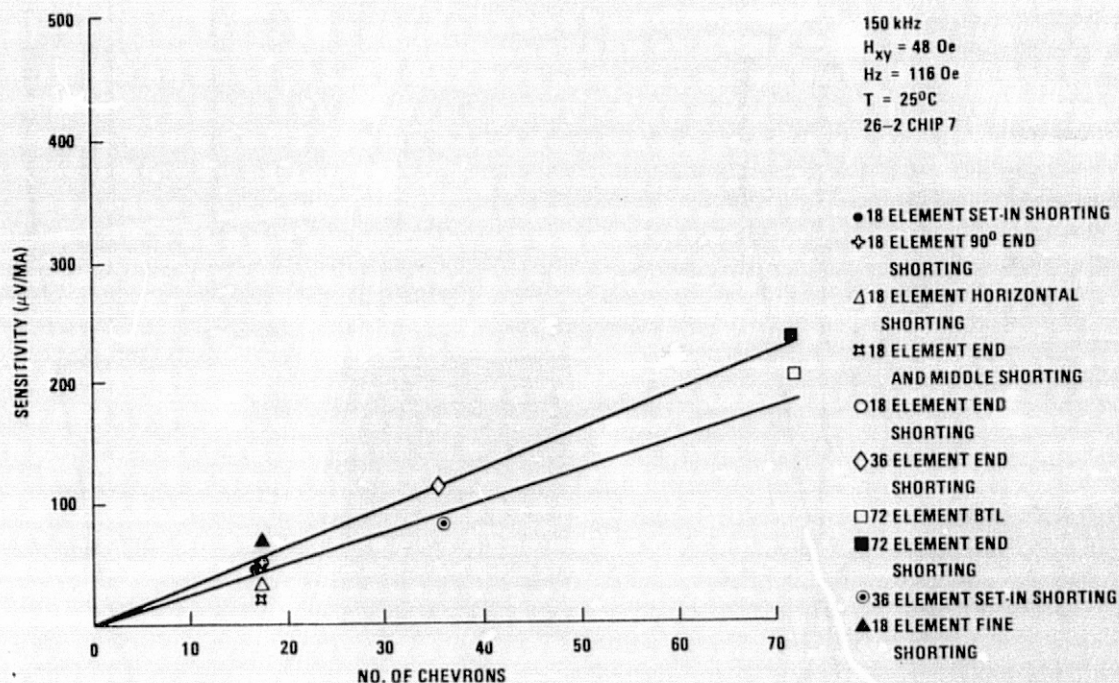


Figure 63. Sensitivity Measurements for One Level 16 μ Period Detectors

about a factor of two reduction in margin occurred and the minimum drive field increased by about a factor of 1.6. Accompanying these changes the output sensitivity decreased very slightly from $50 \mu\text{V/ma}$ to $40 \mu\text{V/ma}$ at a 50 Oe drive field in going from 7000 to 10,000 Å spacing. Hence it appears that spacing has very little effect upon the detector output particularly near the optimum of 0.5μ (for 16 μ period devices).

7.2.6 Thickness dependence of output for one-level detectors. - As was mentioned in connection with two-level detector optimization decreasing the permalloy thickness can be used to improve the output. This is also expected to be the case for the one-level detector and to investigate the effect of varying this parameter a magnetoresistance characteristic was taken on a 28 μ period pattern of 3000 Å. The results which are summarized in Figure 64 when compared with those of Figure 68 (noise study) for a 4000 Å thick pattern show the expected decrease in drive field corresponding to saturation in the $\phi = 0$ deg direction (direction of propagation). Also one finds a corresponding increase in the slope of the $\phi = 0$ deg curve as might have been anticipated on the basis of the two-level results. The similarity of the $\phi = 0$ deg curves for one- and two-level detectors is discussed in detail in Para 7.3.4. Comparison of the $\phi = 90$ deg curves in Figures 64 and 66 reveals that reducing the thickness increases the slope of the thinner detector. As is pointed out in Section 7.3.4, the total output for this detector consists of a contribution from the $\phi = 0$ deg amplitude shift due to the bubble and a $\phi = 90$ deg amplitude shift. Hence the higher $\phi = 90$ deg slope contributes to an improved output in the 30 to 40 Oe drive field range. In view of the increase in resistance of the detector with decreasing thickness these results are not unexpected. The limit on thickness is set indirectly by the operating drive field and the device margins. These depend in turn upon the device components

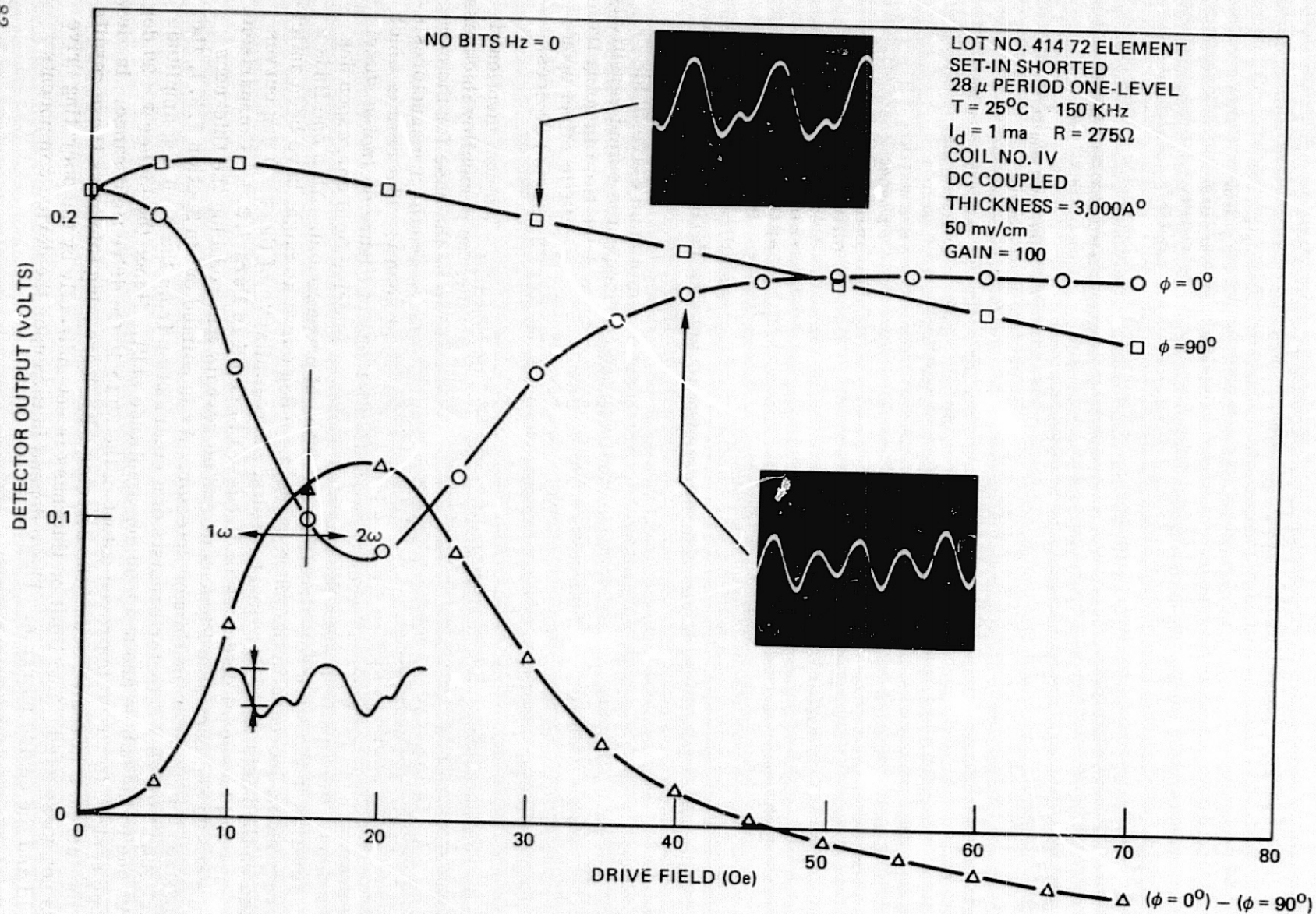


Figure 64. Drive Field Dependence of the Magnetoresistance for a Thin 28 μ m Period One-level Set-in Shorted Detector

employed and the mobility of the garnet. From the standpoint of being able to optimize the detector output Figures 64 and 68 show that a low drive field (20 to 30 Oe) is desired so as to move the operating point into the region of highest slope for the $\phi = 0$ deg curve. When this is possible reducing the permalloy thickness from its common value of 4000Å appears advantageous. Note that the 1ω to 2ω transition (see p 87) remains around 15 Oe although the effective demagnetizing factor for a given direction is reduced by three-quarters due to the thickness change since the effective demagnetizing factor is expected to be related to t/L where t is the permalloy thickness and L is the chevron period. Based upon a thickness reduction from 4000Å to 3000Å we expect a 75 percent reduction in saturation field.

7.3 Detector Noise Study

7.3.1 Introduction. - Very little fundamental device work has been done in the area of magnetoresistive detection as it relates to field access bubble domain devices. Most of the work reported in the literature⁽²⁵⁻²⁸⁾ is either aimed at optimizing permalloy deposition parameters or simply presents device characterization data such as drive field dependence of the output, etc⁽²⁹⁻³⁰⁾. The noise properties of such detectors have been studied only indirectly in connection with limited error rate measurements⁽²⁴⁾. Because detection represents a fundamental function required for device operation it is surprising that so little device work had been done in this area. Thus this portion of the detector study was aimed at characterizing the noise properties of magnetoresistive detectors, the results of which are described in the following sections. This study is useful from two standpoints: (1) the estimation of device error rates, and (2) the understanding of the detection process. As it turns out the noise properties of the various detection states (0 or 1) give one a clue as to how the detector actually works which is an invaluable result in itself.

Historically, field access detection has evolved from the Chinese character detector⁽³¹⁻³⁴⁾ to the thin chevron strip detector⁽³⁵⁻³⁷⁾ and finally to the thick permalloy chevron strip detector^(29,30,38,39). This evolution basically reflects a change in philosophy from stretching the bubble along the propagation direction to stretching perpendicular to it. The thin to thick transition was made as an accommodation to processing simplicity. Elongating the bubble into a strip is necessary to increase the detector signal output particularly for the thick detector where the effect of the bubble stray field must overcome the high demagnetizing fields involved. Expanding the propagating bubble into a strip serves to increase the flux available for switching thus enabling the interaction to occur over a larger volume of permalloy. The one level thick detector^(29,30,39) clearly has an advantage from the processing standpoint particularly for smaller bubble circuits where alignment becomes critical. For this reason the noise study was aimed at understanding the thick chevron strip detector. To provide contrast, however, measurements were also made on a thick chevron strip detector in which the permalloy interconnections were replaced by gold. As will be discussed the effect of replacing the permalloy by gold is profound both from the noise and signal output standpoints. In essence it is the permalloy interconnections which are responsible for the large output seen by Bobeck at low rotating drive fields⁽³⁹⁾ and discussed in detail in Para 7.3.4. A hint of the origin of the 1ω to 2ω instability responsible for the large output may be seen in the basic magnetoresistance variation which is presented in Para 7.3.3 as an introduction to the noise properties of the detectors studied. The experimental apparatus and electronic circuits used to obtain these results as well as those in Para 7.3.5 to 7.3.7 are described in some detail in the following section.

7.3.2 Experimental apparatus - electronic circuits. - A photograph of the experimental kit setup used for much of this study is shown in Figure 65. A simplified version of the magnetoresistance sense channel used for the detector study is shown in Figure 66. This sense channel utilizes a differential preamplifier (733) to amplify the differential voltage induced to ground across the detector active and detector dummy arms of the detector bridge circuit formed by two internal $1\text{ K}\Omega$ resistors and the externally connected active and dummy elements. For much of the study a passive (graphite resistor) dummy detector was used. For detector resistances on the order of 100Ω , the signal amplitude reduction due to voltage division across the bridge elements is approximately 10 percent. The detector bridge is dc coupled to the 733 differential preamplifier.

The 733 differential preamplifier is ac coupled to both a second stage (315) amplifier and an 7528 signal discriminator. The values of the interstage capacitors are chosen to bandwidth limit the signal to the 10 to 300 kHz frequency range for 150 kHz operation. The detector signal is frequency analyzed using the signal available at the output of the 218 second stage amplifier. A Type 1L5 Tektronix Spectrum Analyzer plug-in and a type RM35A Tektronix oscilloscope are used. The signal clamping circuit is not employed in order to permit evaluation of the entire signal when used in conjunction with the spectrum analyzer.

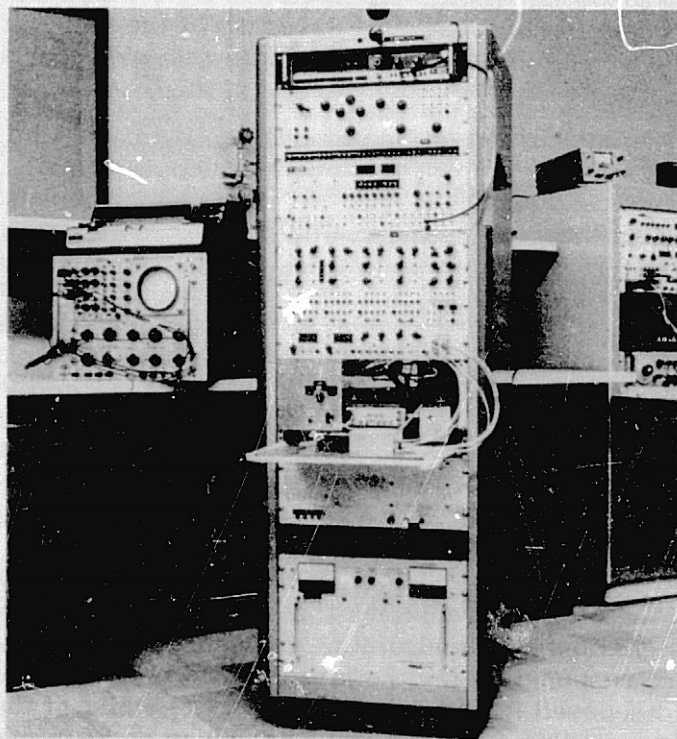
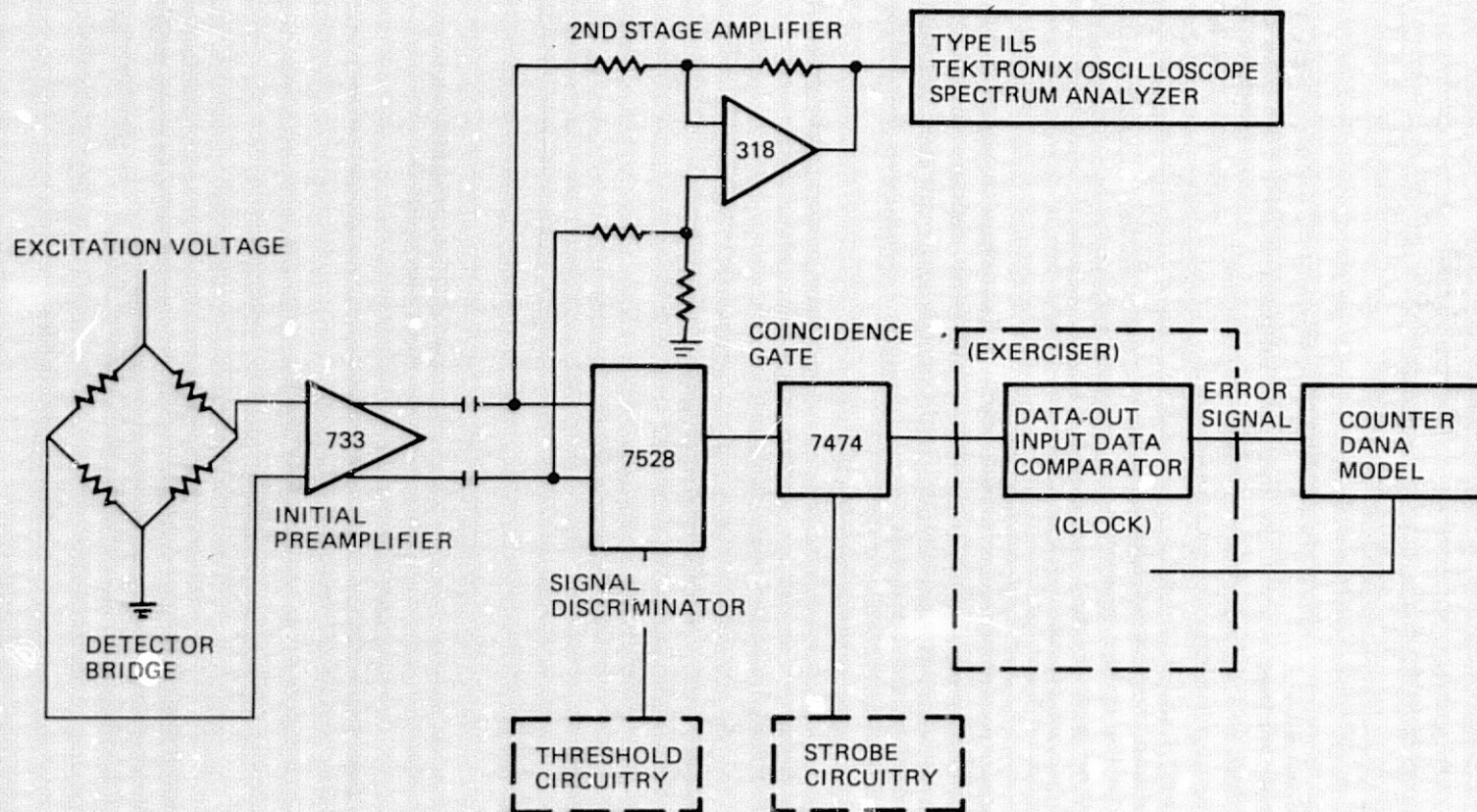


Figure 65. Photograph of Experimental Test Station Used for Making Detector Error Rate Studies



NOTE: THE D&LDT AND SIGNAL CLAMP CIRCUITS ARE OMITTED FROM THIS DIAGRAM

Figure 66. Block Diagram of Test Equipment Circuitry Used for Error Rate Studies

A 7528 externally injected threshold controlled signal discriminator circuit is used to convert the amplified analog signal of the 733 into TTL level digital bubble - no bubble pulses capable of controlling the exerciser logic. A 7474 coincidence gate ensures that only those pulses occurring at the detector strobe time are transmitted back to the exerciser. The use of this gate permits systematic noise such as uncanceled $d\phi/dt$ pickup to be ignored.

The logic level data generated in the sense channel is fed back into the main part of the bubble exerciser where the data are compared with that data indicated as having been read into the bubble memory loop. Non-agreement between the sense channel logic level signals and the exerciser write/read indicator leads to the generation of an error pulse which is fed into a Dana Model 8010B counter. The error rate curves can thus be obtained by counting the number of error pulses generated for a given number of exerciser clock pulses. For simple closed loop operation soft errors are readily discernable from hard errors and each clock pulse corresponds to one detector operation.

7.3.3 Basic magnetoresistance variation. - As a first step in understanding the noise properties of the thick permalloy chevron strip detector measurements of the angular variation of the magnetoresistance were made on the gold-shorted version and the results appear in Figure 67. Here the peak-to-peak response of the magnetoresistance

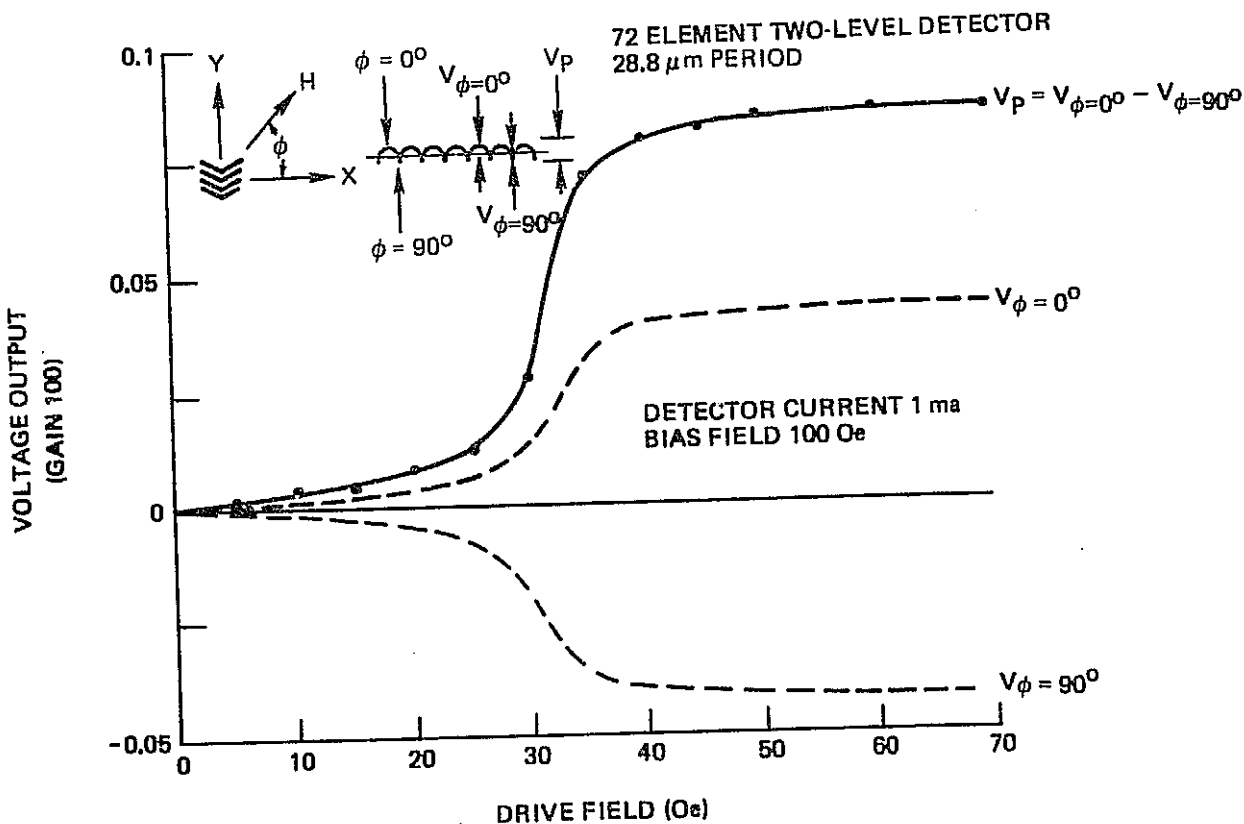


Figure 67. Peak-to-Peak Magnetoresistive Output for Two-level 28 m Period Detector

output voltage with the dummy detector replaced by a passive resistor is plotted vs drive field. The form of the output is indicated schematically in the insert. A dc measurement of the output indicates that the signal develops symmetrically about the zero dc level. This means that the dc response at $\phi = 0$ deg is just one half of value of the curve shown and the response at $\phi = 90$ deg makes up the other half. The dc response at $\phi = 90$ deg decreases with drive field thus producing the total peak-to-peak output shown. What Figure 67 indicates is that the isolated chevron does not begin to magnetize significantly until the drive field reaches in excess of 30 Oe and then an abrupt transition occurs between the low magnetoresistance state and the fully saturated state. Assuming the permalloy switching noise to be proportional to the degree of magnetoresistance saturation the drive field region extending from 0 to 30 Oe is expected to be very quiet while above 30 Oe is expected to be noisy. This is indeed confirmed experimentally as will be discussed in connection with the zero state (no bubbles) noise properties in Section 7.5. On the other hand experimentally one finds that for such a device operating in the zero state at 25 Oe (quiet) the one state (all bubbles) is noisy. The paradox can be resolved by realizing that the effect of the bubble field is equivalent to an increase of the uniform drive field by about 10 Oe which means that while the zero state at 25 Oe is quiet the one state at 35 Oe will be noisy according to our understanding of Figure 67. Hence the zero state noise properties of a detector give us an indication of how it actually works - when combined with other information. For this reason the emphasis of our noise measurements was placed on characterizing the zero state of both the gold and permalloy interconnected thick chevron strip detectors.

The basic magnetoresistance variation of the permalloy interconnected detector (one level) as well as a schematic of its layout is presented in Figure 68. The angular variation of the magnetoresistance with drive field is very different from that shown in Figure 67 for the two-level detector. Whereas the magnetoresistance is highest in Figure 67 when the field is oriented along the propagation direction ($\phi = 0$ deg) in Figure 68 the magnetoresistance is highest when the field is oriented perpendicular to the propagation direction or along the axis of the detector ($\phi = 90$ deg). Also to be noted is the pronounced transition at 15 Oe of the signal waveform from a 2ω fundamental frequency dependence to a 1ω dependence at lower drive fields. A similar transition is found in connection with the gold shorted version but because the magnetoresistance is so low in the accompanying drive field range its importance is minimal. For the permalloy shorted version, however, the transition occurs in a region where the detector magnetoresistance is high which means that there is the possibility of obtaining a large output signal if the operating drive field is low.

It is our contention that the large 40 mv output observed in ref 40 is associated with this transition. The following physical model is proposed to explain these experimental results. The key to understanding what is going on in Figure 68 lies in recognizing that the highest magnetoresistance state occurs when the drive field is essentially zero. The only way that this can be the case is if the domain structure is highly ordered along the current path when no field is applied. Experimental confirmation of such a configuration has been provided by ferrofluid measurements made on permalloy detector patterns deposited on glass. Figure 69 shows two sketches of the observed domain configuration for detectors which are end shorted and set-in shorted. As can be seen a domain pattern is formed so as to minimize the

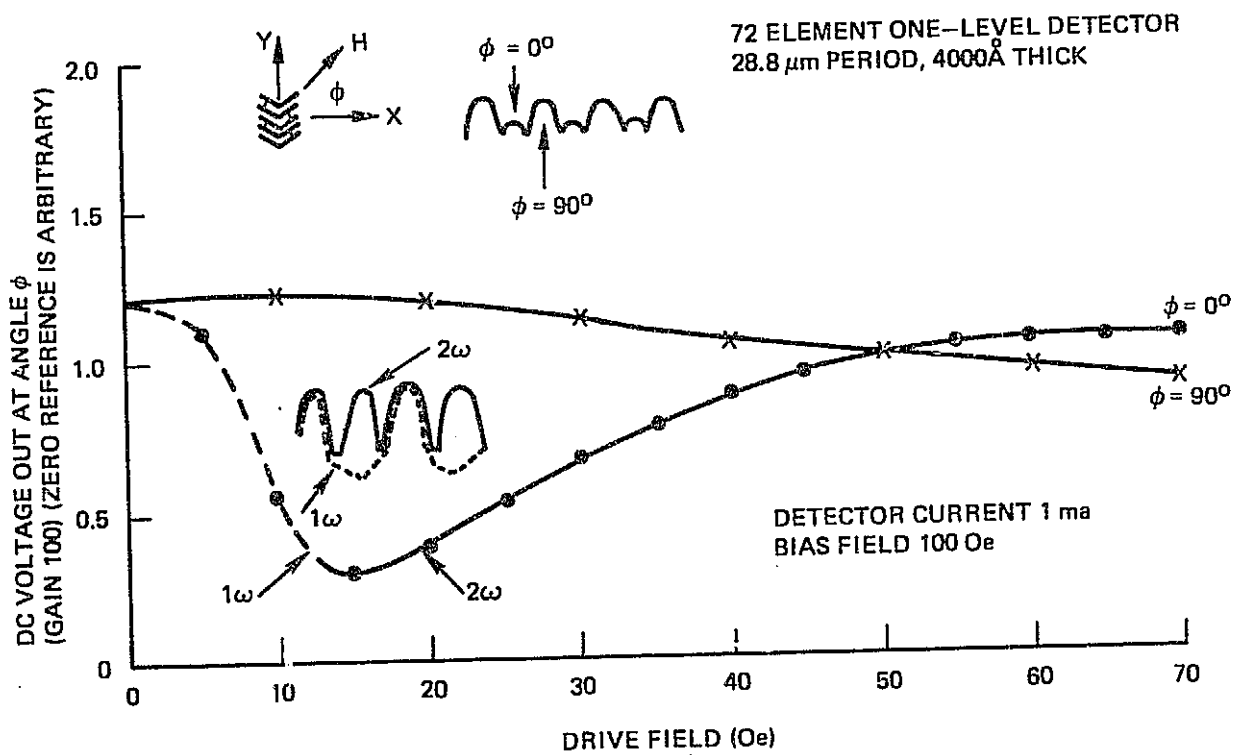


Figure 68. Magnetoresistive Output for One-level 28 μm Period Detector

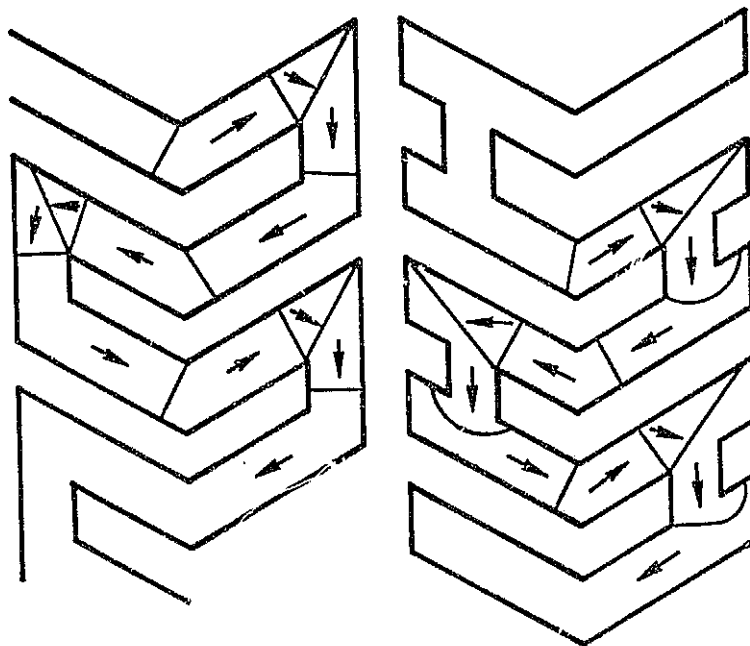


Figure 69. Ordered Domain Structure Observed by Ferrofluid Decoration

occurrence of external poles thereby reducing the magnetostatic energy. In this case domain closure is achieved by forming a serpentine pattern along the entire length of the detector. (Of course the magnetization directions may also be reversed by 180 deg from those shown in Figure 69). Because the current flows along essentially the same path and is parallel or anti-parallel to the magnetization direction the associated magnetoresistance is high. With this picture in mind the interpretation of Figure 68 is relatively straightforward. At very low drive fields the ordered state of the detector persists whether the field is oriented parallel ($\phi = 0$ deg) or perpendicular ($\phi = 90$ deg) to the propagation direction. The detector resides in a ordered state with the magnetization direction along the detector determined by its past history or, if an in-plane component of the bias field is present, by this field itself. To completely reverse the magnetization direction apparently involves overcoming some sort of a magnetostatic energy barrier with the result that at low drive fields the magnetization is not switched in the reverse sense thereby giving rise to the 1ω behavior illustrated in the inset.

For $\phi = 0$ deg the magnetoresistance is lower than for $\phi = 90$ deg because the applied field tends to partially reverse the magnetizations of adjacent chevrons thus destroying the closure domain formed along the permalloy and thus decreasing the magnetoresistance from its ordered value at $H = 0$ Oe. Above about 15 Oe the drive field is enough to completely reverse the magnetization along the detector and saturate it in the reverse sense with the result that a 2ω dependence of the magnetoresistance is obtained. As the drive field is increased beyond this point it becomes strong enough to rotate the magnetization in the chevron parts of the detector away from the current direction with the result that the output at $\phi = 90$ deg decreases slightly from its zero field value. What appears to be happening for $\phi = 0$ deg is that as the drive field is increased adjacent chevrons magnetize in the same direction more and more-similar to what happens for $\phi = 0$ deg for the two-level detector of Figure 67. At a drive field of 70 Oe the adjacent chevrons are essentially saturated resulting in nearly the same magnetoresistance state as for a drive field of zero. Hence the curve for $\phi = 0$ deg in Figure 68 may be thought of as being the same as the $\phi = 0$ deg curve for Figure 67, (divide plotted curve by 2). The major difference in the permalloy interconnected detector is that as the field is reduced it becomes saturated with the result that the magnetoresistance for $\phi = 0$ deg increases and approaches an asymptotic value instead of going to zero. In reality the smaller bumps shown in the insert of Figure 68 at $\phi = 0$ deg can be thought of as the tops of the output signal shown in the insert of Figure 67. Thus this domain closure model can be seen to explain the qualitative features of the experimental data on one-level thick permalloy detectors.

Because the magnetoresistance state of the permalloy interconnected detector in the low drive field region is high in contrast to the gold interconnected version the noise properties are expected to be quite different. For very low drive fields (<10 Oe) very little change in magnetoresistance state is involved so the noise output is expected to be small. At or around a drive field of 15 Oe corresponding to the 1ω to 2ω transition the incomplete switching of the magnetization should give rise to an extremely large noise signal. At higher drive fields (>40 Oe) the permalloy switching is expected to become more coherent with the result that the detector noise goes down as also holds true for the gold interconnected version.

A more complicated consideration than the drive field dependence of the noise is its angular variation. Because the bubble produces an output over a restricted range of drive field angles it is important to know where in relation to this signal the permalloy switching noise occurs. In the following section, therefore, we discuss how and where the detector signal is produced in relation to the basic angular variation shown in Figures 67 and 68.

7.3.4 Detector operation and origin of the large 1ω output at low drive field. - To a first approximation the effect of the bubble as it passes through the detector is to increase the effective drive field acting on the permalloy during the time of transit. This is because the bubble generally follows the magnetostatic energy minimum closely which means that geometrically it is in a position to aid the uniform applied field. Strictly speaking, however, the bubble field is spatially rapidly varying in contrast to a uniform field. If one takes this equivalent uniform field viewpoint then the process of detecting a bubble may be thought of in terms of Figures 67 and 68 and as shifting the drive field temporarily to the right by about 8 Oe. The bubble output then is the difference between the signal waveforms for the states corresponding to the drive field and the drive field plus 8 Oe. This type of detector operation is referred to as the amplitude shift mode in contrast to the phase shift mode which will be discussed subsequently. Clearly the output for the amplitude shift mode will be highest in the neighborhood of abrupt magnetoresistance transitions such as encountered in connection with the gold interconnected detector at about 30 Oe. Accordingly a study of this mode of operation has been made for this detector and the results are summarized in Figure 70. Shown are two magnetoresistance curves taken with no bubbles in the circuit and with bubbles in every bit position. The effect of the bubble field is equivalent to about 8 Oe uniform rotating field as is confirmed by the translation of the no-bubble field curve to the left. Experimentally it is impossible to obtain all bubble data below about 10 Oe drive field because the bubbles fail to propagate at 150 kHz. Also shown as insets on the plot are various signal waveforms meant to illustrate the amplitude shift mode. At 23 and 30 Oe drive field the all-bubble and no-bubble waveforms are shown to be nearly identical thus confirming the equivalence of the bubble field and an 8 Oe uniform drive field. At 28 Oe the bubble-no-bubble state overlap is shown which corresponds to a vertical transition (as opposed to the just mentioned horizontal transition) between bubble and no-bubble magnetoresistance curves. The latter transition corresponds to the zero to one-state used to distinguish between bubble and no-bubble in a actual operating device. Also shown at 54 Oe is the no-bubble waveform once again confirming the equivalence of the all-bubble signal at 28 Oe and the no-bubble signal at 34 Oe. The vertical distance between the all-bubble and no-bubble curves in Figure 70 is a measure of the amplitude shift output of the corresponding detector and therefore one would expect an increasing signal with drive field which goes through a maximum at about 25 Oe and then decreases at higher field values. This is confirmed experimentally by the dashed curve at the bottom of Figure 70. This curve was obtained by measuring the output at the peak magnetoresistance point of the no-bubble signal ($\phi = 0$ deg). Because the two solid curves are for the peak-to-peak output a factor of two is required in comparing their difference with the dashed curve.

In reality at higher drive fields the output of the gold interconnected detector does not drop off as rapidly as indicated in Figure 70 and this is because another mode of operation becomes dominant. This is illustrated by the waveform inset at 60 Oe and is referred to as the phase shift mode. As can be seen from Figure 70 at this drive field little amplitude change occurs between the all-bubble and no-bubble state.

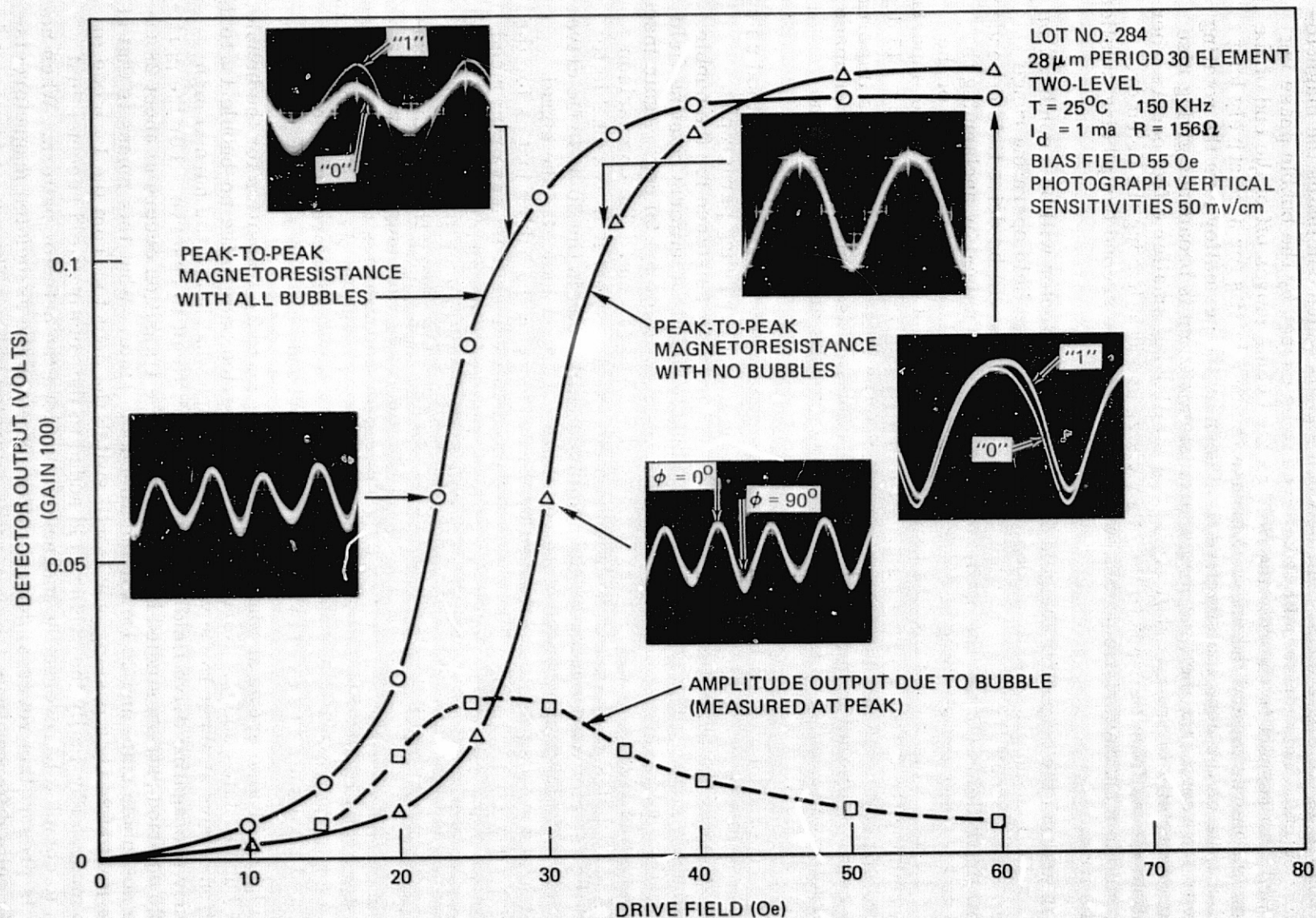


Figure 70. Magnetoresistance Variation for Two-level Detector Illustrating Amplitude and Phase Shift Modes of Operation

As a result it is the slight phase shift between signals which dominates the magneto-resistive output. This phase shift is believed to be caused by the bubble phase lag developed with respect to the rotating field as the bubble moves off of the end of the chevron and moves toward the apex. Because the bubble sits for a relatively long period of time on the end, the effective field seen by the permalloy lags the rotating field with the result that the first magnetoresistance bump is broadened giving rise to what essentially is a phase shift signal. A similar but smaller effect occurs when the bubble moves from the apex to the other chevron end in leaving the detector, giving rise to a characteristic double bump output with the second bump being smaller than the first.

In general the output for the gold interconnected detector will be a combination of the amplitude and phase shift modes in the normal drive field operating range (35 Oe). As a result the phase at which the output occurs will be drive field dependent. For low drive fields (28 Oe) the optimum signal may be obtained by unclamping the signal at $\phi = 0$ deg and strobing at $\phi = 90$ deg thereby utilizing the full extent of the bipolar output. This means that the noise in the vicinity of $\phi = 90$ deg will be important in determining the detector error rate. At higher drive fields clamping at $\phi = -45$ deg and strobing at $\phi = +45$ deg is appropriate. Hence the noise at $\phi = +45$ deg is important in this case. With this in mind zero state (no bubble) measurements have been made to characterize the noise in these regions and the results are presented in the following section.

The operation of the permalloy interconnected detector may be understood using the same reasoning as applied to the gold version in the preceding paragraphs. Figure 71 shows the drive field dependence of the magnetoresistance for the bubble and no-bubble states. The equivalence of the bubble field to a uniform rotating field of about 8 Oe holds very well for $\phi = 0$ deg but not so well for $\phi = 90$ deg. Again insets are provided in Figure 71 comparing various signal waveforms. The comparison between all bubbles at 30 Oe and no bubbles at 40 Oe shows that it is reasonable to regard the detector as operating in the amplitude shift mode in the 30 to 40 Oe drive field range. As the magnetoresistance curves in Figure 71 indicate, the signal amplitude at $\phi = 0$ deg will be increased by the presence of the bubble just as for the gold interconnected version. For $\phi = 90$ deg the amplitude shift is less pronounced than for $\phi = 0$ deg due to the slower variation of the magnetoresistance with drive field. Comparison of Figures 70 and 71 reveals that in the amplitude shift mode the output for the gold interconnected version should be considerably higher than for the permalloy interconnected detector. In Figure 71 the amplitude shift output may be obtained by adding up the differences in bubble-no-bubble voltages for both $\phi = 0$ deg and $\phi = 90$ deg. The result then corresponds to that which would be obtained by unclamping at $\phi = 0$ deg and strobing at $\phi = 90$ deg. In Para 7.3.5 the noise properties of the associated zero state are examined in this neighborhood.

Figure 71 also shows at what drive fields the 1ω to 2ω transition for the bubble and no-bubble states occur. Normally for a 28μ period pattern the no-bubble 1ω to 2ω transition occurs at about 15 Oe which places it somewhat below the normal high frequency propagating drive field range making it difficult to observe. For the particular 20μ period pattern studied here, however, the transition occurs at about 28 Oe for the no-bubble state and 20 Oe for the all-bubble state. What this means is that at a drive field of 24 Oe a passing bubble will switch the detector from the 1ω mode to the 2ω mode. Physically the bubble field added to the rotating field becomes just enough to completely reverse the magnetization along the detector pattern. When no bubble is present this reversal does not take place and the associated magnetoresistance is quite different from the (reversed) saturated value. The output corresponds

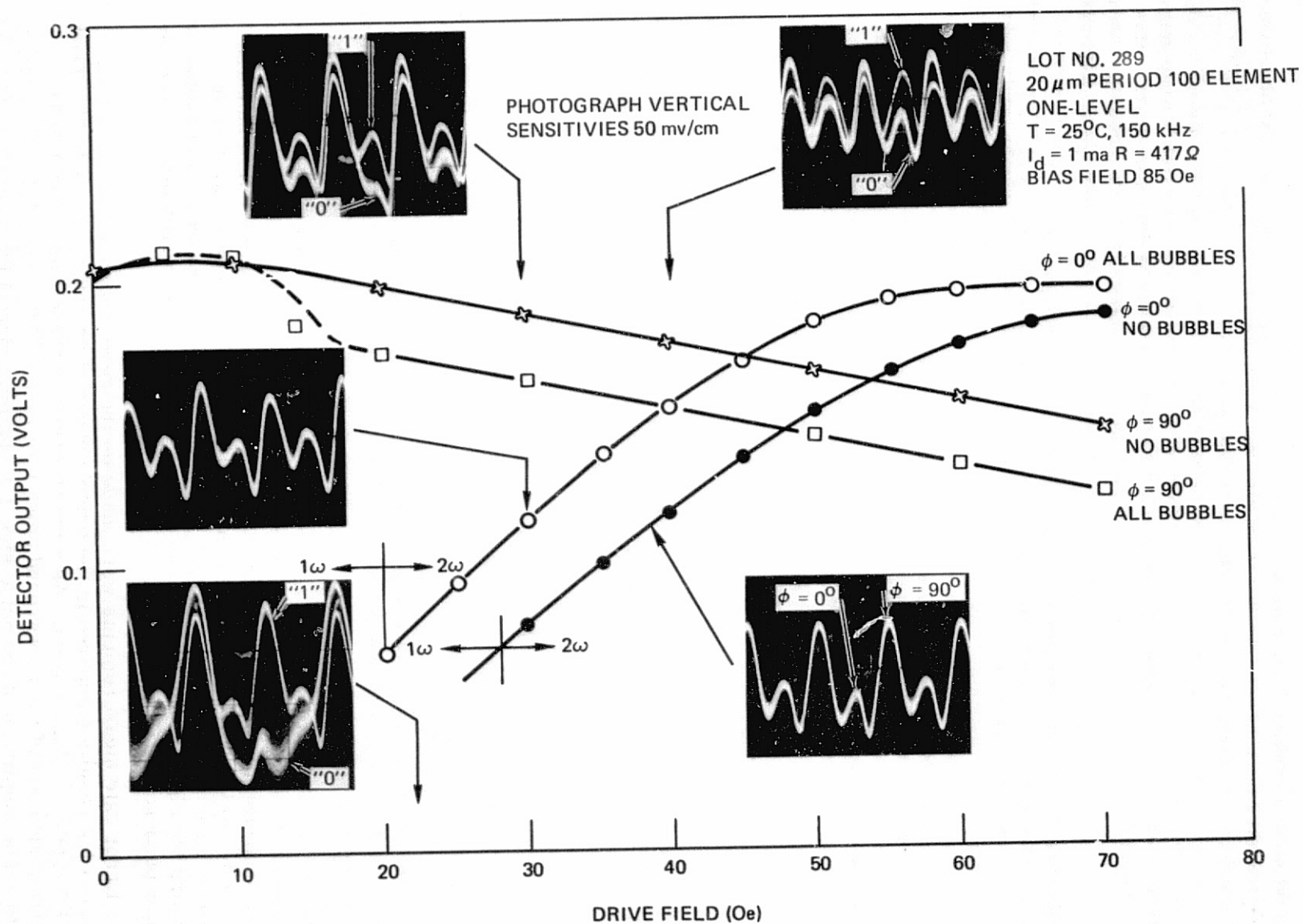


Figure 71. Magnetoresistance Variation of One-level Detector Illustrating Amplitude Shift Mode

to just about the difference between the $\phi = 0$ and 90 deg no-bubble curves at 24 Oe which is large compared to normal amplitude shift outputs. The inset at 22 Oe shows the bubble-no-bubble signals for this mode of operation. The noisy no-bubble output is a result of the nearness of the drive field to the 1ω to 2ω transition. Reducing the drive field somewhat can be used to improve the noise but at lower fields propagation becomes erratic. Our overall impression is that in terms of device operation this mode of detection is impractical. The main problem arises from the incompatibility of the drive fields required for its use and those required to produce viable propagation margins. If extremely high mobility materials were used resulting in low drive fields then considerations might change. Normally it is difficult to obtain quiet bubble and no-bubble states simultaneously due to the drive field breadth of the transition. For these reasons very few measurements were made in connection with this low drive field instability.

7.3.5 Geometrical and drive field dependence of the zero state error rate. - If the switching noise produced by wall motion in the permalloy is described by a Gaussian distribution as might be expected for a random process then the probability of obtaining an output at the threshold voltage V_T may be described by:

$$P(V_T) = \frac{e^{-\frac{1}{2} \left(\frac{V_T}{V_N} \right)^2}}{\sqrt{2\pi} V_N} \quad (7)$$

where, the voltage V_N is a measure of the deviation of output signal from the mean due to a noise signal. The error rate at a given threshold is just the probability of finding the signal above the voltage V_T which is:

$$ER(V_T) = \int_{V_T}^{\infty} \frac{e^{-\frac{1}{2} \left(\frac{V_T}{V_N} \right)^2}}{\sqrt{2\pi}} dV_T, \quad (8)$$

and yields the characteristic curves shown in Figure 72 for both the zero and one states. In general the standard deviation for these states will be different. Usually one finds that (8) provides an excellent fit to experimental data. To further check the validity of the assumed distribution, measurements were made to determine the dependence of V_N on the number of chevrons in the detector. For independent elements such as found in the gold interconnector detected V_N is expected to vary like \sqrt{N} . While this does not necessarily follow for the permalloy interconnected version due to the non-independence of the elements it has been shown true for the latter case also. This means that for both the gold and permalloy interconnected detectors the signal to noise ratio increase as the \sqrt{N} . The confirmation of the \sqrt{N} noise dependence is shown in Figure 73 by two methods.

Error rate measurements were made on the zero state and the asymptotic slopes of the results compared in the neighborhood of an error rate of 10^{-6} . These results appear in Figure 73(a). As a cross-check on these data a 0 to 1 MHz spectrum analysis of the background noise was recorded for each different detector length. The amplitude of the noise signal at the fundamental frequency was then taken as a measure of the noise output. The results of these measurements appear in

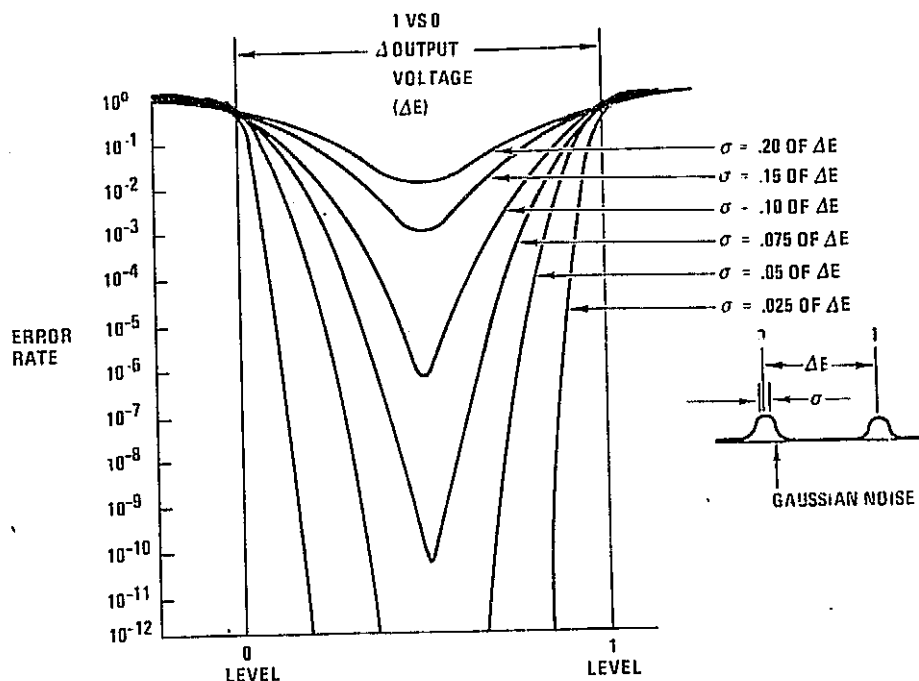


Figure 72. Typical Error Rate Characteristics for Gaussian Noise (Calculated)

Figure 73(b). The latter technique gives information on the noise amplitude throughout an entire field rotation whereas the error rate technique gives information on the noise at a particular field angle where the detection strobe occurs. The interest in the spectrum analyzer technique stems from its possible use as a processing monitor. The permalloy noise can be characterized extremely simply with this technique in contrast to making error rate measurements.

The results of Figure 73(a) correspond to a strobe phase of $\phi = 0$ deg which is the point at which the first large output occurs in both of the detectors at normal drive fields. The strobe position in this case has not been optimized for maximum zero to one output nor has clamping been employed. The difference in noise between the end shorted permalloy interconnected detector and the set-in shorted version is most likely simply a reflection of the increased permalloy involved. From data taken on the output of these detectors it appears that while the signal output for the end shorted detector is larger, the signal to noise ratio is probably the same as for the set-in shorted detector. The fact that the gold interconnected detector is quieter than the one-level versions is not of particular significance since the strobe position is not optimized. Also shown are results for a $16\mu\text{m}$ period pattern.

Figure 74(a) shows the drive field dependence of the noise for the same detectors of the previous figure. As was anticipated in Para 7.3.3, the noise for the gold interconnected detector increases almost like the magnetoresistance curve of Figure 68 and then at higher drive fields begins to decrease rapidly presumably due to more coherent switching at these field values. In contrast the results for the one-level detectors simply fall off rapidly even at low drive fields. It is felt that this behavior supplies further confirmation of our hypothesis that the one-level detector is in a high magnetoresistance state at low drive fields. In Figure 74(b) the spectrum

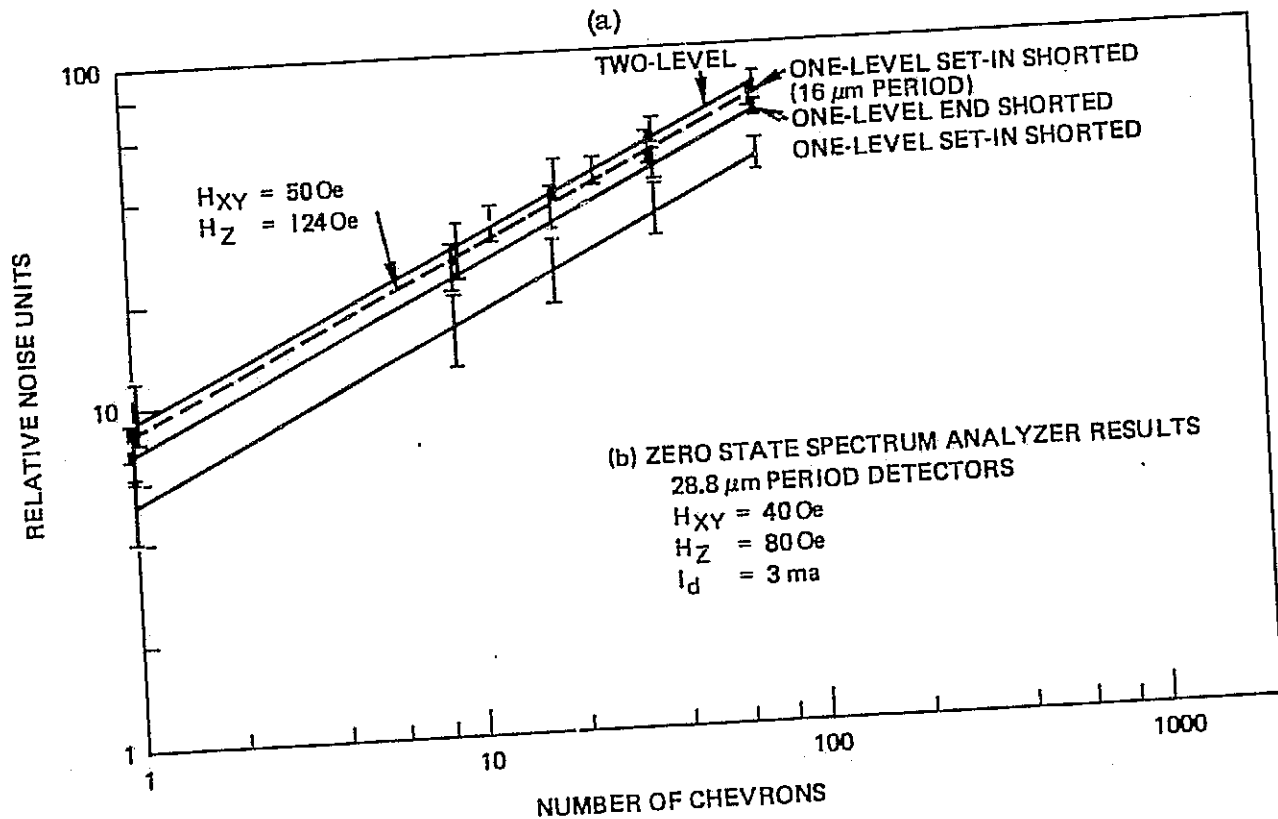
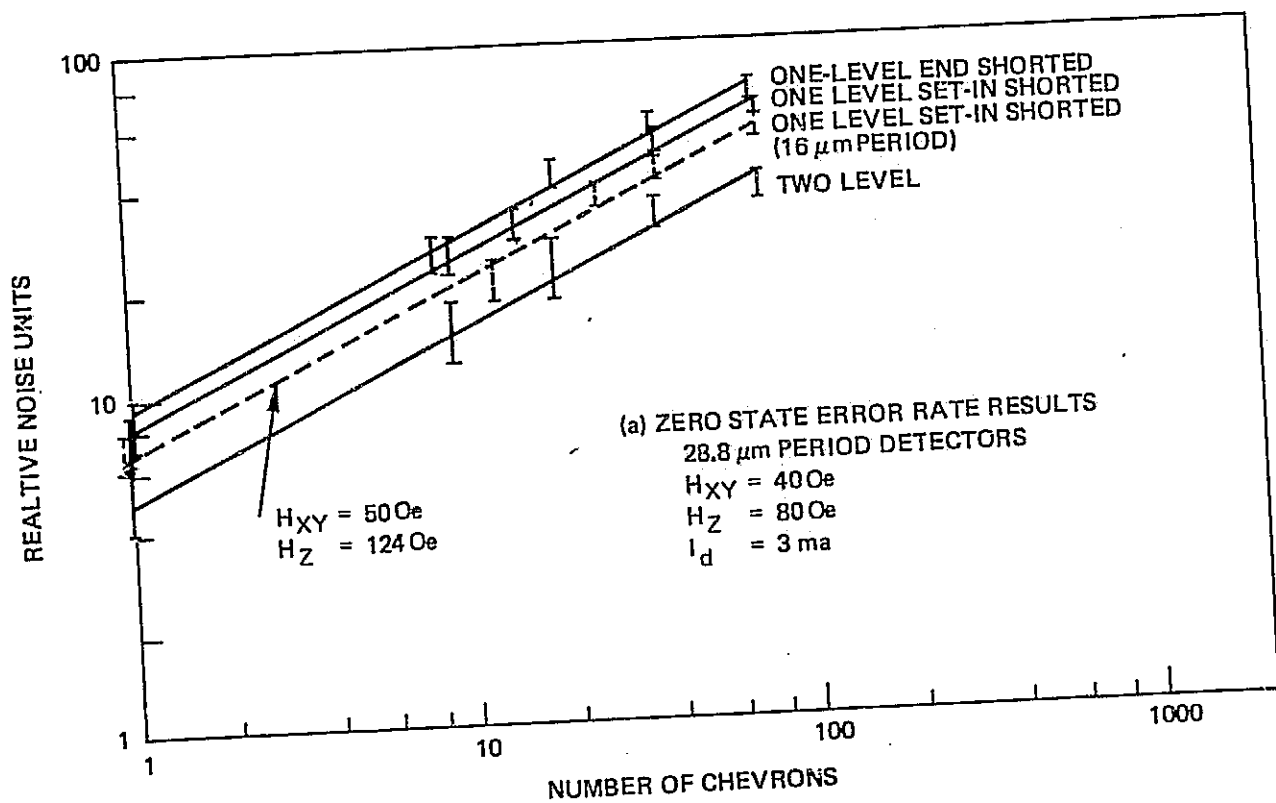


Figure 73. Zero State Noise vs Number of Chevrons in Detector;
(a) as Determined by Error Rate Measurements;
(b) as Determined by Spectrum Analyzer

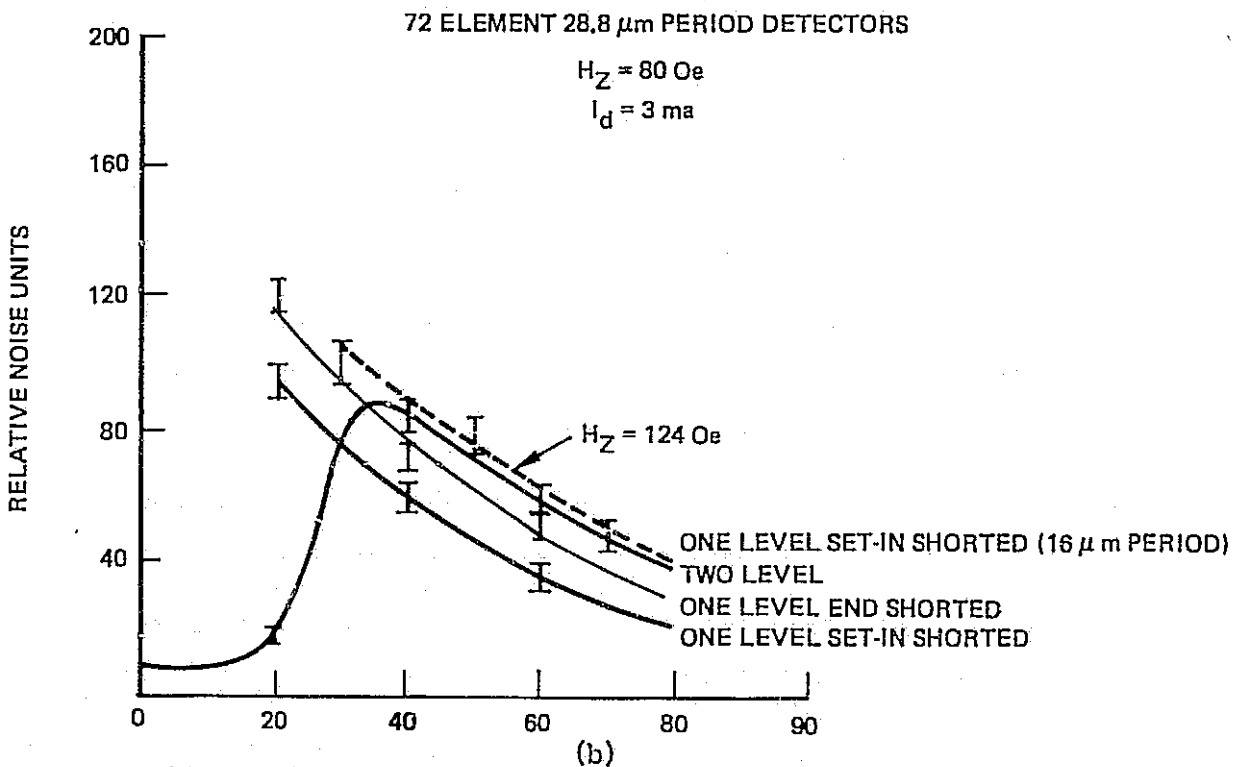
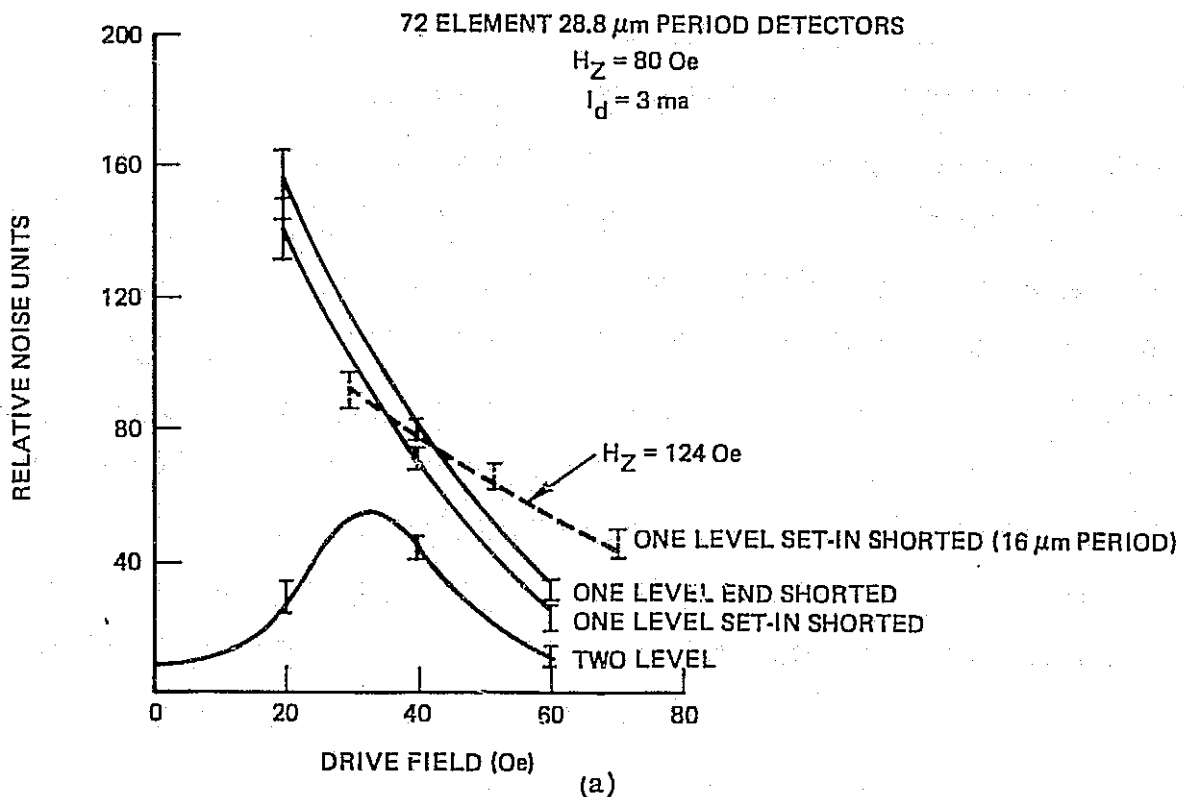


Figure 74. Zero State Noise vs Drive Field for Fixed Stretch;
 (a) as Determined by Error Rate Measurements;
 (b) as Determined by Spectrum Analyzer

analyzer results qualitatively confirm the error rate measurements. Figure 74(a) shows that a factor of two decrease in noise is obtained when the drive field is increased from 30 to 50 Oe.

The fact that as additional chevron elements are added to a detector the noise increases like \sqrt{N} suggests that when a detector is placed in a bridge configuration with a matching permalloy dummy the noise should go up by a factor of \sqrt{N} unless there is some sort of correlation between the switching in the separate detectors. For true random noise there should not be. To further test this idea error rate measurements were made on a 36-element detector, two 36-element detectors in a bridge and on a 72-element detector. The results which are presented in Figure 75 show that the noise from the two 36-element detectors in a bridge is exactly the same as for the 72-element detector and furthermore is about a factor of $\sqrt{2}$ higher than for the 36-element detector alone. Also checked at the same time was the effect of clamping the signal to ground and unclamping $1 \mu s$ before strobing. As can be seen the results indicate virtually no difference between the clamp and strobe mode and strobing alone. This is because the ac coupling capacitors filter out the low frequency noise components making clamping redundant from the low frequency noise standpoint. Also checked was the effect of increasing the detector current. Figure 75 indicates that the slope of the error rate curves increases linearly with current. This means that the signal to noise ratio is independent of current and thus as expected the error rate cannot be improved or degraded by increasing the current assuming that no temperature change takes place. Finally it should be mentioned that since $d\phi/dt$ is a systematic mode the only effect of uncanceled $d\phi/dt$ "noise" is to shift the detection threshold. It does not in any way change the slope or form of the basic error rate curve determined by the random permalloy switching.

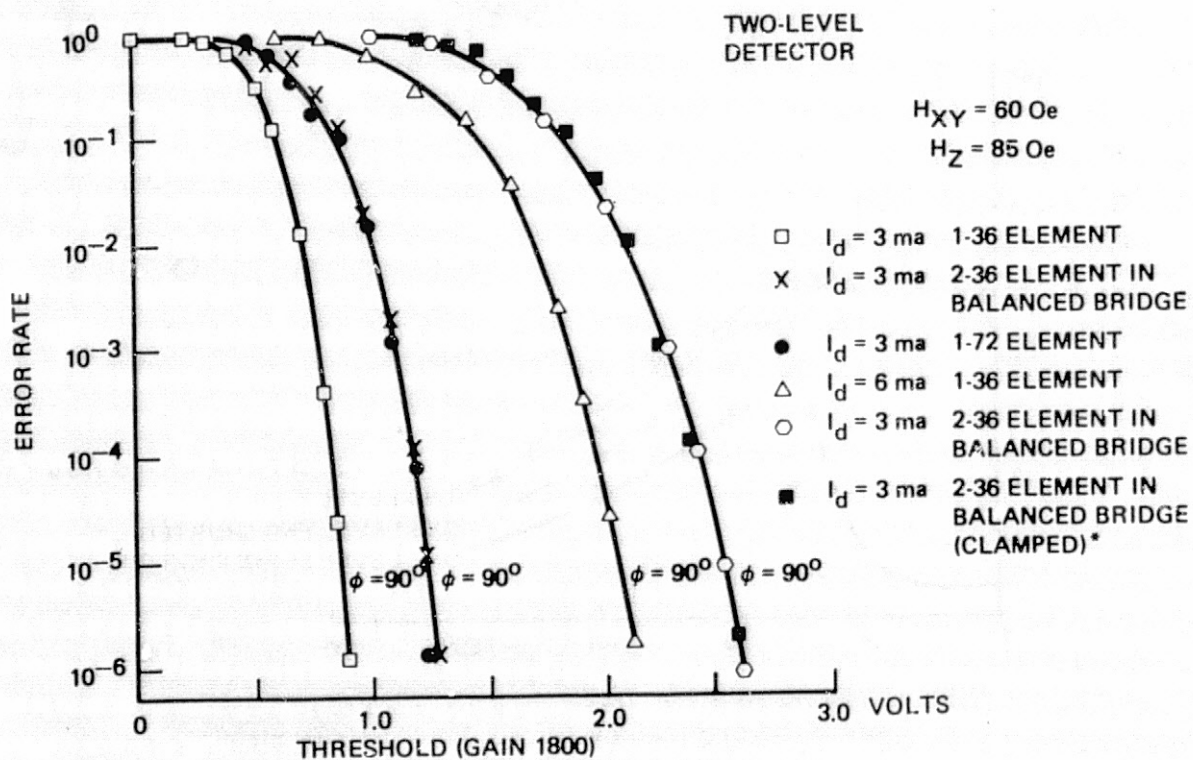


Figure 75. Error Rate vs Bridge Scheme, Current and Detection Mode

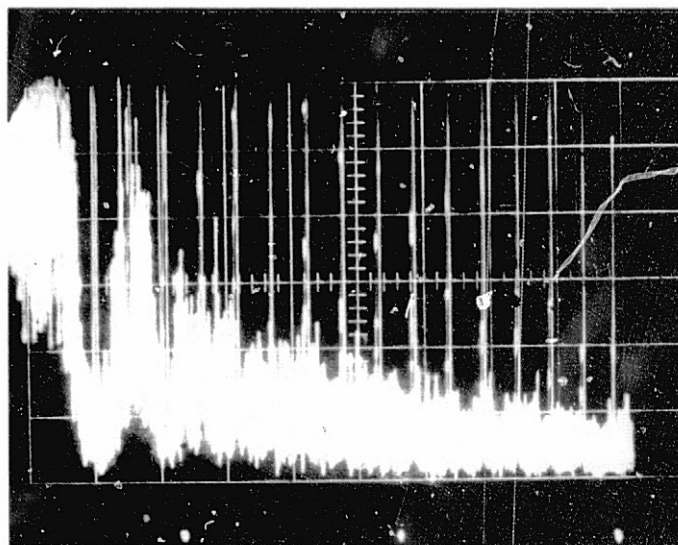
7.3.6 Frequency dependence of zero state noise. - The spectrum analyzer results of the previous section indicated a $1/f$ dependence of the switching noise which suggests that going to higher frequency might improve the signal to noise ratio. However, comparison of the noise spectrums shown in Figure 76 shows why this might not be the case. The spectrum for 200 kHz contains as much integrated noise as that for 50 kHz. Furthermore the noise amplitudes in the region of 2ω are comparable even though the high frequency noise spectrum falls off above this like about $1/f^5$. Figure 77 confirms that the error rate is essentially frequency independent from 0 to 200 kHz. Spectrum analyzer results at frequencies up to 500 kHz suggest that this holds true up to much higher frequencies. Hence, the common observation that the permalloy switching noise goes down with increasing frequency is misleading. While this may be true for some of the low frequency components in Figure 76 it is not true for the whole spectrum. The gaps in the spectrums in Figure 76 are caused by saturation of the spectrum analyzer by the large 2ω magnetoresistive component.

7.3.7 Zero and one state noise for one- and two-level detectors. - To further confirm how the one- and two-level detectors work and also the \sqrt{N} dependence of the one state error rate, measurements were made on detectors in a bridge configuration operating as they would in an actual memory. Clamping and strobing was optimized for maximum zero to one output in all cases. Figure 78 indicates clearly that for the one- and two-level detectors the effect of the bubble field on the permalloy is equivalent to increasing the uniform field by about 8 Oe. The data for the two-level detector show that the zero states lie below the low to high magnetoresistance transition normally found for this detector. In this state the detector is quiet. When the bubble passes through the detector it is switched into the high magnetoresistance state which is reflected in the noisier "0 + 1" state output. If the bubble field were exactly equal to 8 Oe then this state would be approximately $\sqrt{2}$ less than the zero state with $H_{xy} = 40$ Oe. The deviation from this ideal behavior is probably caused by detector mismatch. For the one-level detector the effect of the bubble is to decrease the detector noise. This is because one detector sees a higher drive field than the other thus according to Figure 74 reducing its noise slightly from that of the zero state at $H_{xy} = 40$ Oe. Hence the noise output of the "0 + 1" state is lower than that of the "0" state. These observations tend to confirm the model of detector operation as presented in Para 7.4. As might be expected the "0 + 1" state and hence "1" state exhibit a \sqrt{N} dependence. This is not unreasonable if one regards the one state as simply higher drive field zero state as seems reasonable to do in view of the data obtained.

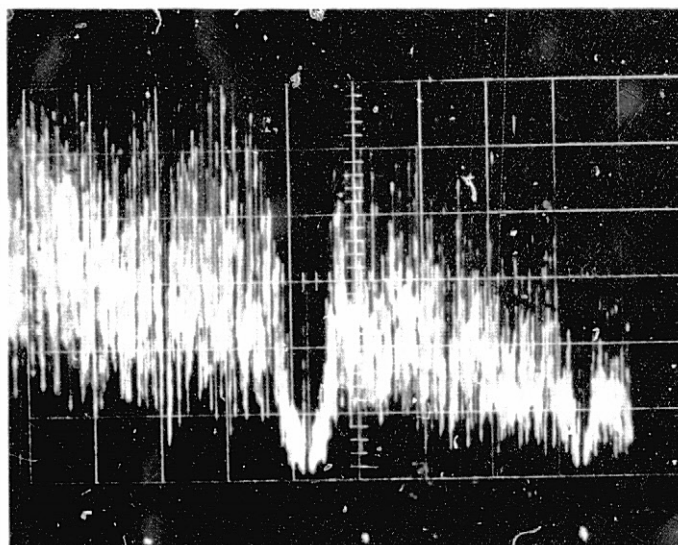
7.4 Conclusions and Recommendations

The sensitivity measurements made on one- and two-level detectors clearly show that the former have about half the sensitivity of the latter. This is because the drive field dependence of the peak-to-peak magnetoresistance for the two-level detector exhibits an abrupt transition in the neighborhood of 30 Oe whereas the comparable transition is more gradual in the one-level counterpart. As has been shown the amplitude shift output for the two-level detector is by far the largest and therefore if one wishes to optimize the output from this detector it is simply a matter of adjusting the drive field or geometry so that the zero state falls in the low magnetoresistance region and the one-state in the high magnetoresistance region. Any number of possible solutions can be proposed. The most desirable is to reduce the drive field by employing high mobility materials. Since the location in drive field of the transition is determined by the effective demagnetizing factor along the direction of propagation the permalloy geometry can also be used to adjust the transition-subject to several limitations. Mobility places an upper limit on the period and so

72 ELEMENT $28\mu\text{m}$ PERIOD -
 TWO-LEVEL DETECTOR
 $H_{XY} = 45 \text{ Oe}$ $H_Z = 100 \text{ Oe}$ $I_d = 3 \text{ ma}$
 LOW FREQUENCY CUT-OFF 1 kHz



50 kHz
 (a)



200 kHz
 (b)

0.1V/ \square VERTICAL 100 kHz/ \square HORIZONTAL
 0.1 MHz SPECTRUM

Figure 76. Zero State Spectrum Analyzer Results for
 50 and 200 kHz Detector Operation

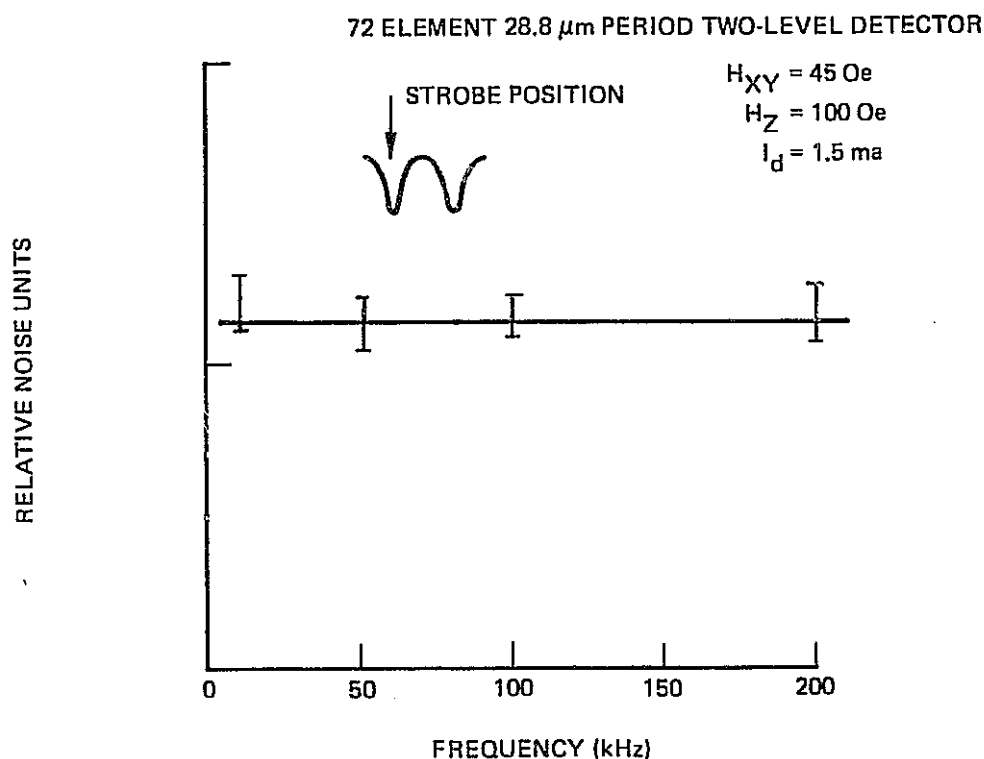


Figure 77. Frequency Dependence of Noise as Determined by Error Rate Measurements

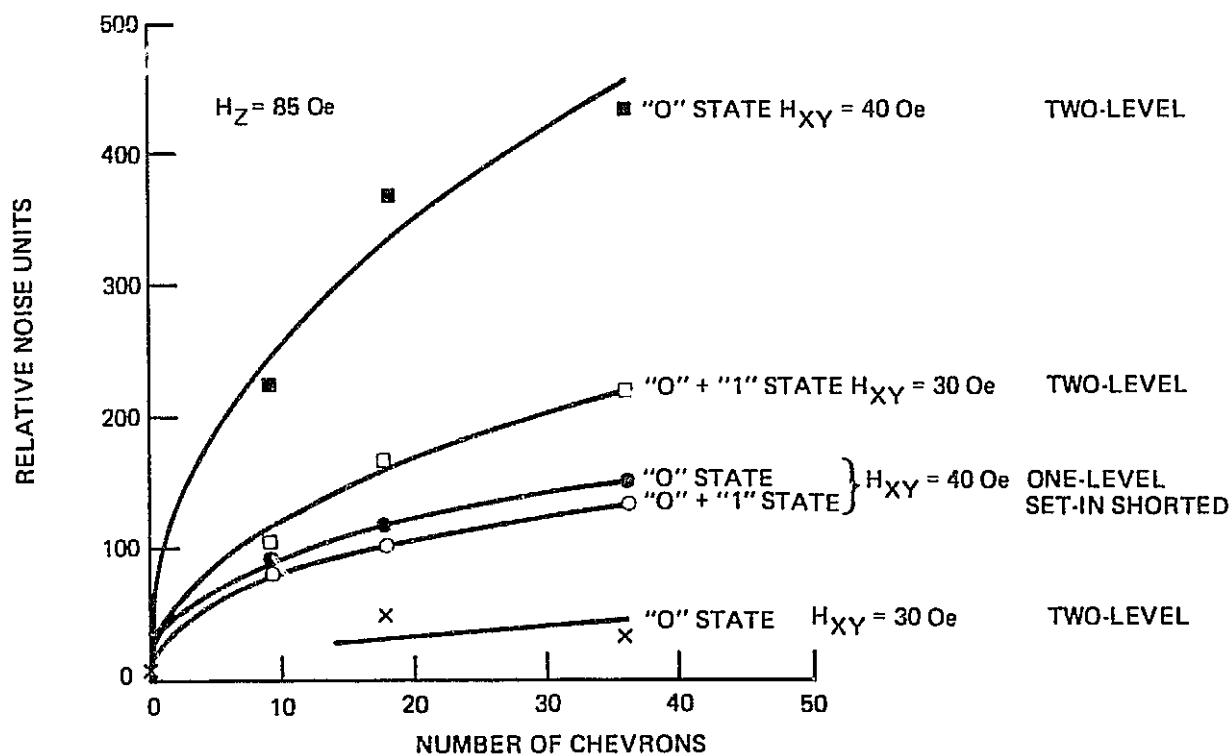


Figure 78. Zero and One State Noise for One- and Two-Level Detectors as Determined by Error Rate Measurements

this parameter is largely fixed. The thickness is also limited on the low end by margin narrowing and increased driving fields. Hence the only parameter really available for detector output optimization of a particular geometry is the line width. Just as the thickness (t) and period (L) can be used to control the demagnetizing factor so can the linewidth (W). While the exact dependence is more complicated the demagnetizing factor is expected to vary roughly like W . Thus decreasing the linewidth is equivalent to increase the period (note: $H_D \propto Wt/L$). By analogy with the period measurements narrowing the line should produce an improved output up to the point where the transition moves below the operating drive field - at which point the amplitude shift output begins to decrease and the sensitivity is expected to saturate. A procedure for doing this optimization would be to (1) first establish the minimum thickness of permalloy required by the components in the circuit for good margins and low drive field, and (2) adjust the linewidth to move the transition to a point just above the operating drive field. This procedure assumes that the operating drive field normally falls below the transition.

While the two-level detector has a much greater sensitivity than the one-level version it suffers from processing complexity. For this reason it is almost universally agreed that the best approach is to use the one-level detector and increase its sensitivity by simply making it longer. For large capacity devices the added chip area is insignificant compared to the total chip area. As has been shown the operation of these two detectors is largely the same in that they both operate primarily in the amplitude shift mode. The similarity of the drive field dependence of the magnetoresistance in the propagation direction was also pointed out. The optimization of the one-level detector therefore is largely the same as the two-level. The idea is to adjust the drive field to fall in the region of maximum magnetoresistance change for a change in drive field. The magnetoresistance transition in this case is less abrupt; however, basically the same principles apply. The magnetoresistance transition we are referring to here falls in the 20 to 60 Oe drive field range and should not be confused with the 1ω to 2ω transition which occurs at about 15 Oe for a 28μ period pattern. It is, however, interesting to compare the ultimate capabilities of the detector in both the 1ω and 2ω modes. This can be done with the aid of Figures 64 or 68. The maximum 1ω output occurs when the zero state corresponds to about 14 Oe and the one state to 22 Oe. The change as measured on Figure 68 is approximately the difference between the respective $\phi = 0$ deg and $\phi = 90$ deg curves. We obtain about 0.9v as compared to 0.3v for the 2ω output corresponding to a 30 Oe zero state and a 38 Oe one state. The outputs differ by about a factor of three. Figure 68 suggests that if the transition is made more abrupt by varying the permalloy parameters the difference between the two modes can be made considerably smaller. In principle it appears to be possible to obtain as much output in the 2ω mode as in the 1ω mode provided the abruptness of the transition can be controlled. The results for the two-level detector suggest that this is probably possible. Figure 64 indicates that thickness certainly changes the transition - it is likely that linewidth will also. It appears, however, that if the optimization procedure is to increase the 2ω output to be on the order of the 1ω , output drive fields in the neighborhood of 15 to 20 Oe will be required. Thus, low drive fields appear to be a fundamental requirement for achieving high detector outputs in both one- and two-level detectors. Whether such low drive fields can be achieved will depend upon innovation in the basic propagation element design. Currently the drive fields for the T-bar are excessively high due to the permalloy mediated bit-bit interaction. Improved designs currently exist which minimize this effect and, therefore, it is likely that with material improvements (low coercivity and high mobility) the low drive field requirement can be approached. The chevron itself presents a difficulty when the bubble size becomes

small (large $4\pi M$) because it requires a large minimum drive field. Here again it is likely that a modification will be discovered which will eliminate this problem. Our feeling is, therefore, that eventually the optimum drive fields for propagation and detection will begin to approach each other more closely.

The question of optimum detector shorting arrangement has been answered experimentally - it has been shown that end shorting yields maximum sensitivity. It is interesting to attempt to explain the result in the light of our understanding of the magnetization process in the permalloy. If we assume that the bubble produced magnetization (bubble sitting on input side of detector) in the chevrons is independent of the shorting arrangement then the dominant (2ω) output signal produced at $\phi = 0$ deg will increase as the active length of the chevron is increased by moving the shorts toward the ends. Experimentally one finds $\Delta R/R$ is independent of geometry for end and set-in shorted detectors which means that since R is higher for the end shorted version it will have a higher output. Fundamentally both of these arguments are equivalent and suggest that increasing R should be one of the prime objectives of detector optimization. If this is indeed the case then end shorting is the ultimate chevron base configuration. It also corroborates the increasing output with period found for both one- and two-level devices. The only mitigating factor revolves around what the effect the bubble phase delay has on the output. Experiments on the set-in and end shorted detectors show that the position vs field angle of the bubble as it passes through the detector element is virtually independent of the shorting. Hence we attribute the differences in sensitivity to the differences in resistance particularly since the corresponding ratios correlate well experimentally. There is, however, the possibility that by proper placement or design of the shorting arrangement a phase shift mode rather than an amplitude shift mode could be accentuated resulting in improved output. In this case end shorting may not be desirable and our criterion of maximum R may not necessarily be the correct one. Our feeling, however, is that not much more bubble phase shift can be tolerated in existing circuits without producing margin degradation. Presently the bubble lags the drive field by more than 45 deg in going from the end to the center of the chevron. It is difficult for us to imagine how to increase this phase lag since experimentally both end and set-in shorting produce nearly identical results. One possibility is to end short the chevrons adjacent to the detector with the hope that this will decrease the pushing effect and hence increase the phase lag. Modifications to the detector itself seem to be limited due to the tight tolerances involved and reluctance to decrease R .

The sensitivity and noise measurements made on the detector test patterns also pointed out another important aspect of detector design and that is in connection with cancellation of the background magnetoresistance in a bridge configuration. To obtain excellent cancellation it is necessary for the active and dummy to be identical and oriented in exactly the same direction (not for example rotated by 180 deg). The lead layouts for both the active and dummy must also be identical to provide exact cancellation in the bridge configuration. Also it is advantageous to make the interconnection leads as short as possible and to place the active and dummy as close together on the chip as possible. For this reason a guardrail detector is viewed as more desirable than the in-line detector because it allows one to realize these features much easier. Whether one uses the layout tested in connection with the on-chip bridge or a side-by-side arrangement is probably unimportant (although the latter generally requires more chip real estate) from the cancellation standpoint. Experience indicates that either approach will produce better results than those obtained for the in-line detectors in connection with the detector test mask.

The real problem with a permalloy dummy and its interconnection leads is that they produce switching noise while failing to improve the signal output. Hence the net effect is a decrease in signal to noise ratio. Since cancellation is usually not perfect anyway and since clamping and strobing techniques are used, there seems to be no reason to employ the permalloy dummy in the first place. The bubble-no-bubble change is present whether or not the sensor is placed in a bridge with a permalloy dummy or with a carbon resistor one. Hence one important conclusion coming out of the noise study is that the permalloy dummy should be eliminated. This change will increase the signal-to-noise ratio by a factor of $\sqrt{2}$. While the magnetoresistive sensor is intrinsically very good from the error rate standpoint, the effect that further increasing the signal-to-noise ratio has is to increase the threshold margin at a given error rate. When constructing a system this is desirable because one threshold is employed for many chips and the larger the net threshold margin the better. The elimination of the dummy detector has yet to be considered and studied from the sense electronic standpoint.

The frequency analysis of the detector output and noise indicates that filtering will improve the signal-to-noise ratio. This is because normally the bubble output is principally 2ω while the noise extends over a broad spectrum from dc to several megahertz. Hence by bandpass filtering at 2ω the high and low frequency components which are associated with the permalloy switching will be eliminated with little loss in signal amplitude. Exactly where to cut off the pass-band was not determined in our study but is a simple matter to determine experimentally. All that is required is to take several error rate curves as a function of the cutoff frequencies. Currently for 150 kHz operation the coupling capacitors are chosen to produce cutoff points at 10 K and 300 kHz. These values are based upon rough qualitative judgements and should be refined in the future.

Finally we conclude by mentioning areas which we feel require further investigation in connection with the detector study. Foremost is the problem of permalloy film reproducibility. Our measurements indicate that both the magnitude and shape of the zero state signals differ from lot to lot. Whether this is a result of placement in our test coils or intrinsic in the permalloy itself is unknown. Differences observed on the wafer prober suggest that it is very likely the permalloy. Other areas such as drive field dependence of the optimum strobe position as well as lot to lot reproducibility merit investigation. Also the processing dependence of the switching noise should be examined using the spectrum analyzer to characterize its amplitude.

8. TASK 7. PASSIVE REPLICATOR AND ON-CHIP BRIDGE DESIGN AND EVALUATION

In order to avoid the additional time and expense involved in obtaining a separate mask for the passive replicators and the on-chip bridge, the decision was made to incorporate both designs in a single mask. For this reason both of these topics will be covered in this section of the report.

8.1 Passive Replicator Design

The passive replicator design reported by T. J. Nelson⁴⁰ suffers from what we consider to be two undesirable features. It is suggested in the description of this component that the permalloy to garnet spacing is extremely critical. This has subsequently been confirmed by our measurements. In terms of 16μ device fabrication the optimum spacing should be about 3500\AA which means that in a two-level design the conductor height and step coverage becomes a problem. Another potential problem area is what happens to the bubble when it does not replicate at high bias. Does it run out the second track being lost permanently or does it simply continue propagating in the main loop? It would be more desirable to operate in the latter mode so that the data is not lost at high bias. It appears that the design in Ref 40 was meant to be used in a one-level chip layout. As is discussed in Para 8.2 (for the simple one-level loop tested) the margin at this spacing is adequate but the drive field is slightly higher than the optimum value. These questions and observations prompted the design of the test mask in which several different patterns were proposed to eliminate the previously discussed difficulties. The test loops are shown in Figure 79 and are motivated by basically four ideas: (1) stripping out at high bias can be improved by making the potential wells deeper and hence a series of long bars should work better than a chevron stack (Patterns A3-A10, C1, C2, C5), (2) a longer cutter means that the replicator should work at a larger spacing (Patterns A3, A5, A8-A10), (3) at high bias the bubble entering the parallel bar stretcher/T-bar configuration should continue in the main track (Patterns A3-A10), and (4) bars inserted in the center of chevron stacks (or between) may be used to steer the bubble at high bias along the desired propagation path (Patterns B9, C3, C4, C9).

The loop layouts simplify testing which may be done by trapping bits in the chevron portion of the test loop and gating these bits all the way around the loop. When this is done a matching bit pattern across from the main loop bits is obtained on the output track thus verifying operation. In Para 8.2 150 kHz results are presented for the test patterns of Figure 79 for permalloy to garnet spacings of 3500 and 5800\AA .

8.2 Fabrication and Characterization of the Passive Replicator Test Patterns

Two wafers of SmGaYIG were selected for testing with nominal stripwidths and thicknesses of $4\mu\text{m}$. The sample parameters are presented in Table 24. On one of these wafers was fabricated the test mask of Figure 79 including Al/Cu conductors for controlled generation and annihilation. The spacing between the permalloy and garnet was 5800\AA in this case. On the other wafer only the permalloy pattern was fabricated after depositing 3500\AA of SiO_2 as a spacer. The thickness of the permalloy was nominally 3000\AA for both of the processed wafers.

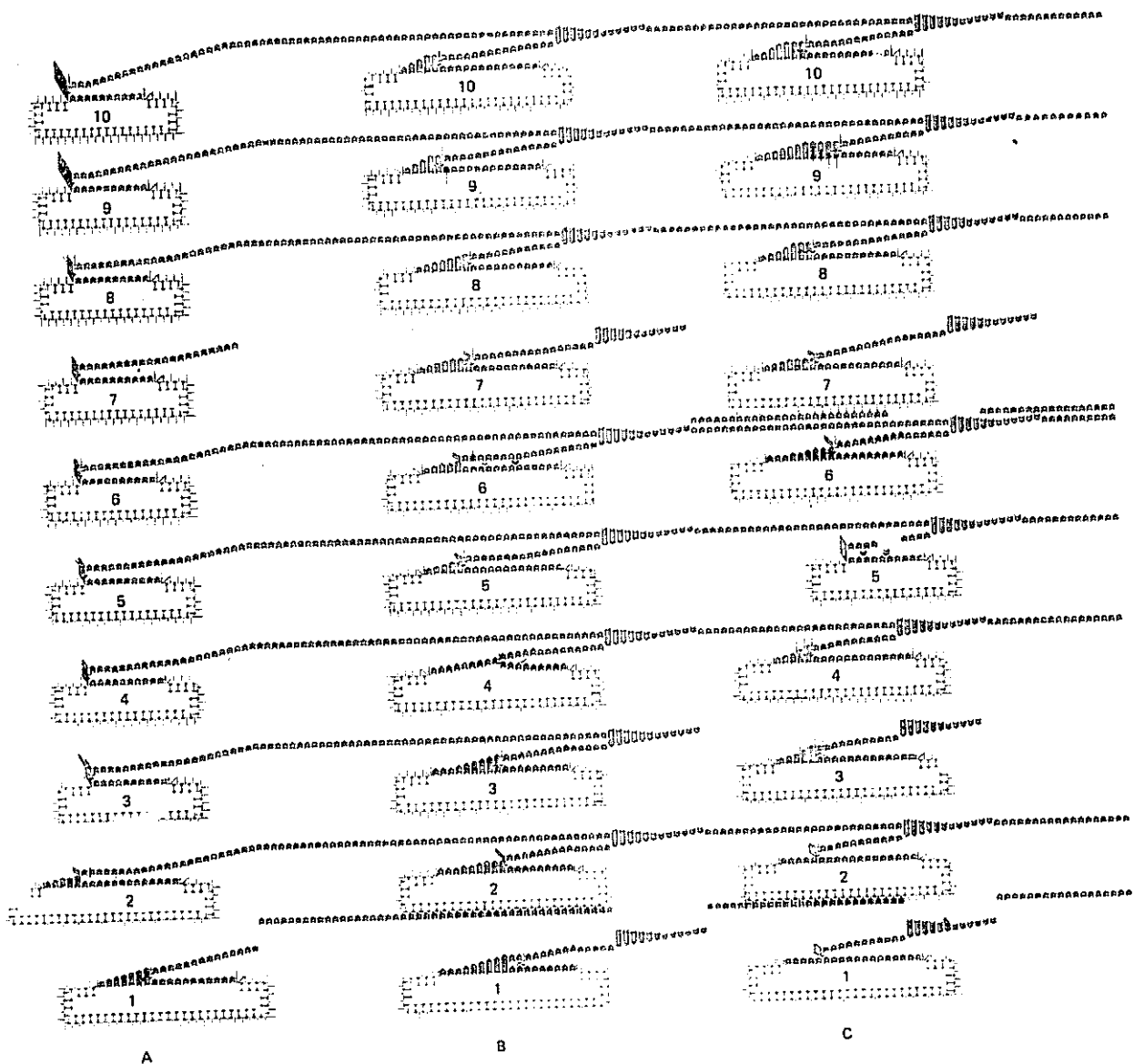


Figure 79. Test Mask Replicator Patterns

TABLE 24. WAFER FABRICATION

Composition	H_{col}	w	σ_w	$4\pi M$	h	ℓ
$Y_{2.62}Sm_{.39}Ga_{1.15}Fe_{3.85}O_{12}$	107.4	3.9	.24	250	3.0	.485
$Y_{2.62}Sm_{.39}Ga_{1.15}Fe_{3.85}O_{12}$	131.9	3.88	.231	259	3.92	.431

Preliminary margins were taken before dicing at 25 kHz to determine which of the test patterns looked promising. Only the bits at the output of the replicator were observed in these preliminary tests. Examination of the data revealed that Patterns A-1, A-8, A-9, A-10, B-10, B-8, B-3, B-2, C-10, and C-8 showed promise. These as well as some of the other patterns were then tested at 150 kHz for start-stop in the direction of propagation (solid) and in the opposite direction (dashed). The results at large spacings shown in Figure 80 indicate that the parallel bar type replicator (A-8, A-9, A-10, etc) works considerably better than the variations of the design in Ref 43 and that in fact Pattern A-9 works the best, having a 14 Oe start-stop margin. The patterns based on variations of A1 suffer from the problem that the bit one period away from the replicator bar and in front of it is lost prematurely. This occurs for either direction of shut-down and whether or not a holding field is present.

In contrast the results for a small spacing shown in Figure 81 reveal that the A1-based designs have a good margin whereas the parallel bar designs do not. The version employing 90 deg chevrons instead of 110 deg chevrons in the replicator generally does not have as wide a margin as that for 110 deg chevrons (B-8 vs B-3). Slight modifications to the basic design (such as the substitution of parallel bars) operate well which further confirm the intrinsic properties of the original design. Unfortunately a spacing of 3500A is not practical nor desirable for a 16 μ m period design from the standpoint of drive field and also from the standpoint of step coverage. Devices which have been fabricated with 4900A of SiO₂ spacer appear to operate satisfactorily yielding typical margins of 15 Oe drive field. In the future it is likely that with the advent of higher mobility materials the spacing may be increased. When and if this occurs it will be necessary to employ the parallel bar version (A-9) of the replicator. In any event passive replicator designs for large and small spacings have been tested and shown to operate well.

8.3 On-Chip Bridge Design

In most magnetic bubble device designs a dummy magnetoresistance detector in addition to the bubble sensor is included on the chip to balance out the rotating field component of the output. These magnetoresistive elements are usually connected in a bridge configuration; however, there remains the question of where to place the bridge completion resistors. Since it is desirable to keep the size of the memory substrate as small as possible to reduce the coil volume and module power dissipation, including these resistors (and/or preamplifiers) on the substrate is undesirable. The remaining alternatives are to place the completion resistors outside of the module or on the chip itself. From the standpoint of induced $d\phi/dt$ noise both approaches are probably equally good.

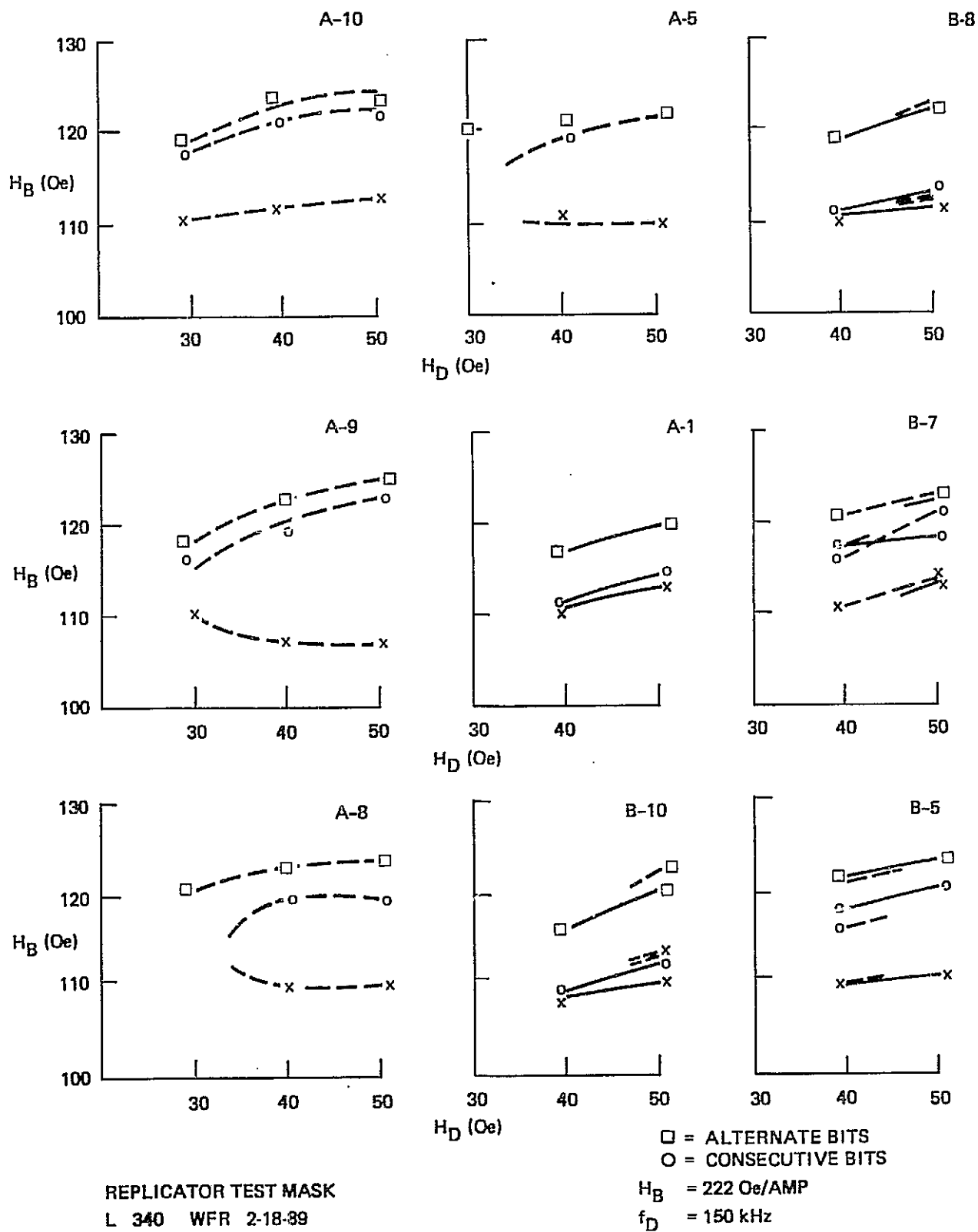
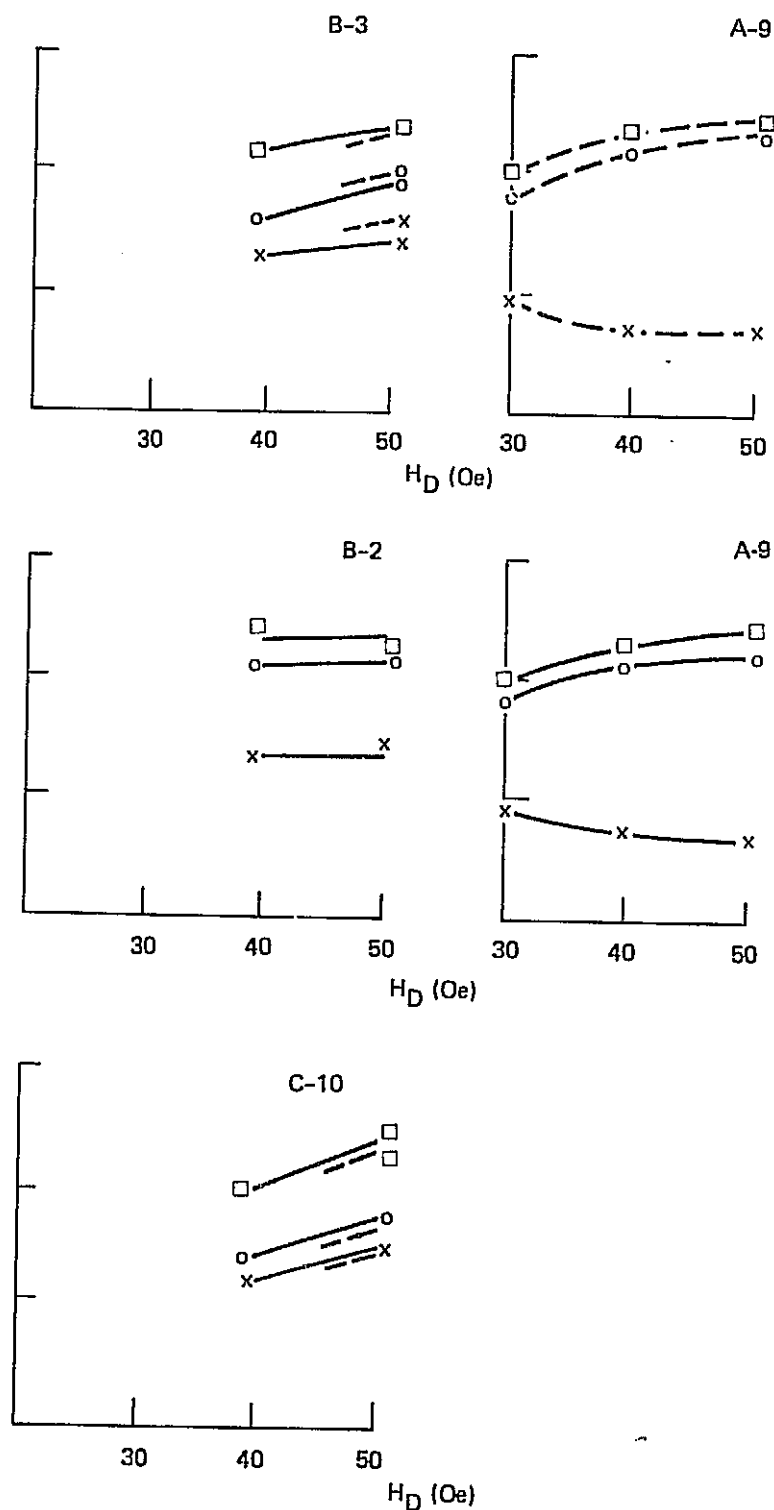


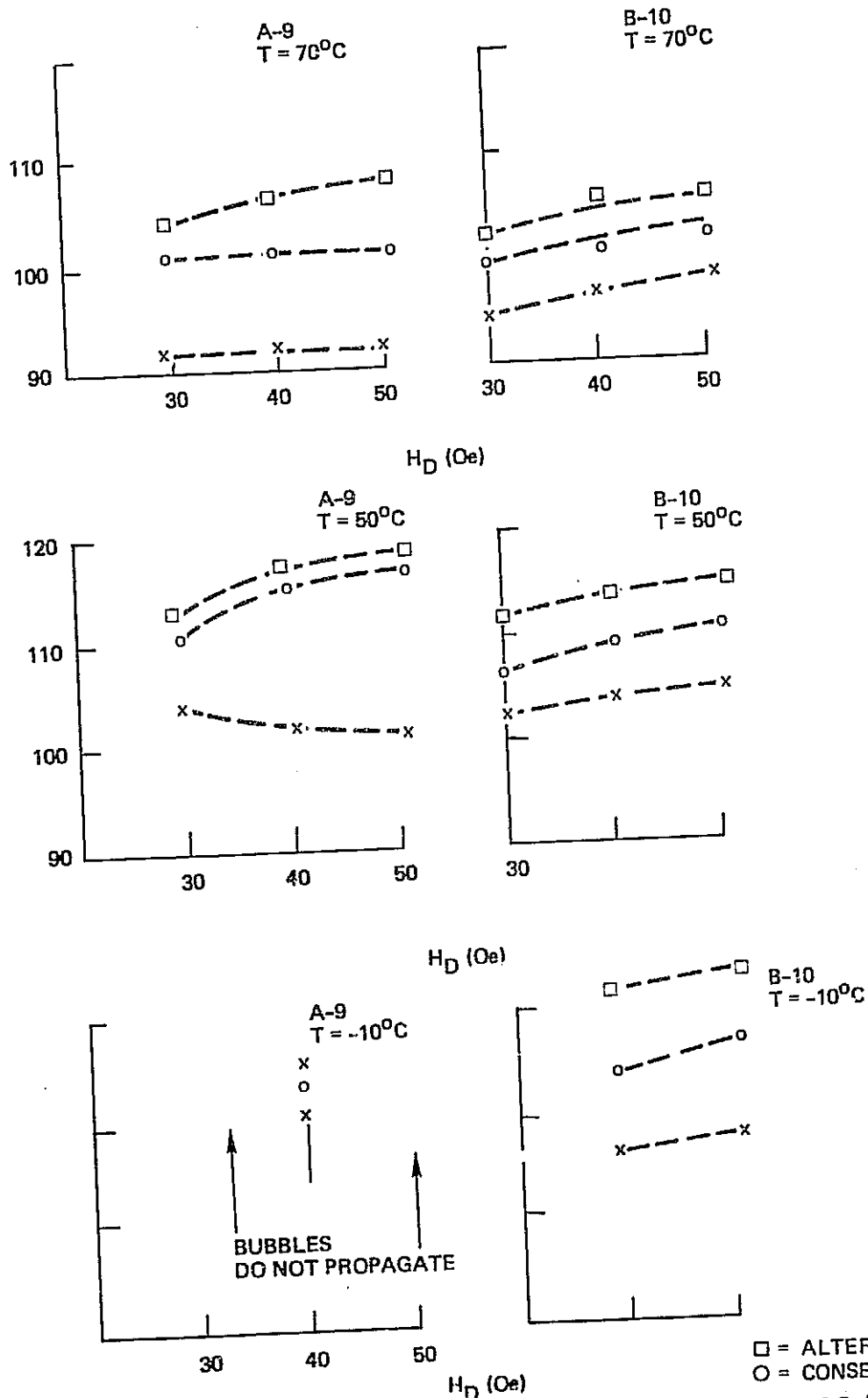
Figure 80. 150 kHz Replicator Test Results for Large Spacing



REPLICATOR TEST MASK
L 340 WFR 2-18-89

Figure 80. (Cont)

□ = ALTERNATE BITS
○ = CONSECUTIVE BITS



REPLICATOR TEST MASK
 L 340 WFR 2-18-89

Figure 80. (Cont)

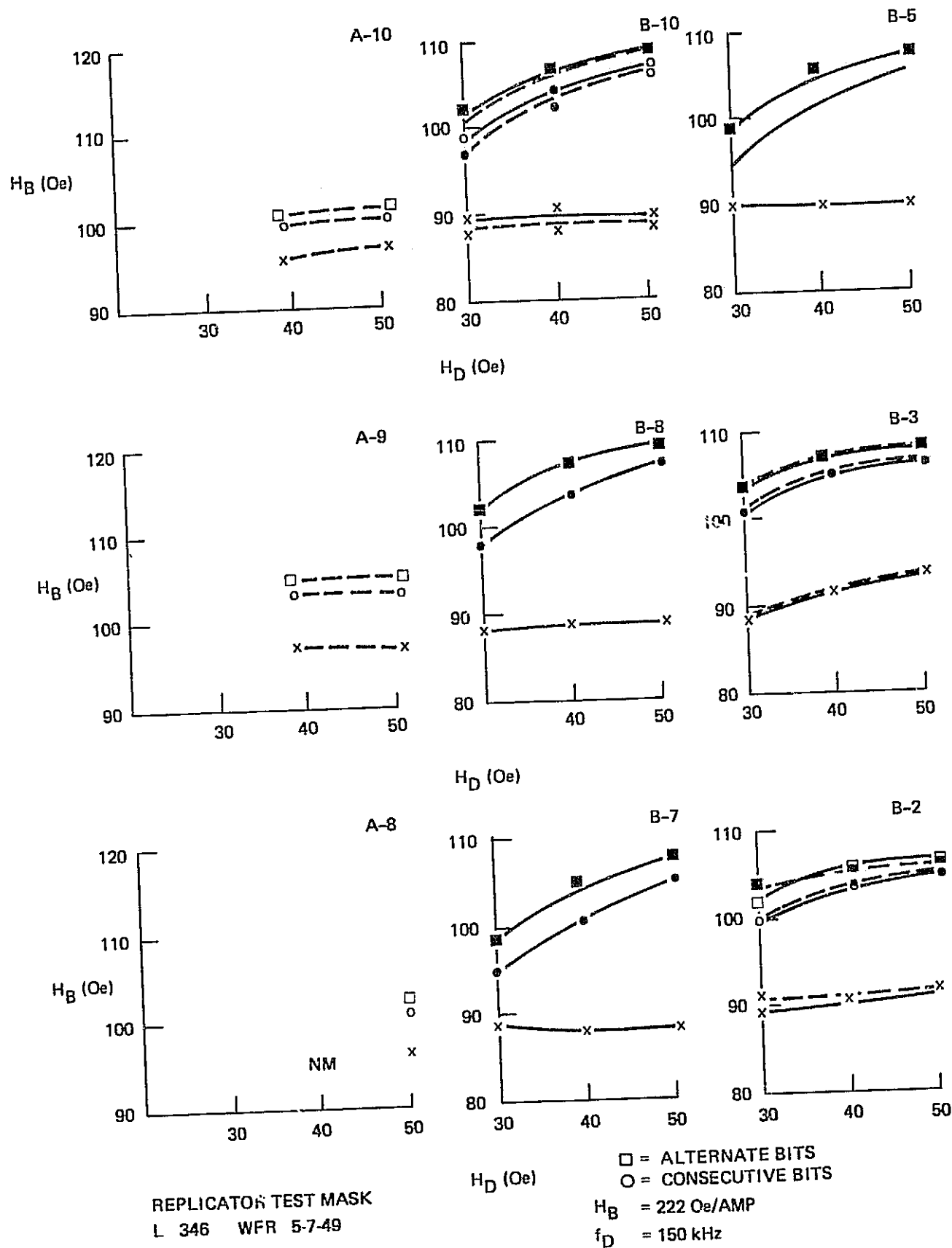
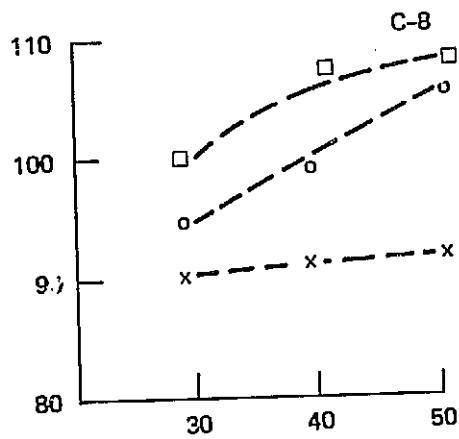
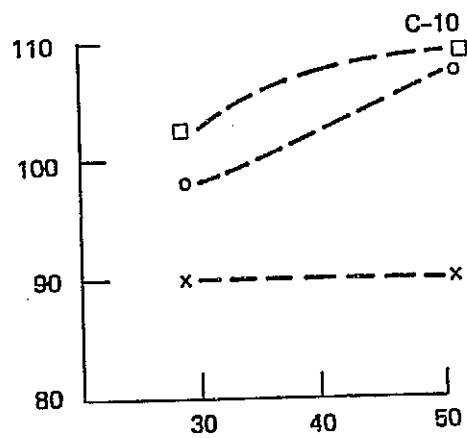
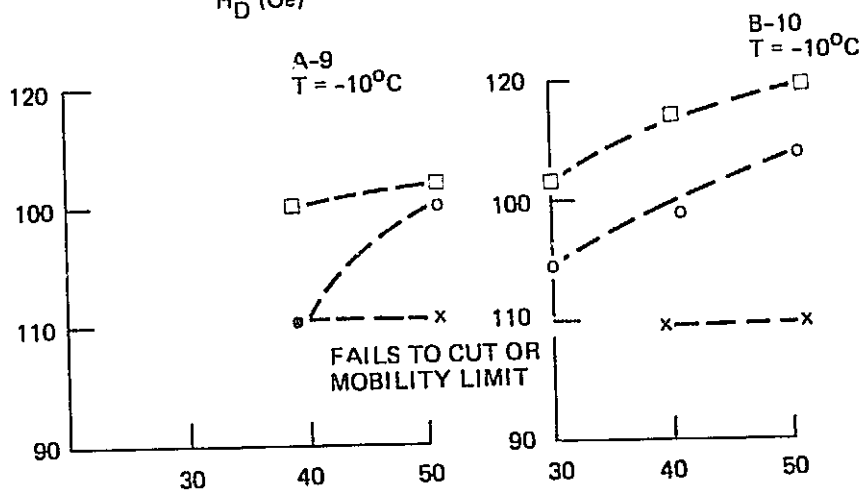
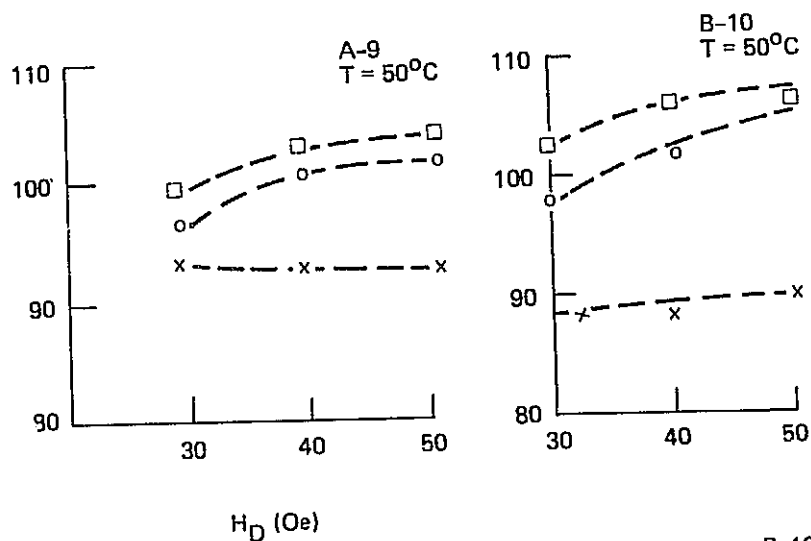
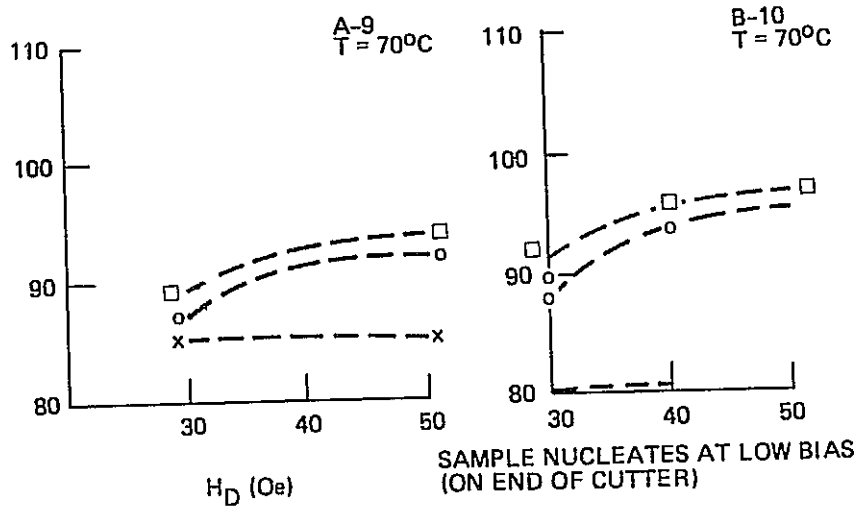


Figure 81. 150 kHz Replicator Test Results for Small Spacing



□ = ALTERNATE BITS
○ = CONSECUTIVE BITS

Figure 81. (Cont)



REPLICATOR TEST MASK
L 340 WFR 5-7-49

$H_B = 222 \text{ Oe/AMP}$
 $f_D = 150 \text{ kHz}$

□ = ALTERNATE BITS
○ = CONSECUTIVE BITS

Figure 81. (Cont)

The on-chip approach involves more chip leads and is likely to involve more switching noise if magnetoresistive elements are used as the completion resistors but would reduce the total parts count of the detector portion of a data recorder system. If a bridge configuration is used the former approach is probably the best one to use since the module package is simplified without suffering any loss in sensing capability. However, in order to determine whether an engineering advantage could be obtained by trading some noise for parts count and to investigate the feasibility of the on-chip approach, it was decided to construct and test an on-chip bridge for a 16 μ period device.

It is possible that non-permalloy bridge resistors could be incorporated into a chip design, however, the increased processing complexity makes this approach unappealing. The other alternative is to make everything out of permalloy. As has been pointed out in the section on detector noise, permalloy being switched by a rotating field acts like a noise generator. From the detector study, balancing the bridge with a permalloy dummy is undesirable from a noise standpoint and incorporating permalloy bridge resistors would seem to be even more so. Clearly this is true if all of the elements are lined up in the same direction. On the other hand rotating the two permalloy bridge resistors by 90 deg places their main noise output away from the detection region possibly improving the overall signal to noise ratio. Because the detectors must be very large to obtain the target 5 mV output it is natural therefore to place them along adjacent edges of the chip. This allows direct interconnection between them and places the associated bonding pads near the edge of the detector. It is clear that adjacent legs of the bridge must be aligned in the same direction to provide cancellation of the rotating field magnetoresistance. The only remaining unanswered questions are: (1) should the dummy be placed inside or outside of the active detector? and (2) how long should the permalloy bridge resistors be? Figure 82 shows the geometrical arrangement that was finally chosen. By allowing the bubble to pass through the dummy first the problem of stray bubbles is eliminated. Furthermore, in this configuration both dummy and active can be matched exactly. In this test pattern gold bonded interconnections between bridge components are made. This arrangement, however, allows the interconnections to be made using only permalloy. When done in this way four bonding pads result - two for the supply voltage and ground and two (located at the chip corner) for preamp inputs. Testing is facilitated by the addition of a loop generator to the input track. The other multiple input detector on the same chip is used in connection with electronic testing of the replicator loops.

For maximum bridge sensitivity the length of the bridge resistors should be made as large as is compatible with the chip geometry. Unfortunately as the length increases so does the corresponding noise. For this reason it was decided to use bridge resistors with the same resistance value as the active and dummy even though this cuts the sensitivity in half.

8.4 Test Results for an On-Chip Bridge

Based upon our previous noise measurements it was likely that the effect of adding on-chip permalloy bridge resistors would increase the magnetoresistive switching noise of the bridge thereby decreasing the signal to noise ratio and increasing the ultimate error rate. In order to test this observation, sensitivity and error rate measurements were made on a bridge with both permalloy and carbon completion resistors. The carbon resistor was chosen to have about the same value (1K) as the

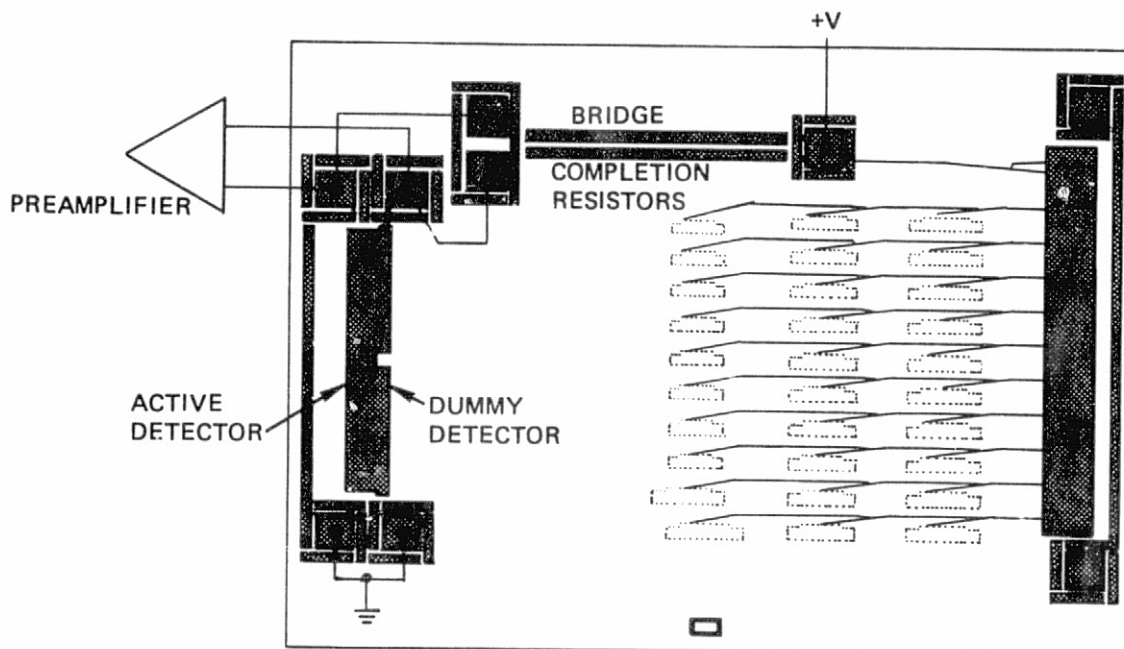
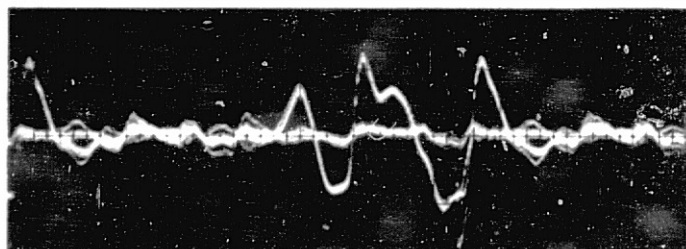


Figure 82. On-chip bridge Test Mask Arrangement

permalloy one (1.2K) which meant that only about half of the true bridge sensitivity could be achieved. As was mentioned in the previous section (for the all permalloy bridge) this was done from the layout and noise standpoint. Choosing the carbon resistors to have similar values was done to allow direct comparison of the sensitivity and error rate data.

Figure 83a shows the zero and one outputs for alternate bits in both bridge configurations. Even for the on-chip bridge the cancellation of the rotating field component of the magnetoresistance is exceptionally good. This is presumably due to the close physical proximity of the elements and also the attention paid to matching the physical layout of both bridge and active detectors. Figure 83a shows that the sensitivity of the detector is unchanged by the substitution of permalloy resistors for the carbon bridge resistors which is expected. Careful examination of the zero and one outputs, however, reveals that the additional permalloy causes the background noise to increase. This is shown more dramatically in Figure 83b where the zero outputs are compared at much higher sensitivity. Clearly the noise level of the on chip bridge is higher. To further quantify this observation error rate measurements were made on the zero and one states at the strobe position corresponding to the second positive going peak in Figure 83b.



ACTIVE + DUMMY

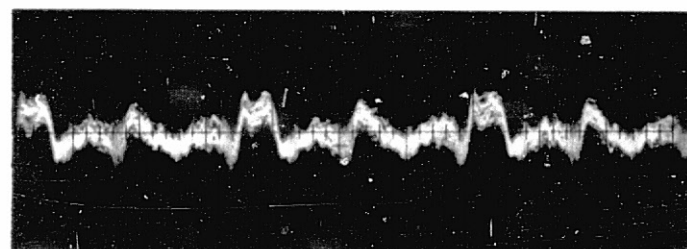
0 AND 1 STATE ALTERNATE BITS

0.2 V/CM VERTICAL

 $H_z = 115 \text{ Oe}$ $I_d = 0.5 \text{ MA}$ $H_{XY} = 1.6 \times 30 \text{ Oe}$

LIN GAIN 550

150 kHz



ACTIVE + DUMMY

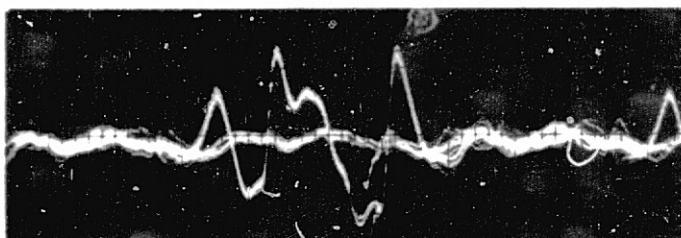
0 STATE

0.05 V/CM VERTICAL

 $H_z = 115 \text{ Oe}$ $I_d = 0.5 \text{ MA}$ $H_{XY} = 1.6 \times 30 \text{ Oe}$

LIN GAIN 550

150 kHz



ON-CHIP BRIDGE

0 AND 1 STATE ALTERNATE BITS

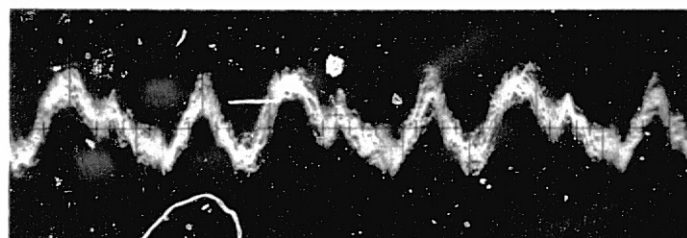
0.2 V/CM VERTICAL

 $H_z = 115 \text{ Oe}$ $I_d = 0.5 \text{ MA}$ $H_{XY} = 1.6 \times 30 \text{ Oe}$

LIN GAIN 550

150 kHz

(a)



ON-CHIP BRIDGE

0 STATE

0.05 V/CM VERTICAL

 $H_z = 115 \text{ Oe}$ $I_d = 0.5 \text{ MA}$ $H_{XY} = 1.6 \times 30 \text{ Oe}$

LIN GAIN 550

150 kHz

(b)

Figure 83. Output Test Results for On-chip Bridge (a) Comparison of Zero State Noise With and Without Permalloy Bridge Completion Resistors, (b) Comparison of Sensitivity for On-chip Bridge and Off-Chip Bridge Completion

Ordinarily one would unclamp at the peak of the first negative going output and then strobe at the peak of the second positive going peak. In this way the sensitivity is essentially doubled from the obtained by simply strobing at a given point in time. Because the bridge was not optimized for sensitivity in the first place this refinement was not employed in our measurements. Figure 84 shows a comparison of the error rate results for the on-chip-bridge and the carbon resistor version. What is of major significance is the difference in slopes of the error rate curves. Clearly using carbon bridge resistors is advantageous from the ultimate error rate standpoint. Figure 84 is somewhat misleading in that had clamping been employed the sensitivity would be essentially doubled which means that the zero and one state curves would be moved twice as far apart. In addition a factor of two in sensitivity is involved due to our choice of the 1K values of bridge resistors. Hence, the ultimate error rate of the on-chip bridge configuration is quite good. On the other hand of the resistor version is much better. At an error rate of 10^{-6} the threshold margin is 55 percent of the zero-one state sensitivity (clamped) for the on-chip bridge whereas it is 75 percent for the resistor version.

8.5 Conclusions and Recommendations

The replicator design B-10 has a very good operating margin below spacings of 0.5 μm . Preliminary tests on its reliability also have been favorable. On the other hand stroboscopic measurements indicate that at larger spacings bubbles are lost at high bias by propagation out along the replicate path. This is not the case for the diagonal bar design (A-9) and for this reason it is felt that it has the potential for better operation over a wider range of spacings. Stroboscopic observations indicate that at large spacings strip-out along the bar farthest away from the T-bar to chevron transition is the limiting factor at low bias. This can be rectified by either adding another parallel bar or one perpendicular to the propagation track in the vicinity of the parallel bar to chevron transition. At smaller spacings multiple cutting of the strip in the vicinity of the cutter becomes a problem. This problem probably can be eliminated by shortening some of the parallel bars. Also in our original design the separation between propagation paths was excessive. This can easily be corrected by reducing the number of parallel bars. Our recommendation, therefore, would be to pursue the development of the parallel bar version of the replicator by making another test mask incorporating the forementioned modifications.

The on-chip bridge has been shown to have an adequate error rate for a 400 element stretch. There is, however, considerable loss in threshold margin due to the noise produced by the bridge completion resistors. In view of the fact that a system involves the overlap of a large number of these characteristics this is not desirable. Furthermore, it is impossible to achieve the full sensitivity of the detector because the noise from the bridge completion resistors then begins to dominate when their resistance values are made large. The additional leads per chip and added power dissipation and chip complexity are also unfavorable factors. For all of these reasons we tend to favor the external bridge completion approach.

A further simplification can also be considered by eliminating even the on chip dummy detector. In this way the noise can be reduced by $\sqrt{2}$ and the signal to noise ratio is increased by the same factor and only two leads per chip are required. The only reservation we have about this approach stems from the $d\phi/dt$ noise imbalance which is likely to occur. However, this is not an unsolvable problem and should be investigated further.

Hz = 115
Id = 0.5 ma
Hxy = 1.6 X 30

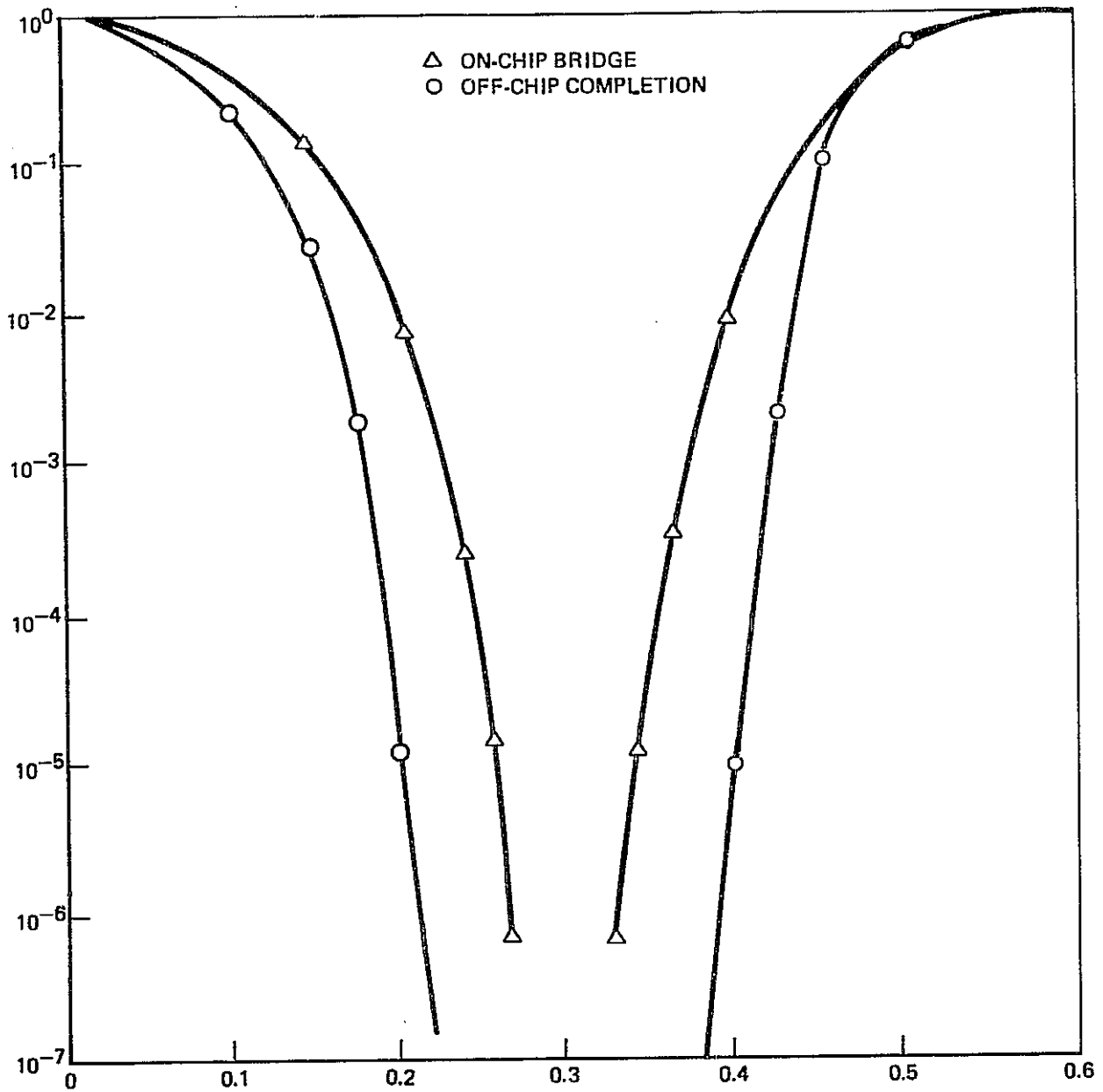


Figure 84. Comparison of Zero and One State Error Rates for On- and Off-chip Bridge Completion

9. TASK 8 - MEMORY CELL FABRICATION

The objective of this task is the fabrication and delivery of an operating bubble domain memory cell. In this respect it is unique among the Item 2 program tasks in that it results in deliverable hardware as well as technical information. The work on this task falls logically into three distinct categories which form the basis for this section of the report:

1. Design, fabrication and evaluation of an improved memory element with a capacity of $\approx 10^4$ bits. The basis for the design is the information gained in the previous tasks.
2. Design, fabrication and characterization of a memory cell package.
3. Integration of memory elements into the package and characterization of the memory cell.

9.1 Memory Element Design and Characterization

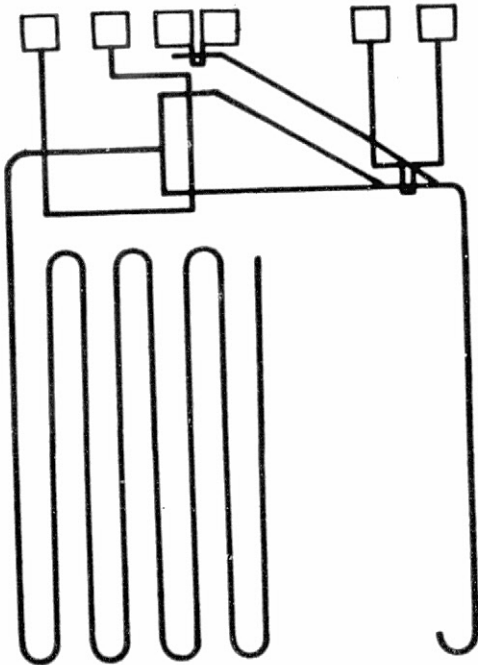
9.1.1 10^4 Bit Chip Architecture. - Several alternative chip layouts exist for the realization of a simple register. The principal factors indicating which approach is more desirable stem from detector and system requirements. From the system point of view it is desirable to have the read, write and erase functions coincident. This simplifies the electronic control and housekeeping requirements. From the sense electronics standpoint a several millivolt output is desirable from noise considerations as well as sense channel availability. In order to get an output of this magnitude from the magnetoresistive sensor it is necessary to make the stretcher one hundred or more chevrons high. Figure 85 summarizes several possible arrangements in connection with a simple register and indicates their advantages.

For the no replicator in-line detector approach, Figure 85a, coincidence of the erase function with read and write cannot be realized. This chip architecture is the one employed in the first and second 100K bit chip versions (see Item I report). For the prototype recorder it is desirable to have this coincidence condition thus this architecture is not very attractive. In addition, for the long detector stretches anticipated this approach becomes rather impractical because of the large area required to reduce the strip back to a bubble.

By employing a guardrail detector in conjunction with a replicator, coincidence of the read, write and erase function can be realized. Also detectors with stretches greater than 100 elements can be easily attained in the guardrail where gradual reduction of the strip to a bubble is not required. The simplest approach uses one-passive replicator and has the same number of leads as the no-replicator design.

Some problems in the single passive replicator approach may be encountered with consecutive bit stripout, especially in the asynchronous mode. Since the design of this 10 Kbit chip is considered to be intermediate between the second and third 100 Kbit versions it was decided that two replicators leading into separate detectors (Figure 85c) be used to enable the comparison of alternate and consecutive bit detection. Such an approach requires an additional set of annihilators and pads. The operation with two

(a) NO REPLICATOR – IN LINE DETECTOR



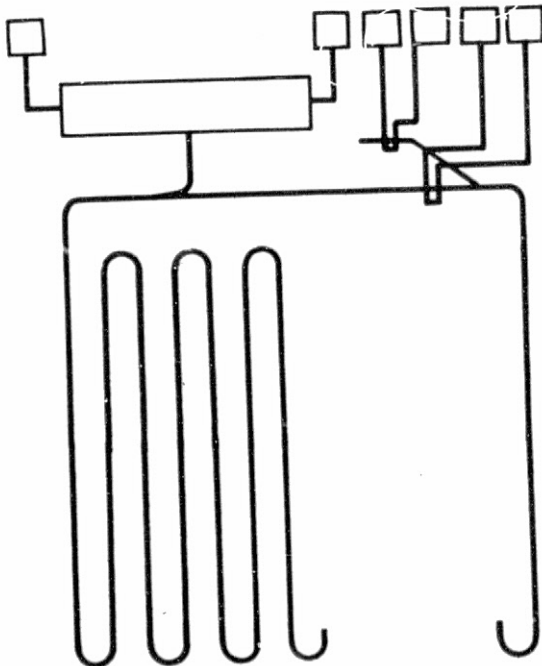
ADVANTAGES

- FEW LEADS

DISADVANTAGES

- STRETCH LIMITED
- EXCESSIVE CHIP AREA REQUIRED
- BIT-BIT INTERACTIONS MAY LIMIT MARGIN
- DELAY FOR ANNIHILATION (ERASE)

(b) SINGLE – PASSIVE REPLICATOR



ADVANTAGES

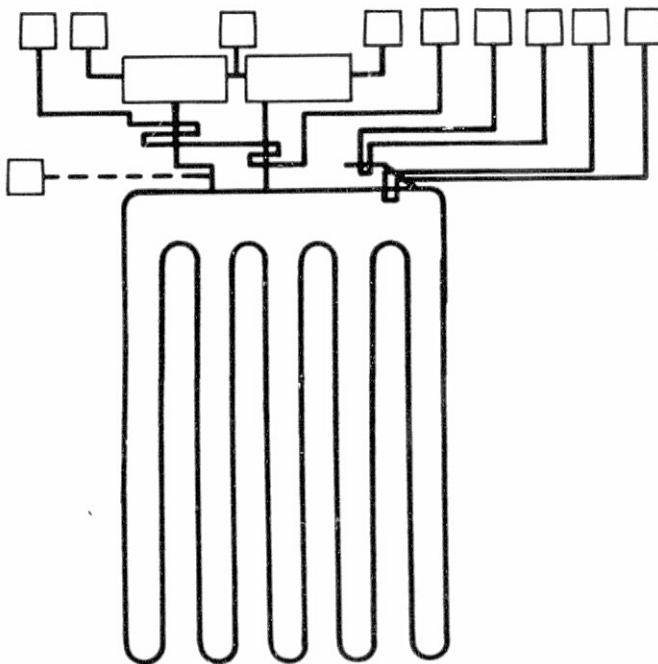
- FEW LEADS
- NO DELAY FOR READ, WRITE, ERASE

DISADVANTAGES

- BIT-BIT INTERACTIONS MAY LIMIT MARGINS (COMPATIBLE WITH REPLICATOR MARGINS, HOWEVER)

Figure 85. Chip Organizations

(c) TWO-PASSIVE REPLICATORS



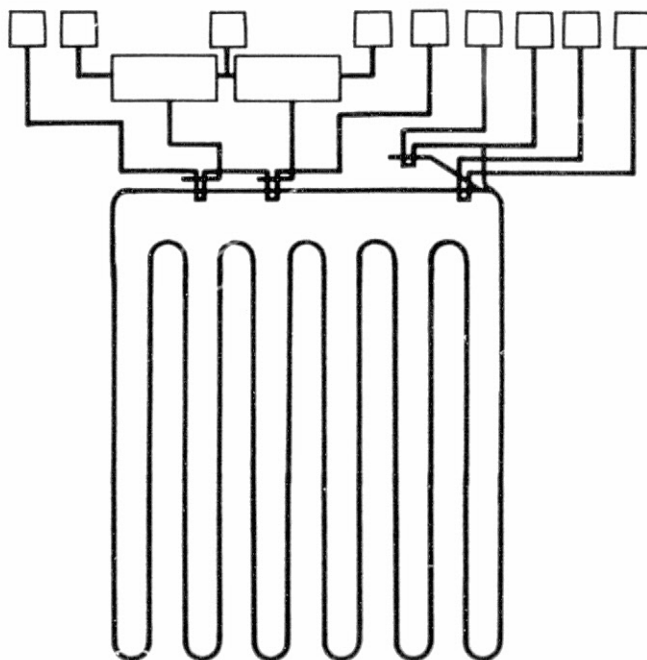
ADVANTAGES

- MARGIN NOT LIMITED BY STRIP-OUT IN DETECTOR.
- MARGIN WIDER THAN WHEN ACTIVE REPLICATORS USED.
- CAN ADD ANOTHER LEAD AND TEST ONE-PASSIVE REPLICATOR DESIGN

DISADVANTAGES

- LARGE NUMBER OF LEADS
- CUMBERSOME LAYOUT
- DIFFICULT TO REALIZE READ, WRITE, ERASE COINCIDENCE

(d) TWO-ACTIVE REPLICATORS



ADVANTAGES

- MARGIN NOT LIMITED BY STRIP-OUT IN DETECTOR.

DISADVANTAGES

- LARGE NUMBER OF LEADS.
- REPLICATOR MARGINS NOT OPTIMUM FOR CONSECUTIVE BITS.
- DIFFICULT TO REALIZE READ, WRITE, ERASE COINCIDENCE

Figure 85. (Concluded)

passive replicators and two annihilators is such that alternate bits are collapsed in each replicator stream and these resulting streams are separated by one bit in time when entering the detectors. In this way each half of the detector detects every other bit with the other half acting as the dummy at the instant of detection. By adding a third lead it is possible to collapse one stream entirely and in this way to test the one replicator version which is really the most desirable if it works well.

Figure 86 shows the phase diagram for the two passive replicator chip layout and Figure 87 shows the actual chip layout and components we have chosen to realize the desired design. The chip capacity is 10,240 bits. T-bar storage is used along with chevron-based input-output components. The basic linewidth and gap parameters in this design were changed from $2.4\text{ }\mu\text{m}$ and $1\text{ }\mu\text{m}$ values of the second version of the 10^5 bit chip to $2\text{ }\mu\text{m}$ and $0.8\text{ }\mu\text{m}$ respectively. These changes were based on the scaling of larger bubble test patterns and the refinement of mask and device fabrication techniques. The gradual chevron corners leading into the detector are required because no tested alternative exists for an outside chevron corner. The inside corner does, however, exist and is used in going into one of the detectors. The detectors are end shorted as it was felt that this would give the highest output (See Section 7). The detector stretch was increased to approximately 280 chevrons. This stretch can provide an ultimate signal sensitivity of at least 2.3 mv/ma which is 2.8 times that of the second version 100K bit chip. About 20 periods is allotted to stretch-out which should be adequate for even the lowest mobility materials provided the bit-bit interaction does not become excessive. Based on the results of Section 7 the period in chevron area was increased to $18\text{ }\mu\text{m}$ whereas it is $16\text{ }\mu\text{m}$ elsewhere in the pattern.

The T-bar to chevron merges have been tried in connection with a previous 10^4 bit design and appear to work well. Dummy T-bar loops are provided outside of the storage area and further act to eliminate stray bubbles from entering the register on the sides. The dummy loops feed out to the guard-rail which is made out of oversized T's to cut down on plotting time. In the vicinity of the detector, standard chevrons are used to isolate the permalloy bonding pads from the register region. The last four chevron stacks of the detector act as a guardrail.

In connection with T-bar storage, the bent-H and T-X corners are employed as has been done in second 100K bit design. The T-X corner has been modified slightly to facilitate the pattern generation and to improve the margin based on comparative testing. The input/output components are chevron based and are the standard loop annihilator and generator design that has been used in the past. The alignment of the loop annihilator has been changed slightly, however, so that the loop is centered on the input side of a chevron rather than in the gap. This alignment increases the phase margin of the annihilators to at least 90 deg because the bubble sits on the input side of the chevron considerably longer than it does in the gap. This has been confirmed experimentally by stroboscopic measurement of the bubble position. No such change has been made in connection with the loop generator because its phase margin is already on the order of 270 deg .

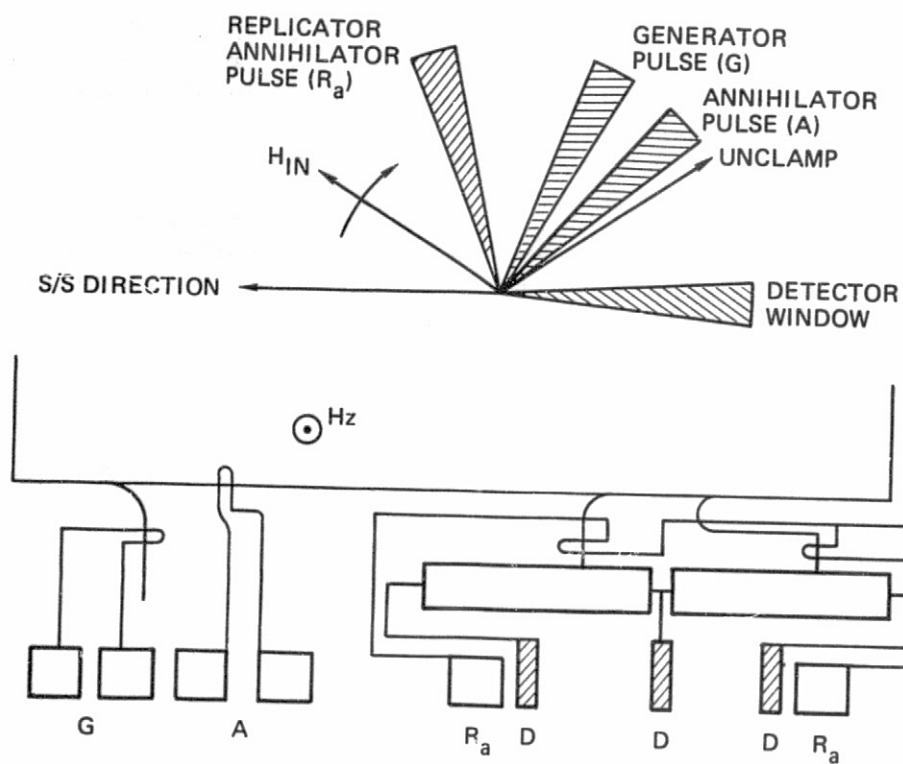


Figure 86. Nominal Pulse Phasing and Pulsewidth for the 10K Bit Chip

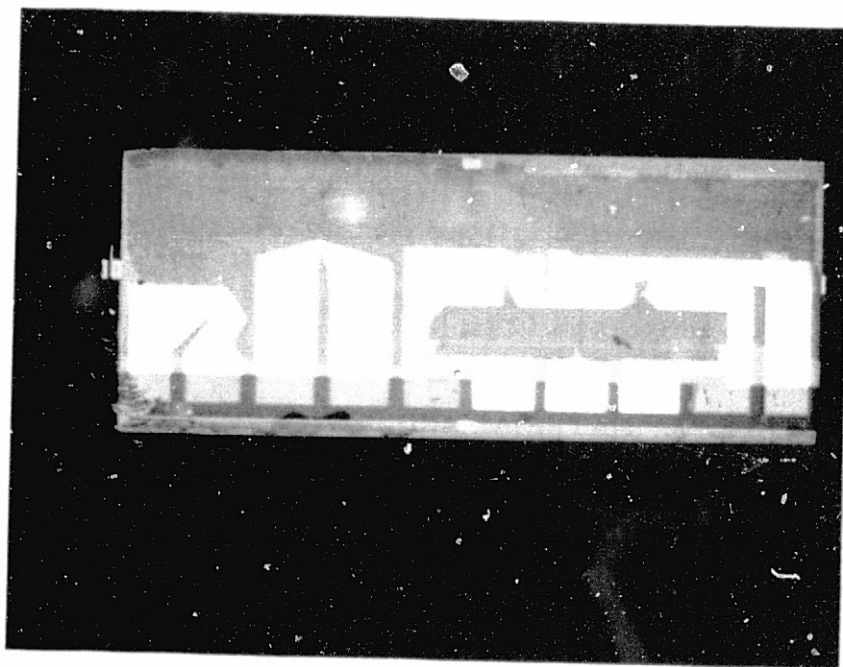


Figure 87. 10K Bit Chip

9.1.2 Design Evaluation (Continuous Operation). - The first device characterization measurements made on the 10^4 bit chip were for continuous operation at 150 kHz and at room temperature. The material and device parameters for the tested chip are presented in Table 25. As was pointed out in connection with the replicator study permalloy to garnet spacing is a critical parameter in-so-far-as replication is concerned. Accordingly as Table 25 indicates the spacing was chosen to be considerably less than 3500 Å for which margin degradation in the replicator was known to occur. The continuous propagating margin is shown in Figure 88. Various bit patterns were written into the chip and the chip operation was observed using the linear detector output signal. It should be noted here that in Para 9.1.3 the chip margins are determined by using the logical detector output which can record errors much faster than by observing the linear output. Thus, the margins presented in this subsection on design evaluation will usually be about 4 or 5 Oe greater than those in the next subsection. As can be seen from Figure 88 at about 50 Oe drive field the full chip margin is 14 Oe for the worst case bit pattern. Note that the minimum drive field is on the order of 36 Oe. Even though a replicator component is being used the minimum drive field is slightly better than the second version 100 K bit chip. This may possibly be due to the reduction in linewidth and gap dimensions, not to mention the reduction in the material stripwidth from 4.1 μm to less than 3.5 μm .

Further measurements were then made to determine what the limiting components were in the design. This was done by pulsing the bias field as a stream of bubbles passed the component in question. The data stream was subsequently electronically detected and the margin limits for that component determined. The results of these measurements appear in Figure 89 and indicate that either replication fails to occur or alternatively collapse occurs in the curved chevron section of track between the replicator and detector. Because the data in latter section of track is a duplicate of that stored in the register this results in a soft error margin limit which falls below the hard error limits of other components and in particular the replicator itself. It is believed that this soft error limit may be a result of the larger permalloy-to-garnet spacing which occurs at the chevron portion of the circuit due to an underlying conductor. Removal of this conductor (added for testing purpose) should improve the margin, and according to Figure 89, yield an overall margin limited by the replicator at the high bias end and the bent-H corner at the low end.

Finally to ensure that the chip would operate over a broad temperature range at 150 kHz continuous margin measurements were made at -10°C and 60°C . The 60°C results are shown in Figure 90 and are largely similar to the 25°C results and for this reason will not be discussed. The -10°C results which appear in Figure 91, however, are somewhat different, particularly at low drive fields. Examination of

TABLE 25. MATERIAL AND DEVICE PARAMETERS

Wafer	H_{col} (Oe)	σ_w (ergs/cm ²)	$4\pi M$ (gauss)	$w(\mu\text{m})$	$h(\mu\text{m})$
(SmGaYIG)	128.8	.22	266	3.31	3.09
Process Layer	SiO_2	AlCu	SiO_2	NiFe	
Thickness	800	4100	4500	3100 Å	

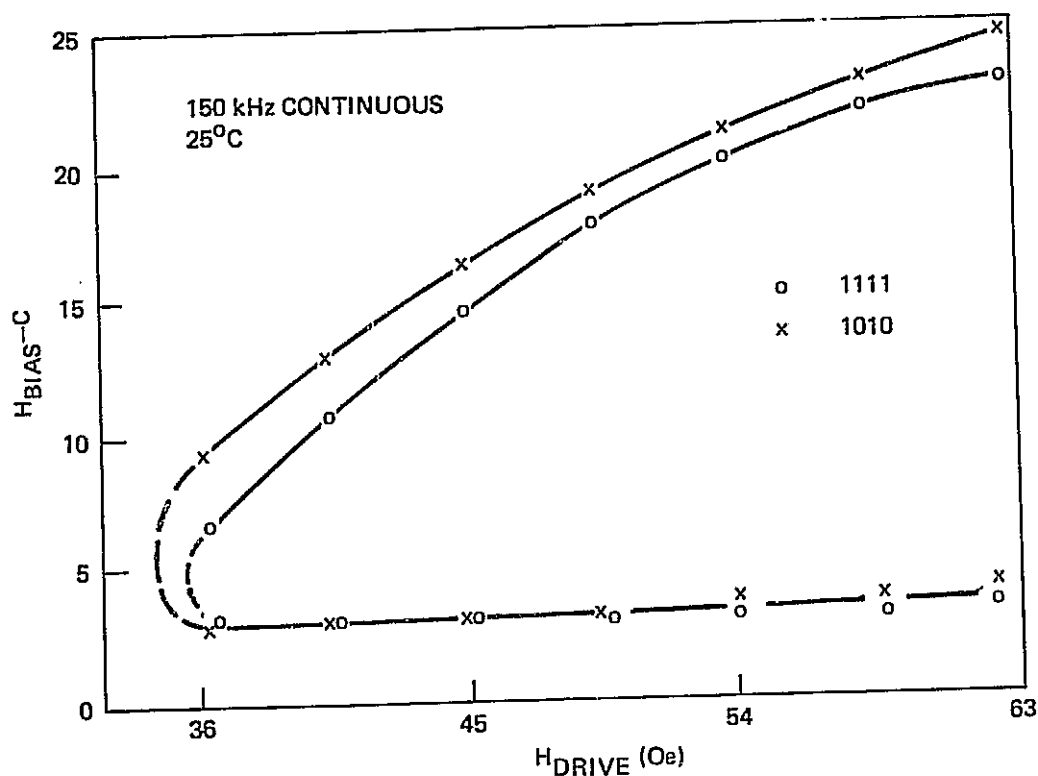


Figure 88. Overall Operating Margin of the 10 Kbit Chip at 25°C

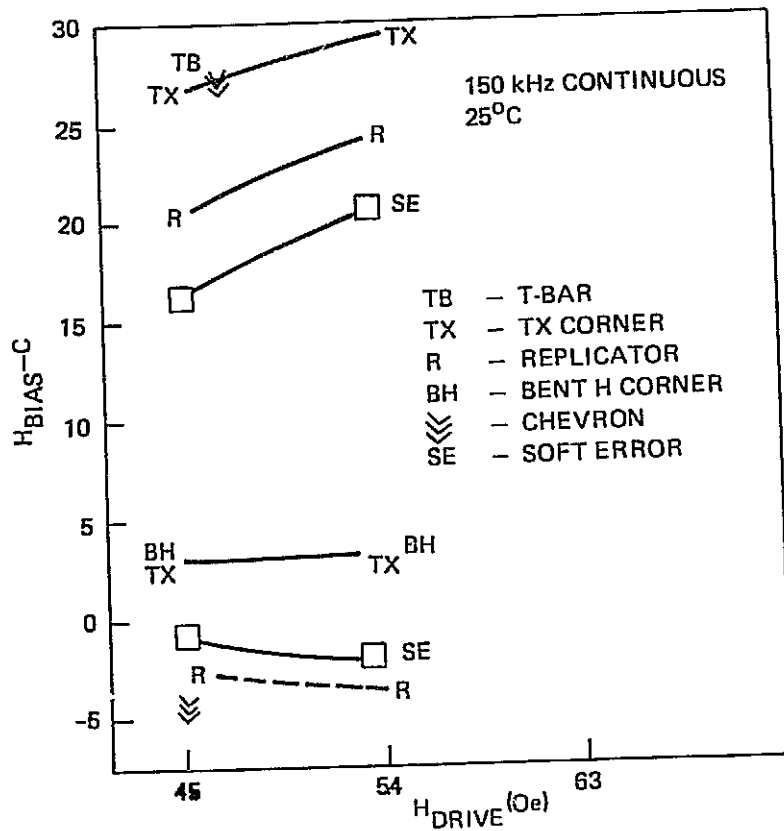


Figure 89. Operating Margins of Several Components of the 10 Kbit Chip

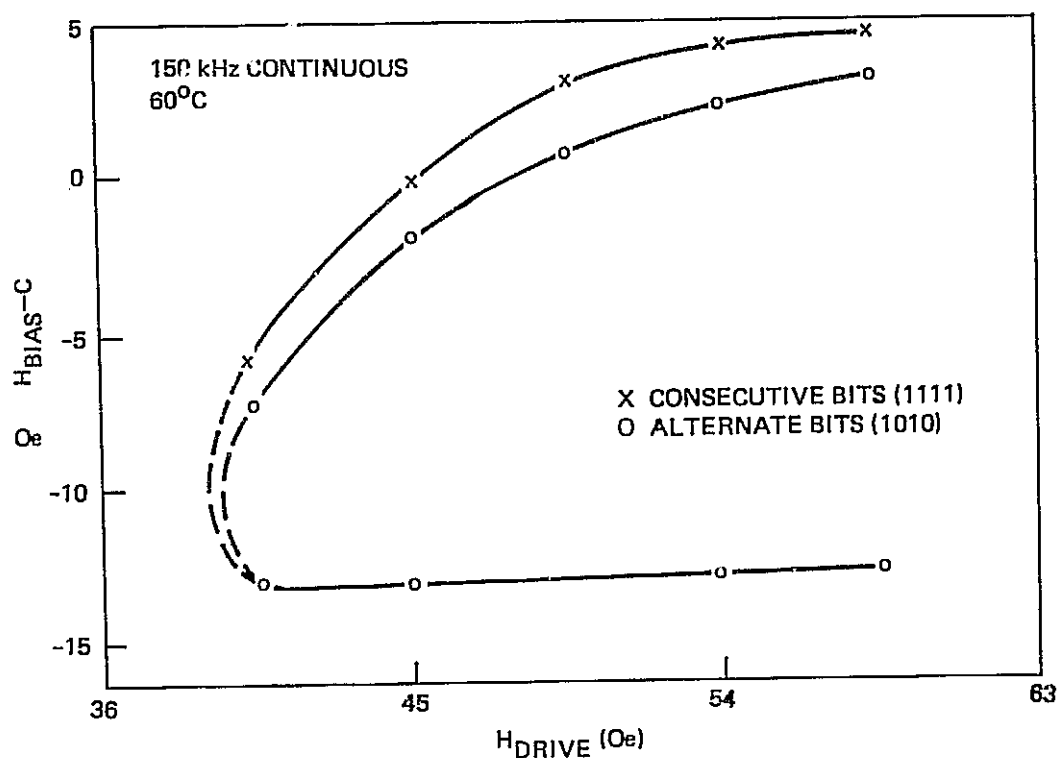


Figure 90. Operating Margin of the 10 Kbit Chip at 60°C

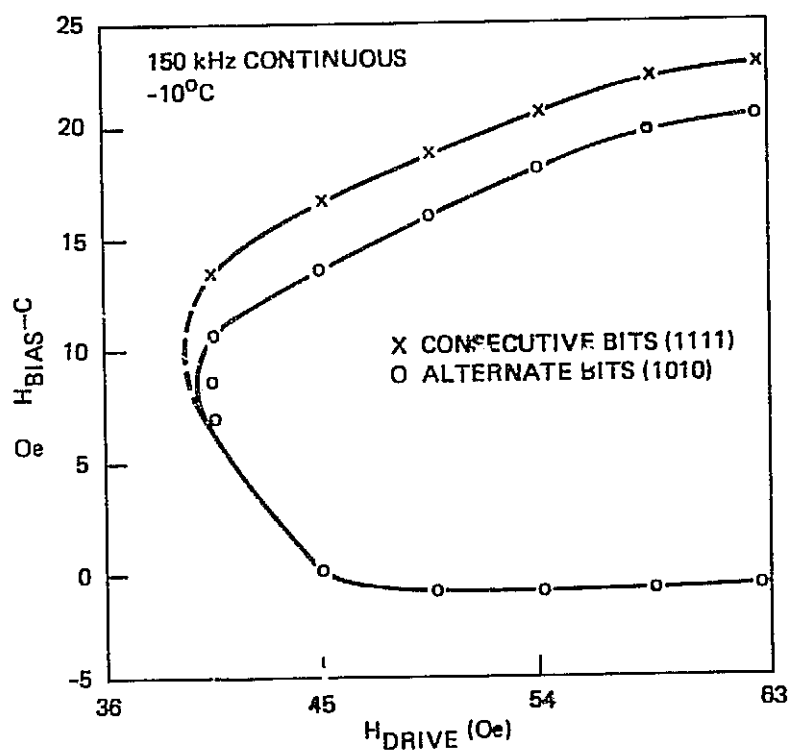


Figure 91. Operating Margin of the 10 Kbit Chip at -10°C

the margin shows that the low drive field end is considerably blunter. This is believed to be a result of the higher wall energy of the garnet which makes replication more difficult at low drive fields. Had the permalloy to garnet spacing been smaller than 5500 Å it is likely this effect would not have been observed. On the whole Figures 88, 90 and 91, show that the design operates continuously quite adequately over the -10 to 60°C temperature range at a drive field of 45 - 50 Oe.

Start-Stop. - Because the test chip is to be operated asynchronously it is necessary to ensure that no loss of data occurs during start-stop. For this reason gated measurements were made at the temperature limits of -10°C and 60°C. These measurements were made by filling the register with several words and then gating the information around to the detector during which time the bias is pulsed positive or negative. Turn-on and turn-off was made to coincide with the direction of propagation in the chevron portion of the register in these measurements which corresponds to the most favorable start-stop direction in the T-bar section of the storage loop. From previous measurements on the replicator it was known that for this component shut-down parallel or anti-parallel to the chevron propagation direction would produce favorable margins. The results for -10°C appear in Figure 92.

A reasonable margin was obtained for this particular orientation; however measurements made on the domain stripout for the bit in the detector indicated that extremely long precharge times would be required in order to detect the first bit upon initiation of the field rotation. The domain for this orientation rests in or near the gap of the chevron columns in the detector. These measurements were obtained in connection with an in-house study in support of this program and are presented in more detail in the Item I report. These data suggested that this start/stop direction will not allow first bit detection. More recent data on a 10^5 bit chip of a similar design indicates that first bit detection can be attained at the expense of reduced margin. Other measurements on the stripout indicated that reasonable stripout times could be obtained for the start/stop direction parallel to the chevron propagation direction in the detector. However, for this case the start/stop direction is such that the bubbles would stop on the apex of the chevrons in the composing track and on the ends of the T's (or H's) in the T-bar area. Preliminary data on the start/stop reliability for this direction for the chip as a whole indicates that reasonable margins can be expected if large holding fields (~6.9 Oe) are employed. Therefore, the start/stop direction for this type of guardrail chip layout should be parallel to the direction of propagation in the detector in order to accomplish first bit detection in the asynchronous mode. It should be noted that this problem was not observed for the in-line chip because the most favorable start/stop direction for the storage region was also the one required for the detector.

Components. - The data of Figure 92 do not indicate that the bent H corner is an important factor in limiting the margin. This is apparently due to the tilt of the chip relative to the Z-bias which makes other components appear worse. It has been noted, however, in connection with other designs that for unfavorable field orientations the diagonal bar bent H corner caused margin narrowing, and therefore investigation of the start/stop characteristics of this corner was made. As the chip is presently laid out diagonal bars produce both favorable and unfavorable environments for turn-off due to the presence of the bent H corner and a 90 deg corner modification. For comparison purposes start/stop measurements were made on the T-bar track alone (bent H region) and these results appear in Figure 93 for both favorable and unfavorable in-plane field. As can be seen, the upper margin shows very little sensitivity to the in-plane field in the 0 to 6 Oe range with the margin limit falling at about 26 Oe for orientation B. At 43 Oe drive Figure 94 shows that for the bent H with the diagonal bar and associated 90 deg

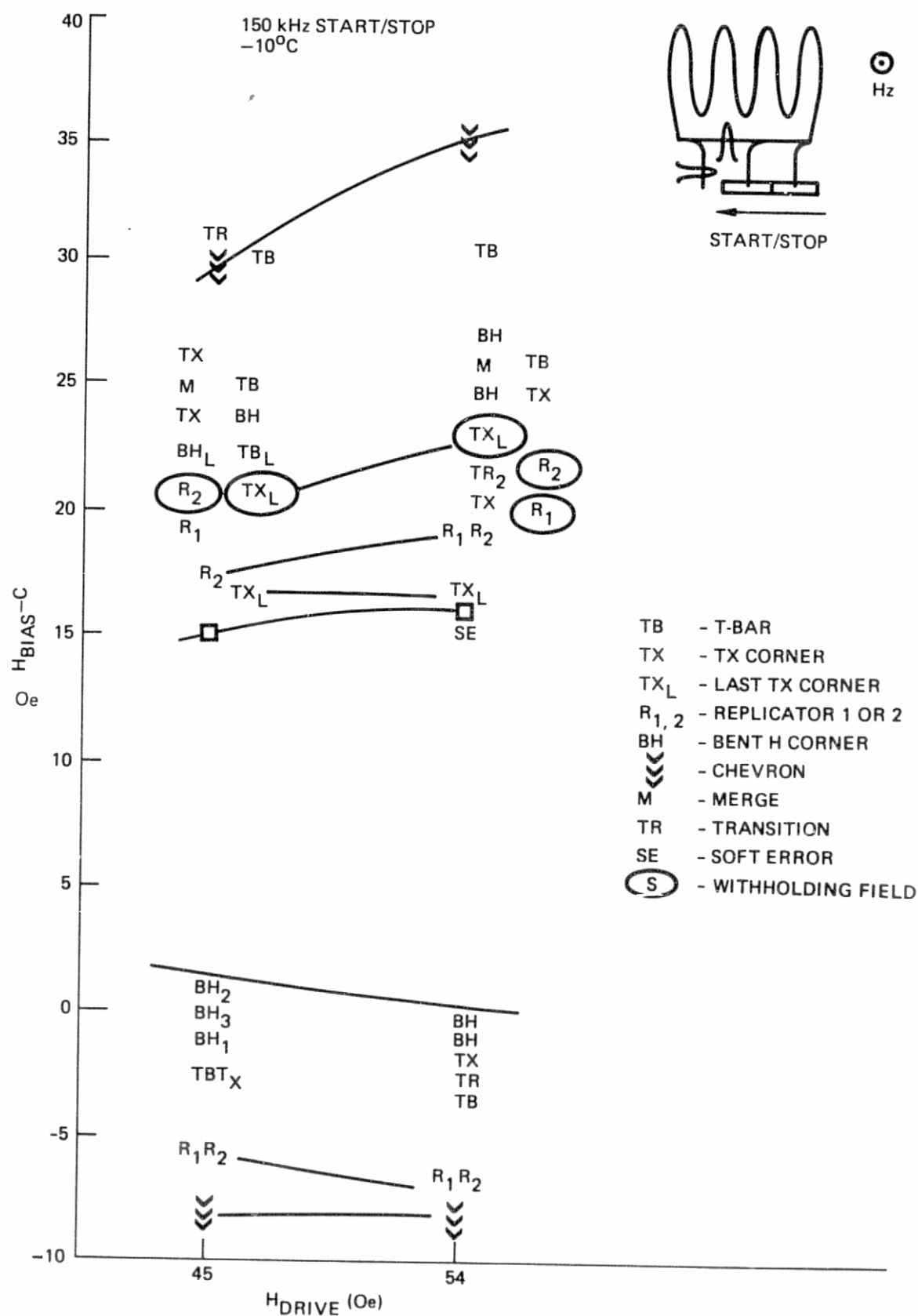


Figure 92. Start/Stop Operating Margins of Several Components of the 10K Bit Chip at -10°C

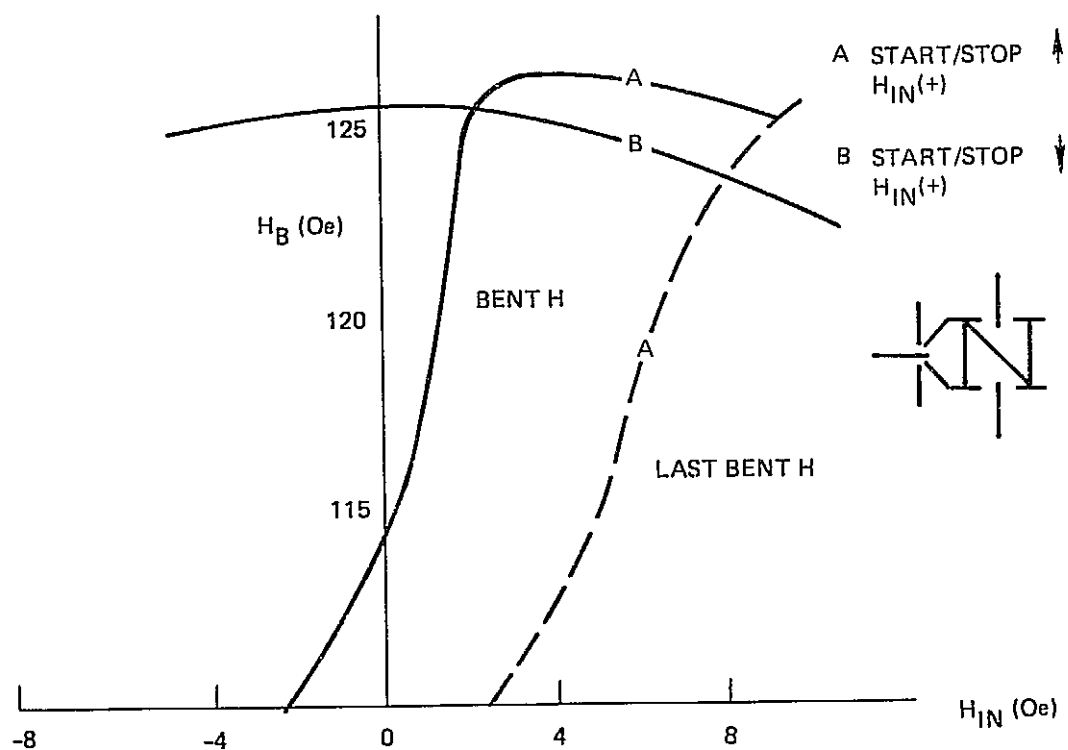


Figure 93. The Upper Margin Edge for Start/Stop vs the d-c In-Plane Field for the Bent II Corner With a Diagonal Bar
130

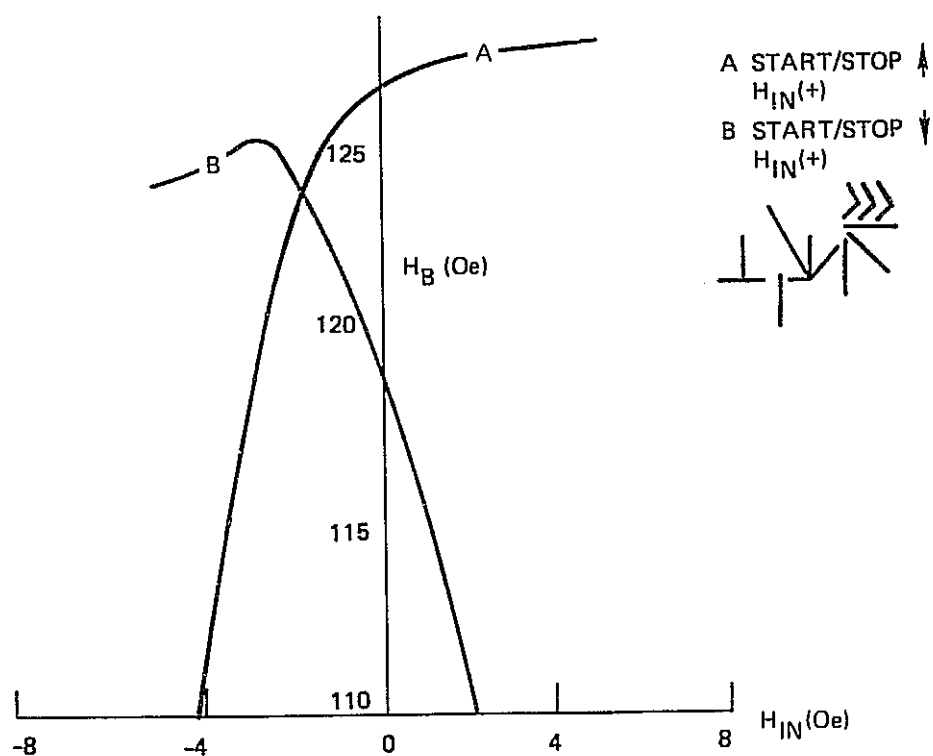


Figure 94. The Upper Margin Edge for Start/Stop vs the In-Plane d-c Field for the 90 deg T-Bar Corner With a Diagonal Bar

corner the situation may be less favorable. Independent measurements made on another sample in a different coil fail to show the same behavior, so that these results currently are in question. The fact that the bent H in the last column of the storage area where there are no adjacent diagonal bar bent H corners shows such a large difference from the other bent H's is particularly puzzling since a special effort was made to maintain identical environments by placing adjacent T's in that area. Figure 93 indicates that nearly 8 Oe favorable in-plane field is required to maintain the upper limit at 126 Oe. Further measurements are still in progress to crosscheck these results.

9.1.3 Testing of devices for the memory cell-wafer level data. - A SmGaYIG wafer was selected for 10^4 bit device fabrication. Standard magnetic bubble device processing techniques were used to fabricate these devices. Prior to the dicing operation the individual registers are tested using the wafer probe station. The wafer probe station provides the necessary magnetic fields and bondless contacts to singularly establish the integrity of each register on the wafer. The operating bias for the continuous mode was measured for H_D - Oe at a fixed temperature ($\sim 40^\circ\text{C}$), and 100 kHz. A device was considered acceptable for further die level testing when the wafer level bias margin was 10 Oe or greater. The results obtained from wafer 8-3-1 were 18 good die of which 13 had at least a 13 Oe overlap in margin. An additional 5 die, designated as backup units, had between 6 and 10 Oe margins. A wafer fracture during dicing caused the loss of some of the better dice.

Die level characterization. - The die level characterization procedure is accomplished by first establishing the validity of each die at nominal bias settings. The nominal annihilator and generator settings were derived experimentally from the first few devices. Once device operations are confirmed, the following test procedures are applied to evaluate the device.

Propagation margin. - The propagation margins are tested by generating a specific bit pattern (11111010) in every 8-bit word and adjusting the exerciser detector circuit (strobe and threshold to be discussed later) for logic detection and error checking. The drive field is then set at 52 Oe and the temperature of the device is stabilized at $25 \pm 5^\circ\text{C}$. The z bias field is then increased until a logic error is detected by the exerciser. The bias field is then slowly lowered until error free annihilation, generation and propagation is achieved for >10 seconds ($<10^{-6}$ error rate). This establishes the upper margin limit ($H_z \text{ max}$). The lower margin ($H_z \text{ min}$) is then established by decreasing the bias field until errors again appear. The bias is then raised slightly to establish error free annihilator, generation and propagation for >10 seconds. This procedure is repeated for $H_D = 45$ and 60 Oe while maintaining a constant temperature. The bias is then set to center bias

$$\frac{H_z \text{ max} - H_z \text{ min}}{2} \text{ for } H_D = 45 \text{ Oe.}$$
 The drive field amplitude is then reduced until

failures occur establishing the minimum drive field ($H_D \text{ min}$). This value varied from 42 to 44 Oe over the eight devices used in the memory cell. It appears that this relatively high value is peculiar to this run since data on devices from other lots (Para 9.1.2) showed minimum drive fields of ~ 35 Oe. Minimum z bias field for most devices is limited by annihilator operation. As the bias field is decreased the annihilator either fails to annihilate or generates bubbles along the outside edge of the loop. Maximum z bias is a function of the replicate and curved chevron track. This test scheme does not provide for further isolation of the high bias failure point but the field interrupt technique mentioned in Para 9.1.2 more clearly

defines these failures. The details of this diagnostic testing will be covered in the Item 1 report.

Generation. - The minimum exerciser pulsewidth of 200 ns was used exclusively throughout the generator evaluation. To evaluate the generator the drive field is adjusted to 52 Oe and the device temperature stabilized at $25 \pm 5^\circ\text{C}$. The bias is then adjusted to one Oersted less than the maximum ($H_z \text{ max}-1$) value previously established. The generator phase margin is then determined by varying the pulse (set at 200 ma pk) over 360 deg of drive field rotation. The nominal phase is then determined by placing the generator pulse at a position where reliable generation is achieved and the detected signal is not affected by any crosstalk or feedthrough. The pulse amplitude is reduced to determine the minimum effective amplitude for error free generation ($i_g \text{ min}$). The pulse amplitude is then set for the nominal (200 ma) value. On this device, three annihilators exist. One is in-line with each of the two detectors and the third is the standard serial on track annihilator. All are of the same configuration and differ only in that the detector annihilators are physically rotated 270 deg from the on track annihilator. The detector annihilators are arranged so that a single pulse serially applied will annihilate alternate bit positions. This technique will allow alternate bits to be passed to each detector, one detector detecting the even bits (0, 2, 4, ...) the other the odd bits (1, 3, 5, ...), when a serial pulse is applied every other clock pulse. If an annihilation/pulse is applied continuously to one detector annihilator all bits to that detector will be annihilated and consecutive bits will be detected in one detector. The continuous bit annihilation technique was used for all parameter testing. The detector annihilator pulse was set for 200 ns, 100 ma at 0 ± 10 deg referenced to the rotating X field. The in-line, on track annihilator was examined at a pulsewidth of 200 ns and an amplitude of 80 ma. The drive field is set for 52 Oe and the z bias is adjusted for the minimum bias plus one Oersted ($H_z \text{ min}+1$). The phase of the annihilator is then measured over 360 deg of drive field rotation. The nominal phase is selected to minimize cross talk and provide reliable operation. At the nominal phase setting the pulse amplitude is reduced to determine the minimum current necessary for annihilation ($i_a \text{ min}$). The amplitude is then increased to determine where the annihilator disturbs the propagating domain or creates bubbles along the outside edge of the loop ($i_a \text{ max}$). The pulse is then reset to the nominal 80 ma pk.

Detection. - The detected signal sensitivity for the 10^4 bit chip is about 2.2 mv/ma for a three to five ma dc total excitation at room temperature ($25 \pm 5^\circ\text{C}$). The maximum signal occurs as the strip domain passes the detector chevron apex. The threshold was varied according to signal amplitude and $d\phi/dt$ unbalance.

The device temperature is then allowed to restablize at $-10 \pm 5^\circ\text{C}$ and then $-60 \pm 5^\circ\text{C}$. At each temperature the test procedures are repeated. Table 26 is an outline of the tests required for device comparison. Figure 95 is a typical margin plot of one of the eight memory cell dice. The bias margin versus drive is shown for all three temperatures. The phase referenced chart depicts the area of operation for the annihilator and generator as well as the conditions existing during measurement. The sine wave represents the X-current and produces a magnetic field vector H_x as indicated. The H_x relationship to the components is also shown. The numbers 0, 90, 180 and 270 refer to the phase in the NASA cell (wherein the coils are rotated 45 deg from those in the test setup). The table in Figure 95 shows the minimum generator current ($i_g \text{ min}$), the minimum annihilator current ($i_a \text{ min}$) and the maximum annihilator current ($i_a \text{ max}$) in milliamps for all three temperatures. The notation WFR104-118 Oe indicates the margin value obtained at the wafer probe level. The parameters thus obtained on all devices are then compared and those with overlapping

TABLE 26. DIE LEVEL TEST PROCEDURES

PARAMETER TESTED	CONDITIONS
ALL TESTS	BIT PATTERN = 11111010; fxy = 150 kHz
ALL TESTS	DETECTOR ANNIHILATOR #2 (right) ON CONTINUOUSLY, DETECTOR #1 MONITORING ALL BITS. ANNIHILATOR PULSE PARAMETERS $i_{pk} = 100 \text{ Ma}$, $P_w = 200 \text{ ns}$, $\phi = 0 \pm 10 \text{ DEG}$
ALL TESTS	DETECTOR STROBE POSITION = $180 \pm 10 \text{ DEG}$ THRESHOLD AND $d\phi/dt$ ADJUSTED AS NECESSARY
H_z VS H_{xy}	$H_{\text{DRIVE}} = 45, 52, 60 \text{ Oe}$ $T = -10 \pm 5^\circ\text{C}, 25 \pm 5^\circ\text{C}, 60 \pm 5^\circ\text{C}$ $H_{\text{DRIVE}} = 50-52 \text{ Oe}, T = -10 \pm 5^\circ\text{C}$
GENERATOR PHASE MARGIN	$i_g = 200 \text{ Ma}$, $P_w = 200 \text{ ns}$ $H_z = H_z \text{ max}^{-1}$
MINIMUM GENERATOR CURRENT ($i_g \text{ min}$)	$H_{\text{DRIVE}} = 50-52 \text{ Oe}, T = -10 \pm 5^\circ\text{C}$, $P_w = 200 \text{ ns}, \phi = \text{NOMINAL (see text)}$ $H_z = H_z \text{ max}^{-1}$
ANNIHILATOR	$H_{\text{DRIVE}} = 50-52 \text{ Oe}, T = 60 \pm 5^\circ\text{C}$ $i_a = 80 \text{ Ma}$, $P_w = 200 \text{ ns}$ $H_z = H_z \text{ min}^{-1}$
MINIMUM ANNIHILATOR CURRENT ($i_a \text{ min}$)	$H_{\text{DRIVE}} = 50-52 \text{ Oe}, T = 60 \pm 5^\circ\text{C}$ $P_w = 200 \text{ ns}, \phi = \text{NOMINAL (see text)}$ $H_z = H_z \text{ min}^{-1}$
MAXIMUM ANNIHILATOR CURRENT ($i_a \text{ max}$)	$H_{\text{DRIVE}} = 50-52 \text{ Oe}, T = 60 \pm 5^\circ\text{C}$ $P_w = 200 \text{ ns}, \phi = \text{NOMINAL (see text)}$ $H_z = H_z \text{ min}^{-1}$

margins are selected for cell operation. Figure 96 shows the comparison of the eight die selected for the cell. Due to the fracture problem mentioned earlier, insufficient die existed to preclude the use of die No. 58, a rather marginal specimen. The margin overlap is significantly reduced by the inclusion of die No. 58 (note the plot excluding die No. 58). By plotting the center of the overlapping margin versus temperature, a composite temperature coefficient of $-0.21 \text{ Oe}/^\circ\text{C}$ is achieved. The composite generation phase overlap was plotted from the -10 deg data and the annihilator from the -60 deg data. The dashed lines indicate the overlapping regions.

The minimum generator current varies from 150 to 180 ma. The generator phase window was designed to exist between 50 and 145 deg and has complete overlap with all eight devices. The minimum annihilator current varies from 75 to 100 ma. The annihilator phase window completely encloses the overlapping phase margin. The detection strobe phase at the cell level is $185 \pm 1 \text{ deg}$. All eight devices performed adequately at this position and allowed for a $\pm 5 \text{ deg}$ variance thereby completely encompassing the cell specification.

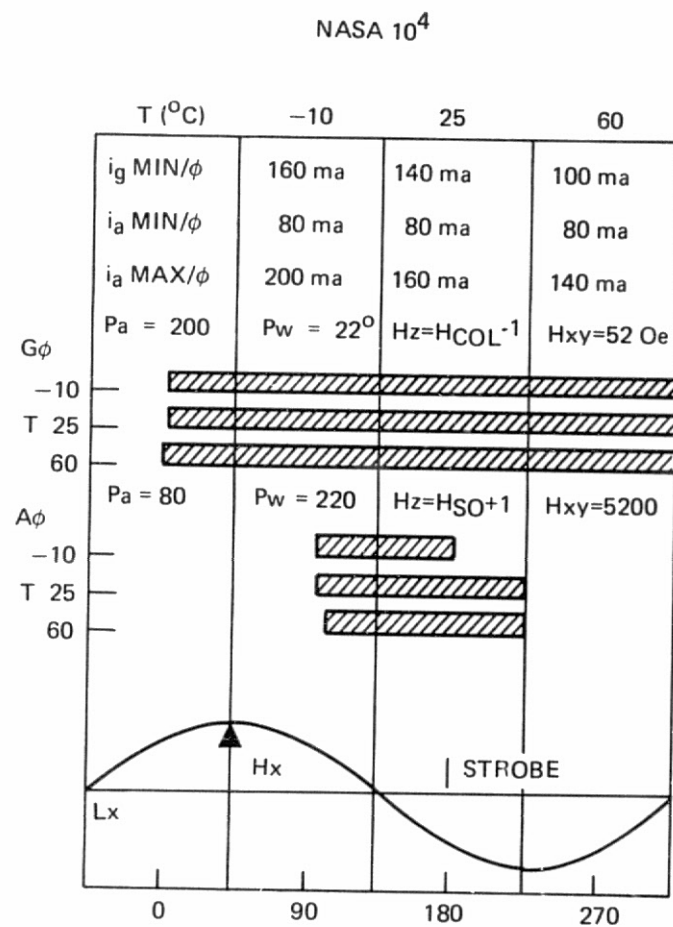
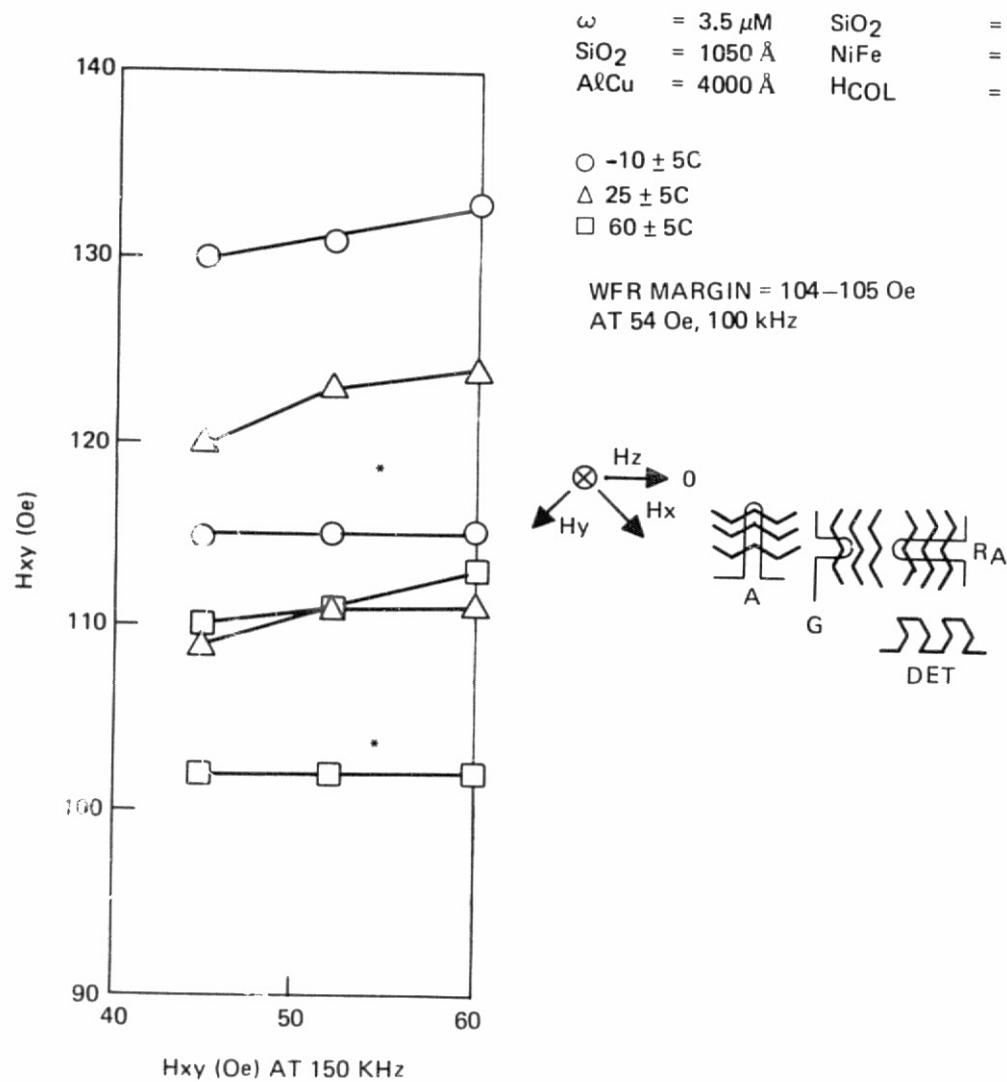


Figure 95. Die Test Data

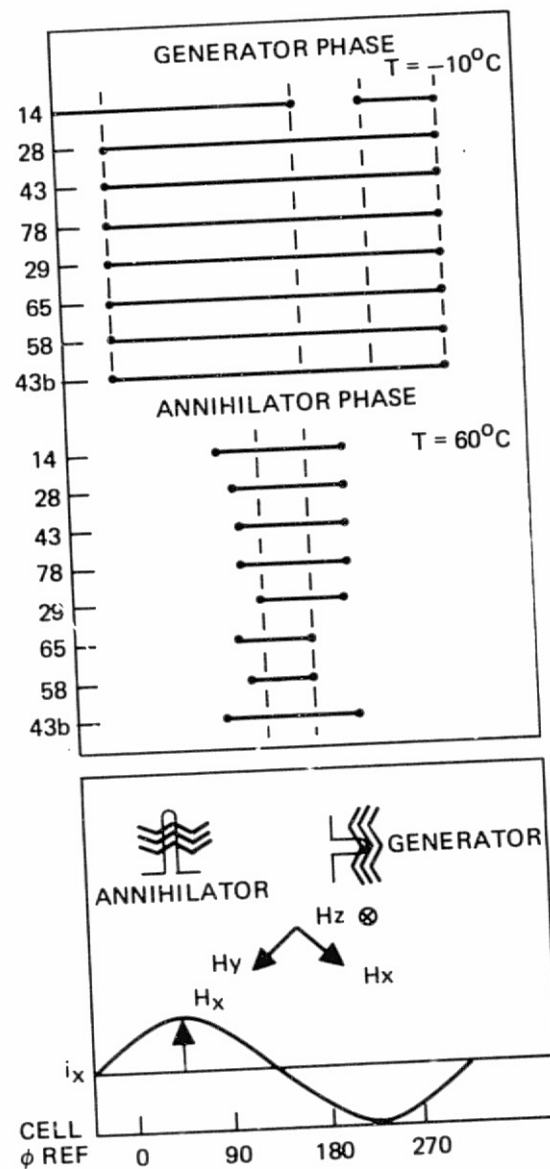
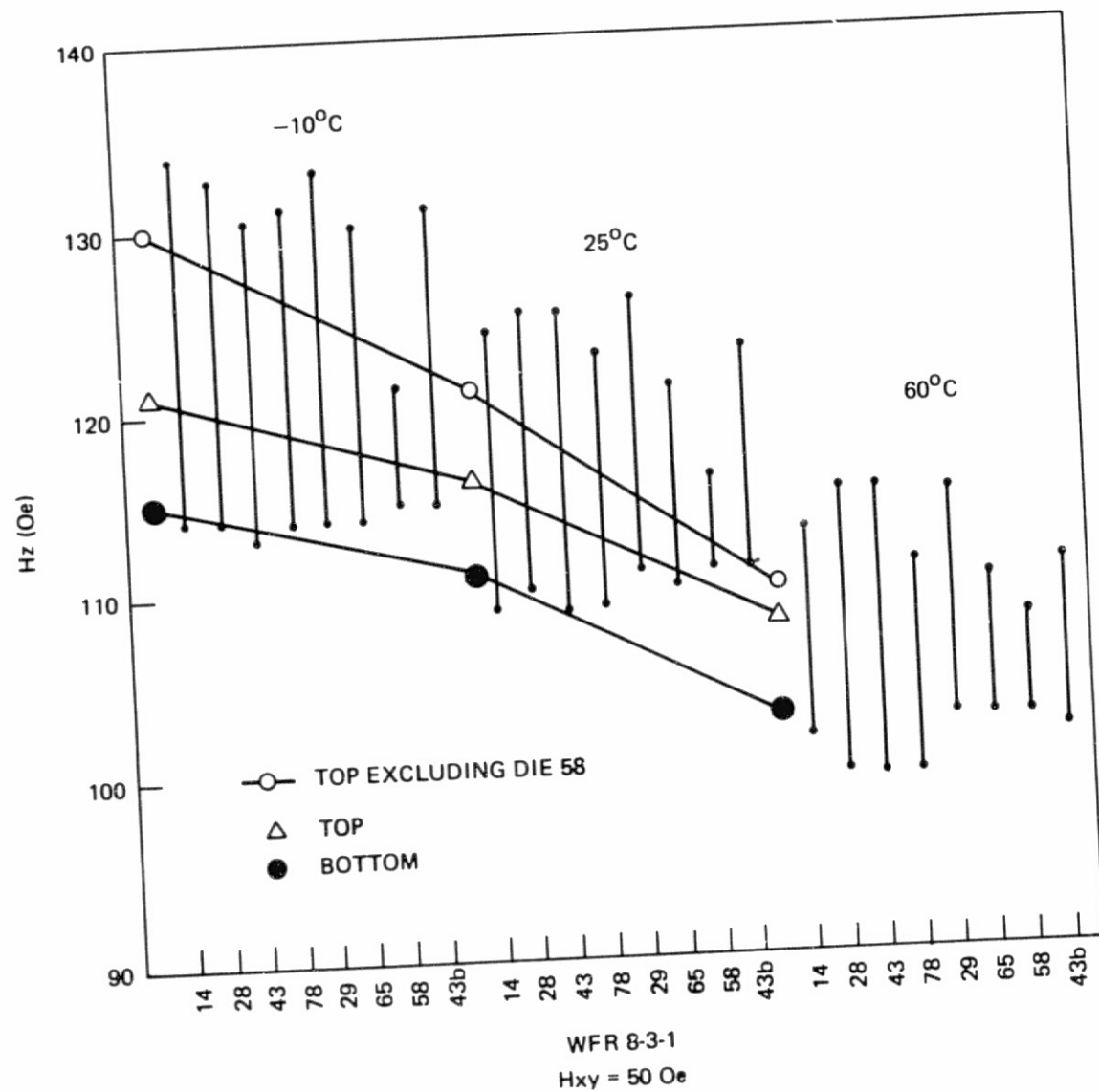


Figure 96. Composite Data on Eight Devices for Memory Cell

9.2 Memory Cell Package

This self-contained memory cell package contains all necessary mechanical hardware for the operation of 8 bubble memory chips ($1/4 \times 1/4$ in. or less) including magnets for the static Z-field and coils for the generation of a rotating field. Major design emphasis was applied toward providing a superior heat conduction path to a cold plate and in producing a uniform field over the 8-chip area.

9.2.1 Mechanical Design. — In assembly, the two machined ceramic substrates (Figure 97) and a ceramic cover are plated with 2 mils of copper (to linearize the rotating field) and bonded to two polyamide tape carriers (Figure 98) which were previously soldered to connectors.

Bubble chips are aligned and cemented in the substrate cavities and each chip pad electrically strap bonded to the tape carrier. The two tape cables are then folded over the loaded chip carriers as shown in Figure 99 (middle left) and inserted inside of the Y coil and in turn inside the X or outer coil. The coil assembly is fastened to the coil base while the chip carriers are nestled and clamped on the ceramic and teflon posts. Three rows of connectors line up on one side of the coil base, two rows for the chip interface and one row for the coil connection.

The bias structure is of three main parts, an aluminum frame which has holes for magnets, two permalloy plates which complete the magnet circuit and a couple of trimmers which provide a variable amount of Z-field shunt. The assembly is shown in Figure 97.

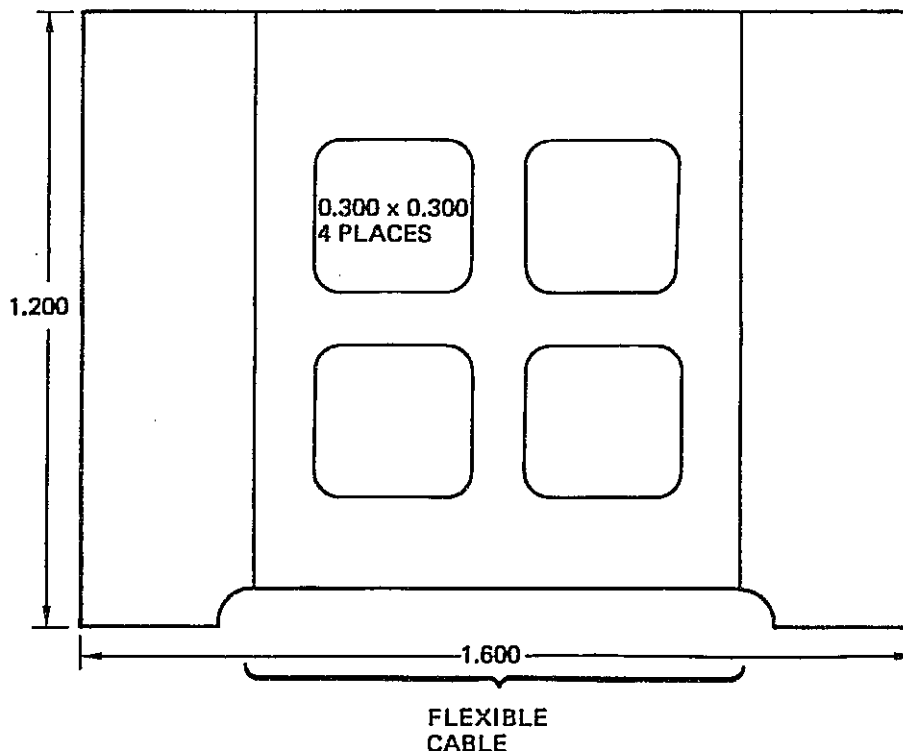


Figure 97. Machined Ceramic Substrate

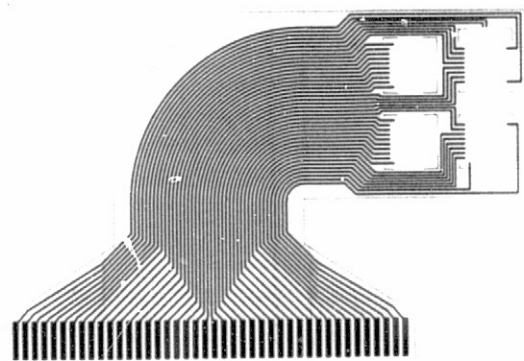
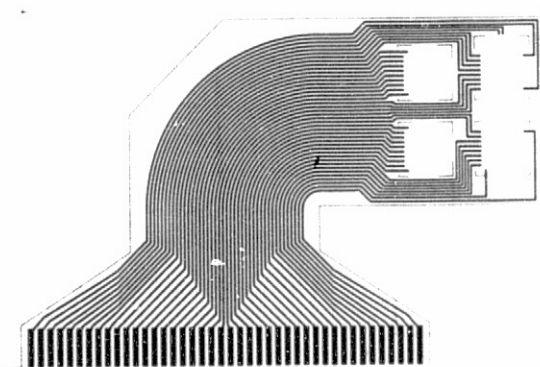
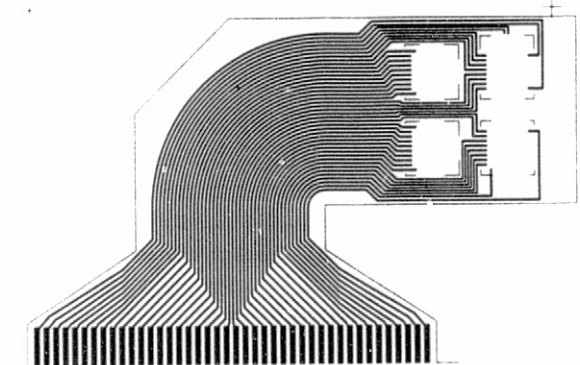
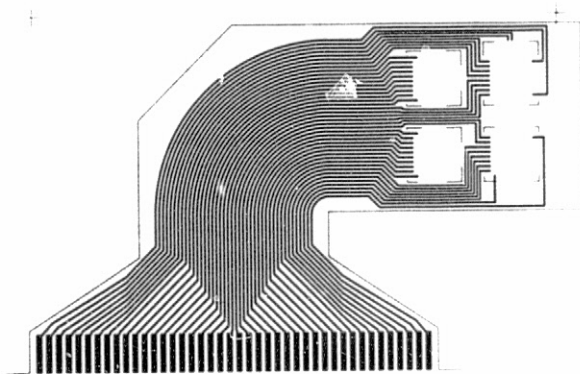


Figure 98. Flexible Circuitry

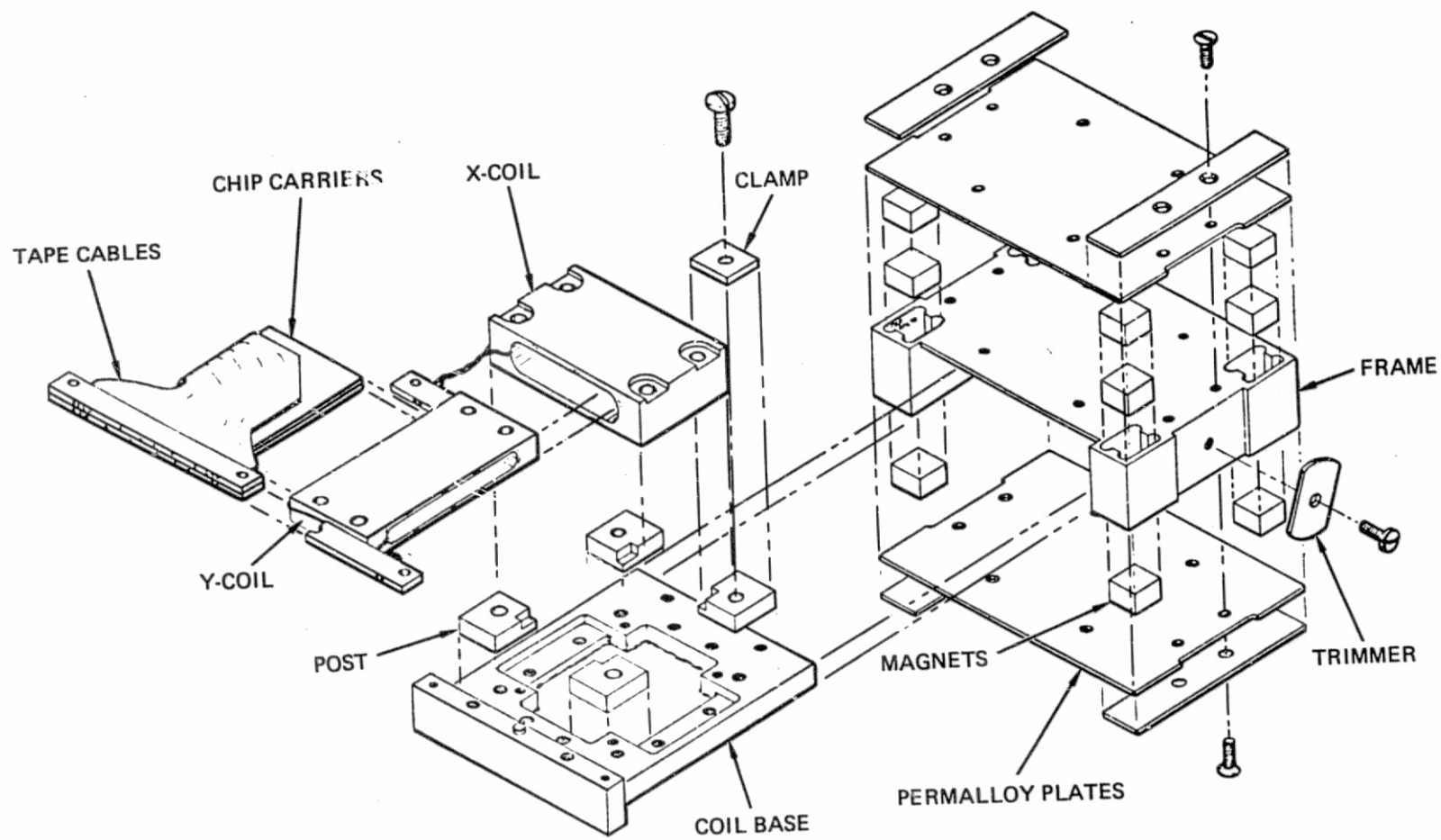


Figure 99. Exploded View of Memory Cell

The set of four photographs (Figure 100 through 103) also show the cell assembly at various stages. An optional Z-bias coil not shown in the photos was installed on the top permalloy plate so that Z-bias can be modulated.

9.2.2 Field Coil Electrical Tests. - The figures and tabulations of this section are electrical data taken on the serial 03 coils and bias assembly which is identical to the NASA cell being delivered under this contract (NAS1-12981).

Figure 104 is a plot of Q , resistive and reactive loads in a series tuned resonant circuit. The plot reflects all effects from the assembled magnetic modules with the coils installed in the bias structure and with the plated chip carriers installed.

Table 27 is a tabulation of coil Q , and resistive and reactive data taken for several states of module assembly. The data show loading effects of the various components on coil performance. The most significant effect is coupling with the bias structure, which for the outer coil at 150 kHz, increases resistance 38 percent and decreases inductance 14 percent.

9.2.3 Field Coil Distribution and Variations. - A coil pair (X03, Y03) was evaluated for field distribution and Z field component: (1) with the coils only, (2), with 3-2 mil plates within the coils, and (3) within the magnetic assembly and using the copper plates. Exact measurements of the closed assembly is not possible because of the necessity to insert the ac probe but simulation was done by using part of the assembly and aluminum plates properly placed. The axial field was measured at 100 kHz using an ac probe (approximately 20 turns, 15 mils high, 15 mils thick and 200 mils long) while the Z conversion of rotating field was measured both with a small probe of similar dimensions and a large 1/4 in. spiral.

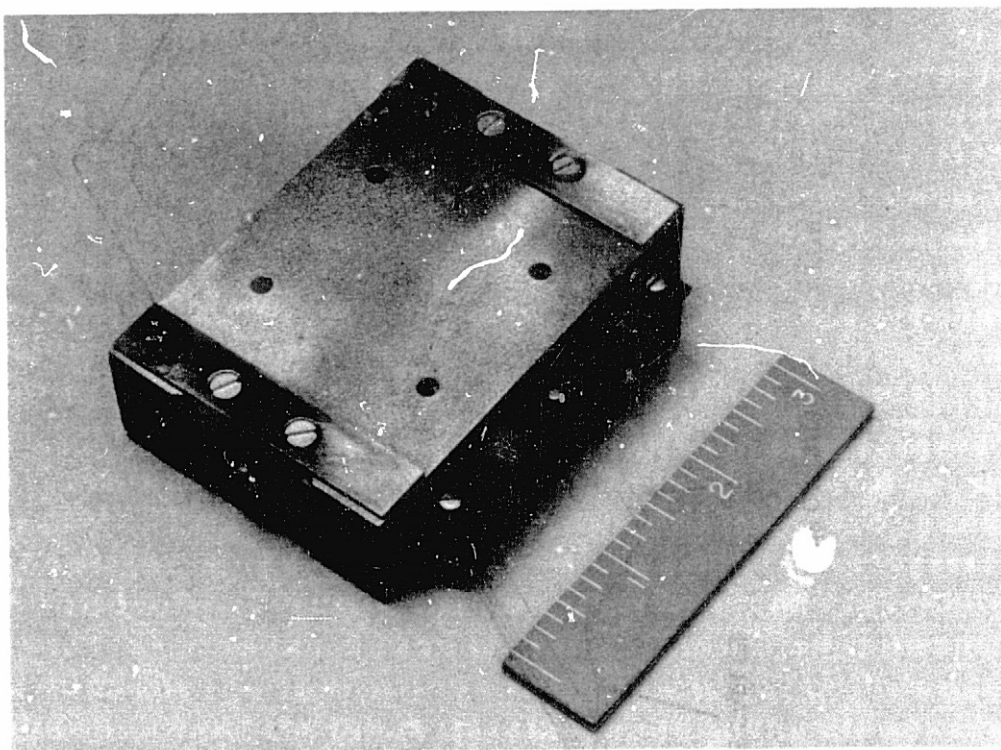


Figure 100. Assembled Cell

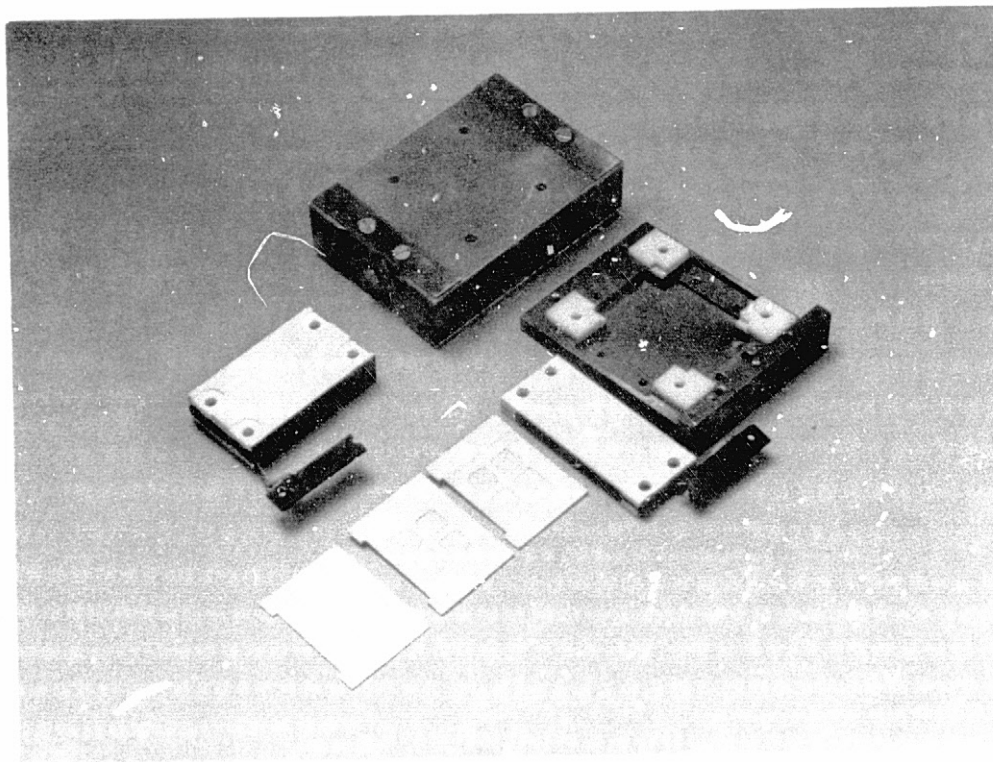


Figure 101. Memory Cell Parts

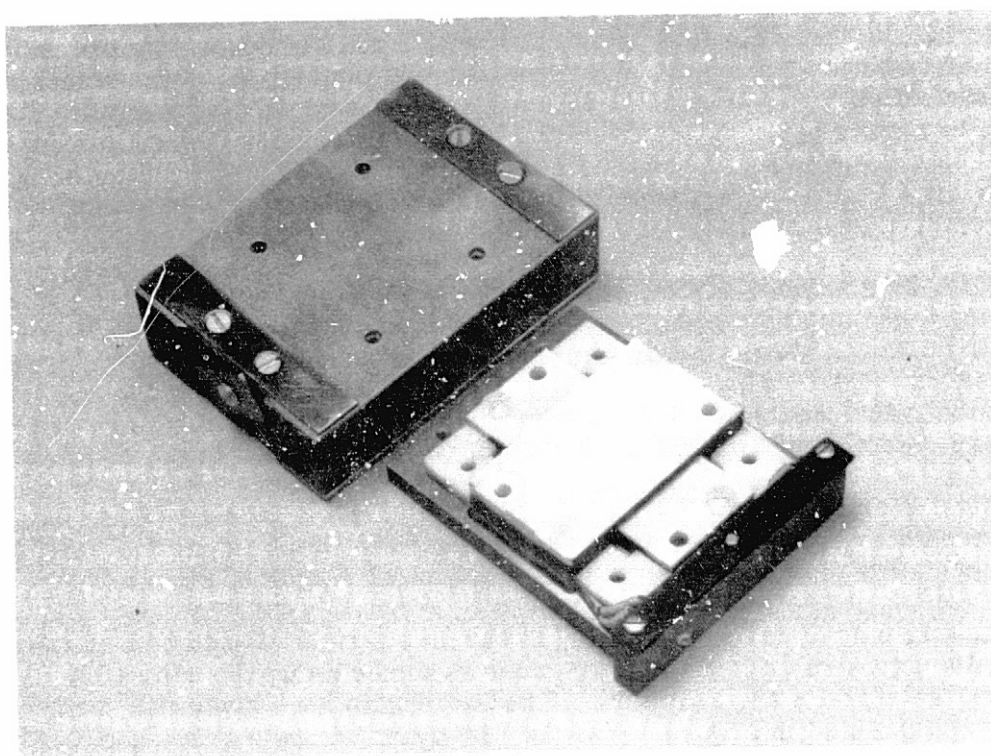


Figure 102. Magnetic Bias Assembly (Left) and Drive Coil Assembly (Right)

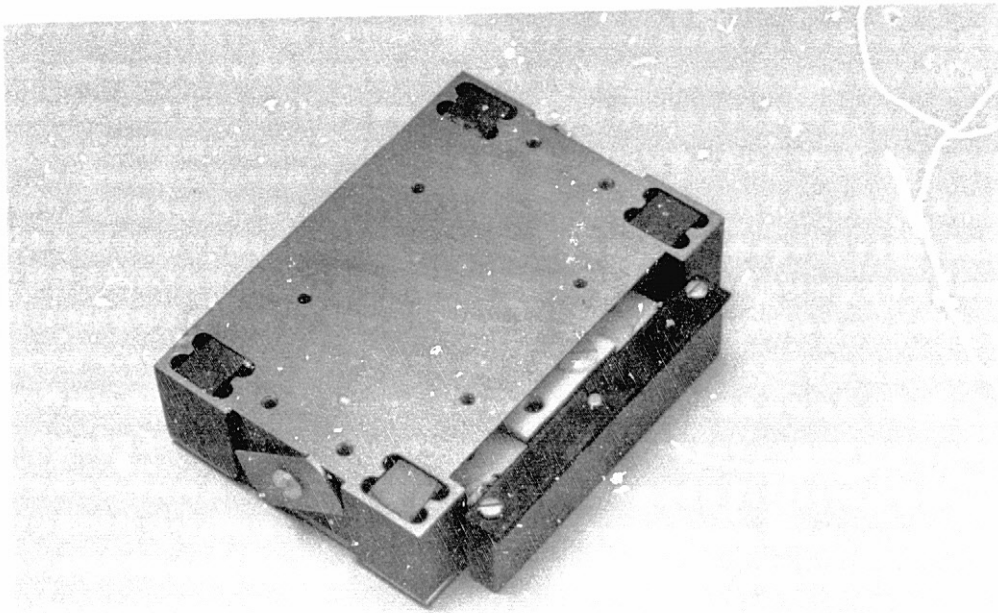


Figure 103. Memory Cell Showing Magnets

Plating the three ceramic substrates with 2 mils of copper significantly improved the field distribution uniformity and reduced the Z-conversion of the rotating field. Field distribution for the two coils with and without surrounding magnetic structure is shown in Figure 105 and Figure 106. The Z-conversion curves are not included in this report because for the test with the 3-2 mil copper plates (simulating plating) separated by 50 mils within the coils there is a barely perceptible variation ($< .1$ Oe/A) over a centered square of 0.6 in. on a side.

As far as a value of Z-conversion using the coil without copper the maximum value using a quarter inch wide spiral sensing loop appears to be 0.6 Oe/A but for safety and acknowledging a factor for local variations a value of 0.9 Oe/A would be recommended. If the coil were to be driven with 3 amps peak then the maximum local Z-field modulation would be ± 2.7 Oe from the operating point. The copper plated substrates are clearly superior and as such will be incorporated in the NASA cells.

9.2.4 Bias Shunt, Tilt, and Z-Bias Modulator Characteristics. - Four sets of barium ferrite magnets are used to provide the Z-bias field which is parallelized by top and bottom permalloy plates as shown in the mechanical sketch of Figure 107.

Shunting pins have been installed in the bias structure (adjacent to magnets) to enable a 100 gauss midrange with ± 10 gauss variance using the adjustable shunts located on the sides of the structure. The two shunts have somewhat different characteristics as tabulated in Figure 107a, the "B" shunt having a greater effect on field than shunt "A". For best uniformity, the shunts should have about the same displacement from horizontal for a desired field setting and should be set using a gaussmeter.

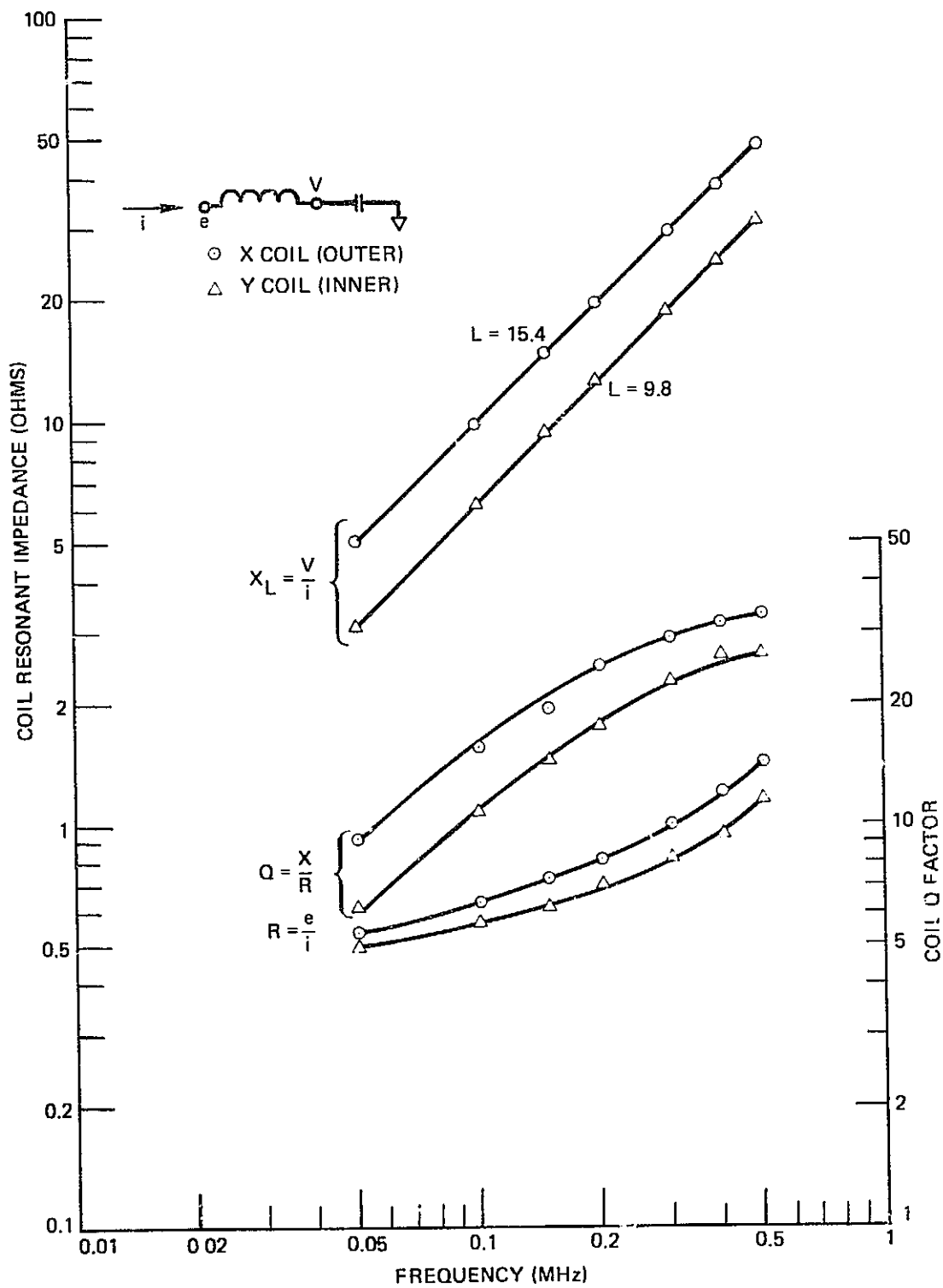


Figure 104. Coil Impedance and Q

TABLE 27. TUNED RESONANT ELECTRICAL DATA

		Frequency - MHz							
		.05	.05	.10	.15	.20	.30	.40	.50
X Coil (Outer) SN X03									
1. Coil Alone	R_R		.43	.47	.53	.60	.73	.83	1.00
	X_L		5.33	11.3	16.7	22.4	33.3	44.7	55.0
	Q		12.3	24.3	31.3	37.2	45.5	53.6	55.0
2.2 Inner Coil Inserted	R_R		.43	.50	.53	.63	.80	.93	1.10
	X_L								
	Q								
3. Installed in Bias with Inner Coil Inserted	R_L		.53	.63	.73	.87	1.03	1.23	1.40
	X_L		4.83	9.67	14.3	19.3	28.7	38.0	46.7
	Q		9.1	15.3	19.6	22.2	27.8	30.9	33.4
4. Installed in Bias with Plated Chip Carriers	R_R		.53	.63	.73	.80	1.00	1.20	1.40
	X_L		4.83	9.67	14.3	19.3	29.0	37.7	46.7
	Q		9.1	15.3	19.6	24.2	29.0	31.4	33.4
Y Coil (Inner) SN Y03									
1. Coil Alone	R_R		.43	.50	.53	.60	.73	.83	.97
	X_L		3.50	7.33	10.7	14.3	21.3	28.0	35.0
	Q		8.1	14.6	20.2	23.8	29.2	33.8	36.1
2. Inserted in Outer Coil	R_R		.43	.50	.53	.60	.73	.83	.97
	X_L								
	Q								
3. Installed in Bias with Inner Coil Insertion	R_R		.47	.53	.60	.67	.80	.90	1.03
	X_L		3.17	6.33	9.67	13.0	19.0	25.4	31.0
	Q		6.73	12.0	16.1	19.4	23.8	28.2	30.1
4. Installed in Bias with Plated Chip Carriers	R_R		.50	.57	.63	.70	.83	.93	1.13
	X_L		3.07	6.14	9.35	12.5	18.7	24.6	30.7
	Q		6.13	10.8	14.7	17.8	22.4	26.4	27.1

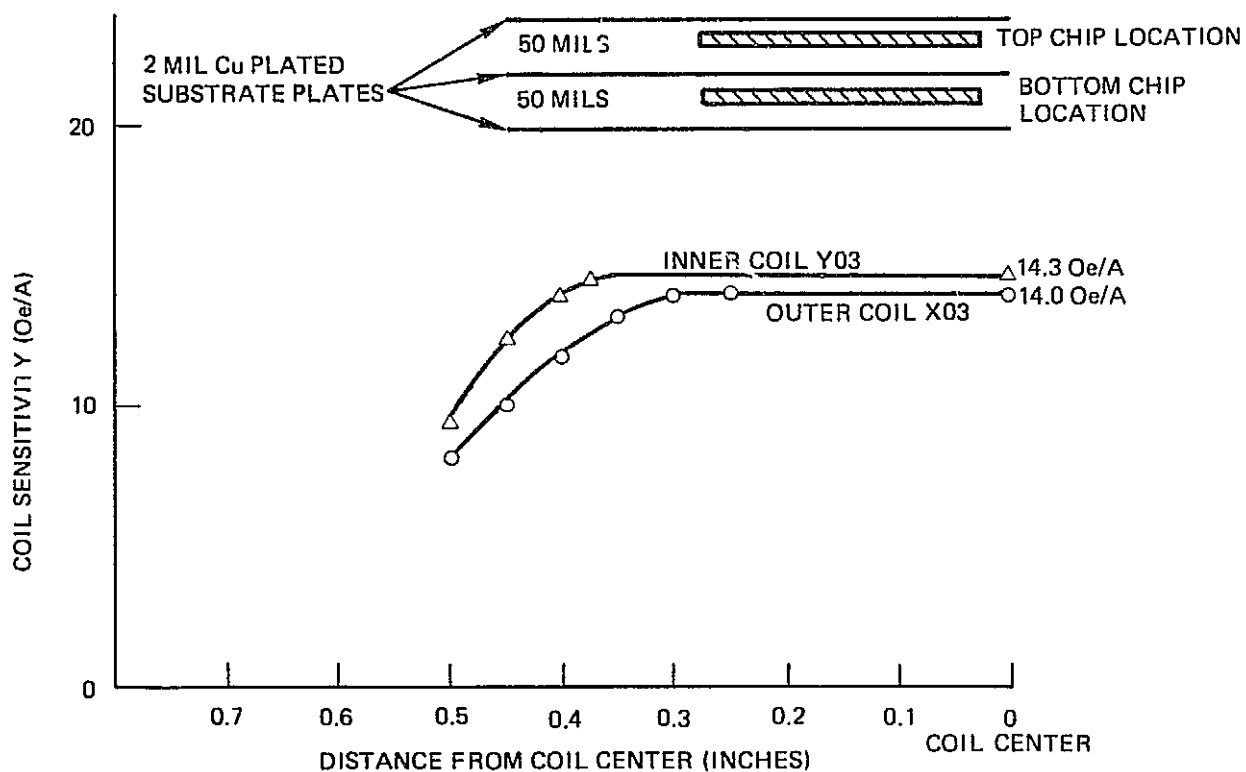


Figure 105. Coil Sensitivity (Outside Magnetic Structure)

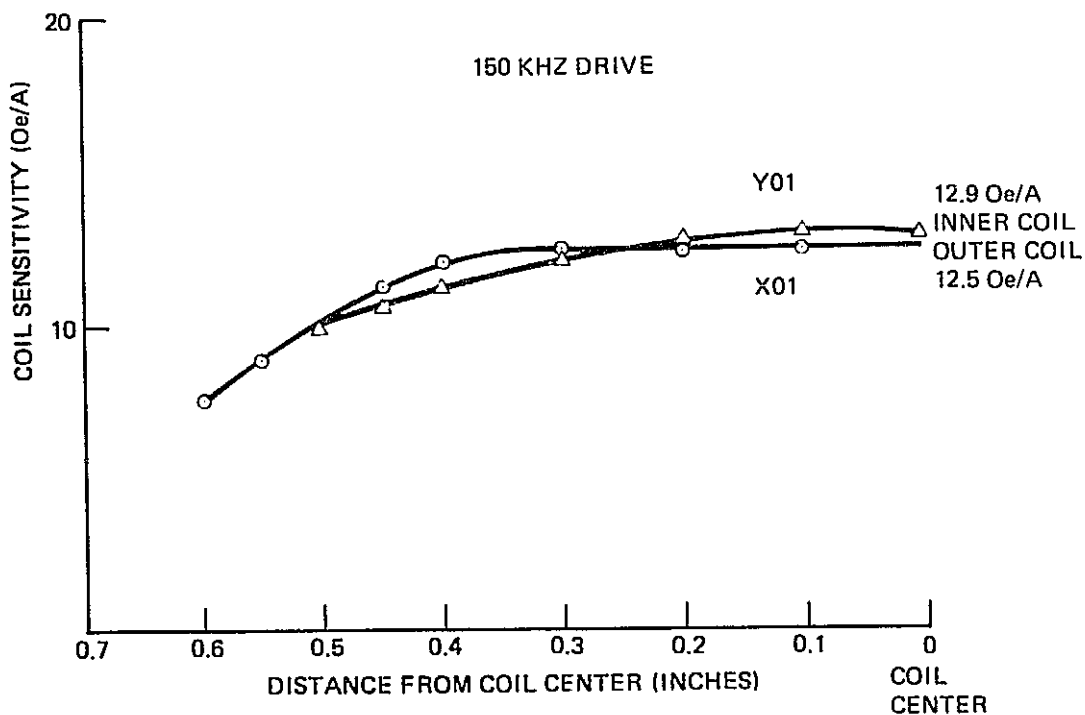


Figure 196. Coil Sensitivity (Assembled Configuration)

Figure 107b shows the orientation of the X-plane component of the bias field resulting from 1.25 deg of fixed tilt of the bias relative to the X-Y coil pair. For a 100 Oe bias field setting the measured in-plane component is 2.27 Oe.

Once the bias field is set, bias field excursions can be made for the purposes of characterization by using the auxiliary bias coils. These are the two coils wound on the bias structure each consisting of 20 turns with individual two-pin connectors. For correct operation the connections and polarity are illustrated in Figure 107c.

9.2.5 Z-Bias Field Gradients and Variances. - Figures 108, 109 and 110 show bias field gradients and X and Y component variances for three shunted conditions; Figure 108, both shunts horizontal, Figure 109, both shunts vertical, and Figure 110, one shunt horizontal with the other vertical. The data was taken over a region of 0.8 in. Comparison of the three sets of curves shows that maximum gradient occurs for the condition with one shunt horizontal with the other shunt vertical. Bias field gradient for this condition is about 1 percent compared with about 0.3 percent for the conditions when both shunts are in the same position. The X-Y plane component variances are approximately the same for all three conditions. X-direction component variance is 0.6 percent maximum and Y-direction component variance is 0.8 percent maximum within the .8 in. 2 region.

9.2.6 Bias Structure Proximity Effects. - Measurements were made to determine the effects of placing the bias structures in close proximity to one another for several physical arrangements and field polarity. The results are tabulated on the Figures 111 through 116. Figures 111 through 114 are Z bias field measurements at the center of the bias structure while Figures 115 and 116 are measurements of the X and Y directed components of the bias field at several locations within the bias structure. Notice that the proximity effect is virtually imperceptible in the X and Y directions. Therefore, once the bias structures are mounted it becomes possible to mechanically adjust the trimming shunts to compensate for the change in bias field resulting from stacking or from placing the structures adjacent to one another.

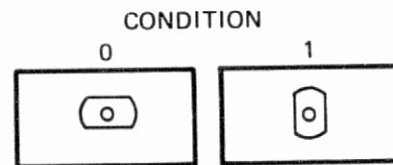
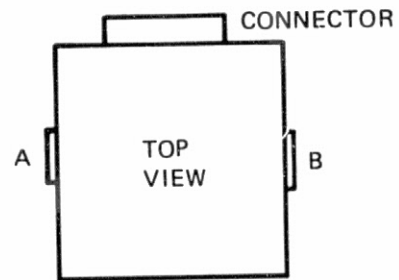
9.2.7 Memory Cell Temperature Measurements. - Temperature measurements were made with the serial 02 coils and bias assembly attached to an aluminum plate, 3-1/2 x 14 x .18 in. thick, acting as a heat sink. Running temperatures were maintained by measuring constant current voltage drop across miniature diodes appropriately located in the assembly.

The coils were driven at 150 kHz with current levels providing representative drive fields (42 and 47 Oe). A chip self-heating load of about 80 mW each was simulated with miniature resistors maintained on the chip carriers.

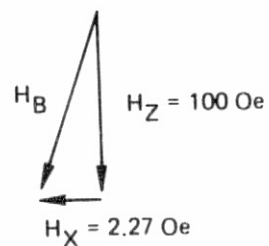
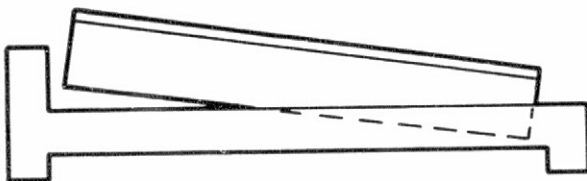
The Figures 117, 118 and 119 are time-temperature plots of the measurements obtained and provide an indication of both time variant and steady state temperature characteristics of the memory cell. As shown, the temperature gradient between the chip carrier and the magnet frame is established within several minutes of continuous running, is less than 5°C with no chip self heating and increases about 3°C with the simulated chip heat of 620 mW (8 chips). The maximum gradient will occur for a condition where chips and coils are powered up simultaneously from ambient. This is seen by comparing Figures 117 and 118.

A. SHUNTING PINS INSTALLED FOR 100 GAUSS MIDRANGE WITH \pm GAUSS MECHANICAL ADJUSTMENT RANGE -

A	B	H	ΔH
0	0	113.0	
0	1	100.6	12.4
1	1	89.8	10.8
1	0	100.9	11.1
0	0	113.1	12.2
1	0	100.7	12.4
1	1	89.7	11.0
0	1	100.3	10.6
0	0	113.0	12.7



B. WITH BIAS SET FOR 100 GAUSS, TILT OF BIAS RELATING TO COILS SHOWS A MEASURED INPLANE COMPONENT OF 2.27 GAUSS -



C. BIAS COIL CHARACTERISTIC WITH BIAS SET FOR 100 GAUSS -

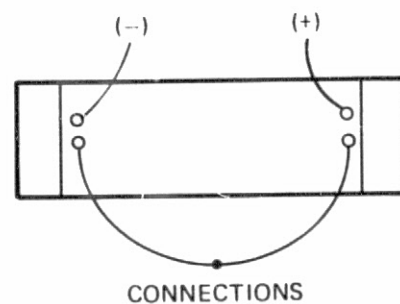
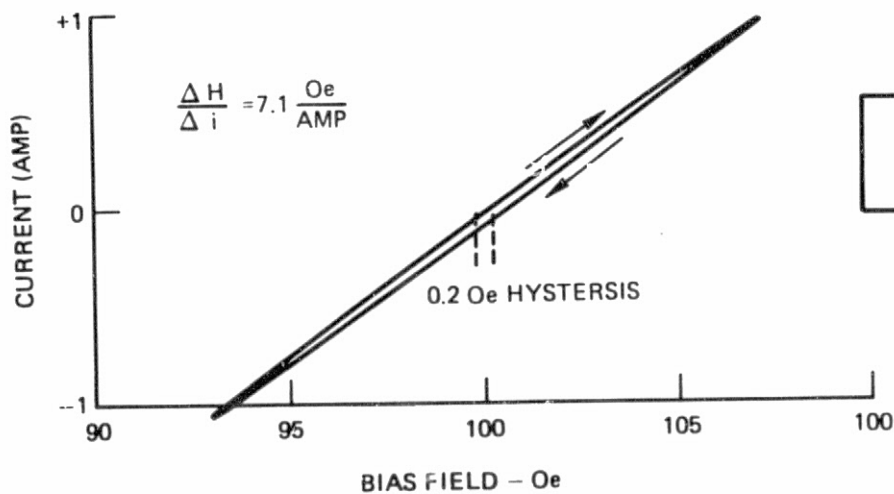


Figure 107. Bias Shunt, Winding, and Tilt Characteristics

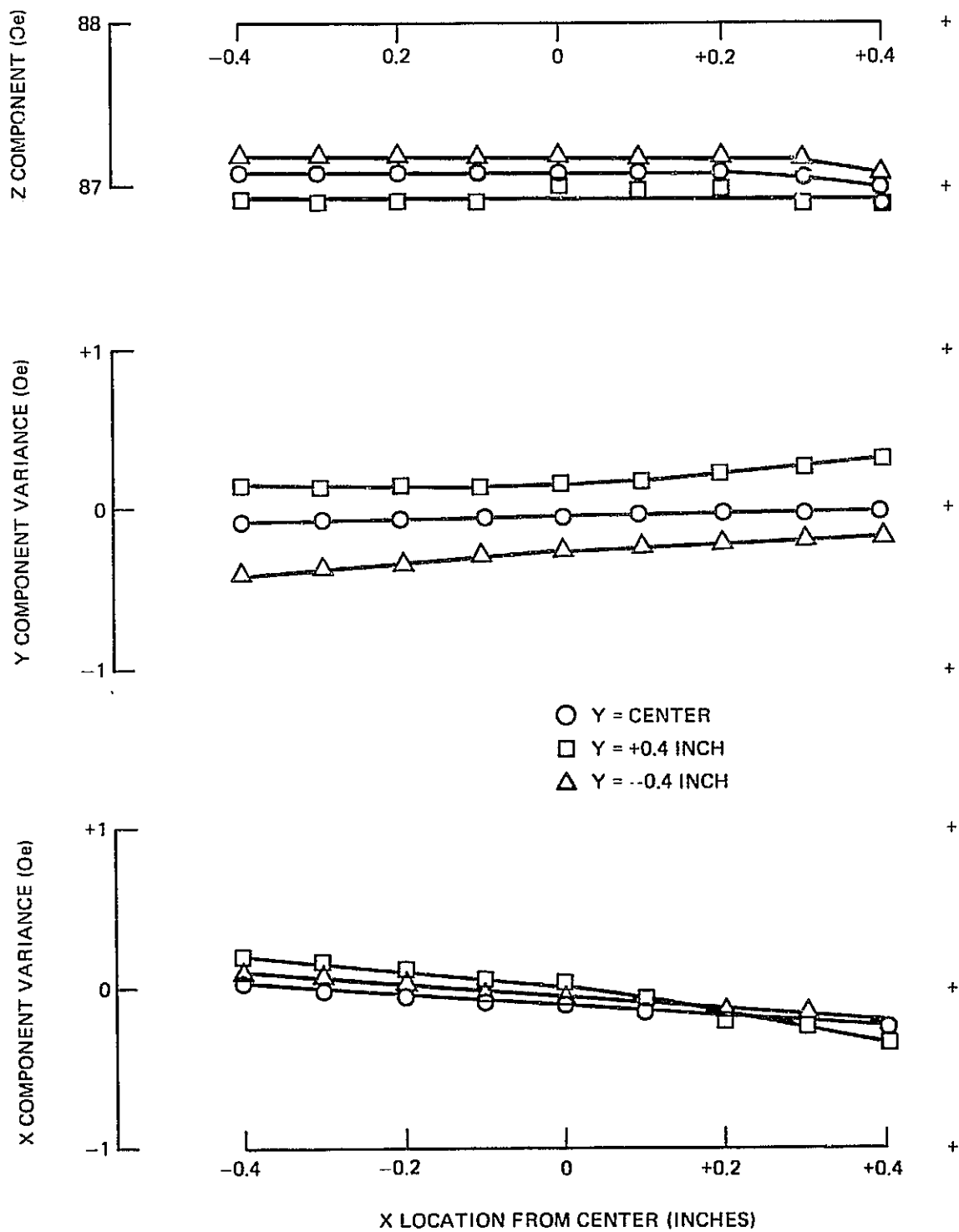


Figure 108. Bias Assembly Field Gradients (Both Shunts at Max Position)

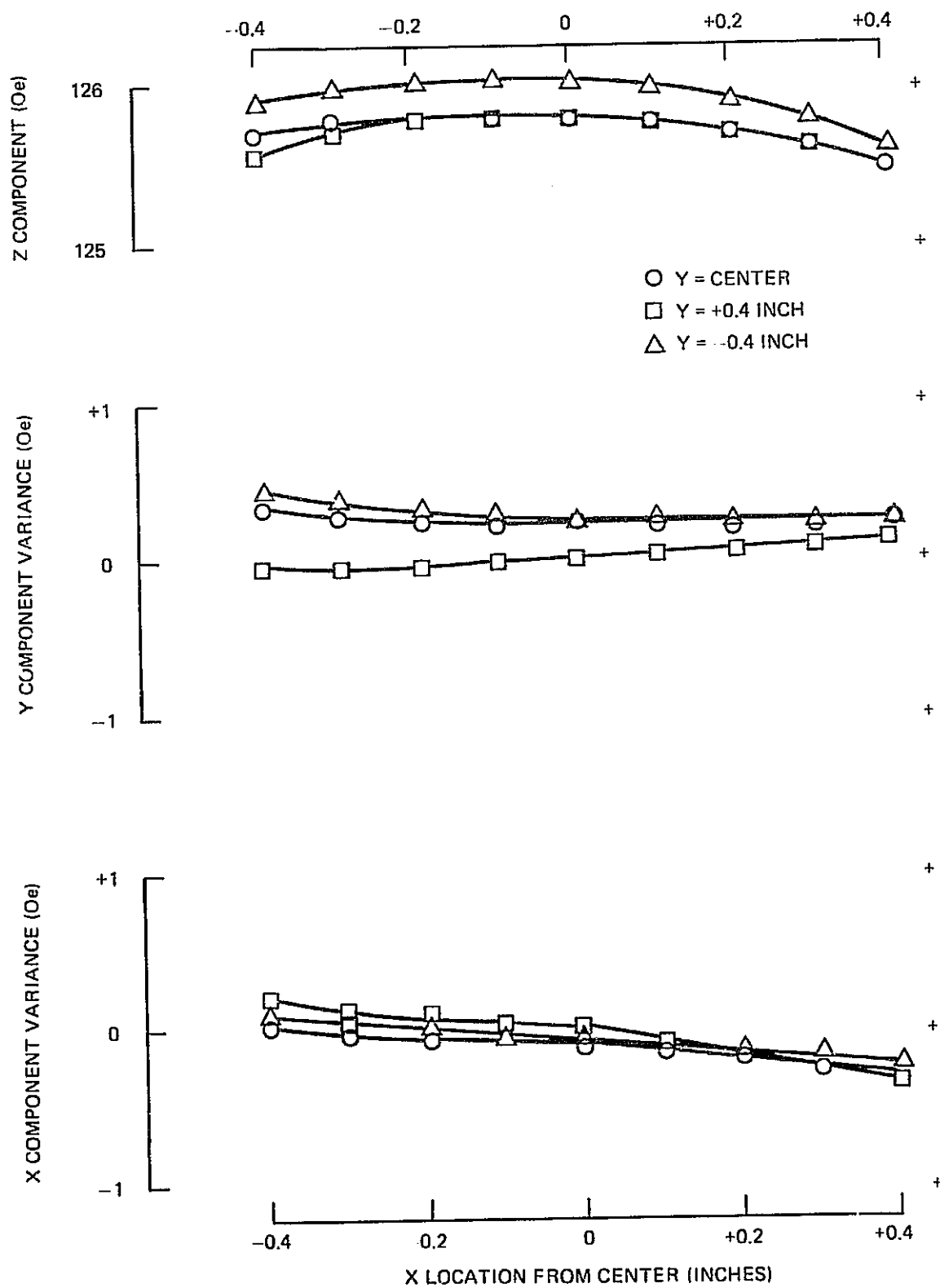


Figure 109. Bias Assembly Field Gradients (Both Shunts at Zero Position)

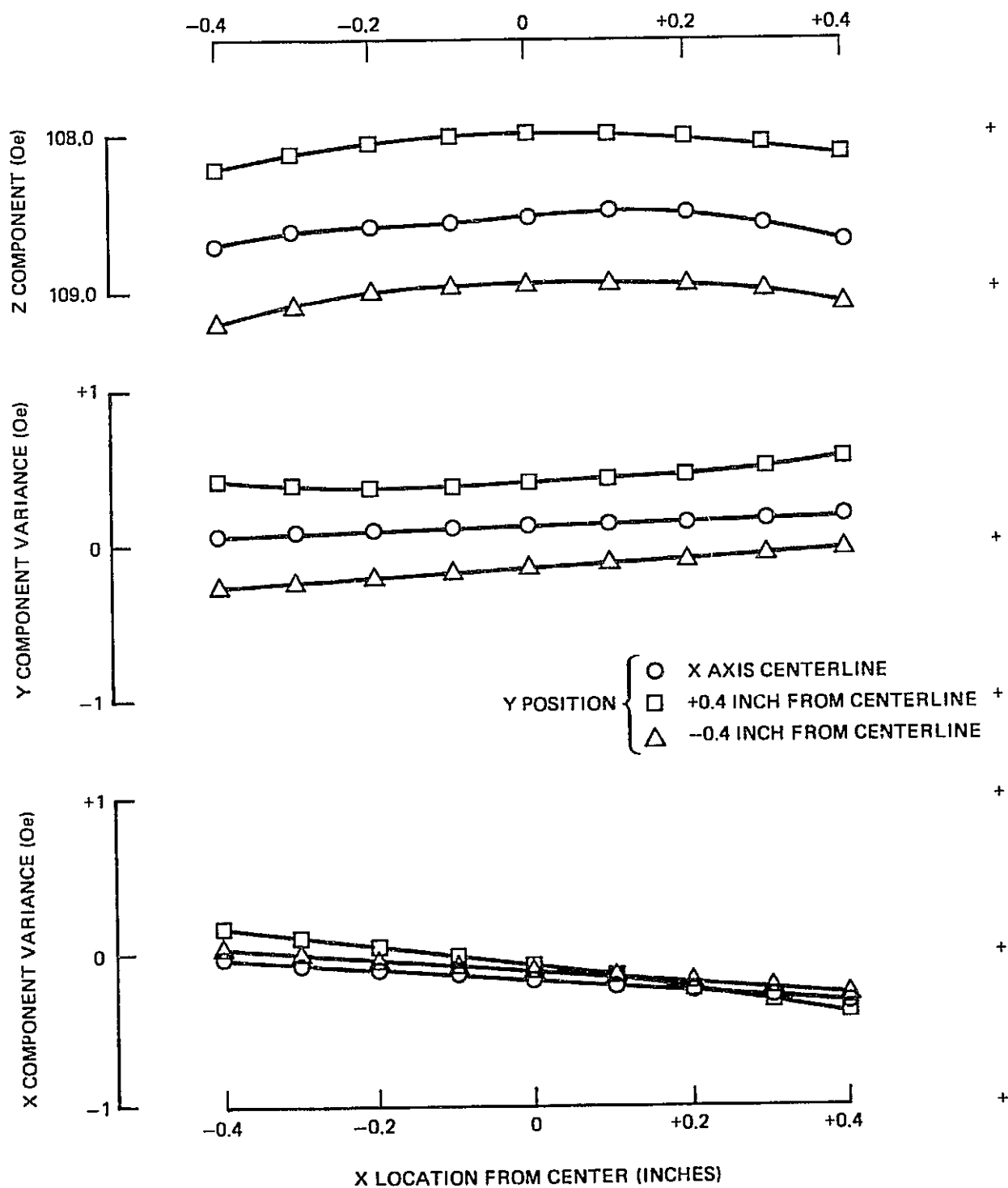
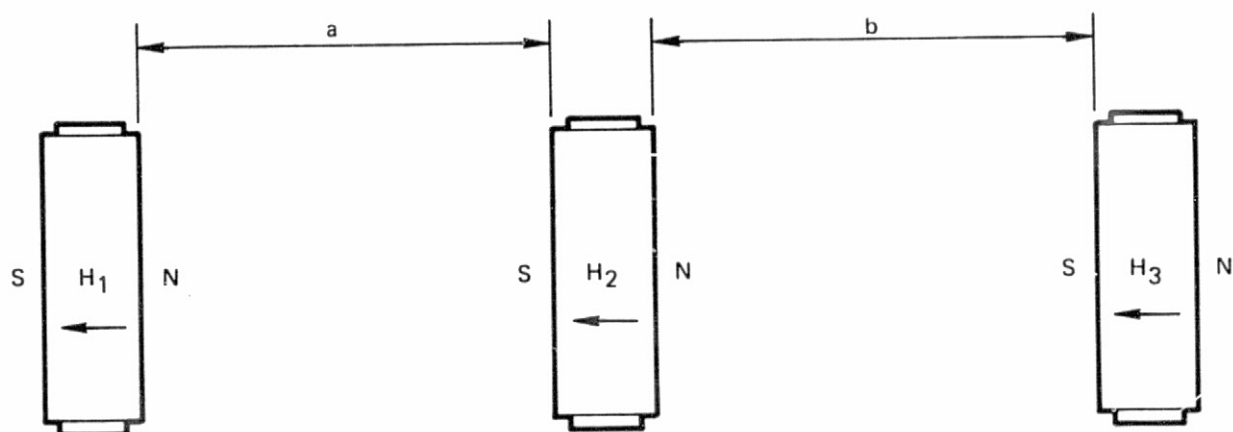
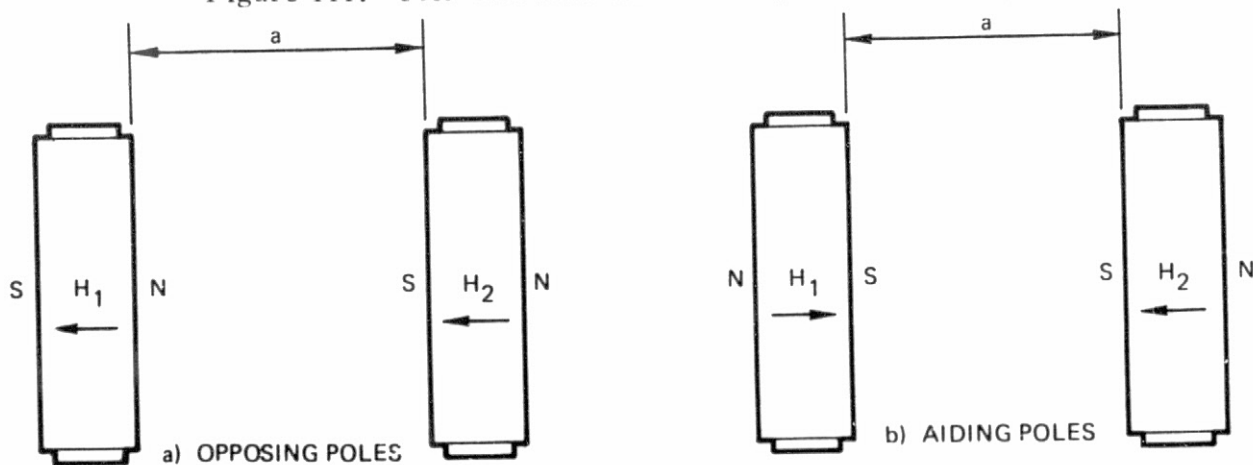


Figure 110. Bias Assembly Field Gradients (One Shunt Max, One Shunt Min)



a (INCH)	b (INCH)	H ₁ (θ_E)	H ₂ (θ_E)	H ₃ (θ_E)
0	0	69.6	55.0	70.9
0.2	0.2	80.2	70.0	81.5
0.5	0.5	86.5	79.1	87.8
1	1	92.5	87.4	93.2
2	2	97.0	94.7	98.0
4	4	99.5	99.3	99.8
6	6	100.6	100.1	100.7
12	12	101.3	101.2	101.7

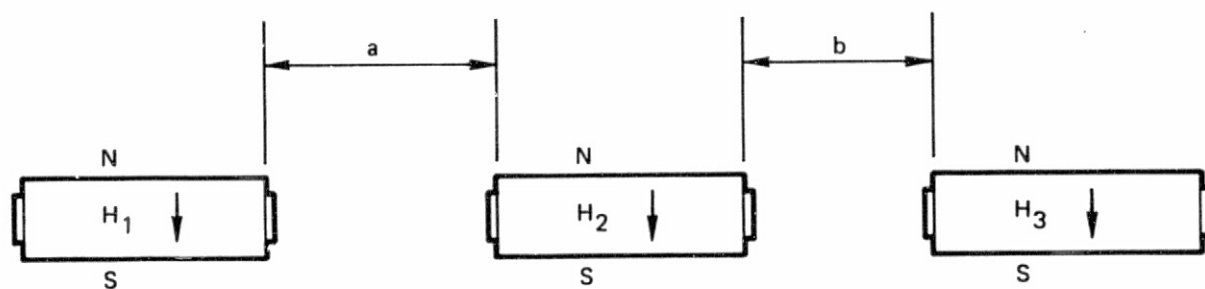
Figure 111. Cell-Cell Bias Interaction (3 Cells Stacked)



a (INCH)	H ₁ (θ_E)	H ₂ (θ_E)
0	78.4	78.9
0.2	85.1	85.4
0.5	89.8	90.1
1	93.9	94.4
2	97.9	97.9
4	100.2	100.8
6		
12	100.3	106.6

a (INCH)	H ₁ (θ_E)	H ₂ (θ_E)
0	119.4	118.0
0.2	114.8	113.2
0.5	110.9	109.9
1	107.7	107.0
2	104.8	104.2
4	102.5	102.2
6	102.0	101.7
12	101.6	101.5

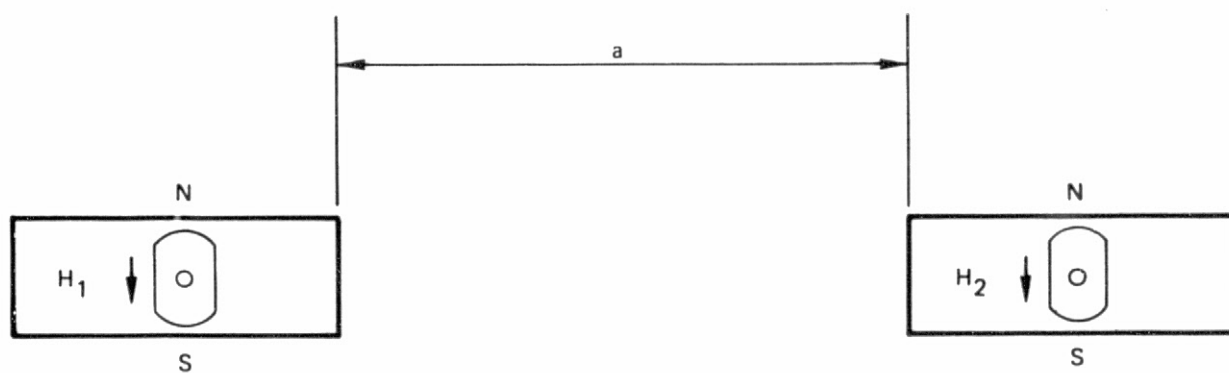
Figure 112. Cell-Cell Bias Interaction (Aiding and Opposing)



$b = 12 \text{ INCH}$

a (INCH)	b (INCH)	H_1 (θ_E)	H_2 (θ_E)	H_3 (θ_E)	a (INCH)	H_1 (θ_E)	H_2 (θ_E)
0.12	0.12	107.0	112.8	108.5	0.12	106.3	106.9
0.5	0.5	104.1	107.9	105.5	0.5	103.8	104.3
1	1	102.4	105.2	104.0	1	102.2	102.8
2	2	101.2	102.4	102.8	2	101.2	101.8
4	4	100.9	101.2	102.1	4	101.1	101.2
6	6	100.4	101.8	101.9	6		
12	12	100.8	100.7	101.3	12	100.9	100.8

Figure 113. Cell-Cell Bias Interaction (3 Cells Adjacent)



a (INCH)	H_1 (θ_E)	H_2 (θ_E)
0.05	112.0	112.8
0.2	109.3	110.1
0.5	105.0	106.1
1	102.9	104.4
2	101.3	102.7
4	100.0	101.9
6	99.9	101.7
12	100.1	101.7

Figure 114. Cell-Cell Bias Interaction (2 Cells Adjacent)

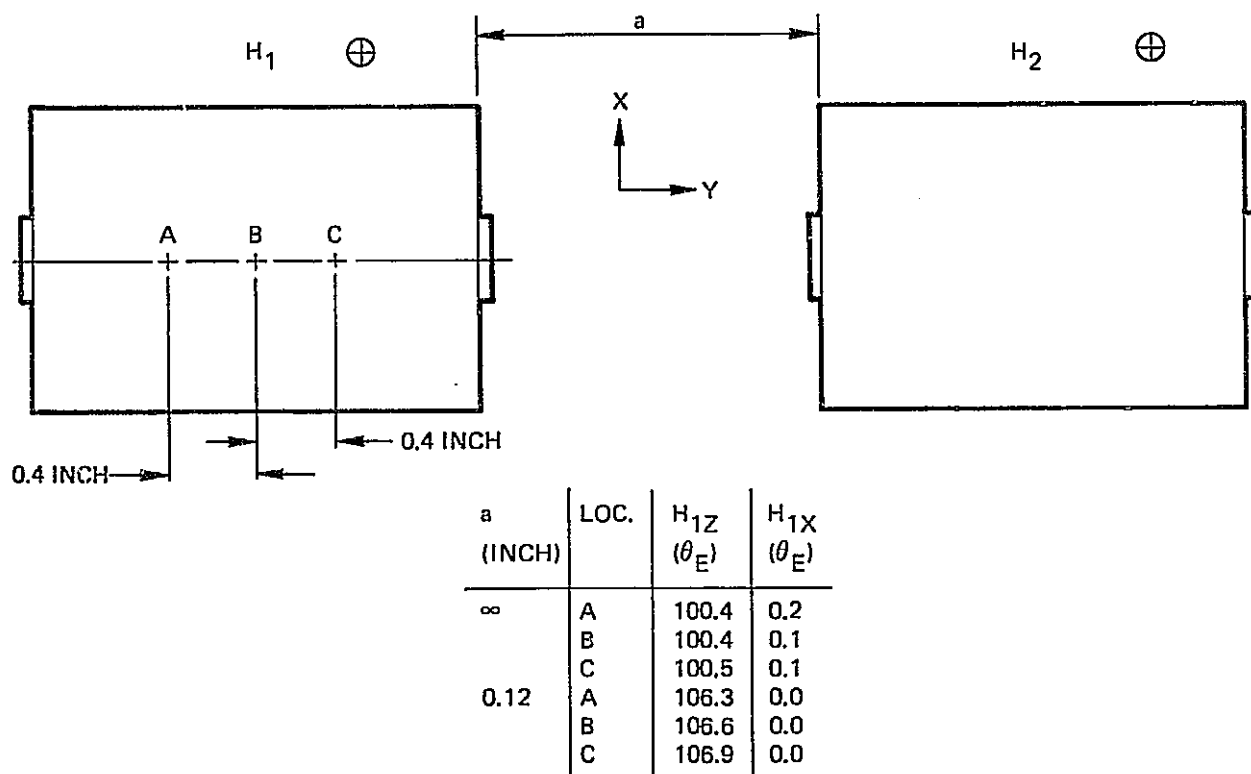


Figure 115. Cell-Cell Bias Interaction Uniformity (X Direction)

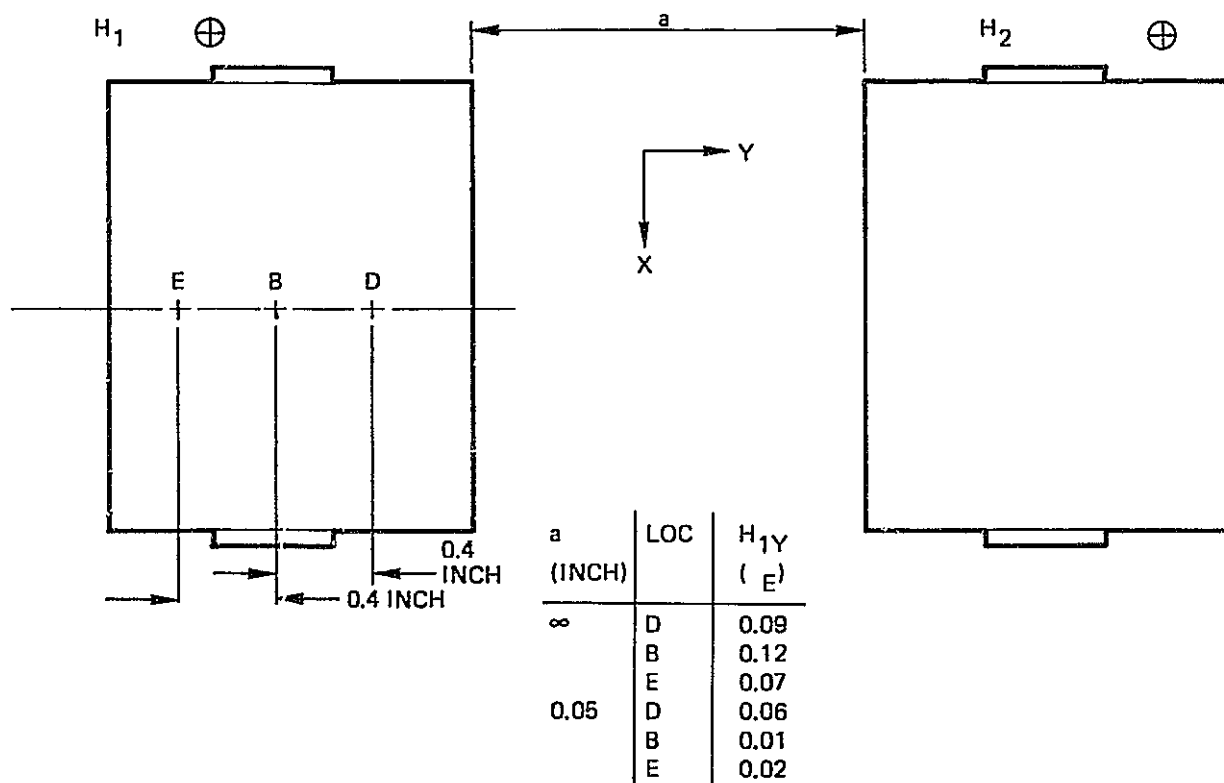


Figure 116. Cell-Cell Bias Interaction Uniformity (Y Direction)

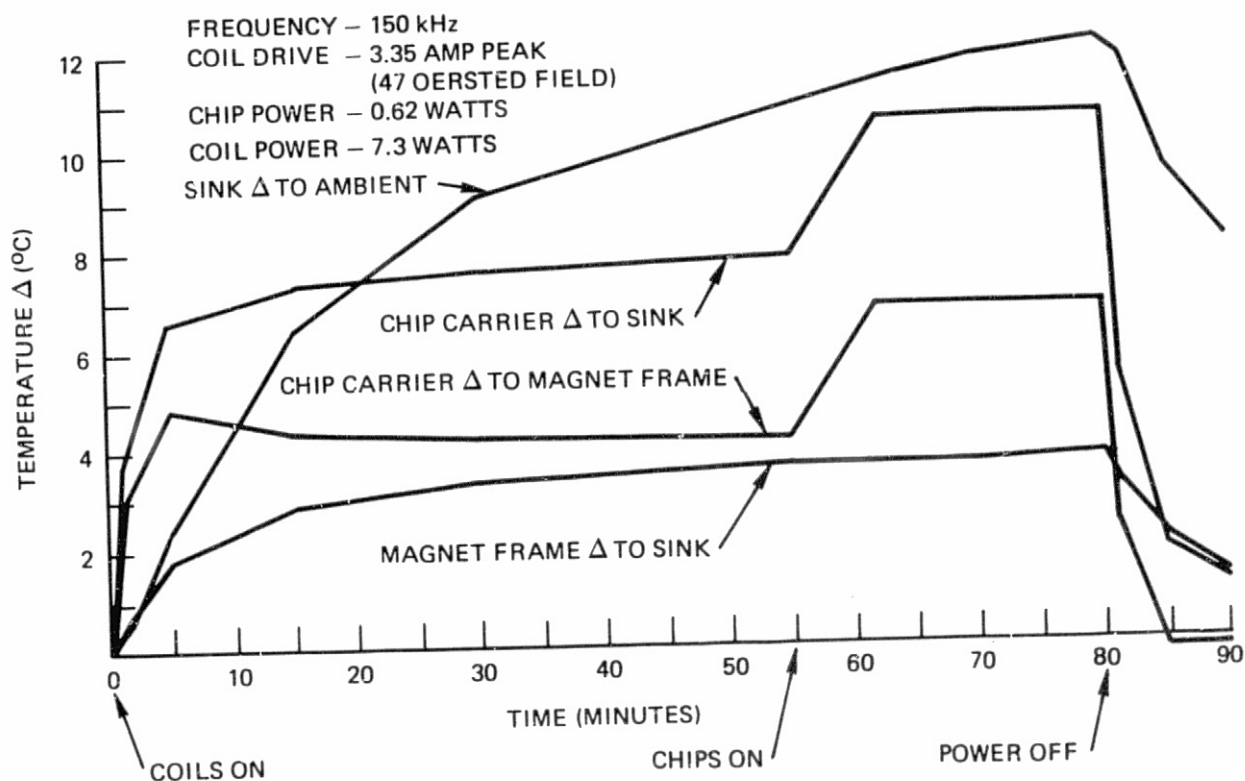


Figure 117. Temperature Gradient at 3 Amp (Chips Switched)

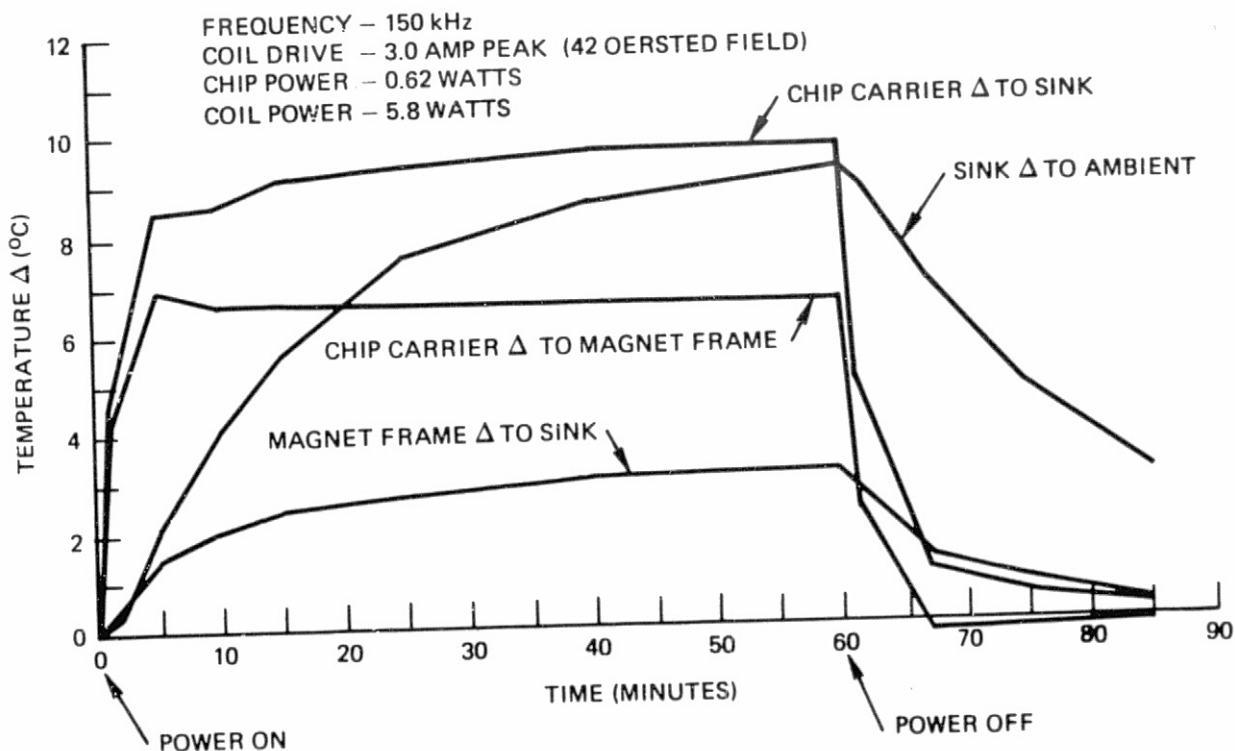


Figure 118. Temperature Gradient at 3 Amp (Chips On)

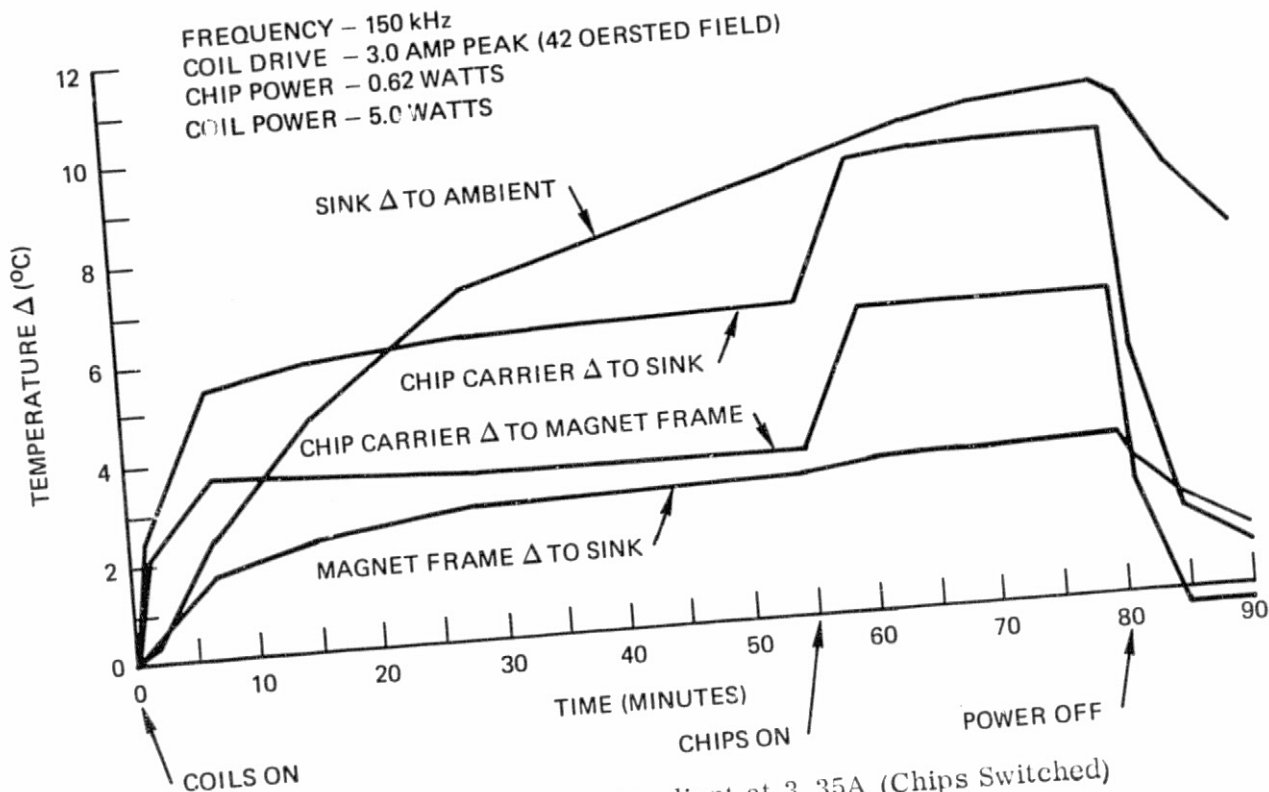


Figure 119. Temperature Gradient at 3.35A (Chips Switched)

The data shown permit prediction of memory cell temperature effects on chip bias margins. For example, for barium ferrite magnets with a temperature characteristic of .2 percent per °C, a nominal room temperature bias setting of 100 Oe, drive field of 50 Oe and chip self-heating of 80 mW or less, the data implies that a worst use temperature related excursion on the order of 1.6 Oe from chip nominal can be obtained provided the magnet and chip temperature characteristics match over the operating temperature range. For the other power loadings, the temperature gradients can be rationed from the data shown.

9.2.8 Test Fixtures and Connector Cabling Identification. - In order to evaluate cell performance and chip matching requirements two test fixtures which interface our characterization exerciser with the memory cell were constructed. A switch box was built (Figure 120) to allow independent testing of each of the chips within the cell. This fixture was used to verify performance and operational limits after chip installation in the cell. For more critical evaluation of chip performance and especially of detector performance a strobing detector (Figure 121) was built. This circuit allows evaluation of open circuit detector output and the use of high current short duration bridge current pulses.

As shown in Figure 99, the signal and drive lines from the chip are brought out of the coil on a flexible circuit. Connections between the four chips and the flexible cable are given in Figure 122. The name of the function describes polarity, function and location according to the legend given on the figure. Connector pin identification is given in Figure 123. The assignments are specifically applicable to the 10⁴ bit chip presently being delivered.

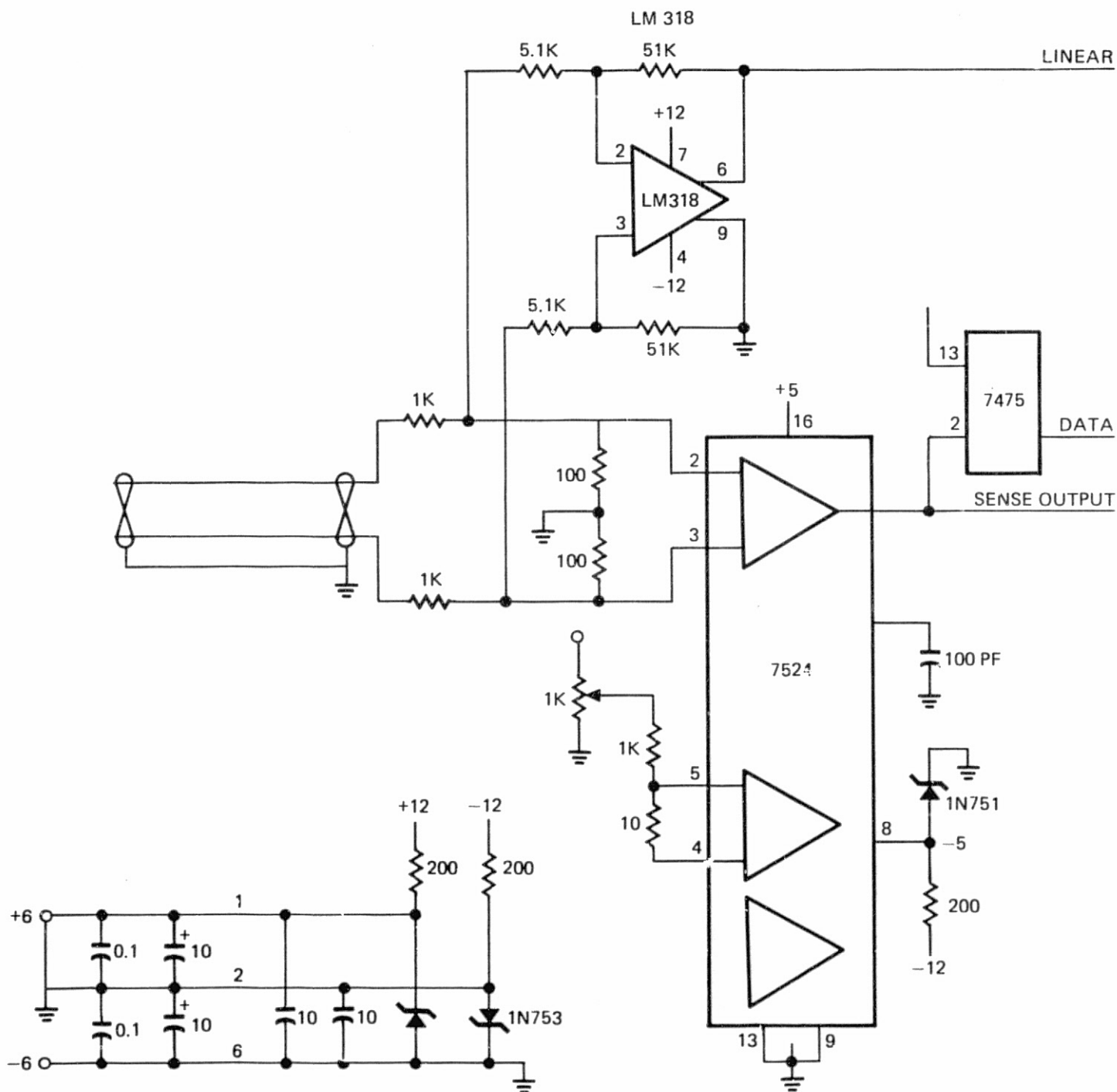


Figure 121. Exerciser Sense Channel

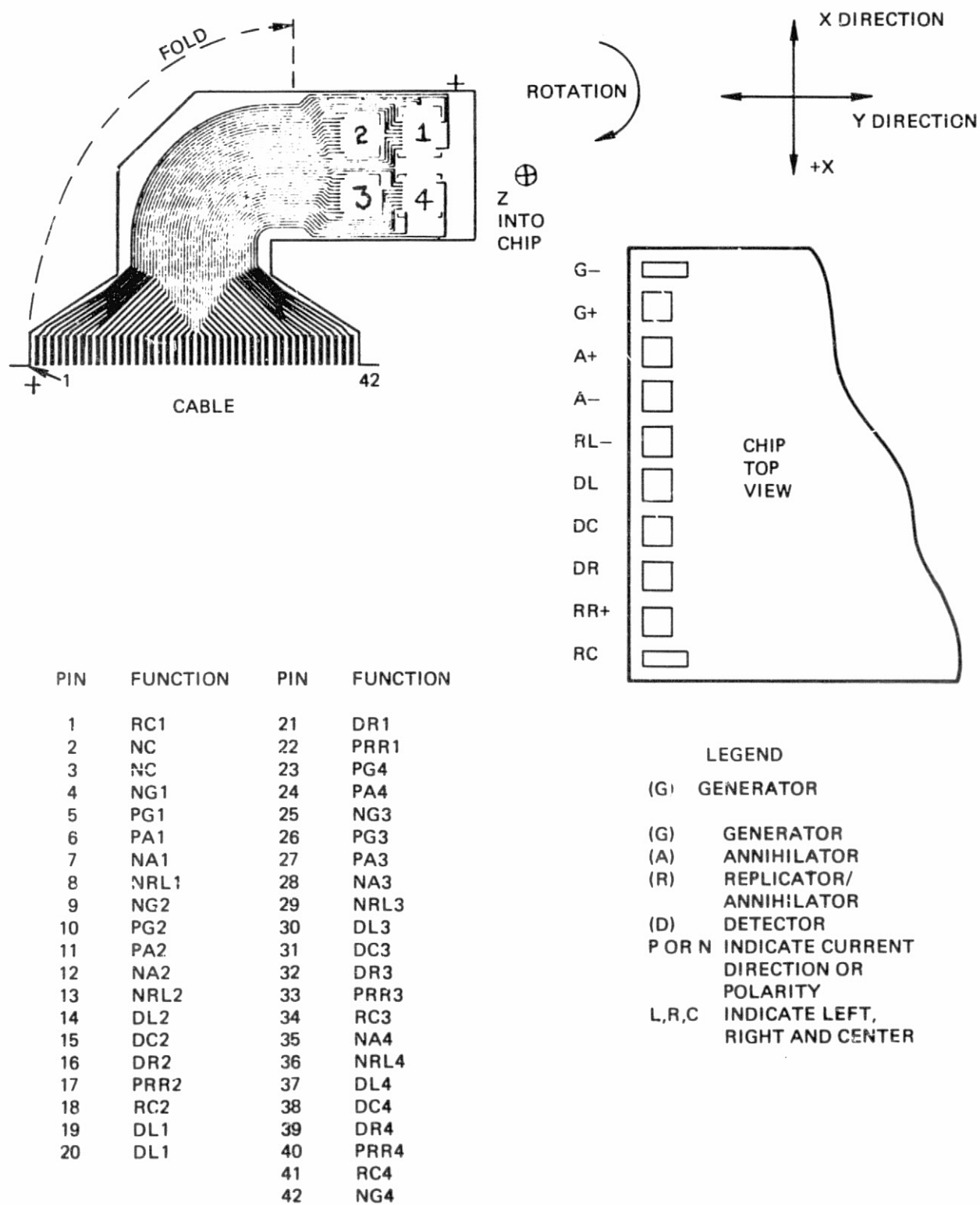


Figure 122. Flexible Cable Winding Diagram

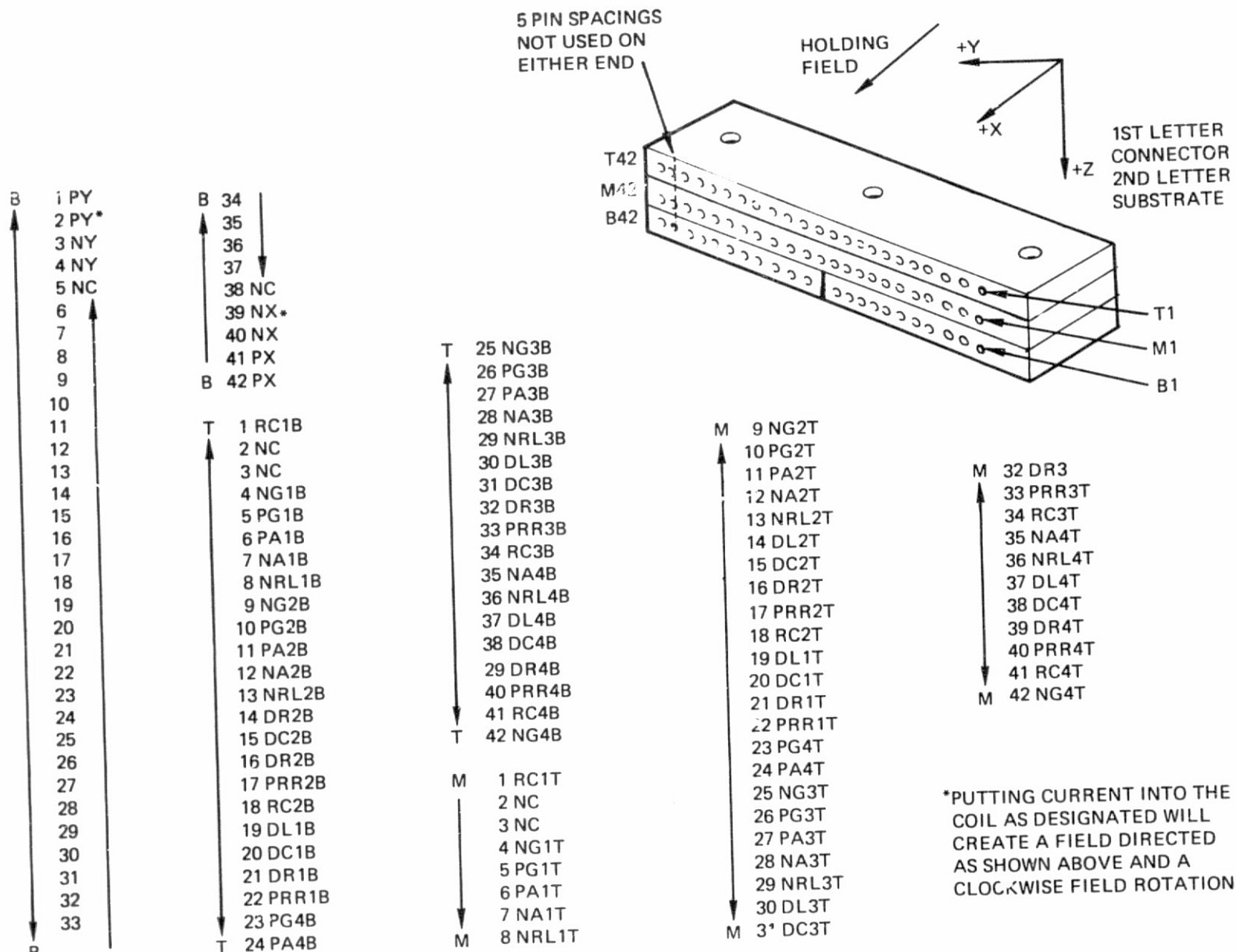


Figure 123. Connector Pin Identification

9.3 Memory Cell Characteristics

9.3.1 Cell Testing. - A series of tests was run to determine how well the selected chips perform as a composite in the magnetic bias assembly. Results confirm operation of the module from room temperature to equilibrium at approximately 50°C with the cell mounted on an aluminum "bud" box without individual adjustment of chip parameters. The only adjustment made in switching from chip to chip was in balancing the $d\phi/dt$ noise to zero each time which is a reflection of cabling layout and routing rather than chip performance.

The raw test results and observations are given in Tables 28 to 30 listed in chronological order from the receipt of the assembled cell. This data was compiled into the list of composite parameter matching tolerances given in Table 31 within which the cell can be set up and operated.

9.3.2 Test Results. - Because the chips were selected and individually characterized before installation on the substrate little difficulty was experienced in setting up the cell for composite operation as indicated in Table 28. A minor difficulty was encountered with a wire bond which was contacting the plated substrate causing a differential line to be unbalanced. All assembly and bonding operations were done in a clean room to minimize potential problems with dust or magnetic particles.

The sequence of testing started by determining composite Z margin as given in the left column of Table 29 while holding all other parameters fixed at the nominal values listed. For the first trial of 112 Oe all chips exceeded the criteria chosen as 1 min of operation which roughly corresponds to 10^7 field rotations or detection trials. The next two trials at 110 Oe and 116 Oe established the room temperature limits of Z bias excursion. Notice that chip 8 fails under high bias while chip 5 fails under low bias which is the expected result based on data taken on individual die given in Figure 96. The next step was to determine annihilator amplitude and phase margin for the worst condition which is a low Z bias. From a system design standpoint the 23 degree or approximately 400 nanosecond or phase margin and the 50 milliamps or nominal ± 20 percent of margin is more than adequate. Next a test of maximum annihilator amplitude to determine susceptibility of spirals bubble generation was done and finally the last room temperature test listed on the right of Figure 29 was to determine Replicator/annihilator amplitude margin.

Table 30 gives the results of temperature testing of the cell. The Z margin as shown on the left was determined to be about 4 Oe at 49 deg. Since the high temperature operation has the least margin the Z bias was adjusted to be in center margin at 50°C by tightening the adjustment plates on the side of the cell.

Temperature tracking of Z bias magnets compared to chip requirements was evaluated next. When the bias assembly was evaluated by itself a temperature coefficient of -0.2 Oersteds per °C was found which perfectly matches the thermal coefficient of this batch of chips. With the bias assembly mounted on a piece of aluminum, a the thermal drop of approximately 8°C occurs between magnets and substrate which effectively reduces the magnet assembly thermal coefficient to -0.15 Oe/°C. This tracking error reduces margin to about 2 Oe over temperature. The composite margin for the eight chips is about 4 Oe as shown in the left columns but tracking error of the assembly reduces the margin to approximately 2 Oe.

TABLE 28. SETUP NOTES

1. Calibration of Temperature Sensing Diodes.

Thermometer reads 27.5°C - Top Substrate Diode 0.583 Volts
 - Bottom Substrate Diode 0.585 Volts

2. Scope Calibrated

3. Gaussmeter Calibrated: Measured standard magnet of 295 Gauss as 293 Gauss

4. Frequency Set at 150, 198 Hz.

5. Set X and Y current at 4 Amps for initial test.

6. Read/write test failure on No. 1 bottom substrate and No. 2 top.
 In both cases the symptom was extraordinary $d\theta/dt$ noise.

7. Disassembled Cell: Found bond wire ends which were high and which probably were shorting to plated substrate. Bond wire ends were pushed down.

8. Suspicions Confirmed. All eight chips passed read/write test.

The third column gives the results of varying X/Y field amplitude : 10 percent at the higher temperature while the last column gives results of the final room temperature test.

Figure 124 shows the linear outputs from the eight detectors. Maximum phase shift as indicated by the "zero" and "one" crossover is about 9 deg on chip number 4 and 6. This is probably due to a slight misalignment of the chips since the whole waveform is delayed in phase, not just a portion. The large systematic noise at 45 deg is due to the replicator/annihilator which is required during read time. The high frequency systematic noise is symptomatic of uncontrolled cabling of the test box and exerciser. Minimum sensitivity of the composite is about 0.9 mV/mA at 50°C . Open circuit sensitivity of the detector is 1.1 mV/mA . Annihilating every other bit in ping-pong fashion provides a bi-polar signal, as shown in Figure 125 unclamped and clamped. The problem of placing equal and opposite polarity thresholds within the signal is clearly shown. Under these conditions the exerciser will run error free for a few minutes but only after much adjustment. Testing for parameter matching was done by annihilating all bubbles in one track and sensing consecutive bubbles in the other. Other waveforms obtained during cell test are shown in Figure 126; $d\theta/dt$ voltage is on the order of 20 mVolts peak as shown in the top two photos. The current pulses shown in the next photo are supplied by a high impedance driver. Because of the large loops on the cable and the uncontrolled impedance (open on one end, shorted on the other) the currents are distorted.

The last photo shows signals in the sense channel from the detector output on the bottom to the digital output on the top.

This raw data is compiled in Table 31 as a list of composite matching requirements. Most of the requirements allow amplitude variations of :10 percent and timing variations of :200 nsec which is the typical performance of integrated circuit and transistorized circuit design. Figure 127 is a definition of the timing used in setting up the cell. Timing is defined as from the peak X current into the positive terminal of the X coil to 50 percent amplitude on the leading edge of a pulse.

TABLE 29. COMPOSITE MARGIN TESTS - I. ROOM TEMPERATURE

	Initial Room Temperature Test			Annihilator Phase and Amplitude			Replicate Annihilate Test
	Lo Bias	Lo Bias	Hi Bias	Min	Max	Max Ampl	
H _z (Oe)	112	110	116	110.0			
H _{xy} (Oe)	48.8			48.8			
Φ (γ respect to x)	90°			90°			
Temp (°C)	20.5			20.5			
I _g (ma)	200 ma 22.5° Wide			200 ma 22.5°			
Φ _g (Deg)	90°			90°			
I _A (ma)	80 ma 22.5° Wide	100 ma		100 (22.5°)		150 ma	125 ma
Φ _A (Deg)	160	135	11	112½	150 Except as noted below	125°	
R/A (ma)	130 ma 22½°			130 ma 22½			(See below) 22½ Wide
Φ _{RIA} (Deg)	22½			22½			22½
Bridge Drive (ma) Each Side	3.2						
Pattern	1111 1010						
Φ Strobe	202°						
Chip No. 1 No. 14	All	> 1 Min	> 1 Min	> 1 Min	> 1 Min	> 1 Min	110 - 200
Chip No. 2 No. 28	> 1 Min	45 Sec ¹		> 1 Min	Limit at 135°		100 - 200
Chip No. 3 No. 43		> 1 Min		> 1 Min	Limit at 135°		120 - 200
Chip No. 4 No. 78		> 1 Min	All	> 1 Min	> 1 Min	All	100 - 200
Chip No. 5 No. 43-b		20 Sec		20 Sec ²	Limit at 135°		120 - 200
Chip No. 6 No. 65		> 1 Min		> 1 Min	1 Min		90 - 200
Chip No. 7 No. 29		> 1 Min		> 1 Min	10 Sec		110 - 200
Chip No. 8 No. 58		> 1 Min	20 Sec ³ 31 Min	20 Sec ²	> 1 Min		100 - 200
¹ Soft Error ² Hard Error ³ At limit occasionally fails							

TABLE 30. COMPOSITE MARGIN TESTS - II. VARIABLE TEMPERATURE

	High Temperature Test		Z Bias Tracking Test		Rotating Field Test		Final Room Temp
	Lo Z	Hi Z	Z-Field Set-Up	Room Temp			
H _z (Oe)	105.3	109.0	108.1 ³	110.8	108.5	108.5	111
H _{xy} (Oe)	48.8				45	54	48.8
φ (y respect to x)	90°				90		
Temp (°C)	49		50°	27	48	48	27°
I _g (ma)	200 ma 22½ Wide				200 ma 22½ Wide		
φ _g (Deg)	90°				90°		
I _A (ma)	125 ma 22½° Wide				125 ma 22½° Wide		
φ _A (Deg)	125				125		
R/A (ma)	130 ma 22½° Wide				130 ma 22½° Wide		
φ _{RIA} (Deg)	22½				22½		
Bridge Drive (ma)	3.2				3.2		
Pattern	1111 1010				1111 1010		
φ Strobe	202°				202°		
Chip No. 1	> 1 Min	> 1 Min			> 1 Min	> 1 Min	> 1 Min
Chip No. 2							
Chip No. 3							
Chip No. 4	All				All	All	All
Chip No. 5							
Chip No. 6							
Chip No. 7							
Chip No. 8		5 Sec ²					
1 Soft Err							
2 Hard Err							
3	Depends somewhat on set-up accuracy probe placement etc. is probably ± ½ Oe						

TABLE 31. COMPOSITE PARAMETER MATCHING REQUIREMENTS

	UNITS	MIN.	NOMINAL	MAX.	TOLERANCE
Z Bias Composite Chip					
Operating Limits					
at 25°C	Oe	110		116	
at 50°C	Oe	105.3		109	
8 Chip and Z Bias Magnet					
Composite Operating Limits					
Chips at 25°C Magnet	25°C Oe	110.0	111.0	116.0	
Chips at 50°C Magnet	≈40°C Oe	105.0	108.3*	109.0	
Thermal Coefficient					
Composite Chips	Oe/°C	—	.2	—	
Magnet Frame		—	.18	—	
Rotating Field					
H _X Oe		45	50	55	±10%
H _X Oe		45	50	55	±10%
Phase H _Y to H _X	Degrees	—	90°	—	
Rotation Freq.	Hz		150, 198	—	
Detector Resistance	KΩ		1.375		
(Each Side)					
Detector Match	Ω		50		
Differential Output "1"—"0"	Millivolts	2.1			
Bridge Drive	MA		3.2		

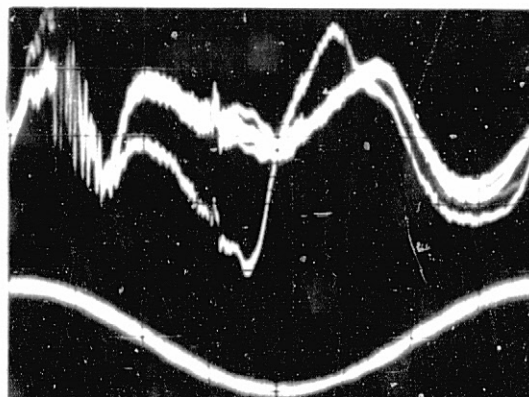
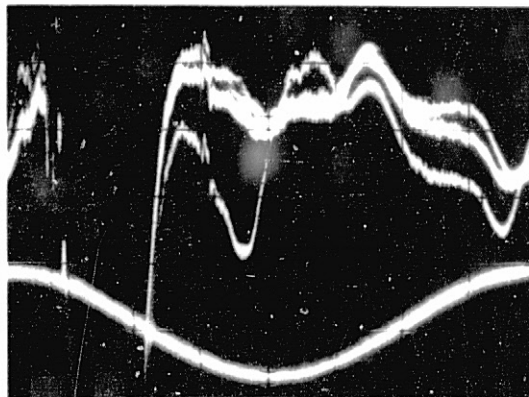
*The Z Bias Magnet was set to this value after running for an hour

TABLE 31 (Cont)

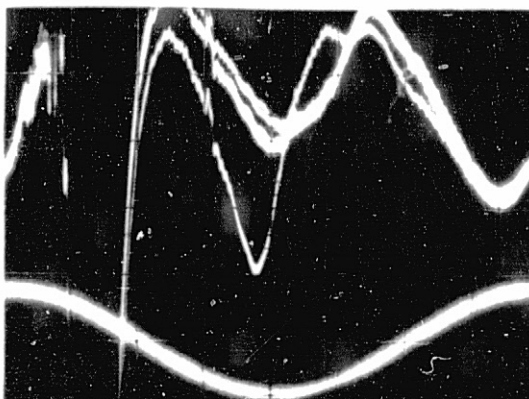
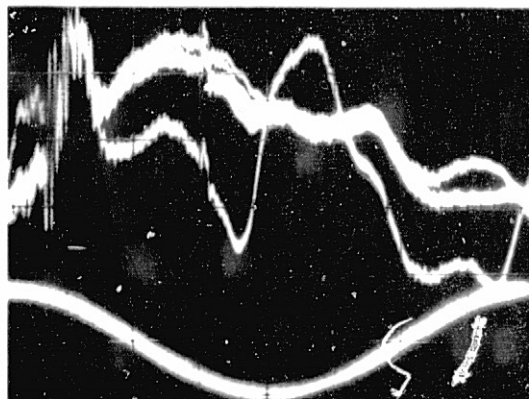
	UNITS	MIN.	NOMINAL	MAX.	TOLERANCE
Generator (\bar{Z})	Ω				
Resistance			3		
Current	mA	180	200		$\pm 10\%$
G_D	Degrees	—	90^0	—	$\pm 20^0$
G_W	Degrees	22-1/2	—	—	$\pm 20^0$
Annihilator (\underline{Z})	Ω				
Resistance			3		
Current	mA	100	111	122	$\pm 10\%$
A_D	Degrees	112	125	135	$\pm 12\%$
A_W	Degrees	22-1/2	—	—	$+ 20^0$
Replicate/Ann. (\underline{Z})					
Resistance	Ω (each)		3		
Current	mA	120	133	147	$\pm 10\%$
A_D	Degrees	20	30	40	$\pm 10^0$
A_W	Degrees	22-1/2	—	—	$+ 20$
Restore					
Release	Degrees	—	165^0	—	
Strobe (ST)	Degrees	—	202^0		

ALL CHIPS FROM
WAFER 8-3-1

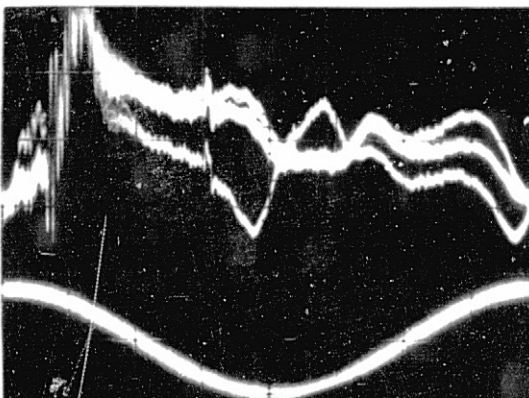
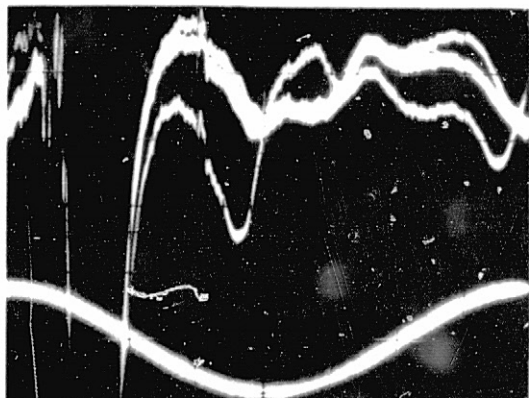
CHIPS NO.1, 2
-14; -28



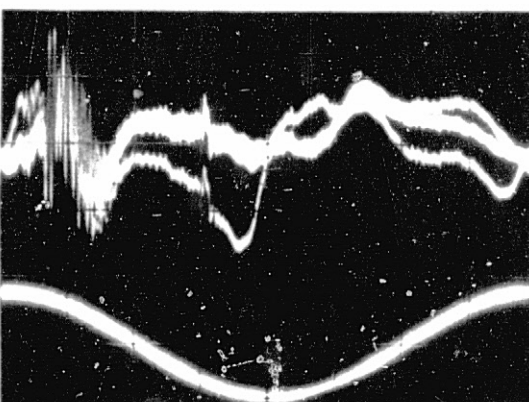
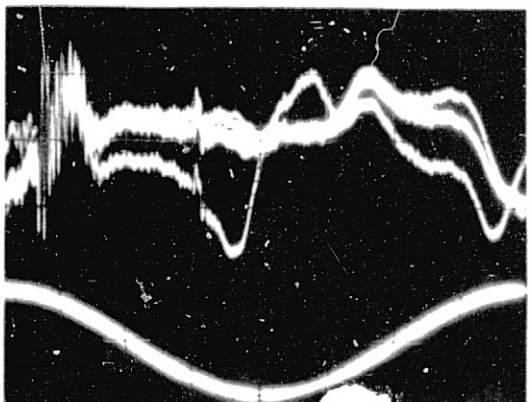
CHIPS NO.3,4
-43; -78



CHIPS NO.5,6
-43b; -65

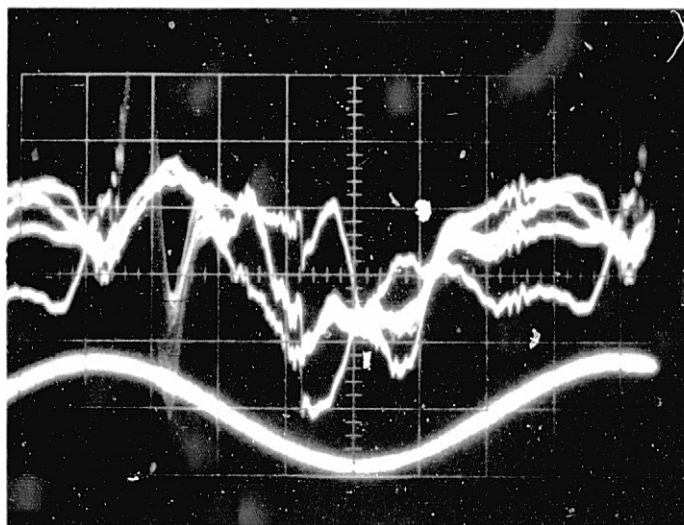


CHIPS NO.8,9
-29; -58



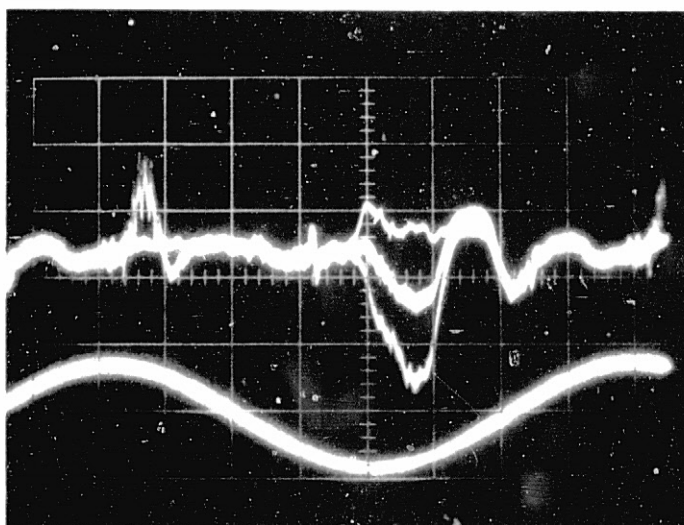
150 KHz, 50°C OPERATION
HORZ - 45°/DIV, VERT - 1.43 MV/DIV
A = 140; X DRIVE CURRENT SHOWN AS
REFERENCE

Figure 124. Module Detector Outputs



(a) UNCLAMPED

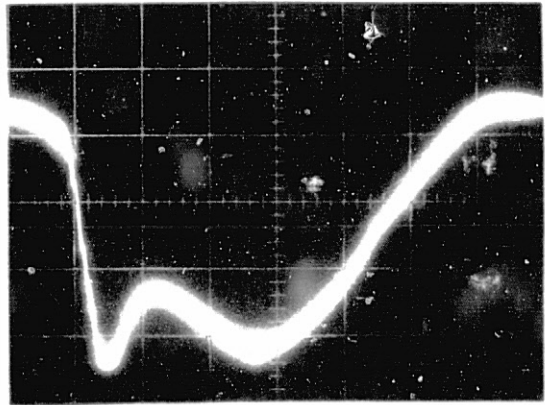
VERT - 1.43 MV/DIV
HORZ - 45 DEG/DIV or 833 NANOSEC/DIV
BOTTOM IS X CURRENT FOR REFERENCE; CHIP 8



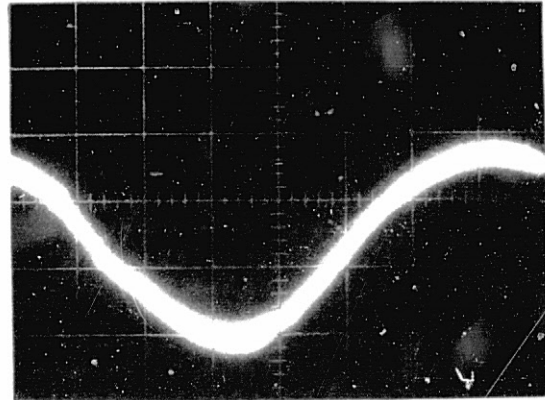
(b) CLAMPED

Figure 125. Ping-Pong Detection

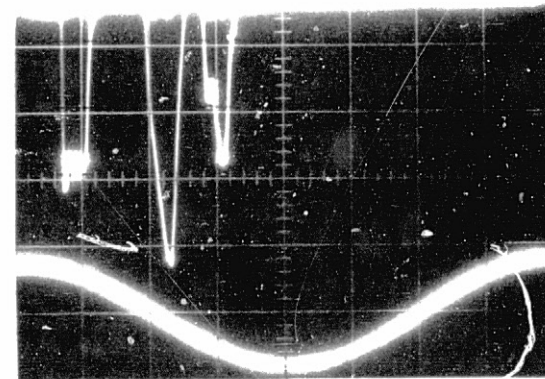
UNBALANCED OUTPUT FROM CHIP NO.1
 VERT - 14.3 MILLIVOLTS/DIV
 HORZ - 45°/DIV



SAME AS ABOVE EXCEPT FROM CHIP NO.2



CELL CURRENTS
 LEFT - REPLICATE ANNIHILATOR
 MIDDLE - GENERATOR PULSE
 RIGHT - ANNIHILATOR
 VERT - 50 MA/DIV
 HORZ - 45°/DIV OR 833 NANOSEC/DIV
 BOTTOM IS X CURRENT FOR REFERENCE



SENSE CHANNEL SIGNALS
 TOP - DIGITAL OUTPUT
 SENSE AMP OUTPUT
 PREAMP OUTPUT CLAMPED
 BOTTOM - PREAMP OUTPUT UNCLAMPED

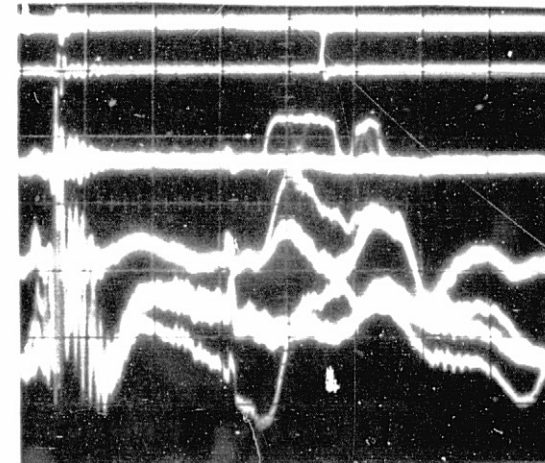


Figure 126. Cell Waveforms

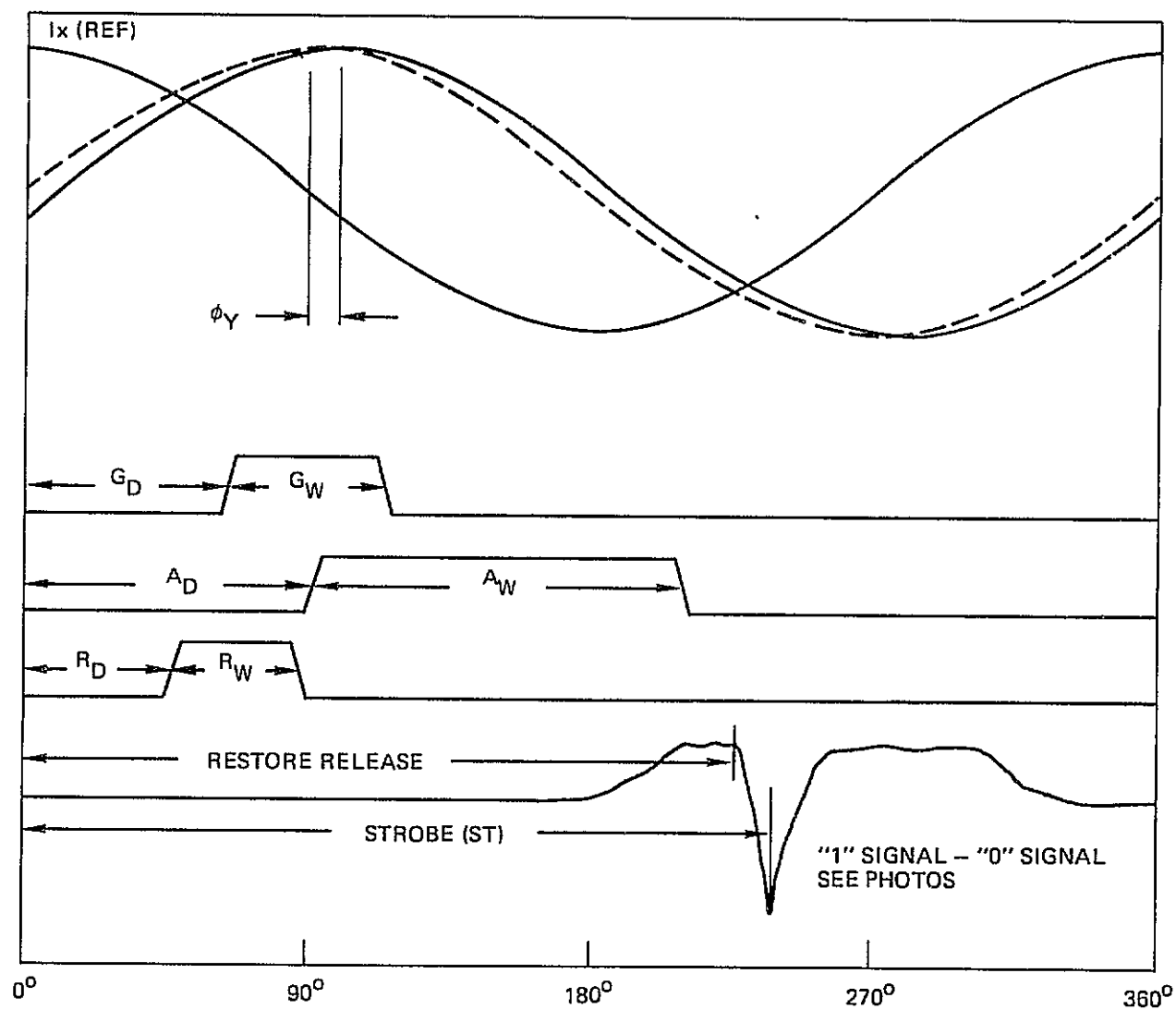


Figure 127. Timing Relationships

REFERENCES

1. F. B. Hagedorn, "Dynamic Conversion During Magnetic Bubble Domain Wall Motion," J. Appl. Phys., Vol. 45, pp. 3129-3140, July 1974.
2. Y. S. Lin and G. E. Keefe, "Suppression of Hard Bubbles by a Thin Permalloy Layer," Appl. Phys. Lett. Vol. 22, pp. 603-604, 1 June 1973.
3. A. H. Bobeck, S. L. Blank, and H. J. Levinstein, "Multilayer Epitaxial Garnet Films for Magnetic Bubble Devices - Hard Bubble Suppression," Bell System Tech. J., Vol. 51, pp. 1431-1435, July - Aug 1972.
4. R. D. Henry, P. J. Besser, R. G. Warren, and E. C. Whitcomb, "New Approaches to Hard Bubble Suppression," IEEE Trans. Magn., Vol. MAG-9, pp. 514-517, Sept 1973.
5. R. Wolfe and J. C. North, "Suppression of Hard Bubbles in Magnetic Garnet Films by Ion Implantation," Bell System Tech. J. Vol. 51, pp. 1463-1440, July - Aug. 1972.
6. G. P. Vella-Coliero and W. J. Tabor, "Measurement of Magnetic Bubble Mobility in Epitaxial Garnet Films," Appl. Phys. Lett., Vol. 21, pp. 7-8, 1 July 1972.
7. B. W. Hewitt, R. D. Pierce, S. L. Blank, and S. Knight, "Technique for Controlling the Properties of Magnetic Garnet Films," IEEE Trans. Magn., Vol. MAG-9, pp. 366-372, Sept. 1973.
8. A. P. Malozemoff and K. Papworth, "High-Speed Photography of Topological Switching and Anisotropic Saturation Velocities in a Misoriented Garnet Film," AIP Conf. Proc. No. 24, pp. 593-594, 1974.
9. F. B. Humphrey, "Transient Bubble Domain Configurations in Garnet Materials Observed Using High Speed Photography," IEEE Trans. Magn., Vol. MAG-11, 1975 (in press).
10. G. J. Zimmer, T. M. Morris, and F. B. Humphrey, "Transient Bubble and Stripe Domain Configurations in Magnetic Garnet Materials," IEEE Trans. Magn., Vol. MAG-10, pp. 651-654, Sept. 1974.
11. G. J. Zimmer, L. G' al, K. Vural, and F. B. Humphrey, "Instantaneous Radial Wall Velocities in Magnetic Garnet Bubble Domains," Appl. Phys. Lett., Vol. 26, 1975 (in press).
12. J. C. Slonczewski, "Theory of Domain Wall Motion in Magnetic Films and Platelets," J. Appl. Phys., Vol. 44, pp. 1769-1770, Apr. 1973.
13. N. L. Shryer and L. R. Walker, "The Motion of 180° Domain Walls in Uniform dc Magnetic Fields," J. Appl. Phys., Vol. 45, pp. 5406-5421, Dec. 1974.

14. A. P. Malozemoff and J. C. DeLuca, "Ballistic Overshoot in the Gradient Propagation of Bubbles in Garnet Films," *Appl. Phys. Lett.*, Vol. 26, pp. 719-721, June 1975.
15. T. Kobayashi, P. K. George, and F. B. Humphrey, "Dynamics of Bubbles in Field Access Devices Studies using a High Speed Optical Sampling Microscope," *Intermag Conf.*, London, Paper 21.2, Apr. 1975; Submitted to *IEEE Trans. Magn.*
16. A. P. Malozemoff and J. C. DeLuca, "Effect of Misorientation on Growth Anisotropy in [111]-Oriented Garnet Films," *J. Appl. Phys.*, Vol. 45, pp. 4586-4589, Oct. 1974.
17. R. A. Abram, R. J. Fairholme, M. D. R. Tench, and K. A. Gehring, "The Effect of Substrate Misorientation on the Magnetic Properties of Epitaxial Garnet Films," *J. Phys. D: Appl. Phys.*, Vol. 8, pp. 94-98, Jan. 1975.
18. T. Hibiya, Y. Hidaka, S. Fujiwara, and K. Matsui, "Easy Magnetization Axis of LPE Garnet Films Grown on Misoriented [111] GGG Substrates," *J. Phys. Soc. Japan*, Vol. 39, 1975 (in press).
19. L. R. Tocci, et al., "Magnetic Bubble Memory," *Air Force Technical Report*, AFAL-TR-75-75, May 1975.
20. E. Della Torre and M. Y. Dimyan, "Anisotropy of Wall Energy in Orthoferrites," *IEEE Trans. Magn.*, Vol. MAG-6, pp. 489-492, Sept. 1970.
21. F. B. Hagedorn and B. S. Hewitt, "Growth-Induced Magnetic Anisotropy in Variousy Oriented Epitaxial Films of Sm-YIGG," *J. Appl. Phys.*, Vol. 45, pp. 925-928, Feb. 1974.
22. E. Schlomann, "Theory of High-Speed Wall Motion in Bubble Films with an In-Plane Anisotropy," presented at the 7th Int. Colloq. on Magn. Films, Regensburg, paper 2-1, Apr. 1975.
23. P. I. Bonyhard et al., "Magnetic Bubble Memory Chip Design" *IEEE Trans. on MAG.*, Vol-MAG9, pp. 433-436 (1973).
24. R. A. Baugh, "Some Aspects of Bubble Memory Module Design," Paper 22-2 *Intermag Conference*, Toronto (1974).
25. C. H. Bajorek and A. F. Mayadas, "Reliability of Magnetoresistive Bubble Sensors," *AIP Conf. Proc.* Vol. 10 pp. 212-221 (1972).
26. J. H. J. Fluitman, "The Influence of Sample Geometry on the Magnetoresistance of Ni-Fe Films," *Thin Solid Films*, Vol. 16, pp. 269-276, (1973).
27. K. Asama, "NiCo Film with Large Magnetoresistance for Bubble Detection," *AIP Conf. Proc.* Vol. 18 pp. 110-114 (1973).

28. K. Komenou, "Permalloy Film for Single-Level Detector with High Sensitivity," AIP Conf. Proc., Vol. 24, pp. 554-555, (1974).
29. W. Strauss, et al., "Characteristics of a Detection-Propagation Structure for Bubble-Domain Devices," AIP Conf. Proc., Vol. 10, pp. 202-206, (1972).
30. A. H. Bobeck, et al., "Multilayer Garnet Films for Hard Bubble Suppression," AIP Conf. Proc., Vol. 10, pp. 498-502, (1972).
31. W. Strauss, "Detection of Cylindrical Magnetic Domains," J. App. Phys., Vol. 42, pp. 1251-1257, (1971).
32. G. S. Almasi, G. E. Keefe, Y. S. Lin, and D. A. Thompson, "Magnetoresistive Detector for Bubble Domains," J. Appl. Phys., Vol. 42, pp. 1268-1269, (1971).
33. W. Strauss, et al., "Magnetoresistance Sensors for Garnet Bubble Domains," AIP Conf. Proc., Vol. 5, pp. 235-239, (1971).
34. G. Almasi, "High Speed Sensing of Small Bubbles," AIP Conf. Proc., Vol. 10, pp. 207-211, (1972).
35. J. L. Archer, et al., "Magnetic Bubble Domain Devices," IEEE Trans. on MAG., Vol. MAG-8, pp. 695-700 (1972).
36. L. R. Tocci, et al., "High Speed Characteristics of a Chevron Stretcher Detector," AIP Conf. Proc., Vol. 10, pp. 197-201, (1972).
37. A. Lill, "Improved Chevron Gap Detector," AIP Conf. Proc., Vol. 24, pp. 556-557, (197).
38. T. T. Chen, et al., "Study on the Thick Film Chevreon Detector," AIP Conf. Proc., Vol. 18, p 115 (1973).
39. A. H. Bobeck, et al., "Evolution of Bubble Circuits Processed by a Single Mask," IEEE Trans. on MAG., Vol. MAG, pp. 478-480, (1973).
40. T. J. Nelson, "Passive Replicator for Magnetic Bubbles," AIP Conf. Proc., Vol. 24, pp. 643-644, (1974).